Synthesis and characterisation of copper zinc tin sulphide photovoltaic materials in bulk and single crystal forms

Ng, Mako

Award date:
2018

Awarding institution:
University of Bath

Synthesis and characterisation of copper zinc tin sulphide photovoltaic materials in bulk and single crystal forms

Tat Ming Ng

A thesis submitted for the degree of Doctor of Philosophy

University of Bath

Centre for Sustainable Chemical Technologies

Department of Chemistry

July 2018

Contents

Acknowledgments

I would like to thank my supervisor Prof. Mark Weller for his help during the course of the PhD. He secured beam time for the synchrotron and neutron experiments and it was great experience visiting these international facilities.

I am grateful to Prof. Laurie Peter for his kind support, precious advice and establishing valuable collaborations. I also thank his post-docs Dr. Gabriela Kissling and Dr. Sara Dale for their help in the laboratory.

I thank Dr. Phillip Dale (University of Luxembourg) and Dr. David Lane (Cranfield University) for hosting me in their institutes; Phil Jones for all the custom-made glassworks; and Dr. Mary Mahon for the help in crystallography.

Funding was provided by EPSRC Doctorial Training Centre in Sustainable Chemical Technologies at the University of Bath (Grant No. EP/G03768X/1) and EPSRC PVTeam project (Grant No. EP/L017792/1).

I wish to thank my fellow students in the Centre for Sustainable Chemical Technologies, all my friends in the UK and my family and friends back in Hong Kong.

Work done in conjunction with others

1. XRF measurements in chapter 4.1.2 were carried out by Dr. David Lane at Cranfield University with myself observing.
2. Spectroscopic ellipsometry experiment and analysis in chapter 5.5 were performed by myself with training from Dr. David Lane at Cranfield University.
3. Sample preparation for AAS in chapter 4.1.2 were carried out by myself. AAS experiments were carried out by Alan Carver at University of Bath with myself observing. Data analysis were carried out by myself.
4. Steady state PL experiments in chapter 5.4 were carried out by Jessica de Wild at University of Luxembourg with myself observing. Data analysis were carried out by Finn Babbe.
5. Time resolved PL experiments and analysis in chapter 5.4 were performed by Dr. Bernard Wenger (University of Oxford).
6. Impedance measurements and analysis in chapter 5 were performed by Dr. Gabriela Kissling (University of Bath, now in University of Southampton)
7. Neutron diffraction experiments in chapter 6.1.2 were carried out by Dr. Oscar Fabelo at Institut Laue-Langevin, Grenoble with myself observing. Data analysis using JANA2006 were self-learnt and carried out by myself with advice from Dr. Pascaline Patureau at University of Bath.
8. The CZTS single crystal devices in chapter 7 were fabricated by Michele Melchiorre at University of Luxembourg with myself observing.

Abstract

The results presented in this thesis focus on the synthesis, structural, optoelectronic and spectroscopic characterisation on Cu_2ZnSnS_4 (CZTS) single crystals. Stoichiometric and off-stoichiometric CZTS single crystals with dimensions in sub-millimetre range were grown using chemical vapour transport method. The elemental composition of the crystals were confirmed with energy-dispersive X-ray spectroscopy, X-ray fluorescence spectroscopy, and atomic absorption spectroscopy. The phase purity were confirmed with powder X-ray diffraction and Raman spectroscopy, and no secondary phases were observed.

The external quantum efficiency (EQE) were measured by photocurrent spectroscopy using electrolyte contact, and approaches 100% close to the bandgap energy, indicating efficient carrier collection. The bandgap was found to be 1.64 – 1.68 eV. The room temperature photoluminescence spectroscopy of the crystals was attributed to radiative recombination via tail states, with lifetimes in the nanosecond range. Electrolyte electroreflectance spectra and spectra of the third derivative of the optical dielectric constant obtained from spectroscopic ellipsometry were fitted to two optical transitions at 1.71 and 1.81 eV in the bandgap region, suggesting a larger valence band splitting than predicted theoretically.

Single crystal devices were fabricated using Mo/CZTS/CdS/Al:ZnO/i-ZnO/Ni configuration and suffered from high series resistance or shunting. IV characteristic, EQE and impedance were measured and analysed.

Cu/Zn disorder were studied on samples annealed between 110 and 425 °C using resonance Raman spectroscopy, single crystal neutron diffraction and powder anomalous diffraction. Very high resonance Raman order parameter, Q, of up to 17 were observed in samples with low annealing temperatures after annealing for > 300 hours. The critical temperature observed is around 250 °C. The occupancy factors of Cu and Zn were successfully obtained using single crystal neutron diffraction, but not with powder anomalous diffraction due to strong correlation between the occupancy factors and the pseudosymmetry of kesterite structure.

1 Introduction

The global carbon dioxide (CO_2) concentration in the atmosphere has reached 400 parts per million (ppm) in 2016.[1] Carbon dioxide is one of the greenhouse gases that absorbs and emits radiation within the thermal infrared range, causing an increase of temperature on the Earth's surface. This is known as the greenhouse effect. If the rate of greenhouse gas emission continues as it is to date, the Earth's surface temperature could exceed the 2.0 °C limit compared to pre-industrial levels, with potentially harmful effects on the ecosystems, biodiversity and human globally.[2]

The largest single source of global greenhouse gas emissions came from electricity and heat production, which accounted for 25% of global greenhouse gas emissions in 2010.[3] With increasing concern over the reserve of fossil fuels and the impact on the environment of extracting and burning them, there is a need to replace fossil fuels with sustainable alternatives. In 2014, 23,816 TWh of electricity were generated, and 66.7% of those were generated from burning fossil fuels.[4] It is noteworthy that the annual global solar energy input is roughly 87 PW[5] a few thousand times more than the current worldwide energy consumption. Solar energy is one of the most abundant, clean and effective energy source for humankind known today. When

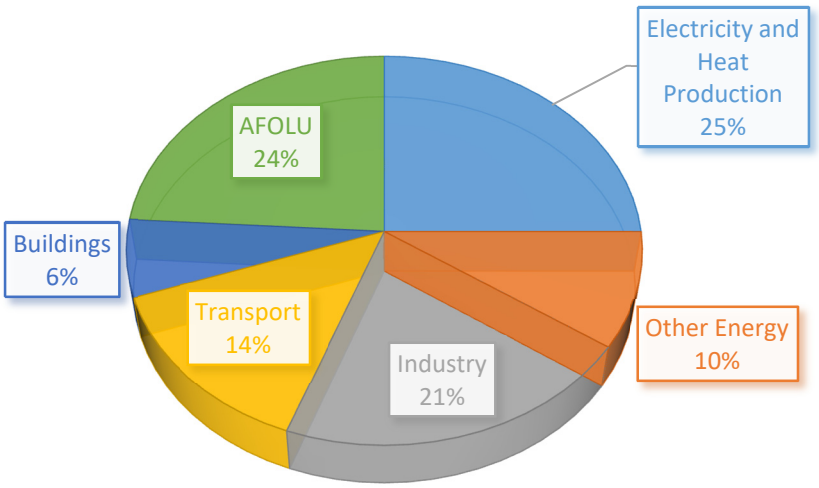

Figure 1.1 Greenhouse gas emissions by economic sectors in 2010. The total emission was 49 Gt CO_2eq. Data acquired from Victor *et al.*[3] *AFOLU: agriculture, forestry and other land use*

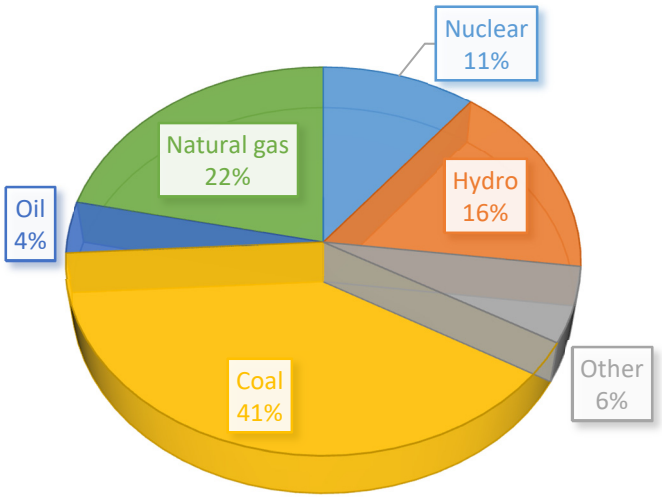

Figure 1.2 Electricity generation by type of fuels in 2014. Data acquired from International Energy Agency.[4]

compared with other renewable sources, the theoretical conversion efficiency of solar energy is relatively high when compared to other power generators; furthermore, solar energy systems do not necessarily contain movable parts, which means there is no system wear due to mechanical movement. Therefore solar energy systems can work continuously free from maintenance longer than other power generation technologies.[6] For all these reasons, it would be wise to increase electricity generation from solar.

There are two ways solar energy can be harvested and converted into electrical energy, concentrated solar power (CSP) and photovoltaic (PV). CSP use mirrors or lenses to concentrate a large area of sunlight onto a small area. Electricity is generated when the concentrated light is converted to heat, which drives a heat engine connected to an electrical power generator. A PV panel contains a number of different layers. The absorber layer which absorbs the light, causing excitation of an electron or other charge carrier to a higher-energy state. Those charge carriers are separated by the other layers before they can relax, and feed into an external circuit. This generates an electric potential and hence produce electricity in the external circuit. A simple illustration of the process is shown in Figure 1.3 .This thesis will only discuss PV materials.

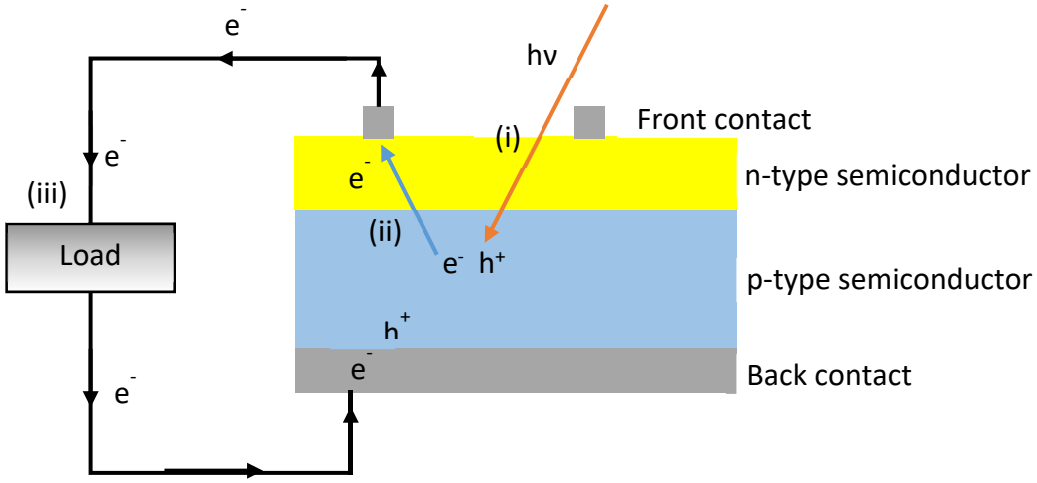

Figure 1.3 A simple illustration showing how electricity is generated from a PV device. (i) The absorption of a photon creates an electron-hole pair. (ii) The carriers are separated by the action of the electric field in the depletion region at the p-n junction. (iii) When the p-side and n-side are connected to an external circuit (*i.e.* under short circuit), these carries will flow and a photocurrent is observed.

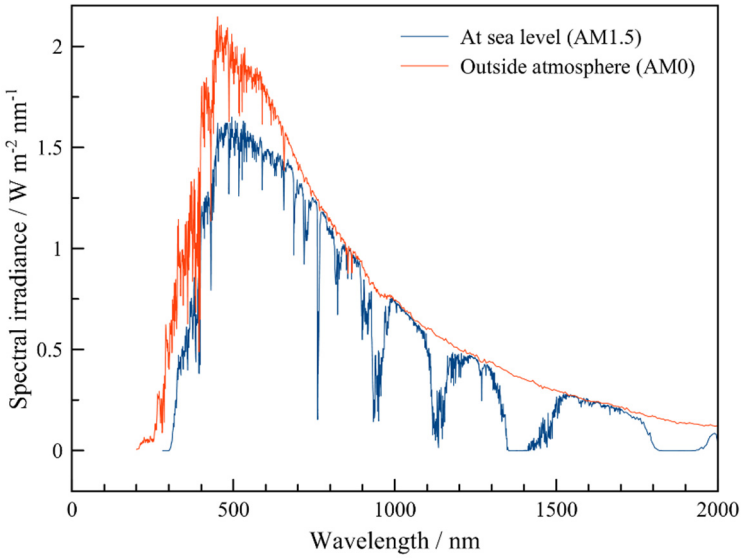

Figure 1.4 Solar radiation spectra at both the top of the earth's atmosphere (AM0) and sea level (AM1.5). Data acquired from ASTM International.[7, 8]

1.1 Characteristics of a photovoltaic cell

The sun emits a spectrum of light at different wavelengths, from ultra violet (UV) all the way into the infrared (IR), with the strongest irradiation in the visible region. As the sunlight passes through the atmosphere, ~98% of UV radiation (200 – 320 nm) is

absorbed by the ozone layer, some other radiations are absorbed by atomic and molecular gases with specific absorption lines and bands, e.g. water at 900, 1100, 1400 and 1900 nm, and CO_2 at 1800 and 2600 nm. The standard spectrum at temperate latitudes is Air Mass 1.5 (AM1.5), which corresponds to a solar zenith angle of 48.2°, 1.5 times the thickness of the atmosphere normally to the Sun.[9] AM0 (zero atmosphere) spectrum is used as the standards for space, and AM1 (sun directly overhead) spectrum is used as the standards for equatorial and tropical regions.

Figure 1.5 shows the current-voltage (J-V) characteristics of a photodiode. Most solar cells behave like a diode in the dark, producing a current in the opposite direction of the photocurrent. This reverse current is usually called the dark current density (J_{dark}):

Equation 1.1

$$J_{dark} = J_0(e^{qV/k_BT} - 1)$$

where J_0 is the diode saturation current, q the electron charge, V is the voltage, k_B is the Boltzmann's constant, and T is the absolute temperature. Under illumination, the photocurrent density under short-circuit (J_{SC}) is given by Equation 1.2:

Equation 1.2

$$J_{SC} = q \int b_S(E) QE(E) dE$$

where $b_S(E)$ is the incident spectral photon flux density, and QE(E) is the probability that an incident photon of energy E will deliver one electron to the external circuit. The net current density in an ideal solar cell is:

Equation 1.3

$$J = J_{SC} - J_{dark} = J_{SC} - J_0(e^{qV/k_BT} - 1)$$

At short circuit conditions, the open-circuit voltage (V_{OC}) is zero. J_{SC} is controlled only by current generated and is the highest obtainable from the cell. When the contacts are isolated, *i.e.* open circuit conditions, the potential difference is at maximum (V_{OC}). This is equivalent to dark current and photocurrent exactly cancels out, *i.e.* Jsc = J_{dark}, and V_{OC} can be calculated by rearranging Equation 1.3:

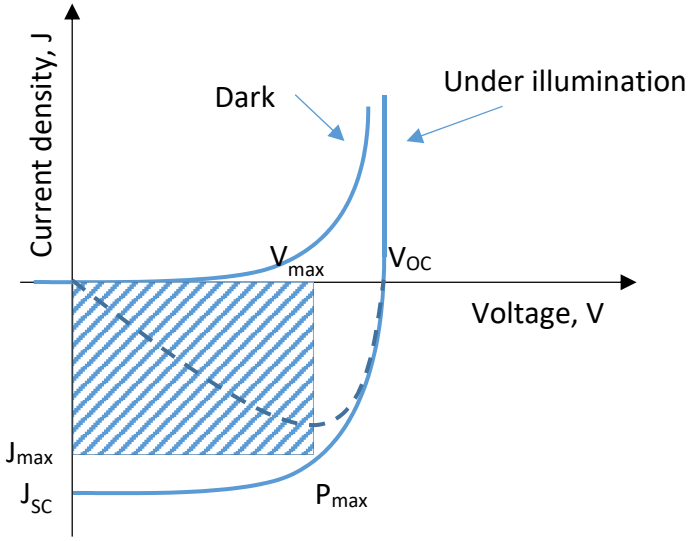

Figure 1.5 Current-voltage (J-V) characteristics of an ideal photodiode in the dark and under illumination. The dashed line represents the power density. The area of the shaded rectangle is the product of V_{max} and J_{max}, which corresponds to the maximum power density, P_{max}.

Equation 1.4

$$V_{OC} = \frac{kT}{q} \ln\left(\frac{J_{SC}}{J_0} + 1\right)$$

Since J_0 is proportional to the electron-hole recombination rate, V_{OC} is also a measure of the recombination of the cell.

The power density of the cell is given by the product of J and V, and reaches a maximum, P_{max}, when the cell is operating as illustrated in Figure 1.5. The fill factor (FF) describes the 'squareness' of the J-V curve:

Equation 1.5

$$\mathrm{FF} = \frac{J_{max} V_{max}}{J_{SC} V_{OC}}$$

and at maximum power density, P_{max}:

Equation 1.6

$$P_{max} = J_{SC} V_{OC} FF$$

The efficiency of a solar cell, η, is defined as the product of the open-circuit voltage, short-circuit current density, and fill factor, divided by the incident power (P_i) of solar radiation, which can also be simplified to the ratio between the maximum output power of the cell and P_i (Equation 1.7). Note that the standard test condition for solar cell is the AM1.5 spectrum, an incident power density of 1000 W m^{-2}, and a temperature of 25 °C.

Equation 1.7

$$\eta = \frac{V_{OC} J_{SC} FF}{P_i} = \frac{P_{max}}{P_i}$$

These four quantities, η, J_{SC}, V_{OC}, and FF, are the key performance benchmarks of a solar cell.

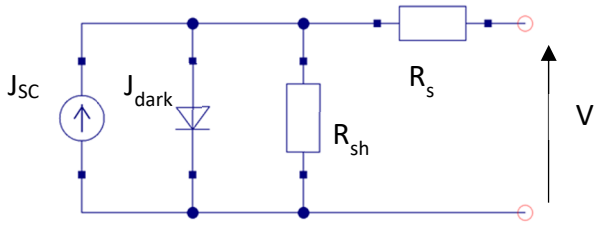

Figure 1.6 Equivalent circuit of a solar cell.

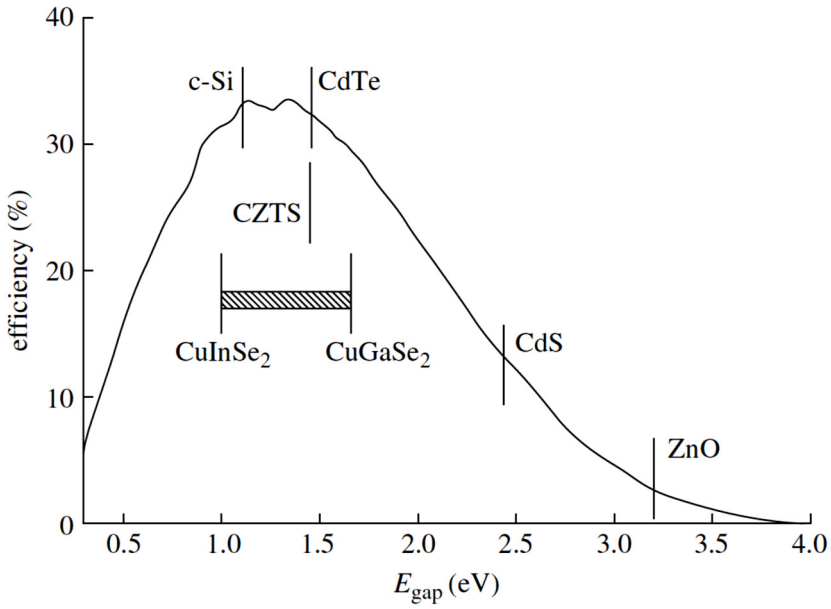

Figure 1.7 Maximum theoretical efficiency (Shockley–Queisser limit) for single junction solar cells under AM1.5 illumination without concentration. Reproduced from Peter *et al.*[10]

Figure 1.6 shows the equivalent electrical circuit of a solar cell. As mentioned earlier, most solar cells behave like a diode in the dark, producing a current (*i.e.* J_{dark}) in the opposite direction of the photocurrent (*i.e.* J_{SC}). In a real solar cell, there are two parasitic resistances to account for internal losses. The series resistance (R_s) arises from the resistance within the cell material, between the contact and the semiconductor, and resistive contacts. The parallel resistance, commonly known as the shunt resistance (R_{sh}), arises from leakage of current between the top and bottom of the cell, and around the edges of the device. For an efficient cell, we want the series resistance as small as possible and the shunt resistance as large as possible.

Equation 1.3 can be rewritten to include both series resistance and shunt resistance:

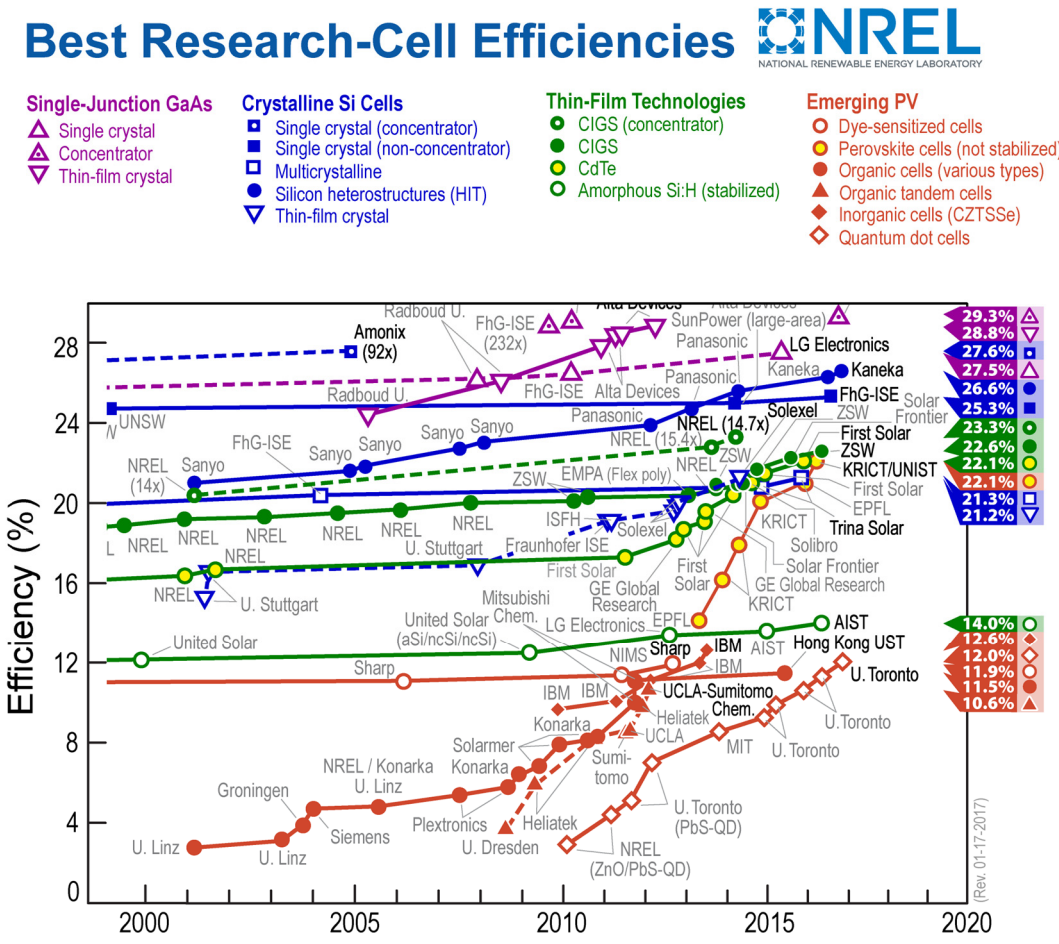

Figure 1.8 Best research single junction solar cell efficiencies as of 17th January 2017. The plot is adapted from and courtesy of the National Renewable Energy Laboratory (NREL), Golden, CO.

Equation 1.8

$$J = J_{SC} - J_0\left(e^{q(V+JAR_s)/kT} - 1\right) - \frac{V + JAR_s}{R_{sh}}$$

The theoretical maximum efficiency of a single junction solar cell was calculated by William Shockley and Hans-Joachim Queisser in the early 1960s. This is widely known as the Shockley–Queisser limit, or SQ limit for short. Example of losses include blackbody radiation, recombination, and spectrum losses etc.[11] The SQ limit for a selection of single junction solar cells are plotted in Figure 1.7.

Figure 1.8 shows the best research solar cell efficiencies for a number of different photovoltaic technologies. It can be seen that crystalline silicon (c-Si) solar cells already achieving efficiencies that are around 80% of the Shockley–Queisser limit, while some of the thin film technologies (Cu(In,Ga)Se_2 (CIGS) and cadmium telluride (CdTe), and an emerging PV (perovskite) are achieving 70% of the limit. However, the cell efficiencies of the different techonogies don't reflect the global market share.

The global market share of photovoltaic technology in terms of annual production is shown in Figure 1.9 and Figure 1.10. Crystalline silicon panels obtain more than 80% of market share since the late 1990s. There was a drop in c-Si market share between

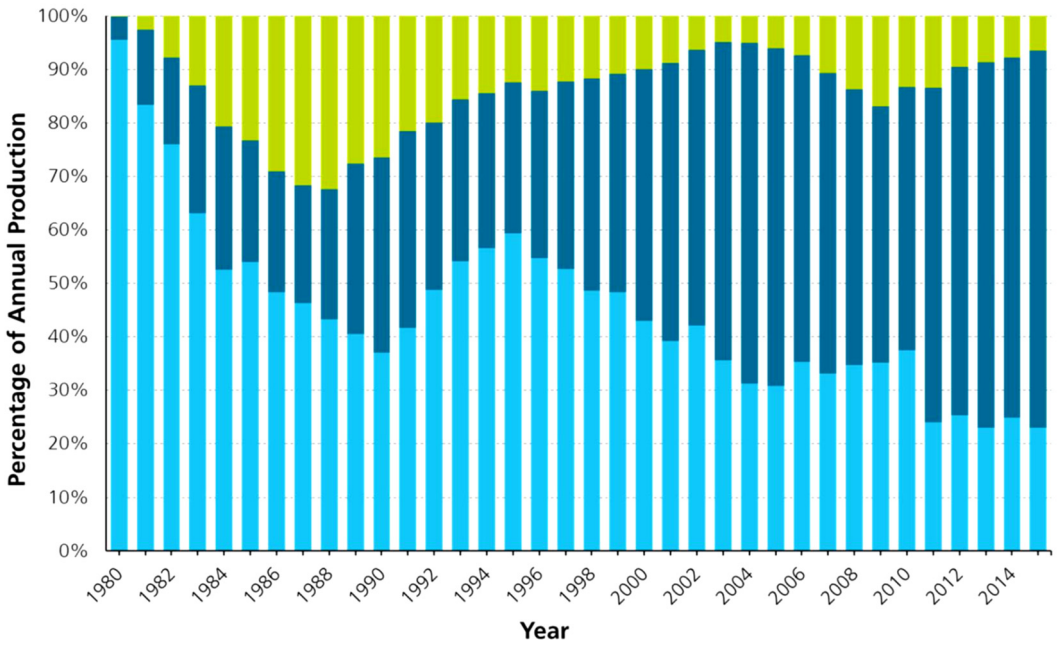

Figure 1.9 Global market share in terms of annual production by PV technology since 1980. Legend: lime = thin film; navy blue = polycrystalline silicon; cyan = monocrystalline silicon. Reproduced from Fraunhofer Institute for Solar Energy System.[12]

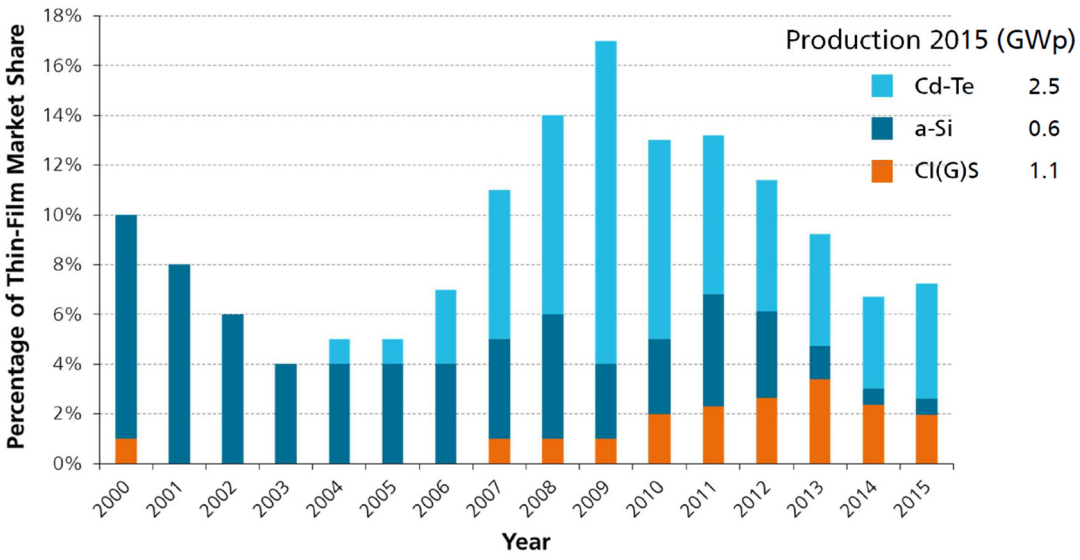

Figure 1.10 Market share for thin film PV technologies. Reproduced from Fraunhofer Institute for Solar Energy System.[12]

2003 and 2009 due to a shortage of high purity Si, and second generation solar cells, also known as thin film solar cells, experienced strong market gains. However, the falling of silicon price due to a rapid increase in polysilicon production capacity, and the slower than expected expansion and efficiency improvements in the thin film sector led to a significant number of start-up companies disappeared.[13] The market share trend in the past few years suggests crystalline silicon PV technology will still be the dominant player in the near future.

1.2 Crystalline silicon solar cells

The substantial availability of Si in the Earth's crust is one of the reasons why Si-based solar cell is, and is likely to continue to dominate the industry for large scale use in the near future. But Si is not perfect and suffers from two fundamental constraints: 1) Si has an indirect bandgap and requires a thickness of a few hundred microns to fully absorb sunlight; and 2) solar cell grade Si requires extremely pure Si feedstock (> 99.999%). The purification process is very energy intensive because the silica is required to be heated to temperatures in excess of 1500 °C. On top of obtaining high purity feedstock, the production of the wafers also require lots of energy, such as the Czochralski process used to produce monocrystalline silicon wafer, and the Siemens process used to produce polycrystalline silicon wafers.

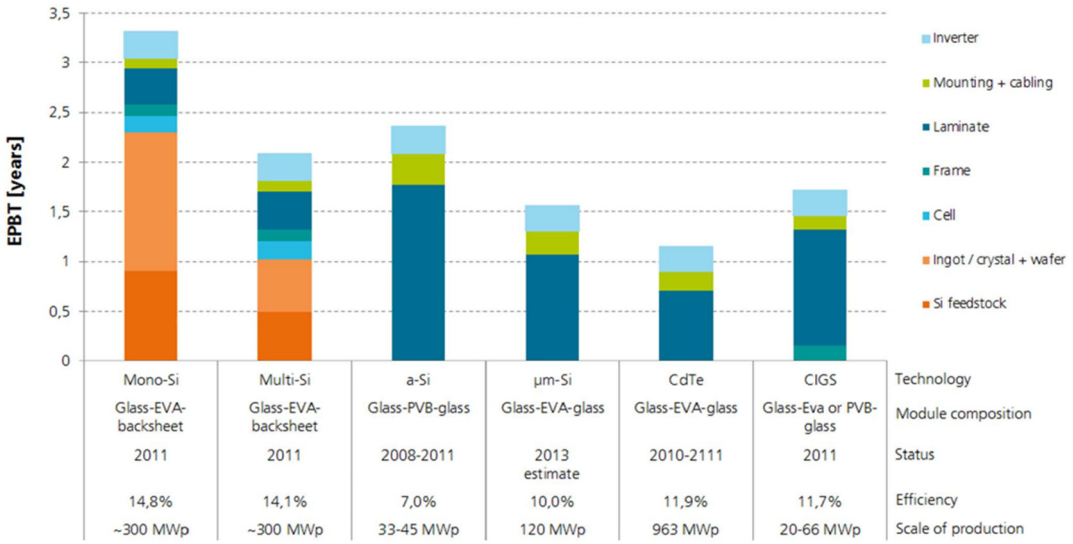

Figure 1.11 A detail breakdown of energy payback time of varies first and second generation solar panels operating in a region with 1000 kWh/m^2/year of solar irradiation. Reproduced from Fraunhofer Institute for Solar Energy System.[12]

A detailed breakdown of energy payback time comparing varies first and second generation solar panels is shown in Figure 1.11. Assuming the solar panels are operating in a region where the annual solar irradiation is 1000 kWh/m^2, the energy payback time for both monocrystalline and polycrystalline silicon are over two years, of which more than half of the time derive from the cost of the very pure Si feedstock and the fabrication of the wafer. CIGS solar panels have an energy payback time of around 1.7 years, while CdTe panels have the shortest energy payback time (1.2 years). The energy payback time can be longer or shorter when operating at regions where the solar irradiation is different.

1.3 Non-silicon thin film solar cells

The majority of market share in thin film PV goes to CdTe-based solar panels. CdTe is attractive because it has a direct bandgap of 1.45 eV, which lays within the optimum range for PV solar cells as defined by the SQ limit as shown in Figure 1.7. Having a direct bandgap also means an absorber layer of only few microns thick can effectively absorb sunlight, as opposed to the few hundred microns in c-Si solar cells. CdTe can also be deposited using a variety of deposition methods which all result in reasonable performance.[13] The most common CdTe cell consists of the n-CdS/p-

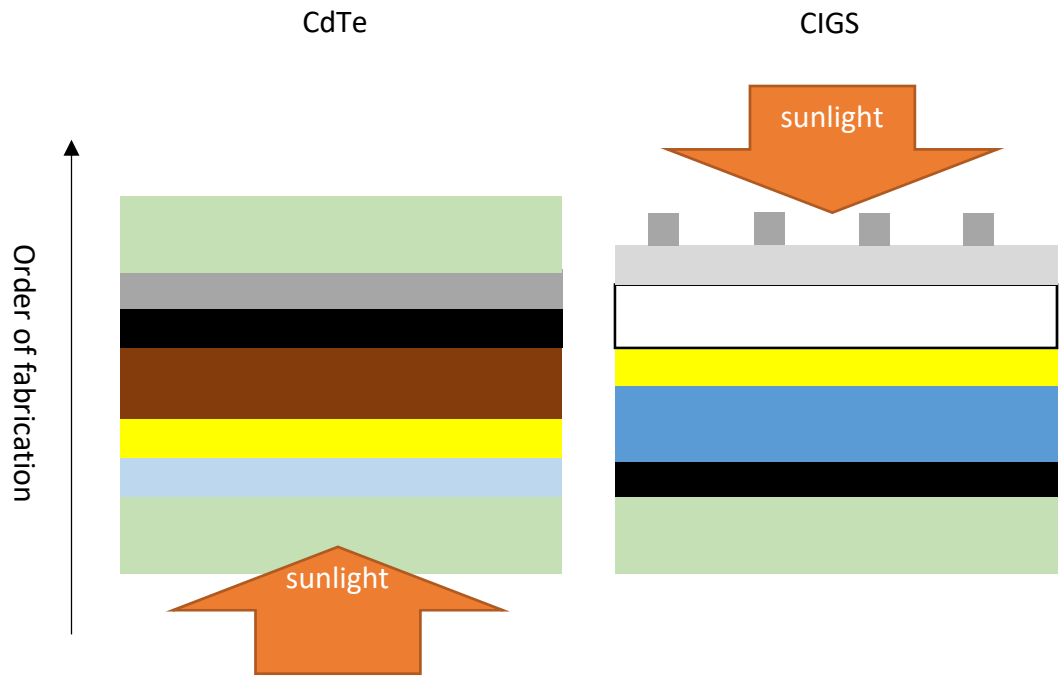

Figure 1.12 Cross-sectional diagram of the structure of a typical CdS cell (left); CIGS cell (right). CdS cell from top to bottom: Glass, metallisation, ohmic contact, CdTe, CdS, FTO, glass. CIGS cell from top to bottom: Top contacts, Al:ZnO, i-ZnO, CdS, CIGS, Mo, glass.

CdTe hetro-junction in the substrate configuration, in which the active materials are deposited on a substrate that also acts as the transparent window to allow solar radiation to reach the device junction. The substrate is a glass sheet coated with a thin layer of transparent conductive oxide (TCO), of which fluorine-doped tin oxide (FTO) is usually used. The fabrication consists of sequential deposition of a thin layer of CdS (around 100 nm), a layer of CdTe (around 2 µm), followed by a conducting back contact. A cross-section of the cell structure is illustrated in Figure 1.12.

Cu(In,Ga)Se_2 (CIGS) is another promising thin film solar cell with efficiency of just above 22% in the laboratory.[14] CIGS adapts the chalcopyrite structure, which is closely related to the ZnS zinc blende structure. The bandgap of CIGS can be tuned by varying the In to Ga ratio, from 1.01 eV for $CuInSe_2$, to 1.68 eV for $CuGaSe_2$. Unlike CdTe cells, most CIGS cells are fabricated in the superstrate configuration, of which the light enters from the 'top' of the cell with regards to the order of cell fabrication. The substrate is a layer or layers of molybdenum (500 nm) sputtered onto a soda lime glass (SLG). The fabrication then consists of sequential deposition of the CIGS absorber (1.5 – 2 µm), a thin layer of CdS (50 nm), followed by a TCO, such as zinc

oxide. The top zinc oxide layer is doped with aluminium to make it highly conductive so that it can collect and transfer the current to the metallic contact grid. A cross-section of the cell structure is illustrated in Figure 1.12.

However, there are concerns over the toxicity of Cd and the scarcity and cost of Te in CdTe cells, and concerns over the scarcity and cost of In and Ga in CIGS cells. There is a need for a thin film solar cell made with earth abundant and benign materials to make production in TW-scale more sustainable.

Kesterite-based solar cells, also known as copper zinc tin sulfoselenide ($Cu_2ZnSn(S,Se)_4$ / CZTSSe), have emerged as a promising candidate for solar absorber materials. CZTSSe has a tuneable direct bandgap of 1.0 – 1.5 eV and a high absorption coefficient in the order of 10^4 cm^{-1}.[15] Furthermore, all the elements in the selenium-free cells, *i.e.* copper zinc tin sulphide (Cu_2ZnSnS_4 / CZTS), are non-toxic, earth abundant and low cost.

1.4 CZTS: history and device efficiency

New semiconductor compounds can be derived from existing semiconductors by isoelectronic substitution as shown by the arrows in Figure 1.13. Isoelectronic substitution can be used to replace toxic and rare elements in semiconductors, as demonstrated in the derivation of CZTS from CIGS and CdTe, while the average number of valence electrons is unaltered.

The photovoltaic effect of CZTS was first reported in 1988, with a V_{oc} of 165 mV achieved with a cadmium tin oxide TCO junction.[15] Katagiri *et al.* spent more than 10 years on improving the efficiency of CZTS device, from 0.66% in 1996,[16] to 6.7% in 2008.[17] These devices adopted the superstrate configuration very similar to that in CIGS cells, with Al/Al:ZnO/CdS/CZTS/Mo/SLG. CZTS did not gain a lot of further interest until Todorov *et al.*[18] from IBM achieved an efficiency of 9.6% on CZTSSe using a solution process in 2010. Todorov *et al.* collaborated with Wang *et al.* and improved the efficiency of CZTSSe cell to 12.6% in 2014[19] and it is still the current record efficiency for kesterite-based solar cells.

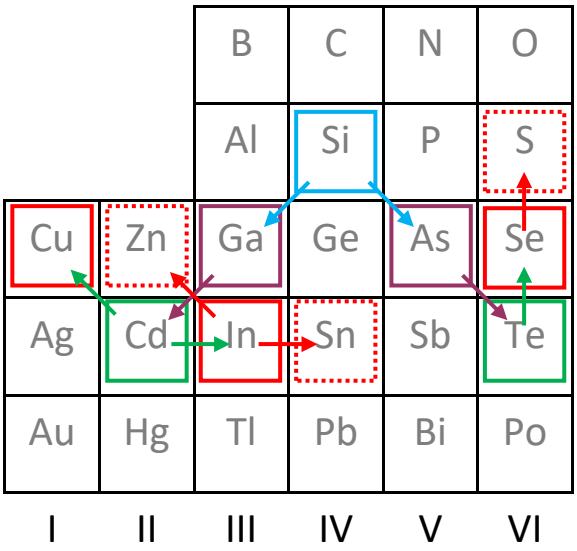

Figure 1.13 A portion of the periodic table showing the derivation of semiconducting materials by isoelectronic substitution, i.e. Si > GaAs > CdTe > CIGS > CZTS. The Roman numbers indicate the group number on the old periodic table. Adapted from Peter *et al.*[10]

1.4.1 Crystal structure

The CZTS(e) structure is derived from the chalcopyrite structure of CIGS by replacing In and Ga atoms with Zn and Sn. Based on symmetry arguments, this replacement produces two similar structures of lower symmetry, known as kesterite and stannite.[20] All these structures are based on the cubic ZnS (zinc blende) structure by doubling the unit cell along the c axis and replacing Zn with the corresponding cations. The chalcopyrite, kesterite and stannite structures are illustrated in Figure 1.14 and Table 1.1. Density functional theory (DFT) calculations predict kesterite as the most stable phase for both CZTS and CZTSe, although stannite only has a slightly higher energy difference of 1.3 – 3.4 meV per atom.[21] Since Cu^{+} and Zn^{2+} are isoelectronic, their atomic scattering form factors are very similar and it is not possible to distinguish between the kesterite and stannite structures using single wavelength X-ray diffraction (XRD) methods. On the other hand, neutrons interact with the nuclei and can resolve the position and distribution of Cu and Zn atoms. A comprehensive neutron diffraction study of various CZTS(e) compounds in bulk powder form shows that both CZTS and CZTSe occur in kesterite form, with nearly 30% of Cu_{Zn} and Zn_{Cu} antisite defects in the 2c and 2d Wyckoff positions on samples controlled with a slow cooling rate of 1 K/h. The antisite defects increase to roughly 50% on quenched

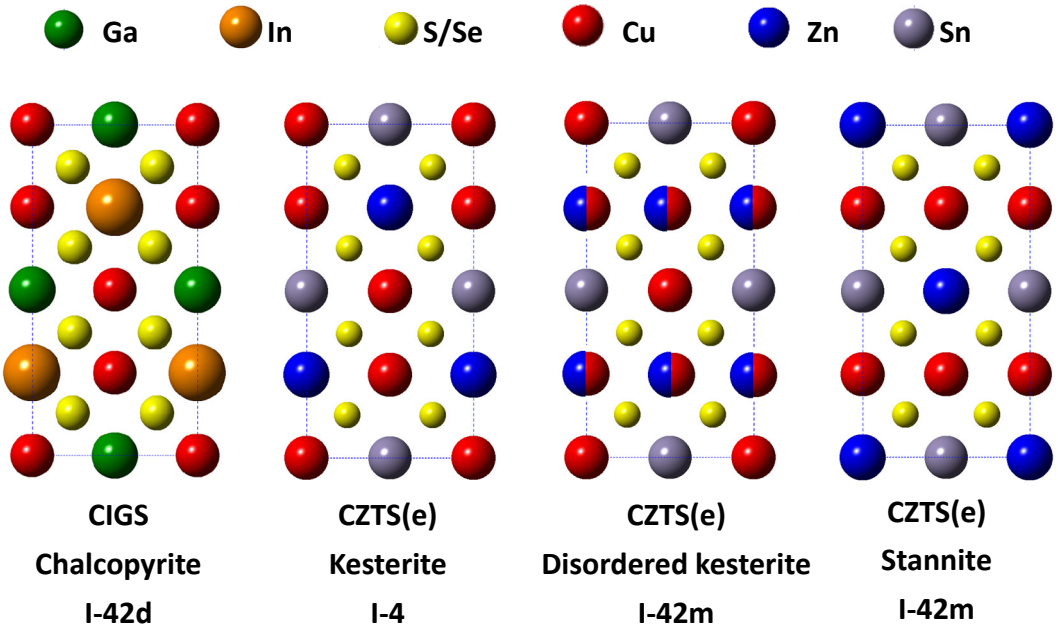

Figure 1.14 Crystal structures of chalcopyrite, kesterite, partially disordered kesterite and stannite with their space group.

samples.[22] This antisite defect is commonly known as the Cu/Zn disorder in the community. Cu/Zn disorder may be explained by a co-existence of kesterite and stannite, but a co-existence of both structures could lead to a high V_{oc} deficit as observed in Mitzi *et al.*'s[23] device, because stannite has a smaller predicated bandgap than kesterite.

Table 1.1 Wyckoff positions and atom coordinates in chalcopyrite, kesterite, partially disordered kesterite and stannite

Wyckoff positions in chalcopyrite	**Coordinates in I-42d**	**Wyckoff positions in kesterite**	**Coordinates in I-4**	**Wyckoff positions in disordered kesterite**	**Wyckoff positions in Stannite**	**Coordinates in I-42m**
4a (Cu)	0, 0, 0	**2a (Cu)**	0, 0, 0	**2a (Cu)**	**2a (Zn)**	0, 0, 0
	0.5, 0, 0.75	**2b (Sn)**	0, 0, 0.5	**2b (Sn)**	**2b (Sn)**	0, 0, 0.5
4b (In, Ga)	0, 0, 0.5	**2c (Cu)**	0, 0.5, 0.25	**4d (Cu, Zn)**	**4d (Cu)**	0, 0.5, 0.25
	0.5, 0, 0.25	**2d (Zn)**	0, 0.5, 0.75			0, 0.5, 0.75
8d (S, Se)	x, 0.25, 0.125	**8g (S, Se)**	x, y, z	**8i (S, Se)**	**8i (S, Se)**	x, x, z

1.4.2 Cu/Zn disorder

The ordering state of a material can be quantified based on an order parameter S that depends only on the defect concentration, and ranges from 0 for a fully disordered material, to 1 for perfectly ordered material. Note that S = 1, in theory, is only accessible at zero absolute temperature, T = 0 K. In the case for CZTS(e), the degree of disorder can be expressed as:

Equation 1.9

$$S = \frac{P(Cu_{2c}) - a_{2c}}{1 - a_{2c}} = 2P(Cu_{2c}) - 1 = 2P(Zn_{2d}) - 1$$

$P(Cu_{2c})$ and $P(Zn_{2d})$ are the probabilities that Cu and Zn atoms occupy the 2c and 2d sites in the kesterite structure respectively, which decrease from 1 for perfectly ordered to 0.5 in completely disordered material. a_{2c} is the fraction of 2c sites in the z = ¼ and ¾ lattice planes as discussed by Scragg *et al.*[24], and is equal to 0.5.

It has been demonstrated experimentally that the degree of disorder is related to the cooling rate of CZTS(e) after annealing using powder neutron diffraction,[22] solid state NMR[25] and near-resonant Raman scattering[26] qualitatively, with less disorder observed in a slow cooling sample. Total disorder (S = 0) occurs above the 'critical temperature' of the order-disorder transition. Scragg *et al.*[26] and Rey *et al.*[27] later also experimentally confirmed the critical temperature for CZTS and CZTSe are 260 °C and 200 °C respectively. The transition was shown to be a thermodynamic order-disorder transition, and is reversible. Since the annealing temperature for CZTS(e) films are in the range of 500 °C, which is much higher than the critical temperature, this suggests all CZTS(e) films are at least partially disordered, depending on the cooling rate and any post-annealing of the sample.

1.4.2.1 Resonance Raman spectroscopy

Scragg *et al.*[26] initially carried out resonance Raman spectroscopy on stoichiometric CZTS powder samples which were slowly cooled (ordered) and rapidly cooled (disordered), and highlighted the difference in the peak intensity for a number of peaks. Scragg *et al.* then introduced two empirical parameters, Q and Q', defined in terms of the intensity ratios of the main resonance Raman peaks as follows:

Equation 1.10

$$Q = {I_{287}}/{I_{303}} \qquad Q' = {I_{338}}/{(I_{366} + I_{374})}$$

In the same literature, Scragg *et al.* also carried out a temperature study on Cu-poor Zn-rich CZTS thin films annealed between 373 and 623 K, and showed that i) the critical temperature of CZTS is 533 ± 10 K; and ii) the order / disorder in CZTS is reversible by repeated annealing above and below the critical temperature.

Scragg *et al.*[24, 28] later related the order parameter S (Equation 1.9) with the resonance Raman spectrum parameter Q using the Vineyards model.[29] This model gives rate constants k_O and k_D for the ordering and disordering processes as:

Equation 1.11

$$k_O = 4f \exp\left(\frac{-U}{k_b T}\right) \exp\left(\frac{3\nu S}{k_b T}\right) \qquad k_D = 4f \exp\left(\frac{-U}{k_b T}\right) \exp\left(\frac{-3\nu S}{k_b T}\right)$$

where

Equation 1.12

$$\frac{dS}{dt} = \frac{1}{2}[k_O(1-S)^2 - k_D(1+S)^2]$$

f is the frequency of the vibrational mode by which neighbouring atoms are exchanged, U is the activation energy for the exchange process and ν relates to the interaction energies of the three possible nearest neighbour pairs, *i.e.* Cu-Cu, Zn-Zn and Cu-Zn.[27]

Scragg *et al.* concluded that i) the correlation between S and Q is linear; ii) the S(Q) relationship (*i.e.* the slope) varies with the composition and type of the CZTS; and iii) it is impractical to obtain B-type CZTS with S higher than 0.7 due to the duration of heat treatment required (*i.e.* > 5 days).

1.4.2.2 Neutron diffraction

Schorr *et al.*[22] initially used powder neutron diffraction technique to confirm CZTS(e) compounds adopts the kesterite structure, with Cu_{Zn} and Zn_{Cu} antisite defects at 2c and 2d Wyckoff positions. The concentration of those antisite defects depend on the

cooling rate during sample synthesis. In the quenched CZTS sample, roughly 50% of the copper 2c site is occupied by zinc and vice versa in the zinc 2d site. In the slow cooling sample (1 K/h), only 30% of the copper 2c site is occupied by zinc, and also vice versa in the zinc 2d site.

Schorr *et al.* later collaborated with Ritscher *et al.* synthesising stoichiometric,[30] B- and C-type CZTS[31] using mechanochemical route, and characterising the products using powder neutron diffraction. All samples were found to contain 30 – 35% of Cu_{Zn}-Zn_{Cu} antisite defect pairs on the 2c and 2d sites.

Ritscher *et al.*[32] later performed an investigation on annealing temperature in the range of 473 – 623 K with stoichiometric CZTS samples with powder neutron diffraction. They observed there is a decrease in intensity for the reflection at 2θ = 18.3° (λ = 154.818 pm) in the highest temperature sample when compared with the lowest temperature sample. However, the decrease in intensity is not steady with increasing disorder. They also claimed that a fully ordered (within standard deviation) sample can be prepared with an annealing time of three weeks at 473 K. The critical temperature is 552 ± 2 K, which is 10 K (including standard error) higher than Scragg *et al.*[26]. Ritscher *et al.* attributed that difference to the duration of sample annealing time and the composition of the samples, *i.e.* Zn-rich in Scragg *et al.*'s work.

Bosson *et al.*[33] carried out variable temperature powder neutron diffraction on Sn-poor, Cu-rich and Sn-poor, Zn-rich CZTS samples in the range of 4 – 1275 K. Their Sn-poor, Zn-rich sample showed significant disorder at the 2a site at 300 K, with Cu_{2a} = 0.67(8). This is the first report for disorder at the 2a site below the critical temperature. The critical temperature is 501 K and 489 K for Sn-poor, Cu-rich and Sn-poor, Zn-rich CZTS respectively. Bosson *et al.* attributed the lower critical temperature observed was due to the equilibration and measurement time at each temperature (15 minutes and 90 minutes respectively) not being sufficient for the samples to reach equilibrium state.

1.4.2.3 Anomalous X-ray diffraction

Lafond *et al.*[34] carried out anomalous diffraction on single crystal CZTS samples near the Cu K-edge (1.3825 Å), Zn K-edge (1.2844 Å), and far from the edges (0.66842 Å).

The data were combined and refined using fully ordered and fully disordered kesterite model, with *R*/*wR*(all) = 0.068/0.172 for the ordered kesterite model and *R*/*wR*(all) = 0.048/0.112 for the disordered kesterite model. Lafond *et al.* concluded that the resonant effect at Cu and Zn absorption edges is large enough to enhance the contrast between Cu and Zn, and allow the community to gain direct evidence of Cu/Zn disorder in CZTS(e) structures.

Többens *et al.*[35] performed an investigation on annealing temperature in the range of 100 – 250 °C with B-type CZTSe samples using anomalous diffraction far from the absorption edges (8048 eV), four each below the absorption edges of Cu and Zn (8919, 8955, 8969, 8974 eV and 9599, 9635, 9649, 9654 eV), and one in between (9376 eV). The fit residuals are all similar and Többens *et al.* only listed the ones for the 100 °C sample measured at the two extreme wavelengths (Table 1.2). There is a clear trend on the occupancy of Cu and Zn in the 2c and 2d sites, with more disorder at higher temperatures. The critical temperature was observed at 203(6) °C, which agrees well with Rey *et al.*[27]. Többens *et al.* also observed that Cu/Zn disorder also occurred at the 2a site above the critical temperature (Table 1.3).

Table 1.2 Refinement results of the 100 °C CZTSe sample collected at 8048 and 9654 eV using anomalous X-ray diffraction.[35]

	8048 eV	**9654 eV**
R_{exp}	2.8%	1.3%
R_{wp}	7.6%	2.1%
Bragg *R*-factor	2.2%	3.5%

Table 1.3 Site occupancy factors normalised to chemical composition determined by wavelength dispersive X-ray spectroscopy (WDX).[35]

	100 °C	**125 °C**	**150 °C**	**175 °C**	**200 °C**	**225 °C**	**250 °C**
Cu 2a	0.991(18)	0.991(19)	0.969(14)	0.991(15)	0.929(11)	0.927(11)	0.913(14)
Zn 2a	0.000(17)	0.000(18)	0.022(14)	0.000(14)	0.062(10)	0.064(11)	0.078(12)
Cu 2c	0.771(28)	0.739(24)	0.639(16)	0.665(29)	0.511(15)	0.506(18)	0.505(11)
Zn 2c	0.188(26)	0.219(22)	0.341(15)	0.293(27)	0.509(13)	0.516(16)	0.531(10)
Cu 2d	0.229(35)	0.261(37)	0.361(18)	0.335(24)	0.489(19)	0.494(29)	0.495(36)
Zn 2d	0.812(34)	0.781(36)	0.659(17)	0.707(23)	0.491(18)	0.484(27)	0.469(32)

Besides neutron diffraction experiments, Bosson *et al.*[36] also carried out anomalous X-ray powder diffraction on CZTS samples near the Cu absorption edge (8.98 keV), Zn absorption edge (9.66 keV) and far from the edges (15 keV) at 300 and 600 K. All data were modelled simultaneously. No R-factors were given anywhere in the article, but the authors attached a diffraction pattern of one of the samples taken at 300 K using 15 keV X-ray and showed some residual between the experimental data and the model. The highlight of this article is that Bosson *et al.* observed polymorphic splitting in three out of five samples measured at 300 K. They attributed this splitting to a second CZTS phase with slightly different lattice parameters (> 0.004 Å) and different compositions. Above the critical temperature, at 600 K, the two CZTS phases converge to a single phase in two of the three samples. The site occupancy factors were presented in pie charts without giving any standard errors so it is difficult to include their result for comparison.

1.4.3 Defects

CZTS(e) is comprised of four (or five in the case of CZTSSe) elements and is highly prone to point defects of all kinds, including vacancies (V_{Cu}, V_{Zn}, V_{Sn}, and $V_{s(e)}$), antisite defects (Cu_{Zn}, Zn_{Cu}, Cu_{Sn}, Sn_{Cu}, Zn_{Sn}, and Sn_{Zn}), and interstitial defects (Cu_i, Zn_i and Sn_i). Their formation is driven thermodynamically by minimising the Gibbs free energy of the crystal. It was also found that the formation energy of acceptor defects was lower than that of donor defects. The commonly observed p-type conductivity of CZTS(e) comes mainly from the Cu_{Zn} antisite defects.[6] A selection of the most prevalent defects and defect complexes in CZTS(e) with their electronic levels within the bandgap are shown in Figure 1.15. Many of the mid-gap defects may cause nonradioactive recombination which significantly decreases the open circuit voltage[37]. DFT calculations also predict that many defects in CZTS(e) are self-passivated, forming defect complexes. (Cu_{Zn} + Zn_{Cu}) is likely the dominant defect complex for a variety of compositions, while (Cu_{Zn} + Sn_{Zn}) and ($2Cu_{Zn}$ + Sn_{Zn}) are prevalent in films with compositions close to stoichiometry.[38] While the (Cu_{Zn} + Zn_{Cu}) complex can be viewed as the partial disorder as shown in Figure 1.14, both (Cu_{Zn} + Sn_{Zn}) and ($2Cu_{Zn}$ + Sn_{Zn}) complexes cause the effective bandgap to decrease when present in large numbers, as shown in Figure 1.15.[39, 40] Fortunately, the detrimental

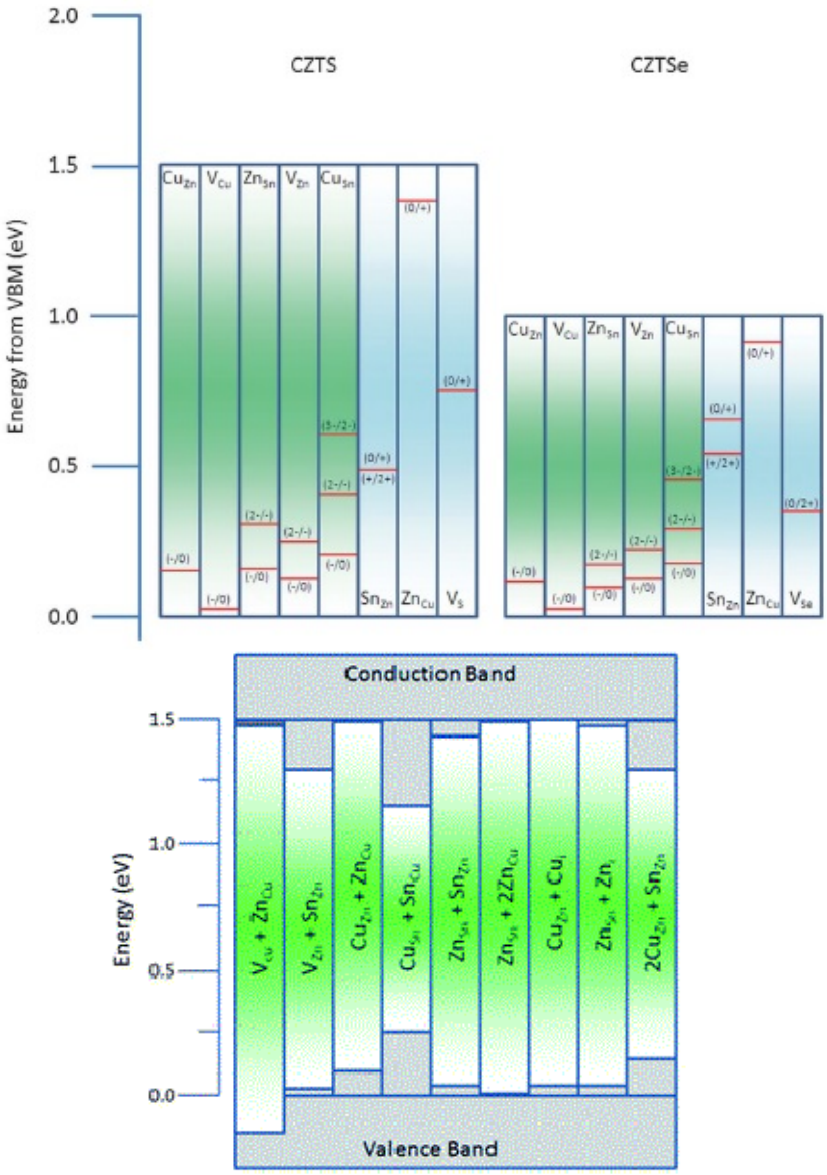

Figure 1.15 Energy levels of some prevalent defects and defect complexes in CZTS(e) from DFT calculations. Reproduced from Polizzotti *et al.*[37]

($2Cu_{Zn} + Sn_{Zn}$) defect complex is significantly reduced under Zn-rich and Cu- and Sn-poor condition.[41] The Zn-rich Cu-poor condition also promotes the formation ($V_{Cu} + Zn_{Cu}$) complex which should be beneficial for maximising solar cell performance.[42] These may be the reasons why the best performing CZTS(e) devices usually have a Zn-rich Cu-poor composition.

Choubrac *et al.* classified CZTS(e) into six different types according to the composition and defects.[43-45]

Table 1.4 The expected defect complexes related to the different types of CZTS(e).

	Equation	Type of defects	Composition region
Type A	$Cu_{2-2x}Zn_{1+x}SnS_4$	2 Cu → V_{Cu} + Zn_{Cu}	Cu-poor, Zn-rich
Type B	$Cu_{2-2x}Zn_{1+3x}Sn_{1-x}S_4$	2 Cu + Sn → 2 Zn_{Cu} + Zn_{Sn}	Cu and Sn-poor, Zn-rich
Type C	$Cu_{2+2x}Zn_{1-3x}Sn_{1+x}S_4$	3 Zn → 2 Cu_{Zn} + Sn_{Zn}	Cu and Sn-rich, Zn-poor
Type D	$Cu_{2+2x}Zn_{1-x}SnS_4$	Zn → Cu_{Zn} + Cu_i	Cu-rich, Zn-poor
Type E	$Cu_{2-2x}Zn_{1-x}Sn_{1+x}S_4$	2 Cu + Zn → 2 V_{Cu} + Sn_{Zn}	Cu and Zn-poor, Sn-rich
Type F	$Cu_{2+2x}Zn_{1+x}Sn_{1-x}S_4$	Sn → Cu_{Sn} + Zn_{Sn} + Cu_i	Cu and Zn-rich, Sn-poor

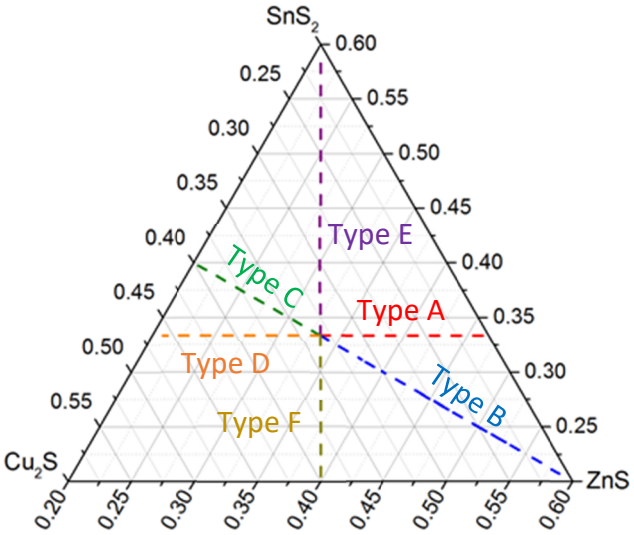

Figure 1.17 Pseudo-ternary phase diagram for CZTS showing the notation initially used by Choubrac *et al.* and later used in the community.

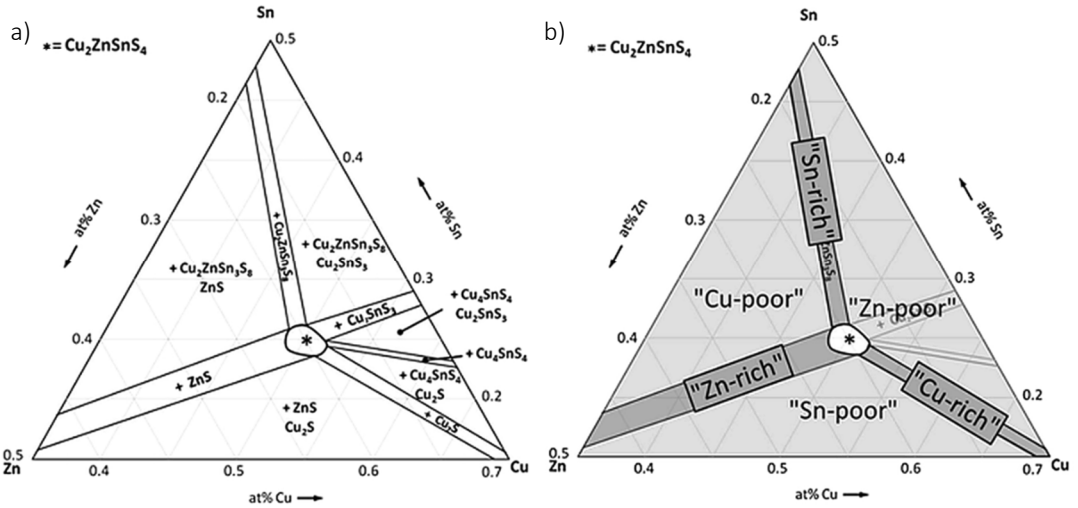

Figure 1.16 a) Ternary CZTS phase diagram including the expected secondary phases at 400 °C. b) Ternary CZTS phase diagram defining compositional labels commonly used in literature. Reproduced from Scragg *et al.*[20] See also Table 1.5.

1.4.4 Composition

Experimental phase diagrams have been published (Figure 1.16) and predict a small region of phase pure CZTS, allowing only 1 – 2% deviation in the composition at around 550 °C. In contrast, CIGS allow a Cu deficiency of 4%.[46] It remains a challenge to synthesise phase pure CZTS because secondary phases such as binary and ternary compounds are much easier to form. Secondary phases with bandgaps lower than CZTS can cause a reduction of the open circuit voltage of the devices due to complete shunting.[47] In fact, the presence of a material with a bandgap lower by only 100 meV will reduce the maximum achievable efficiency by 8%.[48] The bandgaps of the most likely formed secondary phases are shown in Table 1.5. There are three secondary phases with a lower bandgap in the CZTS system, namely Cu_2SnS_3 (0.93 – 1.35 eV),[49] Cu_2S (1.2 eV)[50] and SnS (1.3 eV).[51] In contrast, there is only one secondary phase (Cu_2SnSe_3, 0.76 eV)[52] with a lower bandgap in the CZTSe system, indicating secondary phases are less detrimental in selenide kesterite cells than in sulphide kesterite cells.

Table 1.5 Bandgaps and Raman peaks of the most likely secondary phases.

Compound	**Bandgap / eV**	**Melting point / °C**	**Raman peaks[53] / cm^{-1}**
Cu_2ZnSnS_4	1.4 – 1.5[15]	990[54]	289, 339, 350, 370
tetra-Cu_2SnS_3	1.35[55]	850[56]	297, 337, 352
cubic-Cu_2SnS_3	0.96[55]		267, 303, 356
CuS	~2.0[50]	500[57]	475
Cu_2S	1.2[50]	1130[58]	
SnS	1.3[51]	881[59]	160, 190, 219
SnS_2	2.12 – 2.44[60]	600[59]	314
ZnS	3.67[61]	1650[56]	275, 352

Table 1.6 The expected secondary phases as related to the compositional regions in the CZTS phase diagram (Figure 1.16).

Composition region	**Expected secondary phases**
"Cu-poor"	$Cu_2ZnSn_3S_8$ + ZnS
"Cu-rich"	Cu_2S
"Zn-poor"	Cu-Sn-S + $Cu_2ZnSn_3S_8$/Cu_2S
"Zn-rich"	ZnS
"Sn-poor"	Cu_2S, ZnS
"Sn-rich"	$Cu_2ZnSn_3S_8$

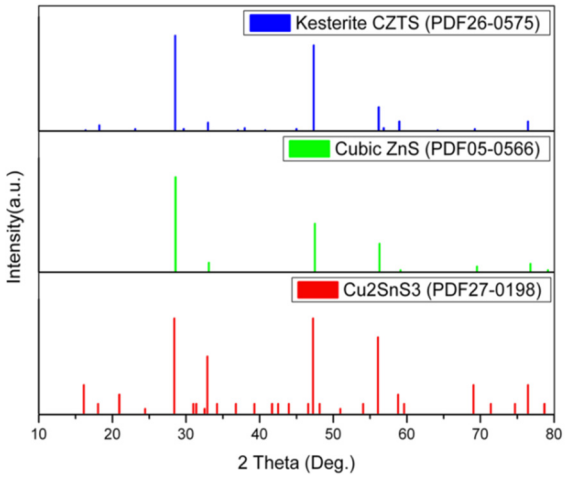

Figure 1.18 Overlapping of PXRD peaks in CZTS, ZnS and CTS. Reproduced from Jiang *et al.*[6]

On the other hand, secondary phases with higher bandgaps are much less detrimental; however they can block the transport when present in large amount, or at least increase the series resistance.[48] For instance, ZnS(e) has a wide bandgap and a relatively low conductivity, which is not expected to reduce the open circuit voltage or decrease the shunt resistance if present in small amount,[46] while $SnS(e)_2$ is unlikely to be present because it is volatile and will evaporate in most annealing conditions.[48] However, detection of these secondary phases using only powder X-ray diffraction (PXRD) in CZTS is not as easy as in CIGS because kesterite CZTS has very similar PXRD patterns to ZnS and Cu_2SnS_3 (Figure 1.18). Berg *et al.*[62] experimentally concluded that the detection limit of using standard laboratory PXRD is 10% for ZnS and 50% for Cu_2SnS_3 in a mixed sample containing CZTS. Raman spectroscopy is therefore often combined with PXRD results to characterise CZTS.[6]

Fernandes *et al.*[53] carried out a comprehensive Raman study on CZTS and a number of the most common secondary phases using an excitation wavelength of 488 nm (Table 1.5).

1.4.4.1 Raman spectroscopy

Raman scattering probes the optical phonon modes at the Γ-point (k = 0). The optical modes of a crystal structure at k = 0 can be enumerated using the crystal's symmetry and group theory analysis. Using Mulliken notation, the optical modes in kesterite are:

$$\Gamma = 3\mathrm{A} + 6\mathrm{B} + 6\mathrm{E}$$

and for stannite:

$$\Gamma = 2\mathrm{A}_1 + \mathrm{A}_2 + 2\mathrm{B}_1 + 4\mathrm{B}_2 + 6\mathrm{E}$$

For kesterite, all the optical modes are Raman active (15 vibrations), and all except A modes are also IR active (12 vibrations). For stannite, the A_1, B_1, B_2 and E modes are Raman active (14 vibrations), and only B_2 and E modes are IR active (10 vibrations). The A_2 mode in stannite is a silent mode.[63] Khare *et al.*[64] and Gurel *et al.*[65] have calculated the Raman spectra for kesterite and stannite using density functional theory (DFT) (Table 1.7).

Table 1.7 Calculated Γ-point phonon frequency for kesterite and stannite CZTS by Khare *et al.*[64] and Gurel *et al.*[65] respectively.

Kesterite			**Stannite**		
Symmetry	**Γ-point phonon freq./ cm^{-1}**		**Symmetry**	**Γ-point phonon freq./ cm^{-1}**	
A	340.04/335.2		**A_1**	334.08/332.7	
	284.30/309.0			277.12/309.1	
	272.72/302.1		**A_2**	263.11/304.3	
B (TO LO)	355.80/354.8	274.05/366.4	**B_1**	291.12/324.1	
	309.56/332.7	313.19/336.1		74.17/88.1	
	238.48/269.1	254.73/285.1	**B_2 (TO LO)**	360.12/358.5	370.63/364.2
	166.65/179.6	168.21/179.9		277.08/306.2	291.82/320.6
	98.82/104.2	98.83/104.3		149.69/171.0	150.91/171.1
	86.70/92.3	87.51/93.1		95.85/96.4	95.86/96.4

E (TO LO)	351.55/341.4	366.35/353.2	**E (TO LO)**	346.01/341.3	364.87/353.7
	281.07/309.7	293.44/314.1		264.34/305.3	275.52/311.9
	250.26/278.2	257.85/289.8		235.41/268.7	246.58/283.3
	150.53/166.1	151.05/166.2		161.68/170.9	162.63/171.0
	105.93/101.4	106.00/101.4		97.34/106.9	97.38/106.9
	83.64/79.2	83.65/79.2		78.39/74.9	78.73/75.5

1.4.4.2 Decomposition of CZTS(e)

It has been proposed that CZTS(e) decomposes in a two-step reaction using kinetic modelling:[66, 67]

Equation 1.13

$$Cu_2ZnSnS(e)_{4(s)} \rightleftharpoons Cu_2S(e)_{(s)} + ZnS(e)_{(s)} + SnS(e)_{(s)} + 0.5S(e)_{2(g)}$$

$$SnS(e)_{(s)} \rightleftharpoons SnS(e)_{(g)}$$

It follows that if the reaction is carried out under a flow of inert gas, vapour phase products, *i.e.* SnS(e) and S(e), will be removed and the equilibrium will be shifted to the decomposition direction. On the other hand, if SnS(e) and/or S(e) are deliberately introduced at a suitable concentration (partial pressure), the CZTS(e) reaction will be favoured; hence decomposition will be reversed, or prevented altogether.

Scragg *et al.*[67] studied the stability of CZTSe film under common annealing conditions (550 °C under vacuum) and compared the result with CIGS. While the CIGS film underwent some decomposition losing around 8% of its Se content, CZTSe film lost around 50% of its Se content, as well as all of its Sn content.

1.4.4.3 Etching

Chemical etching is sometimes performed to remove unwanted secondary phases in an attempt to improve cell efficiency, particularly in off-stoichiometric composition. The effect of different etchants on CZTS(e) thin films was studied by different groups.[68-71] It was summarised that potassium cyanide (KCN), which is often used in CIGS etching, does not dissolve and remove ZnS(e) species which is likely to be formed in the Zn-rich Cu-poor regime. Fairbrother *et al.*[68] suggested hydrochloric

acid (HCl) solution can be used to selectively remove Zn-rich secondary phases, while Mousel *et al.*[69] compared HCl with bromine in methanol (Br_2-MeOH), and concluded that Br_2-MeOH is more suitable to remove Cu and Sn related secondary phases. Finally Timmo *et al.*[70] and Volobujeva *et al.*[71] have used a combination of etchants (1% Br_2-MeOH + 10% KCN) to obtain the highest efficiency device.

Table 1.8 A comparison of solar cell performance for etched and unetched CZTS(e) devices.

	η / %	**V_{oc} / mV**	**J_{sc} / mA cm^{-2}**	**FF / %**	**Ref.**
Unetched	2.7	588	11.5	41.4	[68]
KCN etch	3.3	613	11.4	45.0	[68]
HCl etch	5.2	656	14.6	53.9	[68]
Unetched	4.4	319	28.5	49	[69]
HCl etch	5.0	337	29.8	50	[69]
Unetched	4.6	279	32.5	50	[69]
Br_2-MeOH etch	5.1	325	28.8	54	[69]

1.4.5 Mott-Schottky analysis

It has been reported that semiconductor properties such as the doping density (N_A), built-in potential (V_{bi}), and depletion widths for p- and n-regions (W_p and W_n respectively) in CZTS can be obtained using Mott-Schottky analysis:[72-79]

Equation 1.14

$$\frac{1}{C^2} = \frac{2}{q\varepsilon\varepsilon_0 A^2 N_A}(V_{bi} - V)$$

where C is the capacitance, q the electronic charge, ε the dielectric constant of the semiconductor, ε_0 the permittivity of free space, A the area of the interface, V the applied voltage, k_B the Boltzmann's constant, and T the absolute temperature. Since Equation 1.14 expresses a metal-semiconductor Schottky junction, and only applied to a p-n junction if one side is much more heavily doped than the other, a full expression for a p-n hetrojunction in CZTS/CdS is as follow:

Equation 1.15

$$\frac{1}{C^2} = \frac{2}{q\varepsilon_0\varepsilon_{CdS}\varepsilon_{CZTS}A^2}\frac{N_D\varepsilon_{CdS} + N_A\varepsilon_{CZTS}}{N_A N_D}(V_{bi} - V)$$

where ε_{CdS} and ε_{CZTS} are the relative dielectric constant for CdS and CZTS respectively, and N_D is the donor defect concentration in CdS. Once the doping densities have been calculated, W_p and W_n can then be obtained using the following equations:

Equation 1.16

$$W_p = \sqrt{\frac{2\varepsilon\varepsilon_0}{qN_A}(V_{bi} - V)}$$

Equation 1.17

$$W_{p\sim n} = \sqrt{\frac{2\varepsilon_0\varepsilon_{CdS}\varepsilon_{CZTS}}{q(N_D\varepsilon_{CdS} + N_A\varepsilon_{CZTS})}\frac{N_{D\sim A}}{N_{A\sim D}}(V_{bi} - V)}$$

where Equation 1.16 is the expression for a metal-semiconductor junction and Equation 1.17 for a p-n hetrojunction in CZTS/CdS. Figure 1.19 shows the positions of V_{bi}, W_p and W_n in a p-n junction. Table 1.9 summarises the N_A, V_{bi} and W_p values for CZTS obtained using Mott-Schottky analysis. Note that all authors in Table 1.9 used the equations for a metal-semiconductor junction (Equation 1.14 and Equation 1.16) except Fernandes *et al.*[78], where the p-n junction equations were used (Equation 1.15 and Equation 1.17).

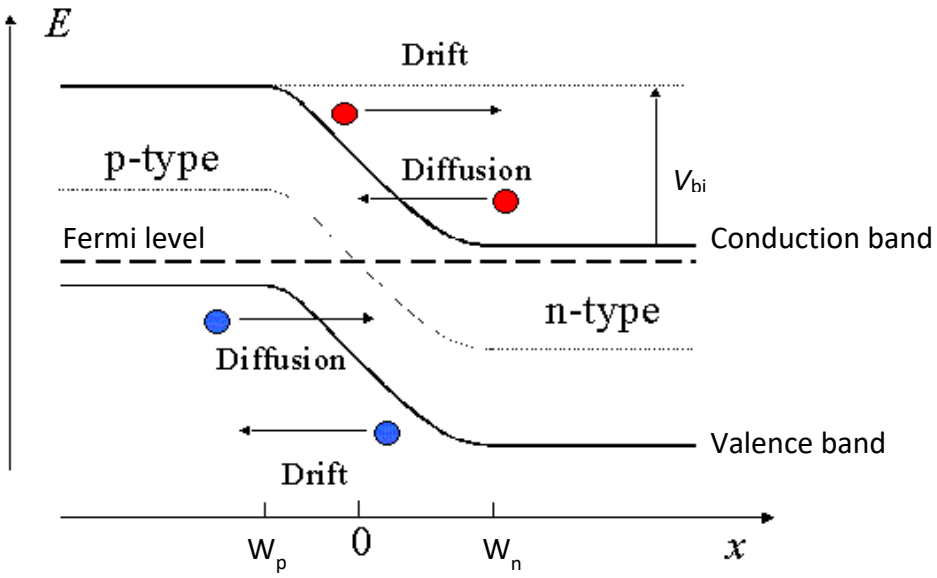

Figure 1.19 Energy band diagram of a p-n junction showing V_{bi}, W_p and W_n in thermal equilibrium. Reproduced from Van Zeghbroeck *et al.*[80]

Table 1.9 Reported values for doping density N_A, built-in potential V_{bi}, and the width of the depletion region W of CZTS obtained from Mott-Schottky analysis.

Sample	**N_A / cm^{-3}**	**V_{bi} / V**	**W_p / nm**	**Ref.**
CZTS film	$1.19 – 3.60 \times 10^{18}$	0.63 vs RHE	-	[75]
CZTS film	-	0.75 vs Ag/AgCl	-	[76]
CZTS film	10^{17}	0.71 vs Ag/AgCl	200	[77]
CZTS device	$0.65 – 20 \times 10^{16}$	0.51 – 0.71	30 – 230	[78]
CZTS device	5.16×10^{19}	-	7	[79]

1.4.6 Growing CZTS crystals

It is important to understand the fundamental properties of CZTS in order to achieve higher efficiencies, such as crystal and electronic structures, phonon frequencies and line widths of Raman active modes, and extension of compositional homogeneity range. Therefore single crystal growth is necessary.[81]

Table 1.10 summarises some of the CZTS crystal growth methods reported. While most of the reactions used elemental precursors, a few used binary precursors or polycrystalline CZTS. Excess sulphur was only introduced in two of the reports despite the fact that it may supress decomposition of CZTS as discussed earlier (Equation 1.13). There is also a huge variation in reaction temperature and duration. The details of these methods will be discussed in the following sections.

1.4.6.1 Solid state and melting growth method

The earliest reported solid state synthesis methods involve reacting stoichiometric amount of Cu, Zn, Sn and S in evacuated silica ampoule at 750 °C for around 2 weeks with quenching in the middle and at the end of the reaction.[82, 83] It is not explained why quenching is required but from the previous section it was suggested that fast cooling rates promote disorder in CZTS.

Table 1.10 A summary of some CZTS crystal growth methods. *The sample was quenched into ice water after 4 days. [+]The sample was quenched into water and grounded after 2 weeks. [^$] corresponds to the method used to obtain the polycrystalline CZTS precursor.

Method	Precursor	Temperature (°C)	Duration	Ref.
Solid state	Cu, Zn, Sn, S	750	*4 days + 12 days	[82]
Solid state	Cu, Zn, Sn, S	750	[+]14 days + 4 days	[83]
Solid state	Cu, Zn, Sn, upto 40% excess S	757	1 day	[84]
[$]Solid state	Cu, Zn, Sn, 50% excess S	700	2 day	[81]
Solid state	Nanocrystalline CuS, ZnS, SnS, excess S	300 – 450	1 hour	[85]
[^]Melting growth method	Cu, Zn, Sn, S	1100	1 day	[86]
Vertical gradient freeze	Cu, Zn, Sn, S	Hot zone: 1050 Cold zone: 980	3 days	[87]
Traveling heater method	[^]Polycrystalline CZTS, molten Sn	900	10 days	[86]
Chemical vapour transport	Cu_2S, ZnS, SnS_2, I_2	Hot zone: 850 Cold zone: 760	14 days	[88]
Chemical vapour transport	[$]Polycrystalline CZTS, I_2	Hot zone: 880 - 790 Cold zone: 820 – 740	1 – 7 days	[81]

Kheraj *et al.*[84] has studied the effect of excess sulphur in the precursor. Sulphur-poor compounds and formation of SnS and SnS_2 was observed when there was less than 20% excess sulphur in the starting material. Compounds with good atomic stoichiometry were obtained with 30 and 40% excess sulphur, with better crystallinity obtained on the 40% excess sample. Colombara *et al.*[81] has also employed excess sulphur (50%) in the preparation of polycrystalline CZTS to prevent any deviation from stoichiometry.

Wang *et al.*[85] has synthesised CZTS from nanocrystalline CuS, ZnS and SnS at a much lower temperature and shorter duration compared to other sold state methods. While the best crystallinity CZTS was obtained at 450 °C, traces of Cu_2S were found at 500 °C. They suggested the low temperature formation of CZTS was due to the

faster diffusion of atoms or ions from the larger interface area of the nano-sized precursors.

The melting growth method uses a reaction temperature higher than the melting point of CZTS. Polycrystalline CZTS, CZTSe and CZTSSe has been synthesised by Nagaoka *et al.* using this method in a vertical furnace.[86, 89, 90]

1.4.6.2 Vertical gradient freeze and traveling heater method

Das *et al.*[87] has outlined the drawbacks of the traveling heater method and chemical vapour transport and hence reported the vertical gradient freeze method. It is similar to the melting growth method apart from a temperature gradient and a much slower cooling rate was applied in vertical gradient freeze. Polycrystalline ingots with grain size of 0.2 – 0.8 mm were obtained using this method with no secondary phases present as confirmed by Raman measurements.

The traveling heater method involved the crystal growth of kesterite in a Sn-kesterite pseudobinary system. It was carried out in a Bridgman furnace using a polycrystalline sample obtained from the melting growth method and molten Sn as precursors. A single crystal of kesterite was synthesised at a temperature of 900 °C with the ampoule pulled through the furnace at a speed of 4 – 5 mm/day for 10 days.[86, 89, 90]

1.4.6.3 Chemical vapour transport

The chemical vapour transport method involves growing of CZTS crystals via a vapour phase with the aid of a transport agent (usually iodine) under a temperature gradient. A simplified approximation of the reaction is:

Equation 1.18

$$2CuI_{(g)} + ZnI_{2(g)} + SnI_{4(g)} + 2S_{2(g)} \rightarrow Cu_2ZnSnS_{4(s)} + 4I_{2(g)}$$

The effect of iodine concentration has been studied. A I_2 concentration of 5 mg/cm^3 was used for most work including the first reported chemical vapour transport for CZTS[91, 92]; Tanaka *et al.*[88] obtained slightly sulphur-poor (Cu:Zn:Sn:S = 2.0:1.0:1.0:3.8) and stoichiometric crystal with 5 and 10 mg/cm^3 of I_2 respectively; Colombara *et al.*[81] obtained highly crystalline needle-shaped crystals (1D

predominance) with 0.9 mg/cm^3 of I_2 and more defective but larger crystals (3D predominance) with 5 mg/cm^3 of I_2.

1.5 Secondary phases as potential absorber materials

Cu_2SnS_3, SnS and Cu_2S all have bandgaps and absorption coefficients in the optimal region for photovoltaic materials with the highest reported efficiency of 4.63,[93] 4.36,[94] and 9.15%[95] respectively. Although binary and ternary compounds have a less complicated structure than quaternary CZTS, Cu_2SnS_3 still has various crystal structures (monoclinic, tetragonal and cubic) that have different bandgaps and it is not known which structure gives the best performance nor how to control the formation of the desired structure; SnS is still in the initial stage of research; and Cu_2S suffered from performance degradation due to copper diffusion.

1.6 Summary and the aim of this work

It has been proposed that there is an urgent need to reduce CO_2 emissions before irreversible harm is done to our living planet. One of the solutions is to increase energy generation using renewable energy, such as solar energy. However, first generation solar cells require intense energy input during manufacture, while second generation solar cells generally use rare metals and toxic materials, and are therefore unlikely to provide a sustainable long term solution for large scale schemes. Kesterite-based materials have been focused on in this study because the bandgap and semiconducting properties met the basic requirement of a promising solar cell, and this phase only contains cheap, abundant, non-toxic materials. However, it remains a challenge to synthesise a high performance kesterite-based solar cell because of the complex phase diagram, formation of detrimental defect states, and tendency to decompose under nominal reaction conditions partly due to the volatility of tin and tin sulphide/selenide etc. These problems were partially solved by using a Zn-rich Cu-poor composition, or the generation of S/Se atmosphere during annealing. Nevertheless, a better understanding of the material is required to troubleshoot the problems in order to improve the efficiency.

In this work, single crystal and bulk forms of CZTS were synthesised, and the elemental composition of the products were analysed to ensure no secondary phases

were present (Chapter 4). A number of large CZTS crystals were then characterised using a variety of techniques to study the structural and optoelectronic properties of CZTS in a holistic approach to try to understand CZTS fundamentally (Chapter 5). Some of these large CZTS crystals were then fabricated into devices to determine their efficiency. (Chapter 7). In order to further support all the qualitative analysis regarding Cu/Zn disorder already reported in literature, experiments using resonance Raman spectroscopy, single crystal neutron diffraction, and synchrotron powder diffraction were carried out in an attempt to quantify the presence of Cu/Zn disorder (Chapter 6). Finally, a number of secondary phases and earth abundant photovoltaic compounds were synthesised and characterised in side projects (Chapter 8).

Reference

1. Dlugokencky, E. and Tans, P.; Available from: www.esrl.noaa.gov/gmd/ccgg/trends/.
2. Mora, C., Frazier, A.G., Longman, R.J., Dacks, R.S., Walton, M.M., Tong, E.J., Sanchez, J.J., Kaiser, L.R., Stender, Y.O., Anderson, J.M., Ambrosino, C.M., Fernandez-Silva, I., Giuseffi, L.M., and Giambelluca, T.W., *The projected timing of climate departure from recent variability.* Nature, 2013. **502**(7470): p. 183-187.
3. Victor, D.G., Zhou, D., Ahmed, E.H.M., Dadhich, P.K., Olivier, J.G.J., Rogner, H.-H., Sheikho, K., and Yamaguchi, M., *Introductory Chapter. In: Climate Change 2014: Mitigation of Climate Change. Contribution of Working Group III to the Fifth Assessment Report of the Intergovernmental Panel on Climate Change*, O. Edenhofer, et al., Editors. 2014, Cambridge University Press, Cambridge, United Kingdom and New York, NY, USA.
4. *Key World Energy Statistics*. 2016, International Energy Agency.
5. Smil, V., *Energy: A Beginner's Guide*. 2006: Oneworld Publications, Oxford, United Kingdom.
6. Jiang, M. and Yan, X., *Cu_2ZnSnS_4 Thin Film Solar Cells: Present Status and Future Prospects*. Solar Cells - Research and Application Perspectives. 2013.
7. *ASTM G173-03, Standard Tables for Reference Solar Spectral Irradiances: Direct Normal and Hemispherical on 37° Tilted Surface*. 2003, ASTM International, West Conshohocken, PA, www.astm.org.
8. *ASTM E490-00a, Standard Solar Constant and Zero Air Mass Solar Spectral Irradiance Tables*. 2000, ASTM International, West Conshohocken, PA, www.astm.org.
9. Nelson, J., *The Physics of Solar Cells*. 2003: Imperial College Press.
10. Peter, L.M., *Towards sustainable photovoltaics: the search for new materials.* Philosophical Transactions of the Royal Society a-Mathematical Physical and Engineering Sciences, 2011. **369**(1942): p. 1840-1856.
11. Shockley, W. and Queisser, H.J., *Detailed Balance Limit of Efficiency of p-n Junction Solar Cells.* Journal of Applied Physics, 1961. **32**(3): p. 510-519.
12. *Fraunhofer ISE: Photovoltaics Report, updated: 17 November 2016*. 2016, Fraunhofer Institute for Solar Energy System ISE.
13. Ito, K., *Copper Zin Tin Sulfide-based Thin Film Solar Cells*. 2015, Chichester, United Kingdom: Wiley. 421.
14. *Solar Frontier Achieves World Record Thin-Film Solar Cell Efficiency: 22.3%*. 2015.
15. Ito, K. and Nakazawa, T., *Electrical and Optical Properties of Stannite-Type Quaternary Semiconductor Thin Films.* Japanese Journal of Applied Physics, 1988. **27**(Part 1, No. 11): p. 2094-2097.
16. Katagiri, H. *Technical digest : 9th International Photovoltaic Science and Engineering Conference, Nov. 11-15/1996, Miyazaki, Japan*. 1996. Tokyo, Japan: International PVSEC-9.
17. Katagiri, H., Jimbo, K., Yamada, S., Kamimura, T., Maw, W.S., Fukano, T., Ito, T., and Motohiro, T., *Enhanced conversion efficiencies of Cu_2ZnSnS_4-based thin film solar cells by using preferential etching technique.* Applied Physics Express, 2008. **1**(4).

18. Todorov, T.K., Reuter, K.B., and Mitzi, D.B., *High-Efficiency Solar Cell with Earth-Abundant Liquid-Processed Absorber.* Advanced Materials, 2010. **22**(20): p. E156-E159.
19. Wang, W., Winkler, M.T., Gunawan, O., Gokmen, T., Todorov, T.K., Zhu, Y., and Mitzi, D.B., *Device Characteristics of CZTSSe Thin-Film Solar Cells with 12.6% Efficiency.* Advanced Energy Materials, 2014. **4**(7): p. 1301465.
20. Scragg, J.J., *Studies of Cu_2ZnSnS_4 films prepared by sulfurisation of electrodeposited precursors*, in *Dept. Chemistry*. 2010, University of Bath: Bath.
21. Paier, J., Asahi, R., Nagoya, A., and Kresse, G., *Cu_2ZnSnS_4 as a potential photovoltaic material: A hybrid Hartree-Fock density functional theory study.* Physical Review B, 2009. **79**(11): p. 115126.
22. Schorr, S., *The crystal structure of kesterite type compounds: A neutron and X-ray diffraction study.* Solar Energy Materials and Solar Cells, 2011. **95**(6): p. 1482-1488.
23. Mitzi, D.B., Gunawan, O., Todorov, T.K., Wang, K., and Guha, S., *The path towards a high-performance solution-processed kesterite solar cell.* Solar Energy Materials and Solar Cells, 2011. **95**(6): p. 1421-1436.
24. Scragg, J.J.S., Larsen, J.K., Kumar, M., Persson, C., Sendler, J., Siebentritt, S., and Bjorkman, C.P., *Cu-Zn disorder and band gap fluctuations in $Cu_2ZnSn(S,Se)_4$: Theoretical and experimental investigations.* Physica Status Solidi B-Basic Solid State Physics, 2016. **253**(2): p. 247-254.
25. Choubrac, L., Paris, M., Lafond, A., Guillot-Deudon, C., Rocquefelte, X., and Jobic, S., *Multinuclear (^{67}Zn, ^{119}Sn and ^{65}Cu) NMR spectroscopy - an ideal technique to probe the cationic ordering in Cu_2ZnSnS_4 photovoltaic materials.* Physical Chemistry Chemical Physics, 2013. **15**(26): p. 10722-10725.
26. Scragg, J.J.S., Choubrac, L., Lafond, A., Ericson, T., and Platzer-Björkman, C., *A low-temperature order-disorder transition in Cu_2ZnSnS_4 thin films.* Applied Physics Letters, 2014. **104**(4): p. 041911.
27. Rey, G., Redinger, A., Sendler, J., Weiss, T.P., Thevenin, M., Guennou, M., El Adib, B., and Siebentritt, S., *The band gap of $Cu_2ZnSnSe_4$: Effect of order-disorder.* Applied Physics Letters, 2014. **105**(11): p. 112106.
28. Rudisch, K., Ren, Y., Platzer-Björkman, C., and Scragg, J., *Order-disorder transition in B-type Cu_2ZnSnS_4 and limitations of ordering through thermal treatments.* Applied Physics Letters, 2016. **108**(23): p. 231902.
29. Vineyard, G.H., *Theory of Order-Disorder Kinetics.* Physical Review, 1956. **102**(4): p. 981-992.
30. Ritscher, A., Just, J., Dolotko, O., Schorr, S., and Lerch, M., *A mechanochemical route to single phase Cu_2ZnSnS_4 powder.* Journal of Alloys and Compounds, 2016. **670**: p. 289-296.
31. Ritscher, A., Franz, A., Schorr, S., and Lerch, M., *Off-stoichiometric CZTS: Neutron scattering investigations on mechanochemically synthesized powders.* Journal of Alloys and Compounds, 2016. **689**: p. 271-277.
32. Ritscher, A., Hoelzel, M., and Lerch, M., *The order-disorder transition in Cu_2ZnSnS_4 – A neutron scattering investigation.* Journal of Solid State Chemistry, 2016. **238**: p. 68-73.

33. Bosson, C.J., Birch, M.T., Halliday, D.P., Knight, K.S., Gibbs, A.S., and Hatton, P.D., *Cation disorder and phase transitions in the structurally complex solar cell material Cu_2ZnSnS_4.* Journal of Materials Chemistry A, 2017. **5**(32): p. 16672-16680.
34. Lafond, A., Choubrac, L., Guillot-Deudon, C., Fertey, P., Evain, M., and Jobic, S., *X-ray resonant single-crystal diffraction technique, a powerful tool to investigate the kesterite structure of the photovoltaic Cu_2ZnSnS_4 compound.* Acta Crystallographica Section B, 2014. **70**(2): p. 390-394.
35. Többens, D.M., Gurieva, G., Levcenko, S., Unold, T., and Schorr, S., *Temperature dependency of Cu/Zn ordering in CZTSe kesterites determined by anomalous diffraction.* physica status solidi (b), 2016. **253**(10): p. 1890-1897.
36. Bosson, C.J., Birch, M.T., Halliday, D.P., Tang, C.C., Kleppe, A.K., and Hatton, P.D., *Polymorphism in Cu_2ZnSnS_4 and New Off-Stoichiometric Crystal Structure Types.* Chemistry of Materials, 2017. **29**(22): p. 9829-9839.
37. Polizzotti, A., Repins, I.L., Noufi, R., Wei, S.-H., and Mitzi, D.B., *The state and future prospects of kesterite photovoltaics.* Energy & Environmental Science, 2013. **6**(11): p. 3171-3182.
38. Chen, S., Yang, J.-H., Gong, X.G., Walsh, A., and Wei, S.-H., *Intrinsic point defects and complexes in the quaternary kesterite semiconductor Cu_2ZnSnS_4.* Physical Review B, 2010. **81**(24).
39. Chen, S., Walsh, A., Gong, X.-G., and Wei, S.-H., *Classification of Lattice Defects in the Kesterite Cu_2ZnSnS_4 and $Cu_2ZnSnSe_4$ Earth-Abundant Solar Cell Absorbers.* Advanced Materials, 2013. **25**(11): p. 1522-1539.
40. Chen, S., Wang, L.-W., Walsh, A., Gong, X.G., and Wei, S.-H., *Abundance of $Cu_{Zn} + Sn_{Zn}$ and $2Cu_{Zn} + Sn_{Zn}$ defect clusters in kesterite solar cells.* Applied Physics Letters, 2012. **101**(22).
41. Xu, P., Chen, S., Huang, B., Xiang, H.J., Gong, X.-G., and Wei, S.-H., *Stability and electronic structure of Cu_2ZnSnS_4 surfaces: First-principles study.* Physical Review B, 2013. **88**(4).
42. Chen, S., Gong, X.G., Walsh, A., and Wei, S.-H., *Defect physics of the kesterite thin-film solar cell absorber Cu_2ZnSnS_4.* Applied Physics Letters, 2010. **96**(2).
43. Lafond, A., Choubrac, L., Guillot-Deudon, C., Deniard, P., and Jobic, S., *Crystal Structures of Photovoltaic Chalcogenides, an Intricate Puzzle to Solve: the Cases of CIGSe and CZTS Materials.* Zeitschrift Fur Anorganische Und Allgemeine Chemie, 2012. **638**(15): p. 2571-2577.
44. Paris, M., Choubrac, L., Lafond, A., Guillot-Deudon, C., and Jobic, S., *Solid-State NMR and Raman Spectroscopy To Address the Local Structure of Defects and the Tricky Issue of the Cu/Zn Disorder in Cu-Poor, Zn-Rich CZTS Materials.* Inorganic Chemistry, 2014. **53**(16): p. 8646-8653.
45. Choubrac, L., Lafond, A., Paris, M., Guillot-Deudon, C., and Jobic, S., *The stability domain of the selenide kesterite photovoltaic materials and NMR investigation of the Cu/Zn disorder in $Cu_2ZnSnSe_4$ (CZTSe).* Physical Chemistry Chemical Physics, 2015. **17**(23): p. 15088-15092.
46. Abermann, S., *Non-vacuum processed next generation thin film photovoltaics: Towards marketable efficiency and production of CZTS based solar cells.* Solar Energy, 2013. **94**: p. 37-70.

47. Colombara, D., Dale, P., Peter, L., Scragg, J., and Siebentritt, S., *CHAPTER 5 Thin-film Photovoltaics Based on Earth-abundant Materials*, in *Advanced Concepts in Photovoltaics*. 2014, The Royal Society of Chemistry. p. 118-185.
48. Siebentritt, S., *Why are kesterite solar cells not 20% efficient?* Thin Solid Films, 2013. **535**: p. 1-4.
49. Berg, D.M., Djemour, R., Guetay, L., Zoppi, G., Siebentritt, S., and Dale, P.J., *Thin film solar cells based on the ternary compound Cu_2SnS_3.* Thin Solid Films, 2012. **520**(19): p. 6291-6294.
50. Itoh, K., Kuzuya, T., and Sumiyama, K., *Morphology and composition-controls of Cu_xS nanocrystals using alkyl-amine ligands.* Materials Transactions, 2006. **47**(8): p. 1953-1956.
51. Raadik, T., Grossberg, M., Raudoja, J., Traksmaa, R., and Krustok, J., *Temperature-dependent photoreflectance of SnS crystals.* Journal of Physics and Chemistry of Solids, 2013. **74**(12): p. 1683-1685.
52. Kuo, D.-H., Haung, W.-D., Huang, Y.-S., Wu, J.-D., and Lin, Y.-J., *Single-step sputtered Cu_2SnSe_3 films using the targets composed of Cu_2Se and $SnSe_2$.* Thin Solid Films, 2010. **518**(24): p. 7218-7221.
53. Fernandes, P.A., Salome, P.M.P., and da Cunha, A.F., *Study of polycrystalline Cu_2ZnSnS_4 films by Raman scattering.* Journal of Alloys and Compounds, 2011. **509**(28): p. 7600-7606.
54. Matsushita, H., Ichikawa, T., and Katsui, A., *Structural, thermodynamical and optical properties of Cu_2-II-IV-VI_4 quaternary compounds.* Journal of Materials Science, 2005. **40**(8): p. 2003-2005.
55. Fernandes, P.A., Salome, P.M.P., and da Cunha, A.F., *A study of ternary Cu_2SnS_3 and Cu_3SnS_4 thin films prepared by sulfurizing stacked metal precursors.* Journal of Physics D-Applied Physics, 2010. **43**(21): p. 215403.
56. Riha, S.C., Parkinson, B.A., and Prieto, A.L., *Solution-Based Synthesis and Characterization of Cu_2ZnSnS_4 Nanocrystals.* J Am Chem Soc, 2009. **131**(34): p. 12054-5.
57. Blachnik, R. and Müller, A., *The formation of Cu_2S from the elements: I. Copper used in form of powders.* Thermochimica Acta, 2000. **361**(1–2): p. 31-52.
58. Greenwood, N.N. and Earnshaw, A., *Chemistry of the elements*. 1984, Oxford: Pergamon.
59. Haynes, W.M., *CRC Handbook of Chemistry and Physics*. 95nd ed., 2014-2015 ed. 2014, Boca Raton, Fla. ; London: CRC.
60. Said, G. and Lee, P.A., *Electrical conduction mechanisms in tin disulphide.* physica status solidi (a), 1973. **15**(1): p. 99-103.
61. Gao, X.D., Li, X.M., and Yu, W.D., *Morphology and optical properties of amorphous ZnS films deposited by ultrasonic-assisted successive ionic layer adsorption and reaction method.* Thin Solid Films, 2004. **468**(1-2): p. 43-47.
62. Berg, D.M., Arasimowicz, M., Djemour, R., Gütay, L., Siebentritt, S., Schorr, S., Fontané, X., Izquierdo-Roca, V., Pérez-Rodriguez, A., and Dale, P.J., *Discrimination and detection limits of secondary phases in Cu_2ZnSnS_4 using X-ray diffraction and Raman spectroscopy.* Thin Solid Films, 2014. **569**(0): p. 113-123.

63. Sarswat, P.K., Free, M.L., and Tiwari, A., *Temperature-dependent study of the Raman A mode of Cu_2ZnSnS_4 thin films.* physica status solidi (b), 2011. **248**(9): p. 2170-2174.
64. Khare, A., Himmetoglu, B., Johnson, M., Norris, D.J., Cococcioni, M., and Aydil, E.S., *Calculation of the lattice dynamics and Raman spectra of copper zinc tin chalcogenides and comparison to experiments.* J. Appl. Phys., 2012. **111**(8): p. 083707.
65. Gurel, T., Sevik, C., and Cagin, T., *Characterization of vibrational and mechanical properties of quaternary compounds Cu_2ZnSnS_4 and $Cu_2ZnSnSe_4$ in kesterite and stannite structures.* Physical Review B, 2011. **84**(20).
66. Scragg, J.J., Ericson, T., Kubart, T., Edoff, M., and Platzer-Björkman, C., *Chemical Insights into the Instability of Cu_2ZnSnS_4 Films during Annealing.* Chemistry of Materials, 2011. **23**(20): p. 4625-4633.
67. Scragg, J.J., Dale, P.J., Colombara, D., and Peter, L.M., *Thermodynamic Aspects of the Synthesis of Thin-Film Materials for Solar Cells.* ChemPhysChem, 2012. **13**(12): p. 3035-3046.
68. Fairbrother, A., Garcia-Hemme, E., Izquierdo-Roca, V., Fontane, X., Pulgarin-Agudelo, F.A., Vigil-Galan, O., Perez-Rodriguez, A., and Saucedo, E., *Development of a Selective Chemical Etch To Improve the Conversion Efficiency of Zn-Rich Cu_2ZnSnS_4 Solar Cells.* Journal of the American Chemical Society, 2012. **134**(19): p. 8018-8021.
69. Mousel, M., Redinger, A., Djemour, R., Arasimowicz, M., Valle, N., Dale, P., and Siebentritt, S., *HCl and Br-2-MeOH etching of $Cu_2ZnSnSe_4$ polycrystalline absorbers.* Thin Solid Films, 2013. **535**: p. 83-87.
70. Timmo, K., Altosaar, M., Raudoja, J., Grossberg, M., Danilson, M., Volobujeva, O., and Mellikov, E. *Chemical etching of $Cu_2ZnSn(S,Se)_4$ monograin powder*. in *2010 35th IEEE Photovoltaic Specialists Conference*. 2010.
71. Volobujeva, O., Mellikov, E., Timmo, K., Danilson, M., and Bereznev, S., *$Cu_2ZnSnSe_4$ films from binary precursors.* Journal of Renewable and Sustainable Energy, 2013. **5**(3): p. 031618.
72. Mott, N.F., *The theory of crystal rectifiers.* Proceedings of the Royal Society of London. Series A. Mathematical and Physical Sciences, 1939. **171**(944): p. 27-38.
73. Schottky, W., *Zur Halbleitertheorie der Sperrschicht- und Spitzengleichrichter.* Zeitschrift für Physik, 1939. **113**(5): p. 367-414.
74. Schottky, W., *Vereinfachte und erweiterte Theorie der Randschicht-gleichrichter.* Zeitschrift für Physik, 1942. **118**(9): p. 539-592.
75. Huang, S., Luo, W., and Zou, Z., *Band positions and photoelectrochemical properties of Cu_2ZnSnS_4 thin films by the ultrasonic spray pyrolysis method.* Journal of Physics D-Applied Physics, 2013. **46**(23).
76. Sekou Mariama, C., Lingling, W., and Xintong, Z., *Easy hydrothermal preparation of Cu_2ZnSnS_4 (CZTS) nanoparticles for solar cell application.* Nanotechnology, 2013. **24**(49): p. 495401.
77. Ananthoju, B., Sonia, F.J., Kushwaha, A., Bahadur, D., Medhekar, N.V., and Aslam, M., *Improved structural and optical properties of Cu_2ZnSnS_4 thin films via optimized potential in single bath electrodeposition.* Electrochimica Acta, 2014. **137**(0): p. 154-163.

78. Fernandes, P.A., Salomé, P.M.P., Sartori, A.F., Malaquias, J., da Cunha, A.F., Schubert, B.-A., González, J.C., and Ribeiro, G.M., *Effects of sulphurization time on Cu_2ZnSnS_4 absorbers and thin films solar cells obtained from metallic precursors.* Solar Energy Materials and Solar Cells, 2013. **115**: p. 157-165.
79. Cui, H., Lee, C.-Y., Li, W., Liu, X., Wen, X., and Hao, X., *Improving Efficiency of Evaporated Cu_2ZnSnS_4 Thin Film Solar Cells by a Thin Ag Intermediate Layer between Absorber and Back Contact.* International Journal of Photoenergy, 2015. **2015**: p. 9.
80. Van Zeghbroeck, B. *Principles of semiconductor devices*. 2004.
81. Colombara, D., Delsante, S., Borzone, G., Mitchels, J.M., Molloy, K.C., Thomas, L.H., Mendis, B.G., Cummings, C.Y., Marken, F., and Peter, L.M., *Crystal growth of Cu_2ZnSnS_4 solar cell absorber by chemical vapor transport with I_2.* Journal of Crystal Growth, 2013. **364**: p. 101-110.
82. Bernardini, G.P., Borrini, D., Caneschi, A., Di Benedetto, F., Gatteschi, D., Ristori, S., and Romanelli, M., *EPR and SQUID magnetometry study of Cu_2FeSnS_4 (stannite) and Cu_2ZnSnS_4 (kesterite).* Physics and Chemistry of Minerals, 2000. **27**(7): p. 453-461.
83. Choubrac, L., Lafond, A., Guillot-Deudon, C., Moëlo, Y., and Jobic, S., *Structure Flexibility of the Cu_2ZnSnS_4 Absorber in Low-Cost Photovoltaic Cells: From the Stoichiometric to the Copper-Poor Compounds.* Inorganic Chemistry, 2012. **51**(6): p. 3346-3348.
84. Kheraj, V., Patel, K.K., Patel, S.J., and Shah, D.V., *Synthesis and characterisation of Copper Zinc Tin Sulphide (CZTS) compound for absorber material in solar-cells.* Journal of Crystal Growth, 2013. **362**: p. 174-177.
85. Wang, Y. and Gong, H., *Low Temperature Synthesized Quaternary Chalcogenide Cu_2ZnSnS_4 from Nano-Crystallite Binary Sulfides.* Journal of the Electrochemical Society, 2011. **158**(8): p. H800-H803.
86. Nagaoka, A., Yoshino, K., Taniguchi, H., Taniyama, T., and Miyake, H., *Preparation of Cu_2ZnSnS_4 single crystals from Sn solutions.* Journal of Crystal Growth, 2012. **341**(1): p. 38-41.
87. Das, S., Krishna, R.M., Ma, S., and Mandal, K.C., *Single phase polycrystalline Cu_2ZnSnS_4 grown by vertical gradient freeze technique.* Journal of Crystal Growth, 2013. **381**: p. 148-152.
88. Tanaka, K., Miyamoto, Y., Uchiki, H., Nakazawa, K., and Araki, H., *Donor-acceptor pair recombination luminescence from Cu_2ZnSnS_4 bulk single crystals.* Physica Status Solidi a-Applications and Materials Science, 2006. **203**(11): p. 2891-2896.
89. Nagaoka, A., Yoshino, K., Taniguchi, H., Taniyama, T., Kakimoto, K., and Miyake, H., *Growth and characterization of $Cu_2ZnSn(S_xSe_{1-x})_4$ alloys grown by the melting method.* Journal of Crystal Growth, 2014. **386**: p. 204-207.
90. Nagaoka, A., Yoshino, K., Taniguchi, H., Taniyama, T., and Miyake, H., *Growth of $Cu_2ZnSnSe_4$ single crystals from Sn solutions.* Journal of Crystal Growth, 2012. **354**(1): p. 147-151.
91. Nitsche, R., Sargent, D.F., and Wild, P., *Crystal growth of quaternary 1_2246_4 chalcogenides by iodine vapor transport.* Journal of Crystal Growth, 1967. **1**(1): p. 52-53.

92. Guen, L. and Glaunsinger, W.S., *Electrical, Magnetic, and Epr Studies of the Quaternary Chalcogenides $Cu_2A^{II}B^{IV}X_4$ Prepared by Iodine Transport.* Journal of Solid State Chemistry, 1980. **35**(1): p. 10-21.
93. Nakashima, M., Fujimoto, J., Yamaguchi, T., and Izaki, M., *Cu_2SnS_3 thin-film solar cells fabricated by sulfurization from NaF/Cu/Sn stacked precursor.* Applied Physics Express, 2015. **8**(4): p. 042303.
94. Sinsermsuksakul, P., Sun, L., Lee, S.W., Park, H.H., Kim, S.B., Yang, C., and Gordon, R.G., *Overcoming Efficiency Limitations of SnS-Based Solar Cells.* Advanced Energy Materials, 2014. **4**(15): p. 1400496.
95. Bragagnolo, J.A., Barnett, A.M., Phillips, J.E., Hall, R.B., Rothwarf, A., and Meakin, J.D., *The design and fabrication of thin-film CdS/Cu_2S cells of 9.15-percent conversion efficiency.* IEEE Transactions on Electron Devices, 1980. **27**(4): p. 645-651.

2 Experimental Techniques

The research work included in this thesis presented the synthesis and characterisation of a few photovoltaic metal chalcogenides which contain only earth abundant and non-toxic materials, with the main focus on Cu_2ZnSnS_4. Products were characterised compositionally, structurally, optically, and electrochemically.

Elemental composition of the products were characterised using energy-dispersive X-ray spectroscopy (EDS), atomic absorption spectroscopy (AAS) and/or X-ray fluorescence spectroscopy (XRF). The morphology of the products were observed using scanning electron microscopy (SEM). The phase purity of the products were determined using powder X-ray diffraction (PXRD) and Raman spectroscopy. Crystal structures were determined using single crystal X-ray diffraction (SCXRD). Since laboratory SCXRD cannot distinguish between Cu and Zn, single crystal neutron diffraction (ND) and anomalous X-ray diffraction techniques were also used. The absorption coefficient and complex dielectric function of CZTS was determined using spectroscopic ellipsometry. The electronic band structure of CZTS was determined using photoluminescence (PL). The external quantum efficiency (EQE) of CZTS were characterised using photocurrent spectroscopy. The built-in potential and doping density of CZTS were determined using impedance spectroscopy. The solar cell performance was measured with a solar simulator.

2.1 Energy-dispersive X-ray spectroscopy (EDS) and X-ray Fluorescence spectroscopy (XRF)

The theory behind both EDS and XRF are very similar because both techniques detect the characteristic X-ray emitted from the sample following the interaction with high-energy beam, *i.e.* electron beam in EDS, and X-ray beam in XRF. The beam interact with the inner shell electrons of the atom in the sample, ejecting an electron from the shell. The atom is left as an ion in an excited energy state. The atom relaxes to its ground state within approximately 1 ps through a limited set of allowed transitions of outer shell electron(s) to fill the inner shell vacancy. This relaxation emits an X-ray photon with energy equals to the energy difference between the electron shells, and is unique for each element.[1] Both EDS and XRF are non-destructive and surface

techniques. The sampling depth depends on the energy of the beam and the density of the sample, and ranging from few tens of nm to few tens of µm.

2.2 Atomic absorption spectroscopy (AAS)

In AAS, the sample is first vaporised under a frame with temperature usually above 2000 °C. The electrons of the atoms is then promoted to higher orbitals for a short period of time by absorbing a defined quantity of energy (*i.e.* wavelength) generated from a light source. The wavelength is specific to a particular electron transition in the element in question, giving the elemental selectivity to this technique. The absorbance of the unknown sample is then compared against the calibration curve generated with samples of known concentrations (calibration standards) to calculate the concentration of the element in question in the unknown sample. AAS is a destructive technique because the samples need to be vaporised, however, it gives the elemental composition of the bulk.

2.3 Scanning electron microscopy (SEM)

SEM is a powerful analytical technique often used in sample imaging because of high magnification and large depth of field compared to optical microscopes. A SEM consists of an electron gun, a lens system, scanning coils, an electron detector, and a cathode ray display tube (CRT). The electron energy is typically 10 – 30 keV for most samples. When the electron beam strikes the sample, electrons are absorbed, emitted, reflected or transmitted, and can also cause light or X-ray emission. Electrons used for imaging in a SEM are secondary electrons and/or backscattered electrons. Both types of electrons are emitted from the sample upon electron irradiation. By convention, secondary electrons exhibit energies between 0 and 50 eV, whereas backscattered electrons cover the energy range between 50 eV and the energy of the primary electron beam.[2]

The standard Everhart–Thornley detector collects both secondary and backscattered electrons. Both signals are collected when a positive voltage is applied to the collector screen in front of the detector. While only a pure backscattered electron signal is captured with a negative voltage because the low-energy secondary

electrons are repelled. Electrons captured by the photomultiplier are then amplified for display on the viewing CRT.[3]

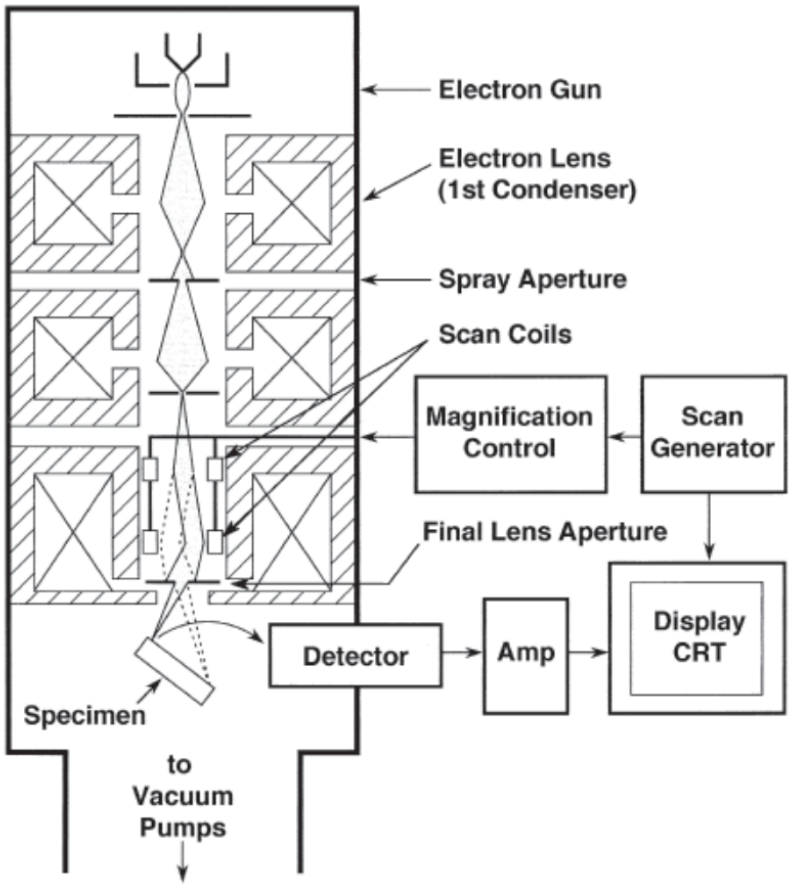

Figure 2.1 Schematic drawing of a SEM. Reproduced from Goldstein *et al.*[3]

2.4 X-ray and Neutron diffraction

In order to understand the crystal structure of a material, X-ray and neutron scattering are often used. Both techniques are complementary of each other. In X-ray scattering, it is almost exclusively the electrons in atoms which contribute to the scattering, whereas neutrons interact with the atomic nuclei. Therefore the response of neutrons from light atoms is much higher than for X-rays, and neutrons easily distinguish atoms of comparable atomic number. Since the size of a nucleus is typically 10^5 smaller than the distance between two nuclei, neutrons can travel large distances through most materials without being scattered or absorbed. Thus, neutrons penetrate materials much more deeply than X-rays and give higher resolution data. On the other hand, X-ray scattering has the advantage that measurement durations are usually much shorter compared with neutron scattering,

due to a larger scattering cross section. Additionally, lab-scale X-ray sources are broadly available.

When X-rays or neutrons interact with a crystalline substance, coherent elastic scattering may occur, which is also called diffraction. When an X-ray beam hits an atom, the electrons around the atom start to oscillate with the same frequency as the incoming beam and emits electromagnetic radiation. The sum of the contributions of these radiations to the scattered amplitude of all the electrons of an atomic species in the crystal is expressed by the atomic scattering factor *f*. At zero angle, all the scattered waves are in phase, and the scattered amplitude is the simple sum of the contributions from all Z electrons, where Z is the atomic number of the atom. As the scattering angle increases, *f* becomes smaller than Z because of the increasing destructive interference effects between the Z-scattered waves. In contrast, the neutron scattering length does not decrease with increasing scattering angle (Figure 2.2).

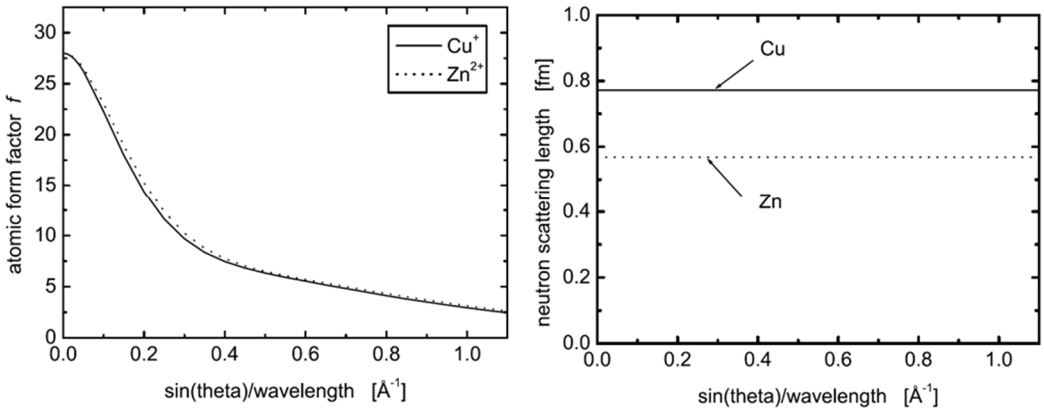

Figure 2.2 Example of scattering amplitudes of two isoelectronic cations related to the scattering angle. Left: The atomic form factor of Cu^{+} and Zn^{2+}. Right: The neutron scattering length of Cu^{+} and Zn^{2+}. Reproduced from Schorr *et al.*[4]

The amplitude of the neutron wave scattered by the nucleus depends on the strength of the interaction between the neutron and the nucleus. It is referred to as the scattering length of the nucleus, *b*. It varies in an irregular way with the atomic number as shown in Figure 2.3. It also varies between isotopes of the same element.

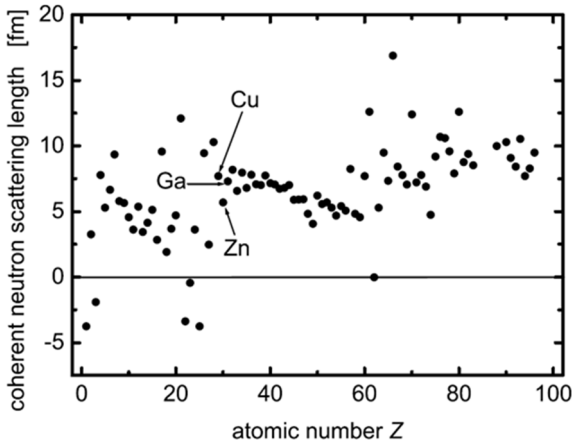

Figure 2.3 The neutron scattering length of different nuclei with respect to their atomic numbers. Reproduced from Schorr *et al*.[4]

The atoms in a crystal are arranged in a regular pattern. In almost all directions into which waves are scattered, the scattered waves are out of phase and destructive interference occurs. However, for a small fraction of these directions, the coincidence of the scattered waves results in constructive interference. The waves are in phase, and scattered X-rays or neutrons leaving the sample into various directions. These specific directions can be determined by the Bragg's law:[5]

Equation 2.1

$$n\lambda = 2d_{hkl} \sin\theta$$

where n is the diffraction order, λ is the wavelength of the radiation, d_{hkl} is the spacing between the lattice planes, and θ is the angle of incident between the incoming beam and the lattice planes. The derivation of the Bragg's law is visualised in Figure 2.4. When the beams are scattered from two adjacent planes, the beam hitting a lower plane travels additional distances. This additional distance travelled must equal to an integral multiple of the wavelength λ in order to remain in phase with the first beam.

In a tetragonal crystal like CZTS(e), d_{hkl} can be related to the lattice parameters (a and c) using the following relationship:

Equation 2.2

$$\frac{1}{{d_{hkl}}^2} = \frac{h^2 + k^2}{a^2} + \frac{l^2}{c^2}$$

where h, k and l are the Miller indices specifying the orientation of the lattice planes by indicating the intercept with the unit cell axes at a/h, b/k and c/l. The lattice parameters of the unit cell can then be calculated by combining Equation 2.1 and 2.2.

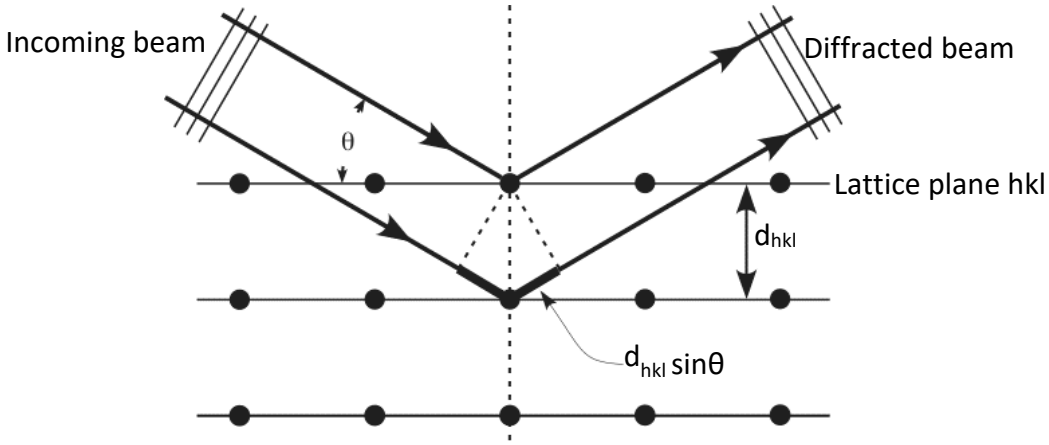

Figure 2.4 Derivation of Bragg's law.

The scattering amplitude of a unit cell is determined by summing the scattering amplitudes *f* or *b*, from all atoms in the unit cell. It is expressed by a dimensionless number, the structure factor $F_{hkl,}$.

Equation 2.3

$$F_{hkl} = \sum_{j=1}^{N} f_j e^{[-2\pi i(hx_j + ky_j + lz_j)]}$$

where the sum is over all atoms in the unit cell, f_j is the scattering factor of the j^{th} atom, and x_j, y_j, z_j are the fractional coordinates of the j^{th} atom.

The intensities I_{hkl} of scattered X-ray or neutron waves are proportional to the squares of their structure factor, F_{hkl}, and hence $I_{hkl} \propto |F_{hkl}|^2$.

2.4.1 Anomalous X-ray scattering

The wavelength dependencies on the X-ray scattering factor were ignored historically. It was not until 1955, when Templeton *et al.*[6] pointed out the importance of the wavelength dependence of anomalous scattering in X-ray diffraction experiments:

Equation 2.4

$$f = f_0 + \Delta f' + i\Delta f''$$

where f_0 is the 'normal' scattering factor, f' and f'' are the real and imaginary anomalous scattering factor; f' and f'' are wavelength dependent. The scattering factors of all the four elements in CZTS are plotted in Figure 2.5. There is a sharp transition in the scattering factors of Cu and Zn near the absorption edge of the corresponding elements, which means, the overall scattering factor of Cu and Zn will be different when the measurement is carried out near the absorption edges, and hence we should be able to distinguish between Cu and Zn in the structure.

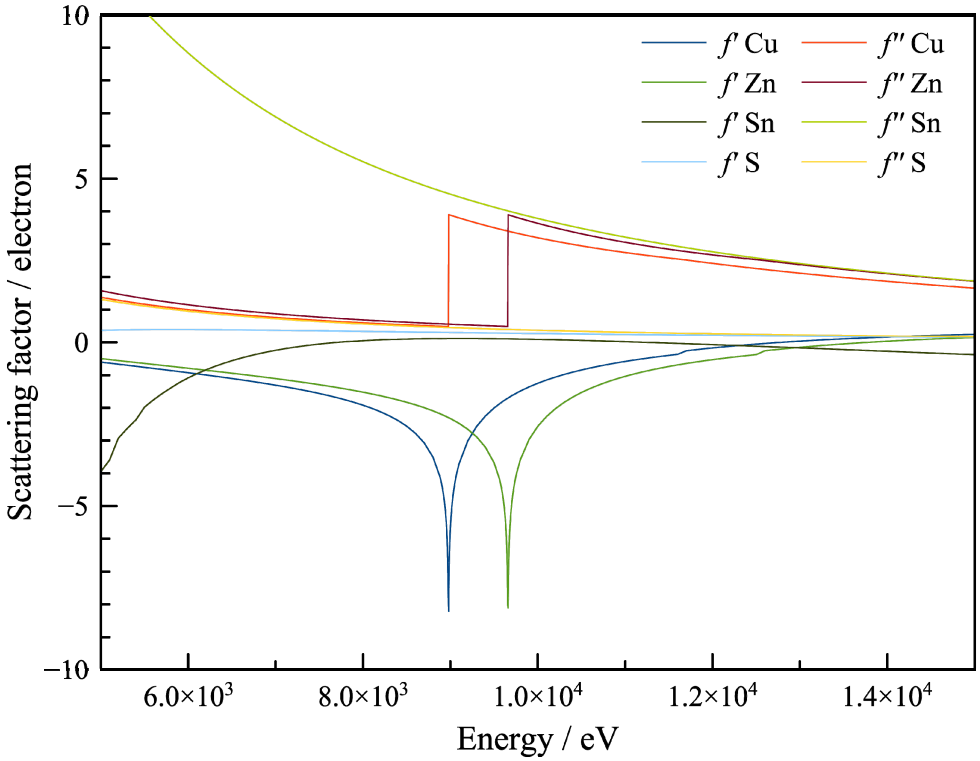

Figure 2.5 Anomalous scattering factor of all the four elements in CZTS. The scattering factor data were downloaded from Merritt *et al.*[7], of which were calculated using the subroutine library and derived using the theoretical approximation developed by Cromer and Liberman *et al.*[8-10]

2.4.2 R-factor

In crystallography, the *R*-factor is a measure of the agreement between the crystallographic model and the experimental diffraction data, and is defined as:

Equation 2.5

$$R = \frac{\Sigma\left||F_{obs}| - |F_{calc}|\right|}{\Sigma|F_{obs}|}$$

where F_{obs} is the observed (or experimental) structure factor, and F_{calc} is the structure factor calculated from the model. Variation on the *R*-factor include using F^2 values instead of $|F|$ values, squaring the differences, and/or incorporating weighting factors, such as the wR_2 factor:

Equation 2.6

$$wR_2 = \sqrt{\frac{\Sigma w(F_{obs}^2 - F_{calc}^2)^2}{\Sigma w(F_{obs}^2)^2}}$$

where w is the weighting factor and each reflection carries a weigh proportional to their structure factor, i.e. a strong reflection contributed more to the wR_2 factor than a weak reflection. Hence, the wR_2 factor is more statistically meaningful than the basic *R* factor. Values of wR_2 and other *R* factors based on F^2 are generally higher than those based on *F* values by a factor of two or more.[11]

2.5 Raman spectroscopy

Raman spectroscopy is an optical, non-destructive technique based on the inelastic scattering of photons with elemental vibrational excitations in a material. The line shape and position of the Raman bands are determined by the crystalline structure and chemical composition of the measured samples, being sensitive to the presence of crystalline defects, impurities, and strain.[12]

When light is scattered from the surface of a sample, the majority of the light is scattered elastically (Raleigh scattering). Some light interacts with the optical phonons in the material and scattered inelastically, and this is called Raman scattering. If the incident photon imparts energy to the lattice in the form of a phonon, it emerges as a lower-energy photon. This down-converted frequency shift

is known as Stokes Raman scattering. In Anti-Stokes Raman scattering the photon absorbs a phonon and emerges with higher energy. This change in energy corresponds to the vibrational energy states inside the crystal, and is detected as the change of wavelength with respect to the incoming laser. Since the intensity of Raman scattered light is very weak (about 1 in 10^8 parts), Raman spectroscopy is only practical when an intense monochromatic light source like a laser is used.[13] A schematic of a Raman spectrometer setup is shown in Figure 2.6.

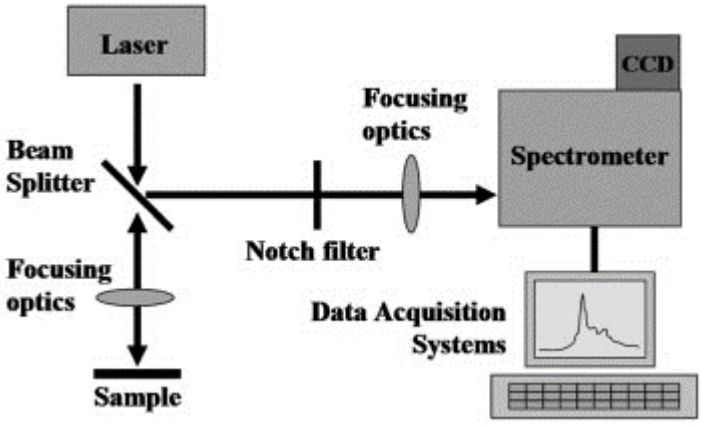

Figure 2.6 Schematic diagram of a Raman spectrometer setup. Reproduced from Álvarez‐García *et al.*[12]

2.6 Spectroscopic ellipsometry

Spectroscopic ellipsometry has emerged as a non-destructive, non-invasive optical technique for the characterisation of thin-film solar cell materials and devices. It measures the output polarisation ellipse reflected obliquely from the sample surface when a beam of light with known input polarisation ellipse was used. The analysis of the ellipse can provide useful optical and structural information about the sample, including optical properties and multilayer thicknesses.

During an ellipsometry measurement, two important interaction parameters, Ψ and Δ were measured at each wavelengths. These are the ellipsometry amplitude and phase components respectively, and are defined as:

Equation 2.7

$$\tan\psi e^{i\Delta} = \frac{r_p}{r_s}$$

where r_p and r_s are the complex amplitude reflection coefficients of the sample for the p-plane and s-plane components of the light wave shown in Figure 2.7.

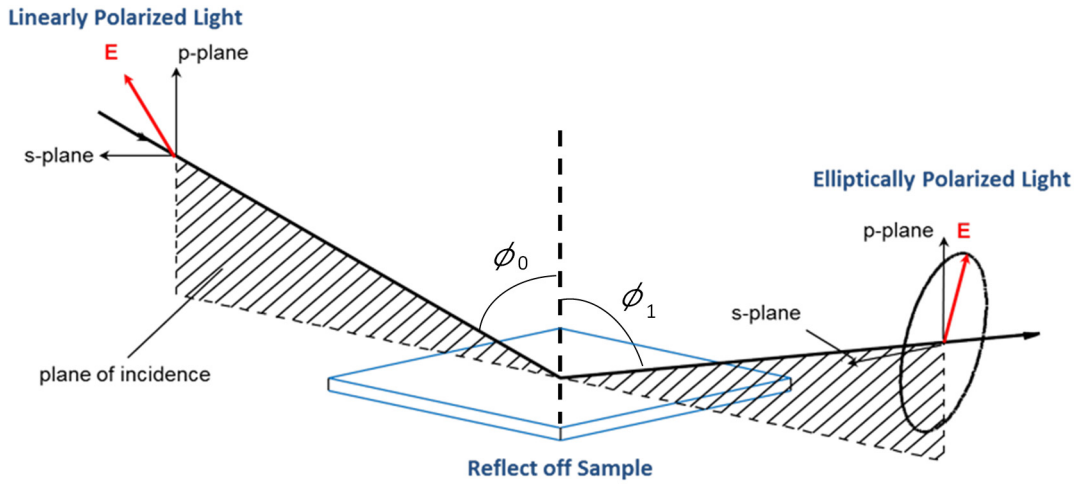

Figure 2.7 A schematic showing how polarised light interacts with a sample during an ellipsometry measurement. Reproduced from Woollam *et al.*[14]

The mathematical expression for r_p and r_s are as follow:

Equation 2.8

$$r_p = \frac{N_1 \cos\phi_0 - N_0 \cos\phi_1}{N_1 \cos\phi_0 + N_0 \cos\phi_1} \qquad r_s = \frac{N_0 \cos\phi_0 - N_1 \cos\phi_1}{N_0 \cos\phi_0 + N_1 \cos\phi_1}$$

where Φ_0 is the incident angle and Φ_1 is the reflected angle as shown in Figure 2.7. N_0 and N_1 are the complex refraction index of the ambient and sample respectively. The complex refraction index can be expressed as:

Equation 2.9

$$N = n - \mathrm{i}k$$

where n is the refraction index and k is the extinction coefficient. These two quantities are referred to as optical constants and used to describe how light interacts with the material. Both are wavelength and temperature dependant. The extinction coefficient k is also related to the absorption coefficient α:

Equation 2.10

$$\alpha = \frac{4\pi k}{\lambda}$$

where λ is the wavelength of light. Alternatively the optical constants of a material can be described using the complex dielectric function:

Equation 2.11

$$\varepsilon = \varepsilon' + i\varepsilon''$$

The complex dielectric function is related to the complex refraction index by:

Equation 2.12

$$\varepsilon = N^2$$

Both optical constants are used in literature, and usage is generally determined by the application.[14]

2.7 Photoluminescence (PL)

PL involves light emission from a material after being excited by photons that have a higher energy than the bandgap of the material. The emission of PL radiation is caused by the transition of electrons from higher occupied electronic states into lower unoccupied states, under the emission of photons if the transition is allowed. A number of different transitions can occur depending on the measurement conditions and the material properties.[15] Figure 2.8 shows the different transitions that can be observed with different measurement temperatures.

At low temperatures in the vicinity of 10 K, electron-hole pairs bound to each other by their Coulomb interaction creating free excitons. Free excitons emissions (FX) are only detectable at sufficiently low temperatures when k_BT is less than the exciton binding energy. Free excitons get easily bound to impurities, and leads to a change of the transition energy. The ratio between FX and bound exciton emission (BX) present in a photoluminescence experiment depends on the number of impurities present in the material and the measurement temperature. If both donors and acceptors are present in significant concentrations and the temperature is low enough, it is possible to observe donor–acceptor pair recombination (DA), which involve transitions between two localised electronic states. Carrier recombination can also occur between free carriers in the valence band and donor (p-D^0), and in the conduction band and acceptor (e-A^0). These are called free-to-bound (FB) transitions.

With increasing temperature, excitons and impurities become ionised, and the conduction and valence bands become increasingly occupied with photoexcited carries so that band-to-band transitions (BB) are more likely to be observed. Since the mathematical expression between FB and BB are very similar, knowledge of the value of the bandgap determined by other means would be helpful in order to distinguish between FB and BB.[15]

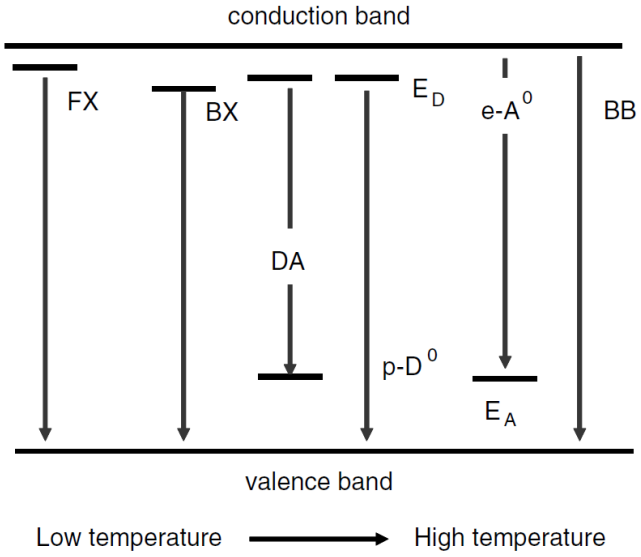

Figure 2.8 Different types of photoluminescence transitions observable with different temperatures. FX: free excitons emission; BX: bound exciton emission; DA: donor-acceptor pair recombination; E_D: donor ionisation energy; p-D^0: valence band to donor state; e-A^0: conduction band to acceptor state; E_A: acceptor ionisation energy; BB: band-to-band transition. Reproduced from Unold *et al.*[15]

A schematic of a typical PL experiment setup is shown in Figure 2.9. The excitation source can be any light source with energy higher than the bandgap of the sample. Because of the widespread availability and high monochromatic power, laser excitation sources are used in most setups. The excitation source is guided or focused onto the sample by a series of optics and filters. The luminescence radiation emitted from the sample is then collected by a light collection device, focused into a monochromator system, and finally reaching a radiation detector.[15]

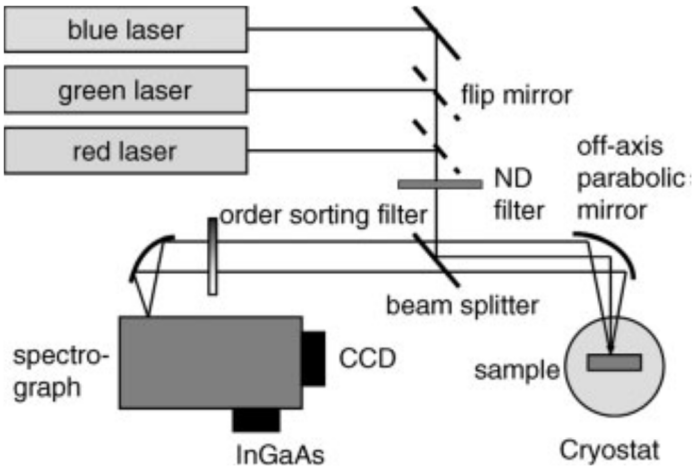

Figure 2.9 Schematic of a typical PL experiment setup. Reproduced from Unold *et al*.[15]

2.8 Current-Voltage (J-V) measurements

Solar cell performance is derived from the J-V characteristic of the solar cell which is discussed in detail in the introduction chapter (Chapter 1.1). It can be measured using a solar simulator shown in Figure 2.10. The solar cell is connected to a potentiostat and the current and voltage are measured during the voltage sweep by varying the load resistance. The illuminated J-V characteristic of a solar cell is usually measured under standard conditions, which is, with an AM1.5 spectrum, an incident power density of 1000 W m^{-2}, and a temperature of 25 °C.

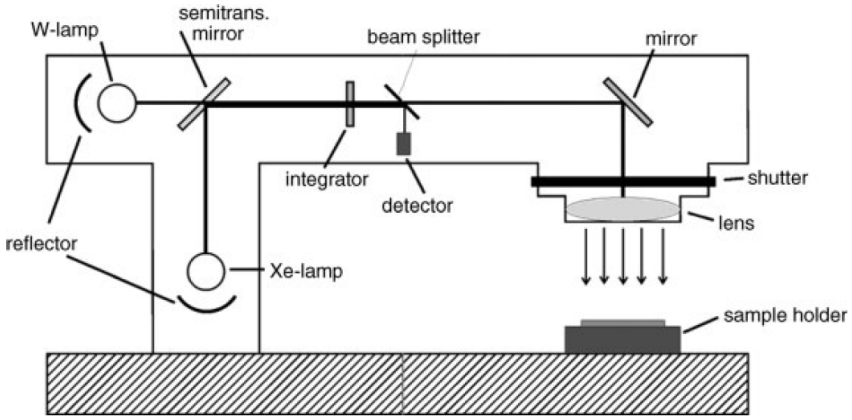

Figure 2.10 Schematic of a solar simulator for J-V measurements. Reproduced from Kirchartz *et al.*[16]

2.9 External Quantum Efficiency (EQE) measurements

Although J-V measurement yields information on the absolute value of the short circuit density (J_{SC}) produced in a solar cell, it does not yield information on the origin of the loss mechanisms because not every photon in the solar spectrum contributes

to J_{SC}. An EQE spectrum records J_{SC} at different wavelengths and is defined as the number of electrons collected per photon incident on the solar cell:

Equation 2.13

$$EQE(\lambda) = \frac{1}{q}\frac{dJ_{SC}(\lambda)}{d\Phi(\lambda)}$$

where q is the electronic charge and Φ is the incident photon flux.

In an ideal solar cell, EQE(λ) = 1 for wavelengths with energy equal or higher than the bandgap and otherwise EQE(λ) = 0. In real solar cells, EQE(λ) < 1 even for wavelengths with energy equal or higher than the bandgap because of optical and/or recombination losses. These losses determine the shape of the EQE spectrum. The optical losses can be further broken down to losses due to reflection and due to parasitic absorption within the solar cell.

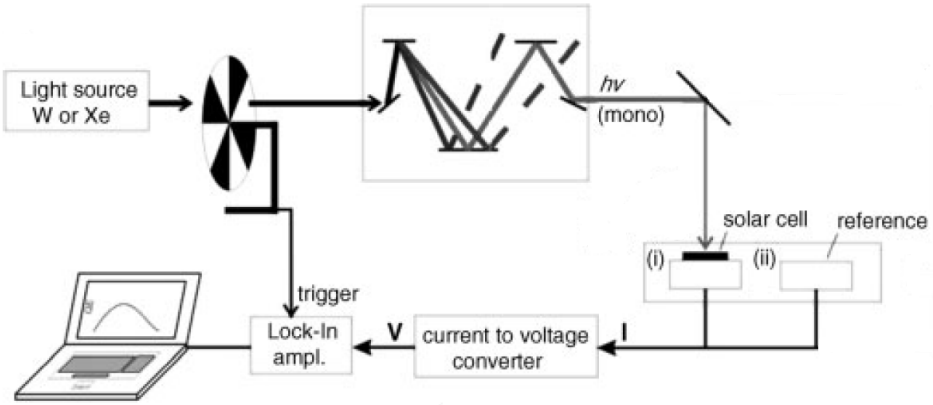

Figure 2.11 Schematic of a setup for EQE measurement. Reproduced from Kirchartz *et al.*[16]

A typical setup for EQE measurement is shown in Figure 2.11. A white light is chopped before entering a monochromator. The chopper gives an alternating state of light on and off, thus the sample can generate output from the light source and background respectively. The frequency of which the chopper rotates is later used as the reference signal in the lock-in amplifier. The monochromatic light is then focused on a reference cell during calibration, or on the sample during the actual measurement. The current signal from the reference cell or sample are then converted into a voltage by a current-to-voltage converter with a typical amplification ratio of 10^4 to 10^6 V/A.

The voltage then synchronises with the reference signal from the chopper in the lock-in amplifier and displayed in a computer.[16]

2.10 Impedance spectroscopy

Impedance spectroscopy has been used in commercial solar cell to obtain information about minority carrier lifetimes, series and parallel resistances, and acceptor impurity densities.[17] The most common approach to measure impedance is by applying a single-frequency voltage, *V(t)*, usually in the range of 10 Hz to 100 kHz, to the semiconductor junction and measure the phase shift and amplitude of the resulting current, *I(t)*.[18] The impedance, Z(ω), can then be determined using the Ohm's law:

Equation 2.14

$$\mathrm{Z}(\omega) = \frac{V(t)}{I(t)}$$

$$V(t) = V_m \sin(\omega t) \qquad I(t) = I_m \sin(\omega t + \theta)$$

where ω is the angular frequency, θ is the phase difference between the voltage and the current, V_m and I_m are the maximum voltage and current in the modulated signal respectively. Impedance is more commonly expressed in complex form:

Equation 2.15

$$\mathrm{Z}(\omega) = \mathrm{Z}' + \mathrm{jZ}''$$

$$\mathrm{Re(Z)} \equiv \mathrm{Z}' = |Z| \cos(\theta) \qquad \mathrm{Im(Z)} \equiv \mathrm{Z}'' = |Z| \sin(\theta)$$

Impedance data are usually presented in Nyquist plot and Bode plot. In a Nyquist plot, the real part of the impedance is plotted on the X-axis and the imaginary part is plotted on the Y-axis. The frequency of which the measurement was taken does not show on in the Nyquist plot unless annotated separately. In a Bode plot, the log of the frequency is plotted on the X-axis and both the absolute value of the impedance |Z| and the phase shift θ are plotted on the Y-axis.

The impedance data were fitted with equivalent circuits to obtain useful information such as series resistance, parallel resistance and parallel capacitance. Examples of equivalent circuits used in CZTS(e) devices[19-23] are shown in Figure 2.12.

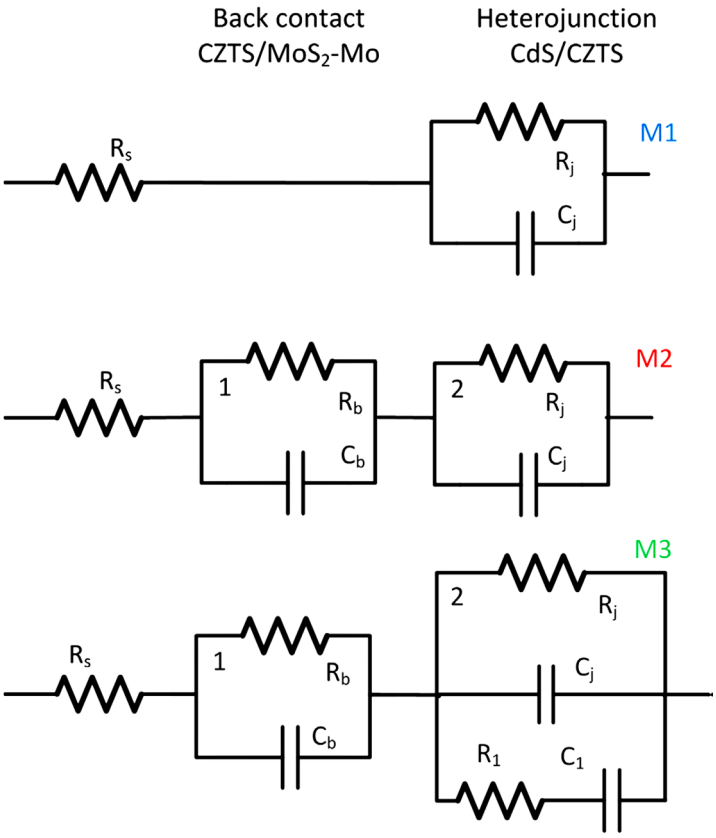

Figure 2.12 Equivalent circuits for fitting impedance data in CZTS(e) thin film and device. Reproduced from Fernandes *et al.*[19]

Reference

1. Goldstein, J.I., Newbury, D.E., Echlin, P., Joy, D.C., Lyman, C.E., Lifshin, E., Sawyer, L., and Michael, J.R., *Generation of X-Rays in the SEM Specimen*, in *Scanning Electron Microscopy and X-ray Microanalysis: Third Edition*. 2003, Springer US: Boston, MA. p. 271-296.
2. Abou-Ras, D., Nichterwitz, M., Romero, M.J., and Schmidt, S.S., *Electron Microscopy on Thin Films for Solar Cells*, in *Advanced Characterization Techniques for Thin Film Solar Cells*. 2011.
3. Goldstein, J.I., Newbury, D.E., Joy, D.C., Echlin, P., Lyman, C.E., Lifshin, E., Sawyer, L., and Michael, J.R., *Scanning Electron Microscopy and X-ray Microanalysis: Third Edition*. 2003: Springer US.
4. Schorr, S., Stephan, C., Törndahl, T., and Mainz, R., *X-Ray and Neutron Diffraction on Materials for Thin-Film Solar Cells*, in *Advanced Characterization Techniques for Thin Film Solar Cells*. 2011.
5. Bragg, W.H. and Bragg, W.L., *The Reflection of X-rays by Crystals.* Proceedings of the Royal Society of London. Series A, 1913. **88**(605): p. 428-438.
6. Templeton, D., *X-ray dispersion effects in crystal-structure determinations.* Acta Crystallographica, 1955. **8**(12): p. 842.
7. Merritt, E.A. *Anomalous Scattering Coefficients*. 2011; Available from: http://skuld.bmsc.washington.edu/scatter/AS_form.html.
8. Cromer, D., *Anomalous dispersion corrections computed from self-consistent field relativistic Dirac-Slater wave functions.* Acta Crystallographica, 1965. **18**(1): p. 17-23.
9. Cromer, D.T. and Liberman, D.A., *Relativistic Calculation of Anomalous Scattering Factors for X Rays.* The Journal of Chemical Physics, 1970. **53**(5): p. 1891-1898.
10. Cromer, D.T. and Liberman, D.A., *Anomalous dispersion calculations near to and on the long-wavelength side of an absorption edge.* Acta Crystallographica Section A, 1981. **37**(2): p. 267-268.
11. Clegg, W., *Crystal Structure Determination*. 1998: Oxford University Press, Incorporated.
12. Álvarez-García, J., Izquierdo-Roca, V., and Pérez-Rodríguez, A., *Raman Spectroscopy on Thin Films for Solar Cells*, in *Advanced Characterization Techniques for Thin Film Solar Cells*. 2011.
13. Schroder, D.K., *Optical Characterization*, in *Semiconductor Material and Device Characterization*. 2005.
14. Woollam, J.A., Hilfiker, J.N., and Synowicki, R.A., *Ellipsometry, Variable Angle Spectroscopic*, in *Wiley Encyclopedia of Electrical and Electronics Engineering*. 2014.
15. Unold, T. and Gütay, L., *Photoluminescence Analysis of Thin-Film Solar Cells*, in *Advanced Characterization Techniques for Thin Film Solar Cells*. 2011.
16. Kirchartz, T., Ding, K., and Rau, U., *Fundamental Electrical Characterization of Thin-Film Solar Cells*, in *Advanced Characterization Techniques for Thin Film Solar Cells*. 2011.
17. Braña, A.F., Forniés, E., López, N., and García, B.J., *High Efficiency Si Solar Cells Characterization Using Impedance Spectroscopy Analysis.* Journal of Physics: Conference Series, 2015. **647**(1): p. 012069.

18. Macdonald, J.R. and Johnson, W.B., *Fundamentals of Impedance Spectroscopy*, in *Impedance Spectroscopy*. 2005, John Wiley & Sons, Inc. p. 1-26.
19. Fernandes, P.A., Salomé, P.M.P., Sartori, A.F., Malaquias, J., da Cunha, A.F., Schubert, B.-A., González, J.C., and Ribeiro, G.M., *Effects of sulphurization time on Cu_2ZnSnS_4 absorbers and thin films solar cells obtained from metallic precursors.* Solar Energy Materials and Solar Cells, 2013. **115**: p. 157-165.
20. Fernandes, P.A., Sartori, A.F., Salome, P.M.P., Malaquias, J., Cunha, A.F.d., Graca, M.P.F., and Gonzalez, J.C., *Admittance spectroscopy of Cu_2ZnSnS_4 based thin film solar cells.* Applied Physics Letters, 2012. **100**(23): p. 233504.
21. Huang, S., Luo, W., and Zou, Z., *Band positions and photoelectrochemical properties of Cu_2ZnSnS_4 thin films by the ultrasonic spray pyrolysis method.* Journal of Physics D-Applied Physics, 2013. **46**(23).
22. Hou, Y., Azimi, H., Gasparini, N., Salvador, M., Chen, W., Khanzada, L.S., Brandl, M., Hock, R., and Brabec, C.J., *Low-Temperature Solution-Processed Kesterite Solar Cell Based on in Situ Deposition of Ultrathin Absorber Layer.* Acs Applied Materials & Interfaces, 2015. **7**(38): p. 21100-21106.
23. Kask, E., Krustok, J., Giraldo, S., Neuschitzer, M., López-Marino, S., and Saucedo, E., *Temperature dependent electrical characterization of thin film $Cu_2ZnSnSe_4$ solar cells.* Journal of Physics D: Applied Physics, 2016. **49**(8): p. 085101.

3 Experimental methods

Materials: Copper powder (Cu, 99.7%), copper(II) nitrate hemi(pentahydrate) ($Cu(NO_3)_2 \cdot 2.5H_2O$, 98%), copper(II) acetate monohydrate ($Cu(OAc)_2 \cdot H_2O$, ≥99.0%), zinc(II) nitrate hexahydrate ($Zn(NO_3)_2 \cdot 6H_2O$, 98%), tin(II) chloride ($SnCl_2$, 98%), tin(II) chloride dehydrate ($SnCl_2 \cdot 2H_2O$, 99.99%), bismuth(III) nitrate pentahydrate ($Bi_2(NO_3)_3 \cdot 5H_2O$, ≥98.0%), iodine (99.999%), sodium iodide (99+%), sodium sulfide nonahydrate ($Na_2S \cdot 9H_2O$, ≥98.0%), sodium acetate trihydrate ($Na(OAc) \cdot 3H_2O$, ≥99%), thioacetamide (≥99.0%), thioglycolic acid (≥99%), propan-2-ol (laboratory reagent grade), hydrogen peroxide solution (H_2O_2, 30% w/w in H_2O), hydrochloric acid (HCl, 37%), sulphuric acid (H_2SO_4, 95.0-98.0%), nitric acid (HNO_3, ≥65%), acetic acid (99.8-100.5%), dimethyl sulfoxide (DMSO, 99.9%) and 2-methoxyethanol (≥99.3%) were purchased from Sigma Aldrich. Zinc powder (Zn, 99.9%), tin powder (Sn, 99.85%), silver powder (Ag, 99.9%), high purity copper powder (Cu, 99.999%), high purity tin powder (Sn, 99.995%), sulphur (S, 99.999%), copper(I) sulphide (Cu_2S, 99.5), and zinc(II) sulphide (ZnS, 99.99%) were purchased from Alfa Aesar. High purity zinc powder (Zn, 99.999%) was purchased from Acros. Thiourea (99%) and potassium cyanide (KCN, 97%) were purchased from Fisher Chemical. All reagents were used as received. For elemental Cu, Zn and Sn, all experiments used the less pure metals unless otherwise stated.

Sealed tubes: The silica ampoules had internal diameter (ID) of 10 mm initially and were increased to 21 mm. The length of the ampoules were 100 mm. After charging the ampoule with reactants, it was put under vacuum for at least one hour before sealing off.

3.1 Synthesis

3.1.1 Synthesis of CZTS

3.1.1.1 Solid state and melting growth synthesis

The synthetic conditions for all solid state and melting growth syntheses of CZTS are summarised in Table 3.1. Elemental Cu, Zn, Sn and S with stoichiometric composition (Cu:Zn:Sn:S = 2:1:1:4) or Zn-rich Cu-poor composition (Cu:Zn:Sn:S = 1.8:1.2:1:4) were charged into silica ampoules. Up to 40% excess sulphur were added in some

syntheses. Syntheses using high purity metals (>99.995%) were also carried out towards the end of the study. The powder mixture was mixed in a Fritsch pulverisette 23 vibratory ball mill for 15 minutes in an Ar-filled glovebox for all the later reactions. The reactions were carried out at 750 °C in a box furnace for 7 days with a heating rate of 300 °C/hour. Reactions were also carried out under different temperatures and durations during preliminary work. At the end of the synthesis, the furnace was switched off so that the product was cooled down 'naturally' inside the furnace overnight. The ampoules in a number of reactions were quenched in ice water at the end of the synthesis to investigate Cu/Zn disorder in CZTS. Experiments using both commercial ZnS and home-made CuS, SnS and/or Cu_2SnS_3 as precursors were also carried out.

Table 3.1 Synthetic conditions for the solid state and melting growth synthesis of CZTS. *The samples were quenched into ice water and grounded after the first 7 days, and then charged into a new ampoule and reacted for another 7 days.

Precursor composition	**Batch size / g**	**Temp. / °C**	**Duration / day**
Stoichiometric with 25% excess S	8	550	14
Stoichiometric	2	750	*7(q) + 7
Zn-rich Cu poor	2	750	*7(q) + 7
Stoichiometric with 40% excess S	2	750	1
Stoichiometric with 25% excess S	8	750	14
Stoichiometric	5	750	14
Stoichiometric	16	750	7
Stoichiometric with 40% excess S	16	750	7
Stoichiometric	24	750	25
Zn-rich Cu poor	16	750	14
Home-made Cu_2SnS_3, commercial ZnS	5	750	7
Home-made Cu_2SnS_3, commercial ZnS with 40% excess S	5	750	7
Home-made CuS and SnS, commercial ZnS	8	750	7
Stoichiometric with 10% excess S	10	900	2
Zn-rich Cu-poor with 40% excess S	10	900	2
Stoichiometric	10	1100	1
Home-made CuS and SnS, commercial ZnS	10	1100	1

3.1.1.2 *Chemical vapour transport method*

Attempts to grow larger CZTS crystals were carried out using the chemical vapour transport method described by Colombara *et al.*[1] Between 5 and 10 g of solid state CZTS were used as-synthesised or ball milled before charging into a silica ampoule. The iodine load was 5 mg/cm^3 during preliminary work, and later increased to 20 mg/cm^3. Sodium iodide (1% w/w) was incorporated into one of the experiments. The syntheses were carried out in a four-zone horizontal tube furnace. Initial experiments were carried out using a two-step procedure illustrated in Figure 3.1. A strong temperature gradient was applied for 3 days with temperatures of 910 °C and 815 °C in the hot zone and cold zone respectively (Figure 3.1a). Precursor materials were located in the hot zone. After 3 days, a reversed temperature gradient at temperatures of 815 and 880 °C was applied in the original hot and cold zone respectively for 7 days (Figure 3.1b). Later experiments used a one-step procedure where the hot zone was 910 °C and the cold zone was 755 °C. The one-step reactions lasted between 4 and 14 days. The cooling step for all chemical vapour transport reactions were carried out naturally.

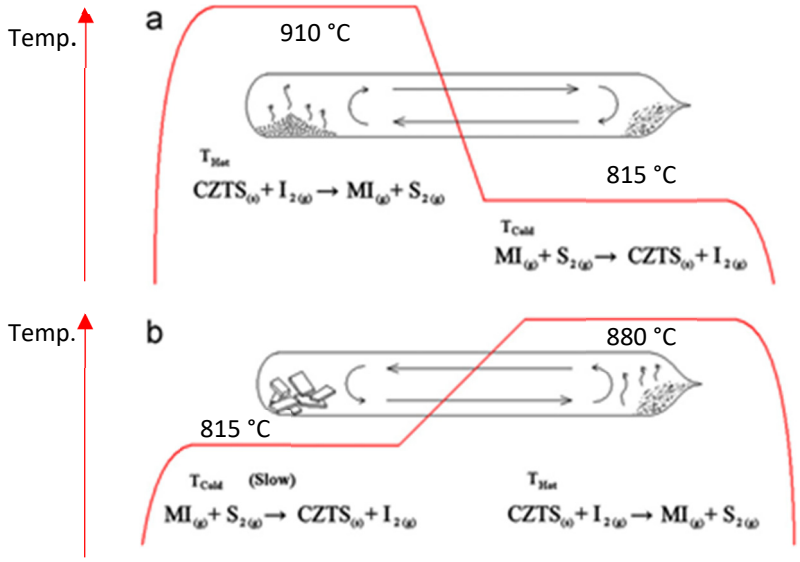

Figure 3.1 Schematic of a two-step chemical vapour transport synthesis of CZTS. Reproduced from Colombara *et al.*[1]

3.1.1.3 *Hydrothermal and solution synthesis*

CZTS were also synthesised via the hydrothermal and solution method using stoichiometric amount of $Cu(NO_3)_2{\cdot}2.5H_2O$ (0.2 M), $Zn(NO_3)_2{\cdot}6H_2O$ (0.1 M),

$SnCl_2 \cdot 2H_2O$ (0.1 M) or $SnCl_2$ (0.1 M), and thiourea (0.4 M). In the hydrothermal synthesis, the precursors were mixed and dissolved in 60 ml of deionised water before transferring into Teflon-lined stainless steel autoclave. A small amount of HCl (2.5 ml) was added to dissolve $SnCl_2$. Reactions were carried out at 180 °C for 1 day. In solution synthesis, the precursors were dissolved in 100 ml of propan-2-ol or dimethyl sulfoxide (DMSO). The reactions were carried out in a round bottom flask on a 120 °C hotplate until all the solvent evaporated. The products from both hydrothermal and solution synthesis were washed several times in deionised water before drying in a 280 °C oven.

3.1.2 Synthesis of CuS

The synthetic conditions for CuS is summarised in Table 3.2. CuS was prepared according to a solid state synthetic route described by Dutrizac *et al.*[2] 10 g of stoichiometric amount of Cu and S were charged into a silica ampoule. The synthesis was carried out at 450 °C for 1 day.

CuS was also synthesised via the hydrothermal method. Stoichiometric amounts of $Cu(OAc)_2 \cdot H_2O$ was mixed with thioacetamide, and dissolved in 60 ml of deionised water before transferring the solution into Teflon-lined stainless steel autoclave. Reactions were carried out at 180 °C for 3 days. One of the reactions was carried out at 175 °C. The products were filtered and washed with both deionised water and ethanol three times before drying in a drying oven.

Table 3.2 Synthetic conditions for the solid state and hydrothermal synthesis of CuS.

Cu precursor	**S precursor**	**Reaction condition**	**Batch size / g**
Cu	S	1 day 450 °C	10
1 M $Cu(OAc)_2 \cdot H_2O$	Thioacetamide (25% excess)	3 day 180 °C	5.7
1 M $Cu(OAc)_2 \cdot H_2O$	Thioacetamide (25% excess)	3 day 175 °C	5.7

3.1.3 Synthesis of SnS and SnS_2

The synthetic conditions for SnS and SnS_2 are summarised in Table 3.3. SnS and SnS_2 were prepared according to solid state synthetic routes described by Sorgenfrei *et al.*[3] and Gnana Kumar *et al.*[4] 8 – 10 g of stoichiometric amount of Sn and S were

charged into a silica ampoule. 25% excess sulphur was used in SnS_2 synthesis. SnS was synthesised at 900 °C for 1 day, while SnS_2 was synthesised at 820 °C for 2 days.

SnS and SnS_2 were also synthesised via the hydrothermal method, similar to that described for CuS in Chapter 3.1.2, using $SnCl_2{\cdot}2H_2O$ and thiourea as the precursors. Up to 25% excess of thiourea were used in some reactions. Reactions were carried out at 180 °C for 1 day.

Table 3.3 Synthetic conditions for the solid state and hydrothermal synthesis of SnS and SnS_2.

Sn precursor	S precursor	Reaction condition	Batch size / g
Sn	S	1 day 950 °C	10
Sn	S (125% excess)	2 day 820 °C	8
$SnCl_2{\cdot}2H_2O$	Thiourea	1 day 180 °C	1.8
$SnCl_2{\cdot}2H_2O$	Thiourea (100% excess)	1 day 180 °C	2.2

3.1.4 Synthesis of Cu_2SnS_3

The synthetic conditions for Cu_2SnS_3 is summarised in Table 3.4. Cu_2SnS_3 was prepared according to a synthetic route described by Chen *et al.*[5] 8 – 10 g of stoichiometric amounts of Cu, Sn and S were charged into a silica ampoule with 0, 20 or 50% excess sulphur. The reactions were carried out at 900 or 1050 °C for 2 days. A sintering step at 700 °C was carried out for 1 – 2 days in batches where the synthetic temperature was 1050 °C.

Dry powder reaction of Cu_2SnS_3 was based on the one described by Tiwari *et al.*[6] Stoichiometric amounts of $Cu(OAc)_2{\cdot}H_2O$, $SnCl_2{\cdot}2H_2O$ and thiourea were ground together and mixed well with a mortar and pestle before transferring into a ceramic crucible. The reaction mixture was placed in a 200 °C oven for 1 hour.

In the solution reaction, stoichiometric amounts of Cu_2SnS_3, $Cu(OAc)_2{\cdot}H_2O$, $SnCl_2{\cdot}2H_2O$ and thiourea were dissolved in 2-methoxyethanol and refluxed overnight. The product was washed and filtered twice using toluene and deionised water, and finally annealed at 280 °C in air.

The hydrothermal synthesis of Cu_2SnS_3 followed a similar process to that used for CuS as described in Chapter 3.1.2, using stoichiometric amounts of $Cu(OAc)_2{\cdot}H_2O$,

$SnCl_2 \cdot 2H_2O$ and thioacetamide as the precursors. In one of the batches, the Cu and Sn precursors were dissolved in water and aged overnight before the addition of thiourea. The hydrothermal reactions were carried out at 180 °C for 1 day.

Attempts to grow larger Cu_2SnS_3 crystals were also carried out using chemical vapour transport method similar to that used for CZTS described in Chapter 3.1.1.2. Cu_2SnS_3 synthesised from the solid state reaction was used as the precursor. An iodine load of 20 mg cm^{-3} was used. The following temperature gradients were applied: hot zone between 710 and 910 °C; cold zone between 555 and 755 °C.

Table 3.4 Synthetic conditions for Cu_2SnS_3 using different synthetic methods.

Precursors	Reaction condition	Batch size / g
Cu, Sn, S	2 day 1050 °C, then 2 day 700 °C	10
Cu, Sn, S (50% excess)	2 day 1050 °C, then 1 day 700 °C	8
Cu, Sn, S (20% excess)	2 day 900 °C	10
$Cu(OAc)_2 \cdot H_2O$, $SnCl_2 \cdot 2H_2O$, thiourea	Powder only, 1 hour 200 °C	10
$Cu(OAc)_2 \cdot H_2O$, $SnCl_2 \cdot 2H_2O$, thiourea	Reflux in 2-Methoxyethanol	3.5
$Cu(OAc)_2 \cdot H_2O$, $SnCl_2 \cdot 2H_2O$, thioacetamide	Metal salts sol^n aged overnight. Then hydrothermal 1 day 180 °C	2
$Cu(OAc)_2 \cdot H_2O$, $SnCl_2 \cdot 2H_2O$, thioacetamide	Hydrothermal 1 day 180 °C	2
Cu_2SnS_3, 20 mg cm^{-3} I_2	Temperature gradient. Hot: 910 °C Cold: 755 °C	4
Cu_2SnS_3, 20 mg cm^{-3} I_2	Temperature gradient. Hot: 810 °C Cold: 655 °C	4
Cu_2SnS_3, 20 mg cm^{-3} I_2	Temperature gradient. Hot: 710 °C Cold: 555 °C	4

3.1.5 Synthesis of Bi_2S_3

The synthetic conditions for Bi_2S_3 is summarised in Table 3.5. Bi_2S_3 was synthesised using hydrothermal reaction. 0.2 – 0.4M of $Bi_2(NO_3)_3 \cdot 5H_2O$ and 25% excess of a sulphur precursor, including thiourea, thioacetamide, thioglycolic acid and sodium sulphide nonahydrate, were dissolved in 60 ml of deionised water, ethanol, propan-2-ol, acetone or dilute nitric acid before transferring into Teflon-lined stainless steel autoclave. Reactions were carried out at 130 or 170 °C for 1 day. All products were

filtered and washed with deionised water and ethanol a few times before drying in a drying oven.

Table 3.5 Synthetic conditions for the hydrothermal synthesis of Bi_2S_3.

S precursor	Solvent	Reaction condition	Batch size / g
Thiourea	Deionised water	1 day 170 °C	6.2
Thiourea	Deionised water	1 day 130 °C	6.2
Thiourea	Ethanol	1 day 130 °C	3.1
Thiourea	Propan-2-ol	1 day 130 °C	3.1
Thiourea	Acetone	1 day 130 °C	3.1
Thiourea	Dilute nitric acid	1 day 130 °C	3.1
Thioacetamide	Deionised water	1 day 130 °C	6.2
Thioglycolic acid	Deionised water	1 day 130 °C	6.2
$Na_2S{\cdot}9H_2O$	Deionised water	1 day 130 °C	3.1

3.1.6 Synthesis of Ag_2ZnSnS_4 (AZTS)

Ag_2ZnSnS_4 was prepared using solid state reaction comparable to the one used in CZTS in Chapter 3.1.1.1. 8 g of stoichiometric amount of Ag, Zn, Sn and 10% excess S were mixed briefly in a vibratory ball mill before charging into a silica ampoule. The reactions were carried out at 750 or 600 °C for 14 days in a box furnace and cooled down naturally.

Attempts to grow larger AZTS crystals were carried out using chemical vapour transport (CVT) method similar to the one used in CZTS in Chapter 3.1.1.2. 8 g of solid state AZTS were charged into a silica ampoule. The iodine load was 40 mg/cm^3. The reactions were carried out in a four-zone horizontal tube furnace for 7 days where the hot zone was between 650 and 750 °C, and the cold zone was between 580 and 650 °C. The reactions were cooled naturally at the end of the synthesis.

3.2 Characterisation

3.2.1 Powder X-ray diffraction (PXRD)

PXRD patterns were recorded on a Siemens Diffractometer D5000 at room temperature operating with Cu-K_α radiation (λ = 1.5406 Å, 40 kV, 30 mA) using a plastic sample holder. Patterns were recorded between 2θ angles of 10° and 80° with

a scan rate of 0.02° per second. Experimental patterns were compared with standard patterns from a database visibly to view and identify phase purity.

3.2.2 Single crystal X-ray diffraction (SCXRD)

Single crystal X-ray diffraction data were collected on an Agilent Xcalibur at room temperature operating with Mo-K_α radiation (λ = 0.71073 Å). Structures were solved and refined using JANA2006[7] by direct method.

3.2.3 Single crystal neutron diffraction

CZTS crystals with sizes between 9 – 25 mm^2 on one plane were selected, placed inside evacuated sealed tubes and annealed in the range of 110 to 300 °C for two months before quenching in ice water. The diffraction pattern of these crystals were briefly screened in a single crystal X-ray diffractometer to inspect the quality of the patterns prior to the neutron diffraction experiments.

Single crystal neutron diffraction data were collected at room temperature at 0.8386 Å (Institut Laue-Langevin (ILL) beamline D9). Neutrons were produced through fission in a nuclear reactor. The diffractometer adapts a standard four-circle configuration similar to the one shown in Figure 3.2. Data were acquired for 20 ± 2 hours per sample, and over 400 reflections were typically recorded. Structures were solved and refined using JANA2006[7] by direct method with SCXRD data of the same crystal simultaneously.

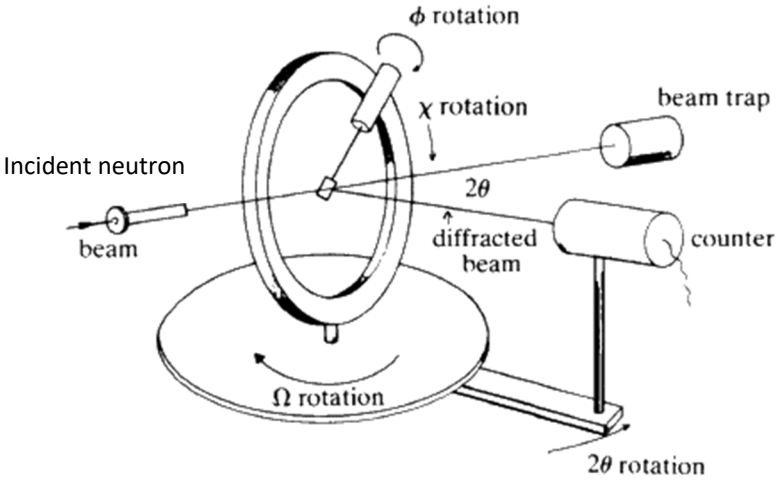

Figure 3.2 Schematic of a four circle diffractometer that was used in the single crystal neutron diffraction experiment. Image courtesy of the International Union of Crystallography.

3.2.4 Powder anomalous X-ray diffraction

Stoichiometric CZTS samples grown using solid state were reannealed in the range of 450 to 700 K for 20 hours before quenching in ambient. Powder anomalous X-ray diffraction data were collected at room temperature near Cu-K_α absorption edge (1.382144(5) Å), near Zn-K_α absorption edge (1.285375(5) Å), and far from the edges (0.825827(4) Å) (Diamond Light Source beamline I11). The source is a synchrotron radiation source produced by in-vacuum undulators. The required wavelengths were controlled by a double-crystal monochromator. The powder patterns were recorded between 2θ values of 0 and 150° with a resolution of 0.001° and a scan rate of 0.08°/s. Structures were refined using TOPAS-academic V5.[8]

3.2.5 Elemental composition

Elemental composition and morphology were analysed with an INCA XACT X-ray EDS system connected to a Jeol 6480LV SEM at 20 kV. The elemental composition of a number of batches were also analysed using atomic absorption spectroscopy (AAS) and/or X-ray fluorescence (XRF). AAS samples were prepared by dissolving 20 mg of CZTS in concentrate aqua regia overnight before diluting with high purity deionised water (18 MΩ). AAS was carried out using a Perkin Elmer AAnalyst 100 Flame Atomic Absorption Spectrometer calibrated with Cu, Zn, Sn and Na standards. XRF samples were polished using 1 µm and 0.3 µm alumina paste with a polishing pad. XRF was carried out using a Hitachi SEA6000VX instrument using a Rh X-ray tube, and calibrated with ZnS, brass, and tin standards. Measurements were carried out using a spot size of 0.5 × 0.5 mm at 50 kV over 300 seconds.

3.2.6 Raman spectroscopy

Raman spectroscopy was performed at room temperature under ambient atmosphere using a Renishaw inVia Raman microscope equipped with a 532 and 785 nm incident lasers. Prior to the measurements, the system was calibrated with a Si standard at 520 cm^{-1}.

Resonance Raman spectroscopy was performed to investigate Cu/Zn disorder in CZTS in relate to the annealing temperature. CZTS samples were single crystals with Zn-rich Cu-poor composition grown using chemical vapour transport detailed in section 3.1.1.2. The crystals were first annealed at 300 °C for one hour in a tube furnace

under nitrogen flow and quenched in ice water to induce Cu/Zn total disorder deliberately. The crystals were then reannealed in the range of 110 to 275 °C for between 1 and 1000 hours before quenching in ice water.

3.2.7 Spectroscopic ellipsometry

CZTS crystals were mounted in epoxy resin and Telfon as shown in Figure 3.3, and polished to 1 µm using alumina paste. Ellipsometry spectra were recorded with a J. A. Woollam M2000U-Xe rotating compensator ellipsometer with focusing optics that gave a 150 µm wide spot. Measurements were carried out over a spectral range of 245 to 1690 nm (0.734 to 5.044 eV) at three angles of incidences (45, 55 and 65°). The resulting data were analysed using the computer program CompleteEASE.[9]

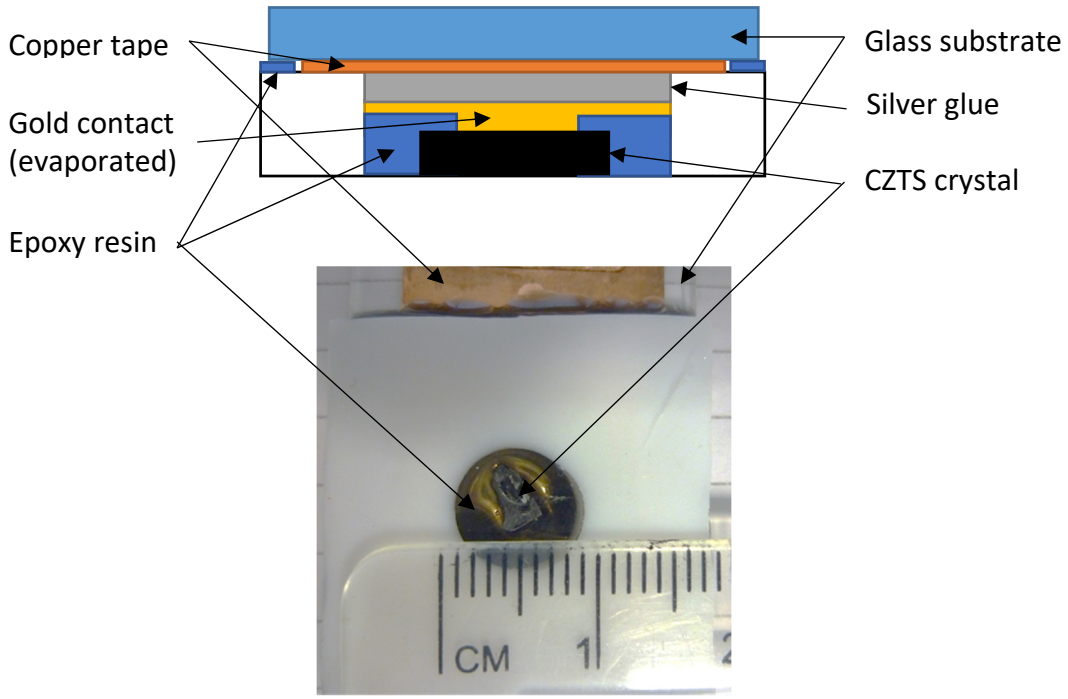

Figure 3.3 A schematic of the cross-section and a photographic image of an embedded CZTS crystal for ellipsometry, photoluminescence (PL), external quantum efficiency (EQE) and electrolyte electroreflectance (EER) measurements.

3.2.8 Photoluminescence (PL)

PL spectra were recorded in a homebuilt set up. A green continuous wave (CW) argon laser (514 nm) was used with power between 1 and 30 mW and a spot size of 100 µm. The spectra were measured between 550 and 1050 nm with a Si detector and

between 900 and 1250 nm with an InGaAs detector. High pass filters of 550 nm and 850 nm were used to exclude laser light and second order light respectively.

3.2.9 External Quantum Efficiency (EQE) measurements

A simplified schematic of the EQE measurement setup is shown in Figure 3.4. Chopped collimated illumination was provided by a tungsten lamp and Bentham Instruments grating monochromator with a variable frequency mechanical chopper operating at 27 Hz. The spectra were measured between 350 and 950 nm. The spot size of the illumination was controlled by image slits and was chosen to be smaller than the smallest dimension of the crystals to ensure that all light fell on the crystal surface. The setup was calibrated using a calibrated silicon photodiode traceable ±5% to NBS standards. The photocurrent was detected by a Stanford Research lock-in amplifier.

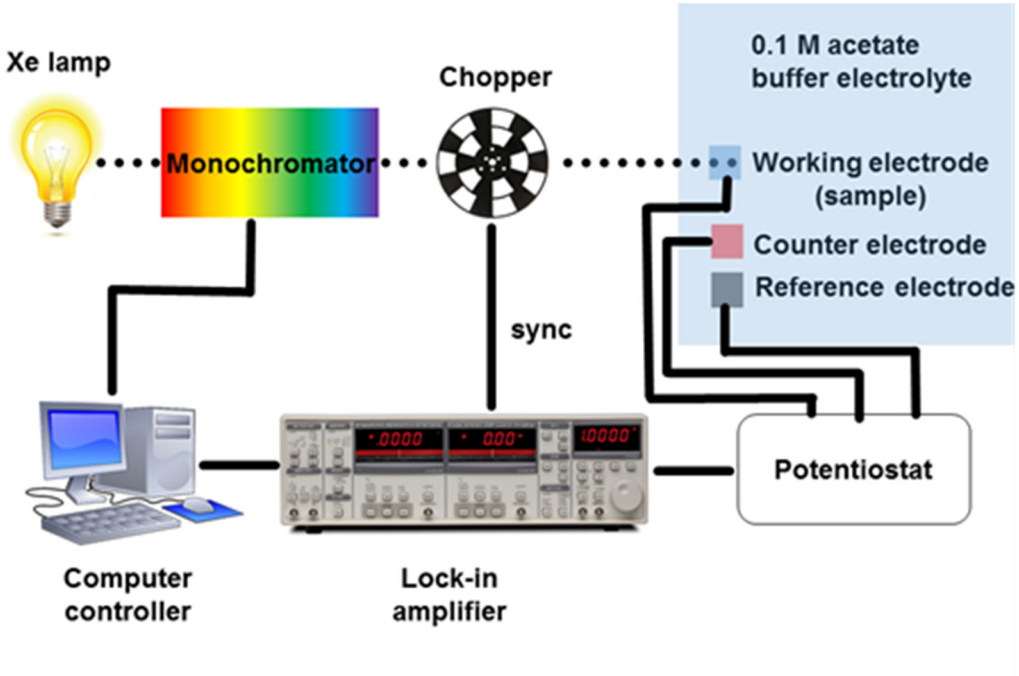

Figure 3.4 A simplified schematic of the EQE measurement setup.

Embedded CZTS samples were etched in saturated Na_2S solution followed by 30% H_2O_2/1 M H_2SO_4. After rinsing, the samples were treated with 1M HCl, to remove metal (hydr)oxides. EQE measurements were then made using an air-saturated 0.1 M acetate buffer electrolyte (pH 4.5) in a 3-electrode cell with Pt counter and

Ag|AgCl reference electrodes controlled by a battery-operated low-noise potentiostat.

3.2.10 Current-Voltage (J-V) measurements

JV performance was measured under AM 1.5 condition with a home-build automated scanner using a Keithley 2400 source measurement unit.

Staircase voltammetry was carried out in the dark and under illumination of a red LED lamp using an Autolab PGSTAT30 Potentiostat at 0.1 V s^{-1}.

3.2.11 Impedance measurements

Impedance measurement was carried out in the dark and under illumination of a red LED lamp using an Autolab PGSTAT30 Potentiostat. The frequency of the ac signal was between 1 MHz – 1 Hz, with amplitude set to 10 mV. The applied dc voltage was between -1.0 to 1.0 V in the dark, and at the open circuit potential under illumination. The impedance data were fitted with equivalent circuits using computer program ZPlot.[10]

3.2.12 Ultraviolet–visible (UV-Vis) spectroscopy

UV-Vis spectroscopy was performed using a PerkinElmer UV-Vis-NIR Spectrometer Lambda 750 S instrument. The absorbance of the samples were recorded between 600 and 1600 nm with deuterium light source (< 860 nm) and tungsten halogen light source (> 860 nm) at a scan rate of 2 nm per second.

3.2.13 Thermogravimetric analysis (TGA) and differential scanning calorimetry (DSC)

TGA and DSC were carried out with a PL-STA module (Polymer Laboratories, Thermal Science Division) under ambient atmosphere between room temperature and 700 °C with a heating rate of 5 °C/min.

3.3 Fabrication of single crystal CZTS device

CZTS single crystals were grown using chemical vapour transport detailed in Chapter 3.1.1.2. The crystals were embedded similar to the one shown in Figure 3.3 without the glass substrate and evaporated gold contact. The back contact was sputtered with Mo. The front of the crystals were etched in saturated Na_2S solution for 30 seconds followed by 30% H_2O_2/1 M H_2SO_4 for 300 seconds. A CdS buffer layer was

deposited immediately after etching using the chemical bath method described elsewhere,[11] to avoid any possible degradation by contact with air.[11] i-ZnO and Al:ZnO were then deposited by RF-magnetron sputtering. Ni-Al grids were finally deposited by e-beam evaporation for front contacting.

Reference

1. Colombara, D., Delsante, S., Borzone, G., Mitchels, J.M., Molloy, K.C., Thomas, L.H., Mendis, B.G., Cummings, C.Y., Marken, F., and Peter, L.M., *Crystal growth of Cu_2ZnSnS_4 solar cell absorber by chemical vapor transport with I_2.* Journal of Crystal Growth, 2013. **364**: p. 101-110.
2. Dutrizac, J.E. and Macdonal.Rj, *Synthesis of Some Copper Sulfides and Copper Sulfosalts in 500-700 Gram Quantities.* Materials Research Bulletin, 1973. **8**(8): p. 961-971.
3. Sorgenfrei, T., Hofherr, F., Jauß, T., and Cröll, A., *Synthesis and single crystal growth of SnS by the Bridgman-Stockbarger technique.* Crystal Research and Technology, 2013. **48**(4): p. 193-199.
4. Gnana Kumar, G., Reddy, K., Nahm, K.S., Angulakshmi, N., and Manuel Stephan, A., *Synthesis and electrochemical properties of SnS as possible anode material for lithium batteries.* Journal of Physics and Chemistry of Solids, 2012. **73**(9): p. 1187-1190.
5. Chen, X.A., Wada, H., Sato, A., and Mieno, M., *Synthesis, electrical conductivity, and crystal structure of Cu4Sn7S16 and structure refinement of Cu2SnS3.* Journal of Solid State Chemistry, 1998. **139**(1): p. 144-151.
6. Tiwari, D., Chaudhuri, T.K., Shripathi, T., and Deshpande, U., *Synthesis of earth-abundant Cu_2SnS_3 powder using solid state reaction.* Journal of Physics and Chemistry of Solids, 2014. **75**(3): p. 410-415.
7. Petříček, V., Dušek, M., and Palatinus, L., *Crystallographic Computing System JANA2006: General features*, in *Zeitschrift für Kristallographie - Crystalline Materials*. 2014. p. 345.
8. Coelho, A.A., Evans, J., Evans, I., Kern, A., and Parsons, S., *The TOPAS symbolic computation system.* Powder Diffraction, 2012. **26**(S1): p. S22-S25.
9. *CompleteEASE*, J. A. Woollam Co., Inc., 645 M Street, Suite 102, Lincoln, NE 68508.
10. *ZPlot*, Scribner Associates Inc., 150 East Connecticut Avenue, Southern Pines, North Carolina, USA 28387.
11. Colombara, D., Dale, P.J., Kissling, G.P., Peter, L.M., and Tombolato, S., *Photoelectrochemical Screening of Solar Cell Absorber Layers: Electron Transfer Kinetics and Surface Stabilization.* The Journal of Physical Chemistry C, 2016. **120**(29): p. 15956-15965.

4 Synthesis and phase determination of single and poly-crystalline CZTS

This chapter details the efforts to synthesise phase pure CZTS using a variety of methods, including high temperature methods such as solid state synthesis, melting growth method, and chemical vapour transport method; and low temperature methods such as hydrothermal synthesis and solution synthesis. The phase purity and elemental composition of the products were analysed using scanning electron microscope (SEM) with energy-dispersive X-ray spectroscopy (EDS), Raman spectroscopy, atomic absorption spectroscopy (AAS) and/or X-ray fluorescence (XRF).

4.1 Results and discussion

4.1.1 Solid state and melting growth synthesis

The first few attempts to grow CZTS crystals were carried out according to the procedures comparable to those previously reported as shown in Table 4.1. The difference between the solid state and the melting growth method is that the reaction temperature in the melting growth method is higher than the melting point of CZTS, *i.e.* 990 °C. Various secondary phases were observed visually by eye (*i.e.* the distinctive blue colour of CuS), or under SEM with EDS.

Table 4.1 A summary of results of first few attempts to glow polycrystalline CZTS from solid state and melting growth methods. The presence of secondary phases were assessed by SEM with EDS. (q) denotes the sample was quenched into ice water and grounded after the first 7 days.

Precursor composition	**Batch size / g**	**Temp / °C**	**Duration / day**	**Product composition** $\frac{Cu}{Zn+Sn}$	$\frac{Zn}{Sn}$	$\frac{S}{metals}$	**Secondary phase**	**Ref.**
Stoichiometric	2	750	7(q) + 7	0.99	0.99	1.03	None observed	[1, 2]
Zn-rich Cu- poor	2	750	7(q) + 7	0.85	1.05	1.07	None observed	[1, 2]
40% excess S	2	750	1	1.01	0.86	1.08	ZnS	[3]
Stoichiometric	10	1100	1	1.10	0.83	1.02	Cu_xS, ZnS, SnS	[4]
Home-made CuS and SnS, commercial ZnS	10	1100	1	1.11	1.24	0.86	CuS	

Since 14 days are needed to produce one batch of phase pure CZTS, the reaction was scaled up from 2 g to 10 g. However, ampoule explosions and implosions were

encountered. Explosions were most likely caused by the high vapour pressure of unreacted sulphur at high temperature, while implosions may be caused by the volume contraction of the final product which adhered to the ampoule during cooling. Since the vapour pressure of sulphur can be decreased if the sulphur reacted with the metals to form one of the secondary phases. Experiments were carried out with (i) a decrease in ramp rate to 200 °C/h; (ii) a decrease in ramp rate to 102 °C/h; and (iii) introducing a 2 hour pause at 500 °C, to allow sulphur to react with the metals thus reducing the amount and pressure of unreacted sulphur at high temperature. However, ampoule explosion still occurred. The solution to the problem was to increase the ampoule internal diameter from 10 mm to 21 mm, which subsequently increased the volume of the ampoule by at least four times. The largest batch obtained using ampoule with 21 mm internal diameter was 24 g.

Attempts were made to prevent formation of secondary phases by employing excess sulphur as suggested in the introduction chapter 1.4.4.2. Some reactions were also carried out at different temperatures (550 and 900 °C). However, these attempts have secondary phase compounds observed in SEM/EDS, as shown in Table 4.2. A photographic example (Figure 4.1) shows the formation of a secondary phase that can be visibly distinguished by the different colours (blue: CuS; orange: SnS_2) on the as-synthesised bulk material. Based on the information available, it can be suggested that the use of excess sulphur alone does not suppress the formation of secondary phase compounds. On the other hand, the presence of secondary phase compounds may indicate incomplete reaction due to larger batch size and shorter reaction time.

Table 4.2 A summary of results for the experiments attempted to suppress secondary phase formation in CZTS. The presence of secondary phases were assessed by SEM with EDS.

Precursor composition	**Batch size / g**	**Temp / °C**	**Duration / day**	**Product composition**			**Secondary phase**
				$\frac{Cu}{Zn+Sn}$	$\frac{Zn}{Sn}$	$\frac{S}{metals}$	
10% excess S	10	900	2	1.14	0.91	0.99	Cu_xS, ZnS
Zn-rich Cu-poor with 40% excess S	10	900	2	-	-	-	ZnS, SnS_2
25% excess S	8	550	14	0.98	0.94	1.02	ZnS, CTS
25% excess S	8	750	14	1.09	0.85	1.07	Cu_xS, ZnS, SnS_2

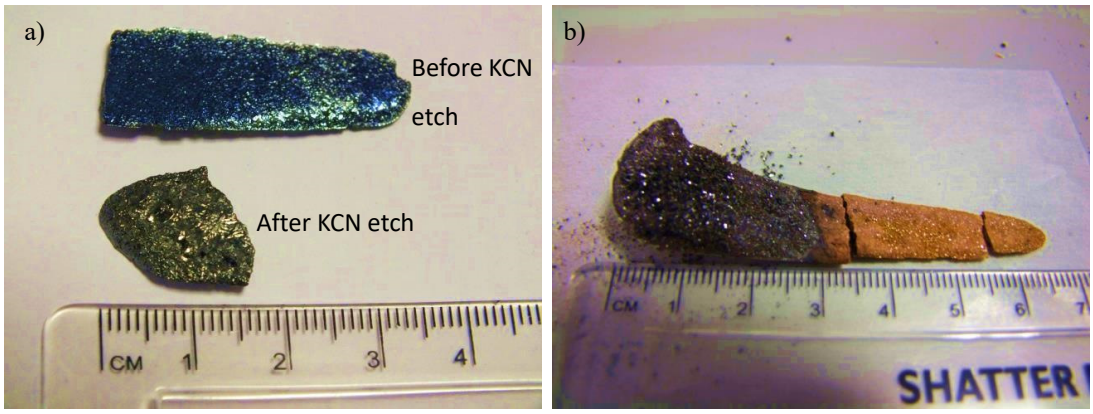

Figure 4.1 Photographic image showing CZTS synthesised from solid state reaction (a) 1 day 1100 °C before and after KCN etch (b) 15 days 750 °C with 25% excess sulphur.

In an attempt to remove the secondary phase from the as-synthesised material, an ingot was etched in 5% KCN solution in an ultrasonic bath for 30 minutes. The blue colour from the ingot disappeared, indicating the removal of CuS on the surface (Figure 4.1a). However, SEM/EDS analysis showed the etched ingot had different elemental composition across different area, such as ZnS zone, Sn poor zone, and Zn poor zone. Chemical etching of impure CZTS ingots was not investigated further.

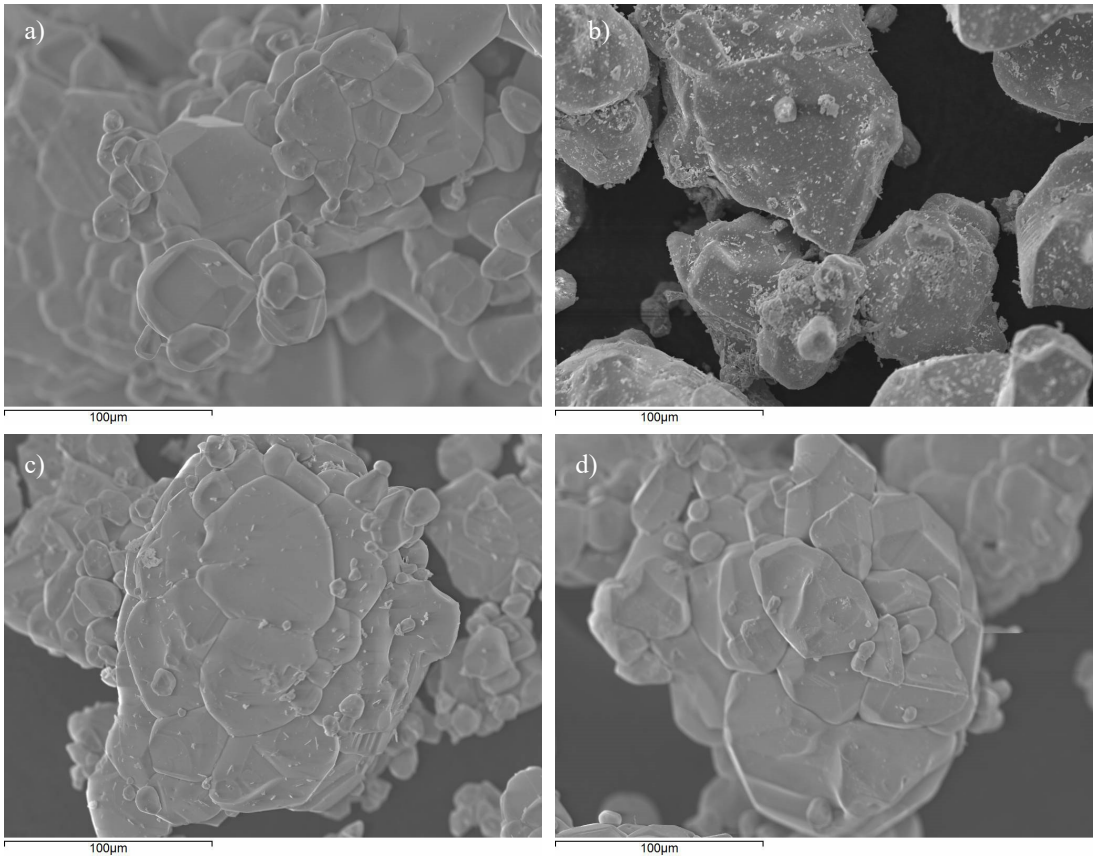

Figure 4.2 SEM images of polycrystalline CZTS synthesised with precursor ball milled before solid state reactions at 750 °C with these variations: (a) 14 days; (b) 14 days with ice quench; (c) 7 days; (d) 7 days with 40% excess sulphur.

In order to simplify the synthesis, the ice quenching step at day 7 was removed, and no change in the composition was observed in the final product. Repeats were also carried out using different batch sizes (5, 16 and 24 g) and different reaction durations (7, 14 and 25 days), with all details listed in Table 4.3. It is also noted that the precursors in these batches were mixed briefly (15 min, 30Hz) using a ball mill before the reactions were carried out. Some batches were quenched in ice water during the cooling step instead of cooling naturally in order to study Cu/Zn disorder, which is discussed in detail in Chapter 6. No secondary phases were observed using SEM/EDS and Raman spectroscopy in those reactions where the metal and sulphur precursors were ball milled, regardless of other experiment parameters such as excess sulphur, batch size, and duration. Examples of SEM images of these batches were included in Figure 4.2. Grains were packed together with an individual grain size of around 50 µm.

Table 4.3 A summary of results showing successful attempts to synthesise CZTS via solid state reaction using elemental precursors that were mixed by ball milling before the synthesis. The presence of secondary phases were assessed by SEM with EDS and Raman spectroscopy. (q) denoted the ampoule was ice quenched during cooling stage.

Precursor composition	**Batch size / g**	**Temp / °C**	**Duration / day**	**Product composition**			**Secondary phase**
				$\frac{Cu}{Zn+Sn}$	$\frac{Zn}{Sn}$	$\frac{S}{metals}$	
Stoichiometric	5	750	14	0.97	1.00	1.00	None observed
Stoichiometric	16	750	7	0.93	0.92	1.08	None observed
Stoichiometric	24	750(q)	25	0.91	0.94	1.12	None observed
40% excess S	16	750	7	0.94	0.92	1.13	None observed
$Cu_{1.8}Zn_{1.2}$	5	750	14	0.80	0.94	1.03	None observed
$Cu_{1.8}Zn_{1.2}$	16	750(q)	14	0.87	1.14	0.93	None observed

A representation of Raman spectra for CZTS synthesised via solid state reaction are shown in Figure 4.3. Raman peaks were fitted using Lorentzian curves following Valakh *et al.*[5] and Dimitrievska *et al.*[6], and is shown as colour solid lines in Figure 4.3. No peaks from secondary phases were observed. The Raman spectra near the resonance frequency of CZTS (785 nm) has shown a difference in peak intensity at 374, 365 and 286 cm^{-1} for batches cooled by ice quenching. This has been reported by Scragg *et al.*[7] and indicates a high level of disorder in the crystal structure, which is expected in fast cooling CZTS. Based on SEM/EDS and Raman data, it can be concluded that phase pure CZTS with stoichiometric and Zn-rich Cu poor composition can be obtained at 750 °C for 7 days or longer if the precursors were mixed briefly with a ball mill.

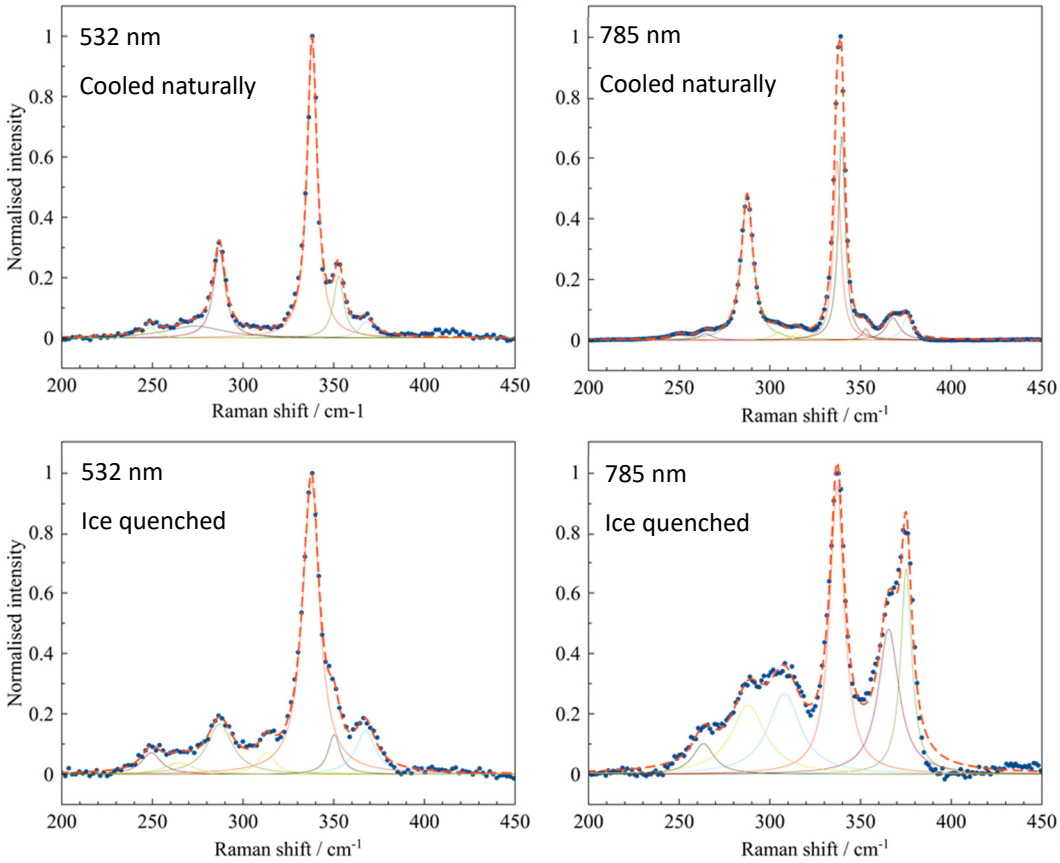

Figure 4.3 A representation of Raman spectra of CZTS synthesised from solid state reaction using elemental precursors. Top left: 532 nm, cooled naturally; top right: 785 nm, cooled naturally; bottom left: 532 nm, ice quenched; bottom right: 785 nm, ice quenched. Blue dots are the experimental data. Colour solid lines are Raman peaks fitted with Lorentzian curves. Red dashed line is the sum of the fitted curves.

CZTS synthesises were also carried out using CuS and SnS synthesised from hydrothermal reactions, post-KCN etched Cu_2SnS_3 synthesised from solid state reactions, and commercial ZnS detailed in Table 4.4. SEM images (Figure 4.4) show similar crystal morphology to batches synthesised using elemental precursors. Raman spectra using 532 nm excitation shows no peaks of secondary phases. However, Raman spectra using 785 nm excitation shows a peak at 319 cm^{-1} for batches using Cu_2SnS_3 and ZnS as precursors (Figure 4.5). That peak can be assigned to Cu_3SnS_4 as described in the work of Fernandes *et al.*[8] The fact that this peak was only observed using 785 nm excitation is because Cu_3SnS_4 has a band gap of 1.60 eV,[9] and the intensity of the peak increases due to resonant Raman effect when excited using 785 nm laser. The Raman spectra for the product using CuS, SnS and

ZnS with 785nm excitation suffered from strong fluorescence and could not be processed and interpreted. Nevertheless, since using binary or tertiary precursors does not yield better quality polycrystalline materials than using elemental precursors, synthesis of polycrystalline CZTS via solid state reaction will be carried out using elemental precursors with ball mill mixing.

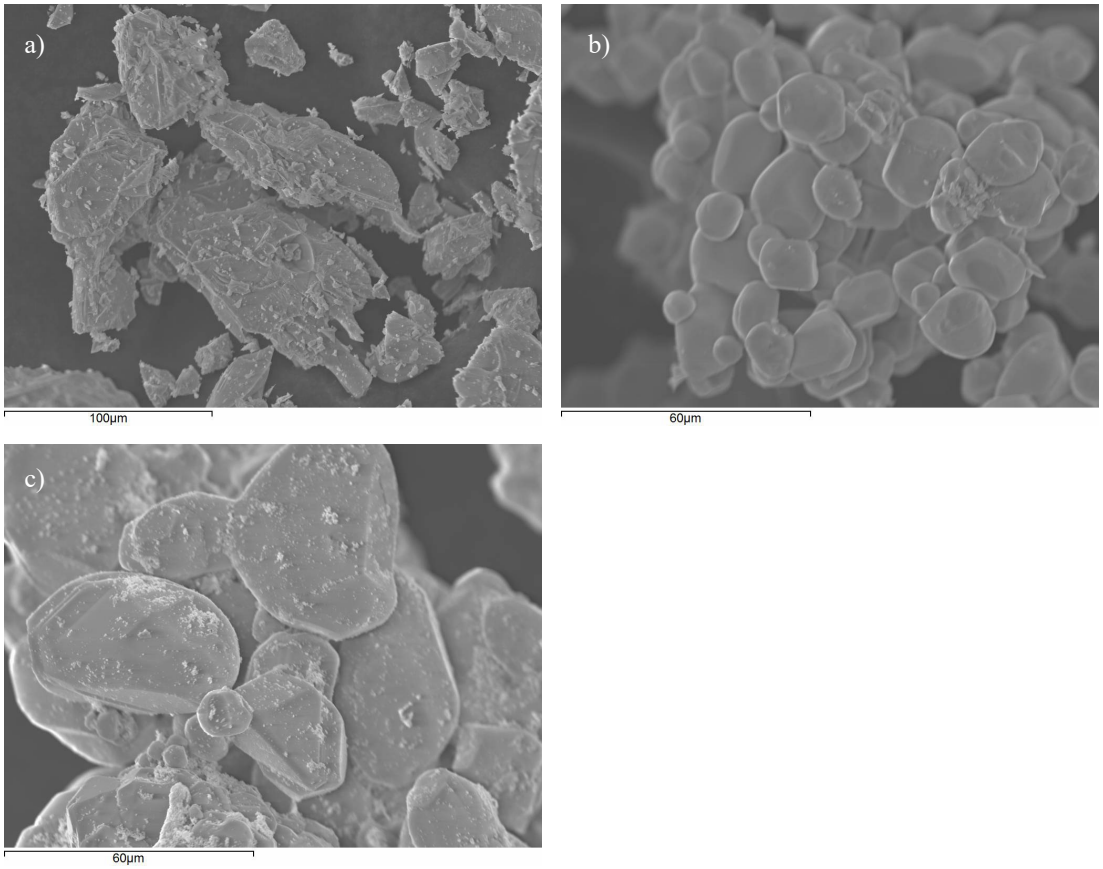

Figure 4.4 SEM images of polycrystalline CZTS synthesised with binary and tertiary precursors at 750 °C for 7 days. (a) CTS and ZnS; (b) CTS and ZnS with 40% excess sulphur; (c) CuS, SnS and ZnS

Table 4.4 A summary of results showing attempts to synthesise CZTS via solid state reaction using CuS and SnS from hydrothermal reaction, Cu_2SnS_3 from solid state reaction, and commercial ZnS.

Precursor composition	**Batch size / g**	**Temp / °C**	**Duration / day**	**Product composition**			**Secondary phase**
				$\frac{Cu}{Zn+Sn}$	$\frac{Zn}{Sn}$	$\frac{S}{metals}$	
Cu_2SnS_3, ZnS	5	750	7	0.96	0.92	1.10	Cu_3SnS_4 or SnS_2
Cu_2SnS_3, ZnS with 40% excess S	5	750	7	0.99	0.96	1.02	Cu_3SnS_4 or SnS_2
CuS, SnS, ZnS	8	750	7	0.96	0.96	1.02	None observed

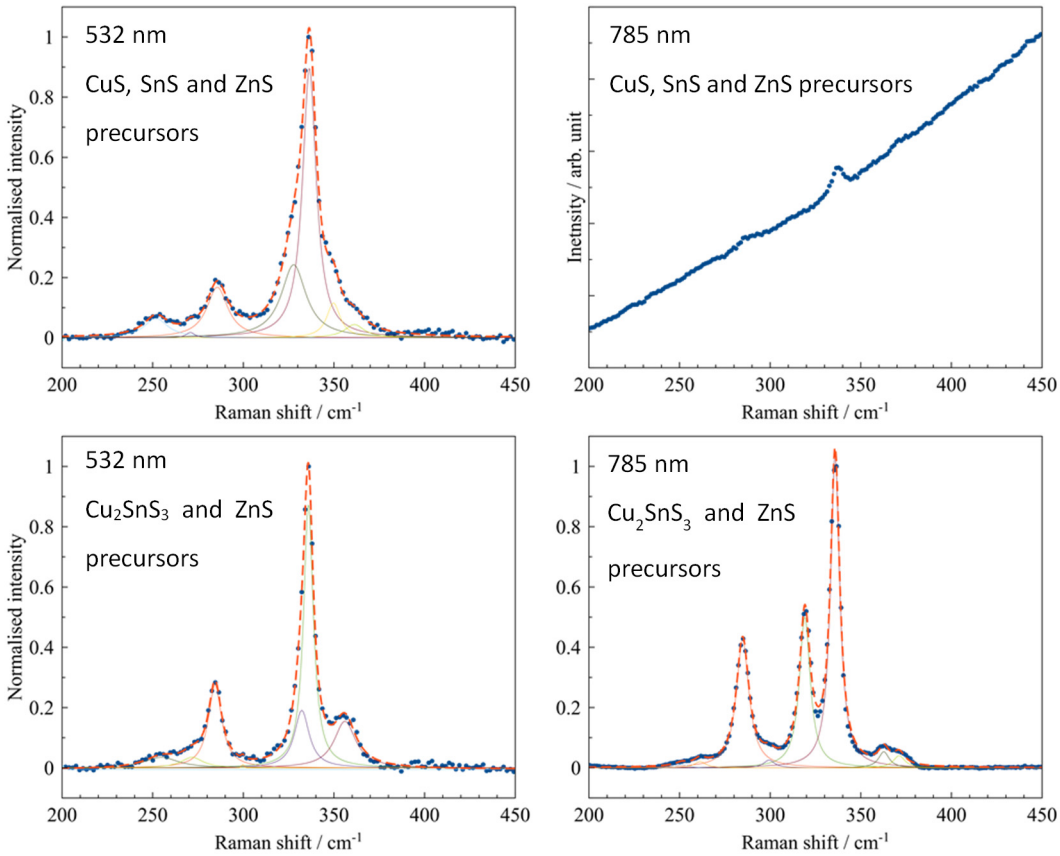

Figure 4.5 Raman spectra of CZTS synthesised from solid state reaction using binary and tertiary precursors. Top left: 532 nm, CuS, SnS and ZnS precursors; top right: 785 nm, CuS, SnS and ZnS precursors; bottom left: 532 nm, Cu_2SnS_3 and ZnS precursors; bottom right: 785 nm, Cu_2SnS_3 and ZnS precursors.

4.1.2 Chemical vapour transport

Attempts to grow larger CZTS crystals were carried out using chemical vapour transport similar to the one described in the work of Colombara *et al.*[10] There were only two successful attempts initially, and both yielded CZTS crystals with different morphologies. In one batch, large crystal grains of sizes around 0.5 – 1 mm were obtained (Figure 4.6a). In another batch, a mixture of smaller crystal grains of sizes around 100 µm and needle-shaped crystals of around 1 mm wide and 10 – 20 mm long were obtained (Figure 4.6b). Colombara *et al.*[10] reported in the literature that the concentration of the transporting agent (*i.e.* iodine) affects the shape of the crystal, with needle-shaped crystals obtained with 0.9 mg/cm^3 of iodine, and grains were obtained with 5 mg/cm^3 of iodine. However, the iodine concentration was 5 mg/cm^3 for both synthesises, suggesting there are other factors affecting the crystal formation.

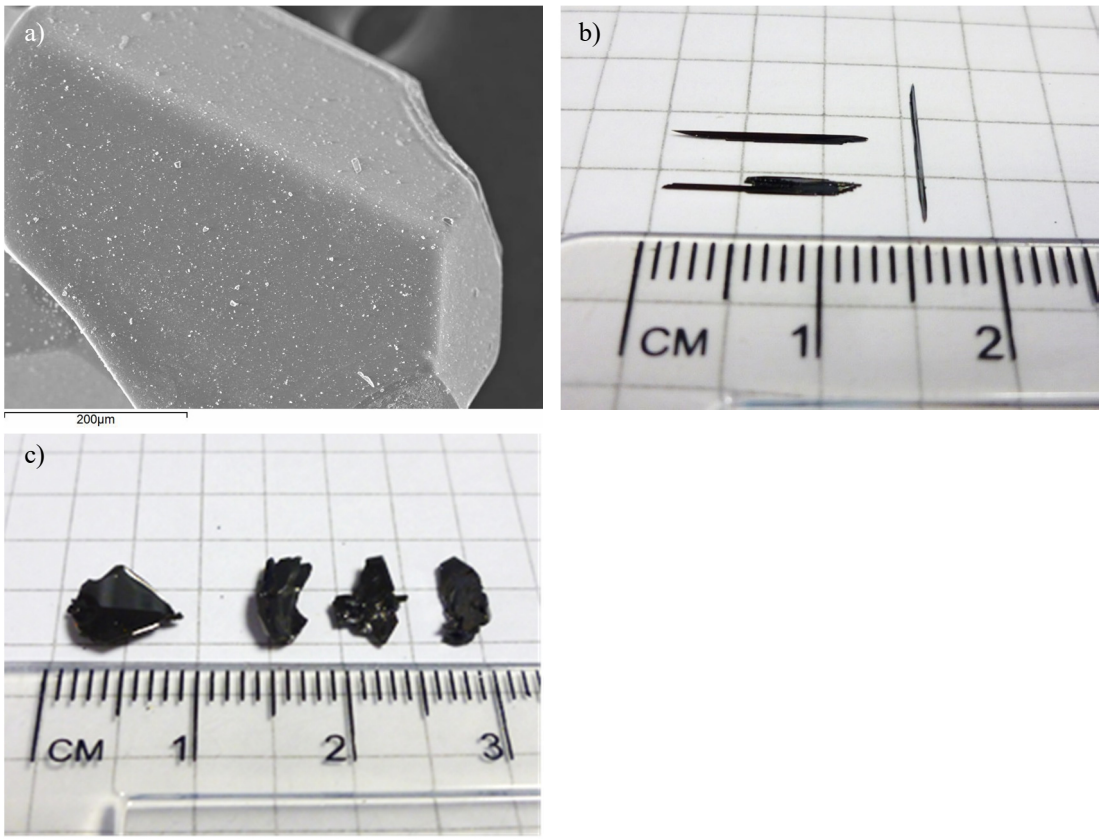

Figure 4.6 Photographic and SEM images showing CZTS crystals synthesised from chemical vapour transport (a) large grain, 5 g/cm^3 iodine; (b) needle, 5 g/cm^3 iodine; (c) blocks, 20 g/cm^3 iodine.

There were problems reproducing CZTS crystals using chemical vapour transport after the first two successful attempts despite using the same reaction conditions, including precursor materials, heating and cooling profile, reaction temperature and duration etc. After a number of trial and error reactions, the solution was to increase the iodine concentration by four-fold, from 5 to 20 mg/cm^3. It was not previously known that the iodine concentration was an important factor because all the reported literature succeeded to grow CZTS using 5 mg/cm^3 of iodine,[10-13] and Tanaka *et al.* used 5 and 10 mg/cm^3 of iodine.[13] When 20 mg/cm^3 of iodine was applied, crystal growth was completed without the need of the reverse temperature gradient step as described in the work of Colombara *et al*.[10] A mixture of crystal grains around 0.5 – 1 mm and block crystals with dimension 8 × 5 × 1 mm were obtained (Figure 4.6c). Most block crystals have a flat surface at the front and a rough surface at the back. Ball milling of the CZTS precursor had no observable effect on

the product. One of the batches used the product from three failed batches as precursor and large crystals were obtained.

Table 4.5 Elemental composition of CZTS single crystals grown by chemical vapour transport. #AAS was carried out using 20 mg of crystals from the same batch.

	EDS			AAS#			XRF		
Crystal ID	$\frac{Cu}{Zn+Sn}$	$\frac{Zn}{Sn}$	$\frac{S}{metals}$	$\frac{Cu}{Zn+Sn}$	$\frac{Zn}{Sn}$	$\frac{S}{metals}$	$\frac{Cu}{Zn+Sn}$	$\frac{Zn}{Sn}$	$\frac{S}{metals}$
needleB	0.91	1.00	1.05	0.93	0.93	1.35	0.98	1.10	1.10
63B	0.95	1.00	1.02	0.93	0.87	1.42	-	-	-
63C	0.91	1.02	1.06				-	-	-
65B	0.96	0.99	1.03	1.04	0.92	1.33	-	-	-
65C	0.95	0.96	1.04				-	-	-
67B	0.95	0.95	1.04	0.88	1.13	1.32	0.99	0.99	1.01
67C	0.89	1.00	1.04				0.97	1.11	1.07
71A	0.94	0.97	1.05	0.96	0.95	1.37	-	-	-
71B	0.96	1.01	1.01				-	-	-
85A	0.95	1.00	1.03	0.92	1.01	1.35	1.01	1.02	1.05
85B	0.96	0.98	1.01				1.02	1.04	1.06
Average error	0.02	0.03	0.02	-	-	-	0.01	0.06	0.02

Elemental analysis were carried out using EDS, AAS and XRF. EDS were carried out on at least four different areas of a crystal. Measurements were then acquired at five different spots in each area. Hence, at least 20 EDS spectra were taken per crystal to increase the reliability of the data. EDS results show crystals from the same batch have the same composition within statistical error. All batches are type AE CZTS and have Cu-poor, near stoichiometric Zn and Sn, and slightly S-rich under EDS. It was repeatedly observed that zinc was lost if Cu-poor Zn-rich precursor was used. In

contrast, the composition of the large crystals were very similar to the precursor if near stoichiometric precursor was used.

AAS were carried out by dissolving 20 mg of crystals in concentrate aqua regia before diluting with deionized water to obtain a concentration within the detection limits of the instrument. Note that mild heating was applied overnight in order to dissolve the CZTS crystals. During data analysis, it was assumed that the mass of sulphur was the sample mass minus the mass of Cu, Zn and Sn, against which the latter three were measured and re-calculated using dilution factor. However, the results show too much sulphur in the samples, with an average $\frac{S}{metals}$ ratio of 1.36. This suggested the CZTS samples were not totally dissolved in the solution despite there were not any observable precipitate in the solution. Samples were also sent to a collaborator for AAS analysis and the result was even worse, with an average $\frac{S}{metals}$ ratio of 1.84.

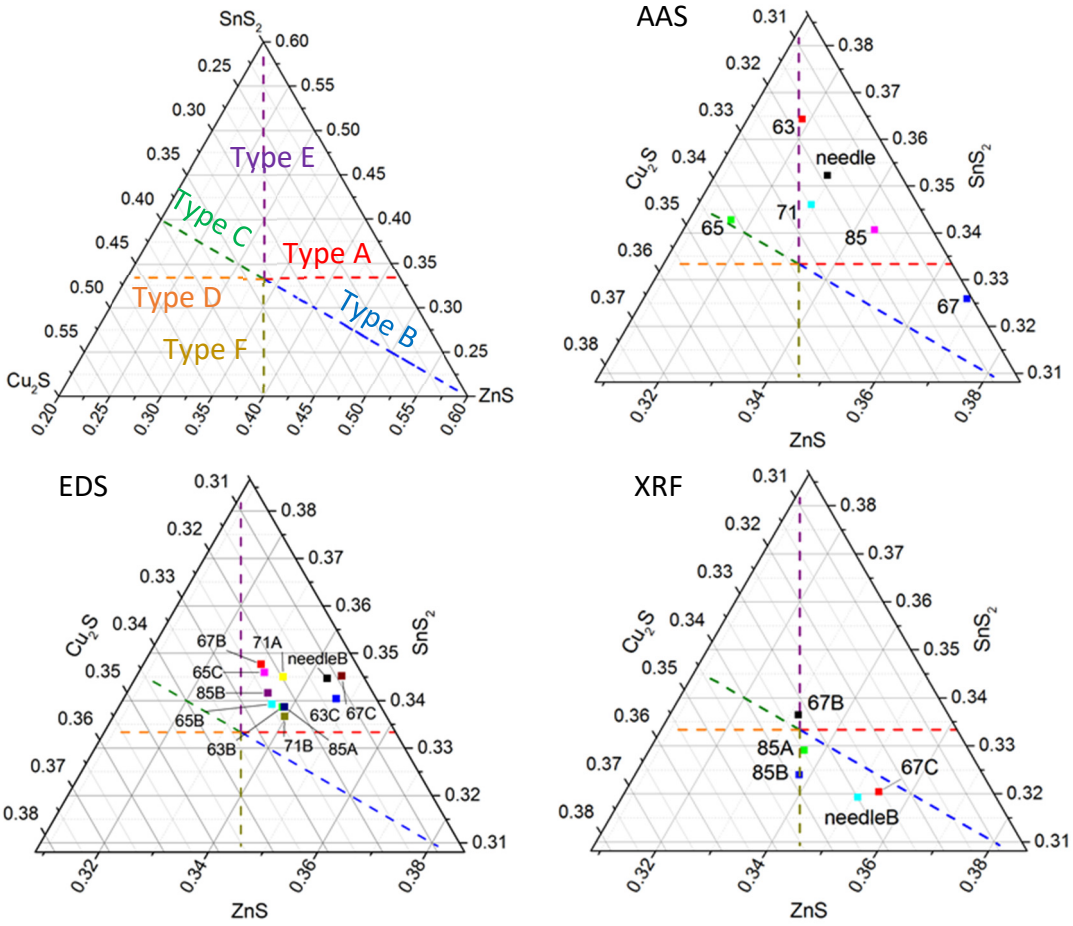

Figure 4.7 Pseudo-ternary phase diagram showing the composition of CZTS single crystals grew by chemical vapour transport analysed using AAS, EDS and XRF.

XRF measurements were carried out on two or three 0.5 × 0.5 mm areas on each crystal. All ratios are slightly higher than the ones obtained from SEM and shift the crystal type from AE to near stoichiometric, type F or type BF. It was also observed that two crystals from the same batch, *i.e.* 67B and 67C, have very different compositions. It was not surprising because crystal 67B had undergone a lot of harsh treatments and testing, such as etching, polishing, soaking in electrolyte etc. In contrast, another crystal pair (85A and 85B) had similar compositions.

1% w/w of NaI was incorporated in the starting material in batch 67 because it is well-known that sodium improves the performance of CZTS devices.[14-16] Since the level of sodium was below the detection limit by EDS and XRF due to the overlapping of the Na and Zn peaks, the sodium concentration was determined by AAS. The sodium concentration in the CZTS crystal was found to be 0.02% w/w (0.07 mol%, 0.07 at%). This concentration is comparable to Nagaoka *et al.*'s Na-doped CZTS single crystals grown using a different synthetic method (cf. 0.04 and 0.13 at%).[17]

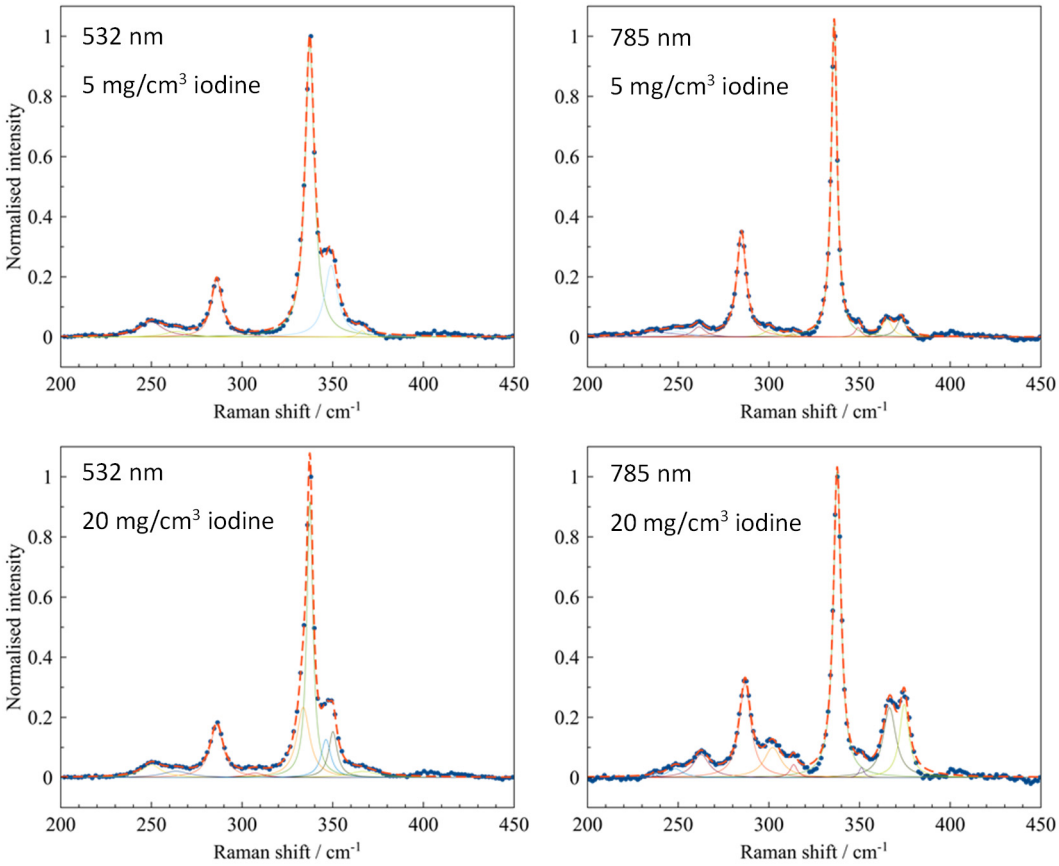

Figure 4.8 Raman spectra of CZTS single crystals synthesised from chemical vapour transport using 5 and 20 mg/cm^3 iodine.

A representation of Raman spectra for CZTS crystal grown by chemical vapour transport is shown in Figure 4.8. No peaks from secondary phases were observed. The difference in peak intensity in 785 nm excitation at 302, 366 and 375 cm^{-1} were due to Cu/Zn disorder, where this particular batch of CZTS synthesised using 20 mg/cm^3 of iodine has more Cu/Zn disorder than the batch synthesised using 5 mg/cm^3 of iodine.

4.1.3 Hydrothermal and solution synthesis

CZTS synthesis were carried out using hydrothermal and solution routes in attempts to obtain CZTS with shorter reaction time and at much lower temperatures. It was observed that an insoluble white precipitate was formed after thiourea was added to the metal salt solution when the solvent was water. A black powder was initially obtained for both routes, which subsequently turned pale green after annealing at 280 °C under ambient atmosphere. EDS images show both samples are amorphous (Figure 4.9) and have very high (> 50 at%) oxygen contents suggesting oxidation of CZTS occurred.

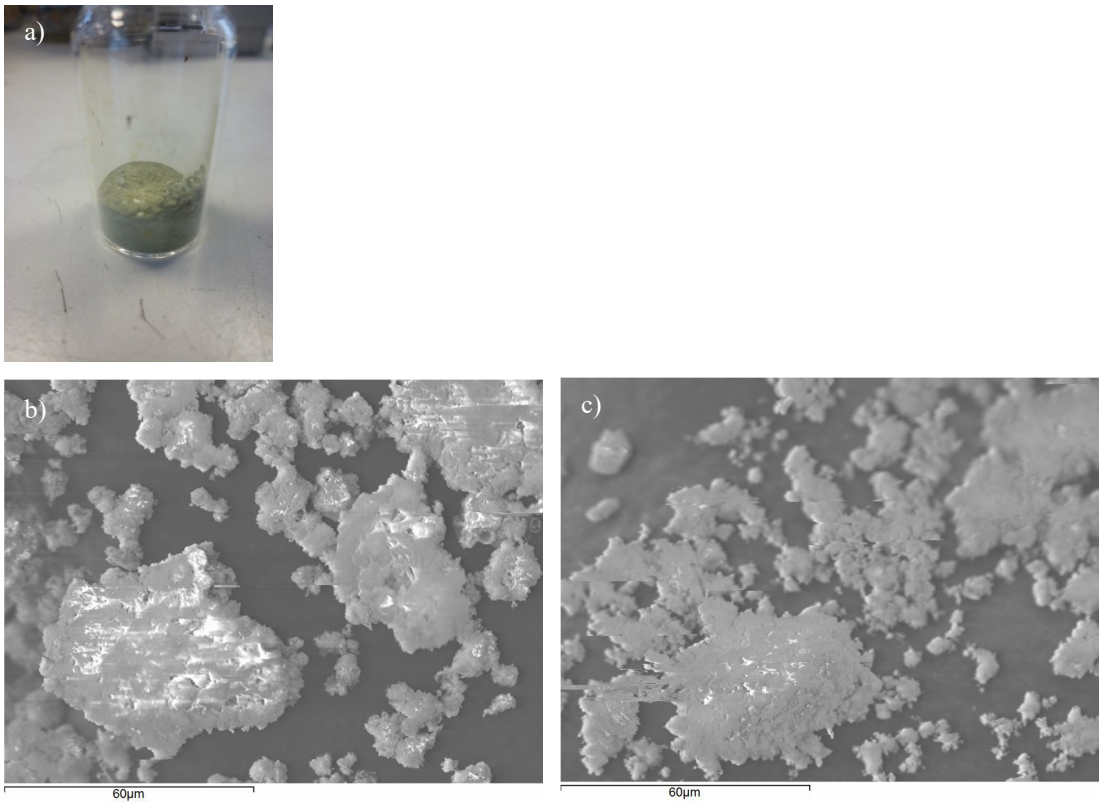

Figure 4.9 Photographic and SEM images showing 'CZTS' synthesised by (a-b) hydrothermal reaction, and (c) solution route.

4.2 Conclusion

Initial synthesis of polycrystalline CZTS were attempted using solid state reaction, and the following conditions were varied: reaction temperature, duration, amount of excess sulphur, and precursors. However, nearly all attempts resulted in some level of secondary phase formation as revealed by SEM/EDS. Single phase CZTS was only obtained with ball milled elemental precursors at 750 °C with a reaction time of at least 7 days regardless of using excess sulphur. The higher temperature and longer reaction time than thin film synthesis is the reason for producing pure phase CZTS.

Initial attempts to grow bigger CZTS crystals using chemical vapour transport resulted in only two successful syntheses. One batch yielded large grains of sizes around 0.5 – 1 mm, and another batch yielded a mixture of smaller crystal grains of sizes around 100 µm and needle-shaped crystals around 1 mm wide and 10 – 20 mm long. Successful growth of crystal by using chemical vapour transport was achieved by increasing the iodine concentration by up to four times the amount reported in literatures. Large CZTS crystals with dimensions in the sub-centimetre range were obtained.

The elemental composition of the CZTS crystals proved difficult to establish precisely. Atomic absorption spectroscopy is unreliable because it was very difficult to completely dissolve CZTS. The disagreement between EDS and XRF results may be due to that fact that the power of the energy beam used were different, *i.e.* 20 kV in EDS and 50 kV in XRF. This affects the sampling depth in EDS and XRF. Hence, the disagreement between EDS and XRF results suggest the elemental compositional in the bulk may be different to the surface.

Nevertheless, a large number of phase pure big CZTS crystals were synthesised, and the next few chapters will see a number of characterisations performed on those crystals.

Reference

1. Bernardini, G.P., Borrini, D., Caneschi, A., Di Benedetto, F., Gatteschi, D., Ristori, S., and Romanelli, M., *EPR and SQUID magnetometry study of Cu_2FeSnS_4 (stannite) and Cu_2ZnSnS_4 (kesterite).* Physics and Chemistry of Minerals, 2000. **27**(7): p. 453-461.
2. Choubrac, L., Lafond, A., Guillot-Deudon, C., Moëlo, Y., and Jobic, S., *Structure Flexibility of the Cu_2ZnSnS_4 Absorber in Low-Cost Photovoltaic Cells: From the Stoichiometric to the Copper-Poor Compounds.* Inorganic Chemistry, 2012. **51**(6): p. 3346-3348.
3. Kheraj, V., Patel, K.K., Patel, S.J., and Shah, D.V., *Synthesis and characterisation of Copper Zinc Tin Sulphide (CZTS) compound for absorber material in solar-cells.* Journal of Crystal Growth, 2013. **362**: p. 174-177.
4. Nagaoka, A., Yoshino, K., Taniguchi, H., Taniyama, T., and Miyake, H., *Preparation of Cu_2ZnSnS_4 single crystals from Sn solutions.* Journal of Crystal Growth, 2012. **341**(1): p. 38-41.
5. Valakh, M.Y., Kolomys, O.F., Ponomaryov, S.S., Yukhymchuk, V.O., Babichuk, I.S., Izquierdo-Roca, V., Saucedo, E., Perez-Rodriguez, A., Morante, J.R., Schorr, S., and Bodnar, I.V., *Raman scattering and disorder effect in Cu_2ZnSnS_4.* physica status solidi (RRL) – Rapid Research Letters, 2013. **7**(4): p. 258-261.
6. Dimitrievska, M., Fairbrother, A., Pérez-Rodríguez, A., Saucedo, E., and Izquierdo-Roca, V., *Raman scattering crystalline assessment of polycrystalline Cu_2ZnSnS_4 thin films for sustainable photovoltaic technologies: Phonon confinement model.* Acta Materialia, 2014. **70**(0): p. 272-280.
7. Scragg, J.J.S., Choubrac, L., Lafond, A., Ericson, T., and Platzer-Björkman, C., *A low-temperature order-disorder transition in Cu_2ZnSnS_4 thin films.* Applied Physics Letters, 2014. **104**(4): p. 041911.
8. Fernandes, P.A., Salome, P.M.P., and da Cunha, A.F., *Study of polycrystalline Cu_2ZnSnS_4 films by Raman scattering.* Journal of Alloys and Compounds, 2011. **509**(28): p. 7600-7606.
9. Fernandes, P.A., Salome, P.M.P., and da Cunha, A.F., *A study of ternary Cu_2SnS_3 and Cu_3SnS_4 thin films prepared by sulfurizing stacked metal precursors.* Journal of Physics D-Applied Physics, 2010. **43**(21): p. 215403.
10. Colombara, D., Delsante, S., Borzone, G., Mitchels, J.M., Molloy, K.C., Thomas, L.H., Mendis, B.G., Cummings, C.Y., Marken, F., and Peter, L.M., *Crystal growth of Cu_2ZnSnS_4 solar cell absorber by chemical vapor transport with I_2.* Journal of Crystal Growth, 2013. **364**: p. 101-110.
11. Nitsche, R., Sargent, D.F., and Wild, P., *Crystal growth of quaternary 1_2246_4 chalcogenides by iodine vapor transport.* Journal of Crystal Growth, 1967. **1**(1): p. 52-53.
12. Guen, L. and Glaunsinger, W.S., *Electrical, Magnetic, and Epr Studies of the Quaternary Chalcogenides $Cu_2A^{II}B^{IV}X_4$ Prepared by Iodine Transport.* Journal of Solid State Chemistry, 1980. **35**(1): p. 10-21.
13. Tanaka, K., Miyamoto, Y., Uchiki, H., Nakazawa, K., and Araki, H., *Donor-acceptor pair recombination luminescence from Cu_2ZnSnS_4 bulk single crystals.* Physica Status Solidi a-Applications and Materials Science, 2006. **203**(11): p. 2891-2896.

14. Gershon, T., Shin, B., Bojarczuk, N., Hopstaken, M., Mitzi, D.B., and Guha, S., *The Role of Sodium as a Surfactant and Suppressor of Non-Radiative Recombination at Internal Surfaces in Cu_2ZnSnS_4.* Advanced Energy Materials, 2015. **5**(2): p. 1400849.
15. Li, J.V., Kuciauskas, D., Young, M.R., and Repins, I.L., *Effects of sodium incorporation in Co-evaporated $Cu_2ZnSnSe_4$ thin-film solar cells.* Applied Physics Letters, 2013. **102**(16).
16. Prabhakar, T. and Jampana, N., *Effect of sodium diffusion on the structural and electrical properties of Cu_2ZnSnS_4 thin films.* Solar Energy Materials and Solar Cells, 2011. **95**(3): p. 1001-1004.
17. Nagaoka, A., Scarpulla, M.A., and Yoshino, K., *Na-doped Cu_2ZnSnS_4 single crystal grown by traveling-heater method.* Journal of Crystal Growth, 2016. **453**: p. 119-123.

5 Optoelectronic and Spectroscopic Characterization of Vapour-Transport Grown CZTS Single Crystals

After obtaining large single crystals of CZTS as described in the Chapter 4.1.2, a series of characterisations, including single crystal X-ray diffraction (SCXRD), energy-dispersive X-ray spectroscopy (EDS), photocurrent spectroscopy (PS) and electroreflectance spectroscopy (EER) using electrolyte contacts, as well as spectroscopic ellipsometry (SE), Raman spectroscopy and photoluminescence spectroscopy (PL) / decay, were conducted on two unique crystals. The experiments, results and discussion, and conclusion were published in the journal article attached at the end of this chapter with permission from the publisher The Royal Society of Chemistry. Readers should read the journal article in full as this chapter is only served as a commentary, with additional results for some of the experiments because the information written in the journal article is very condensed. A detail account of contributions from each co-authors is attached at the end of the commentary, before the journal article. The commentary section headings in this chapter are the same as the headings in the journal article for ease of cross referencing.

5.1 Composition and degree of disorder of the kesterite phase

XRF measurements were made on the same crystals after publication of the paper and are shown in Figure 4.7 (page 92). The XRF analysis yield different compositions to the EDS results because XRF measurements were carried out at 50 kV, while EDS measurements were carried out at 20 kV. This affects the sampling depth and therefore suggests the bulk of the crystals have a different composition to the surface. The composition of the needle (ID: needleB) is shifted from type A to type B, while the platelet (ID: 67B) is shifted from type E to near stoichiometric. The classification for different types of CZTS(e) is covered in Table 1.4 and Figure 1.17 (page 31). It was not possible to gain access to an X-ray photoelectron spectroscopy (XPS) facility so the composition and the depth profile of the unique CZTS crystals could not be further cross checked with a different technique.

5.2 SCXRD structure analysis

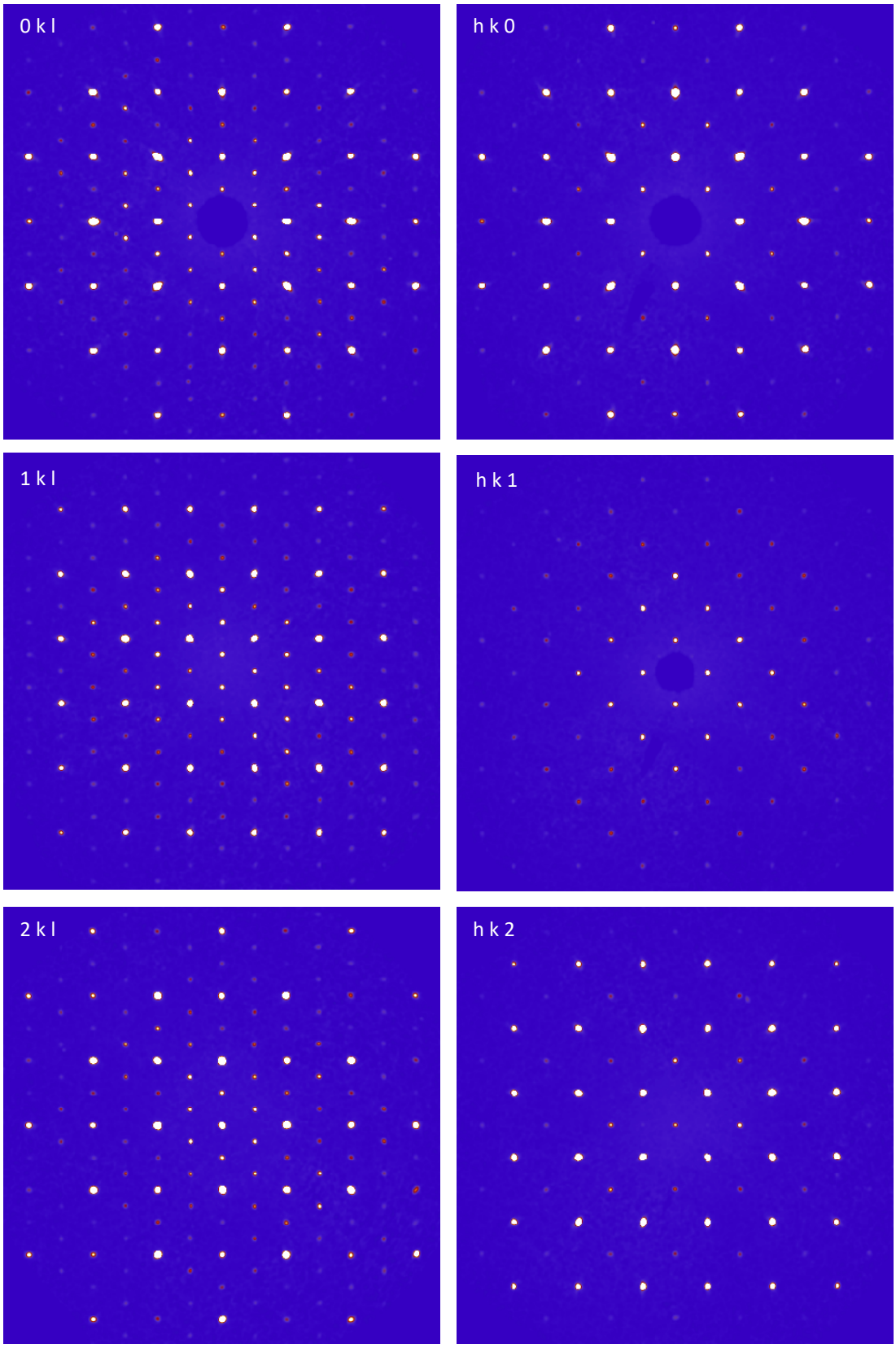

Figure 5.1 Precession diagrams showing 0kl, 1kl, 2kl, hk0, hk1 and hk2 reflections of a needle crystal.

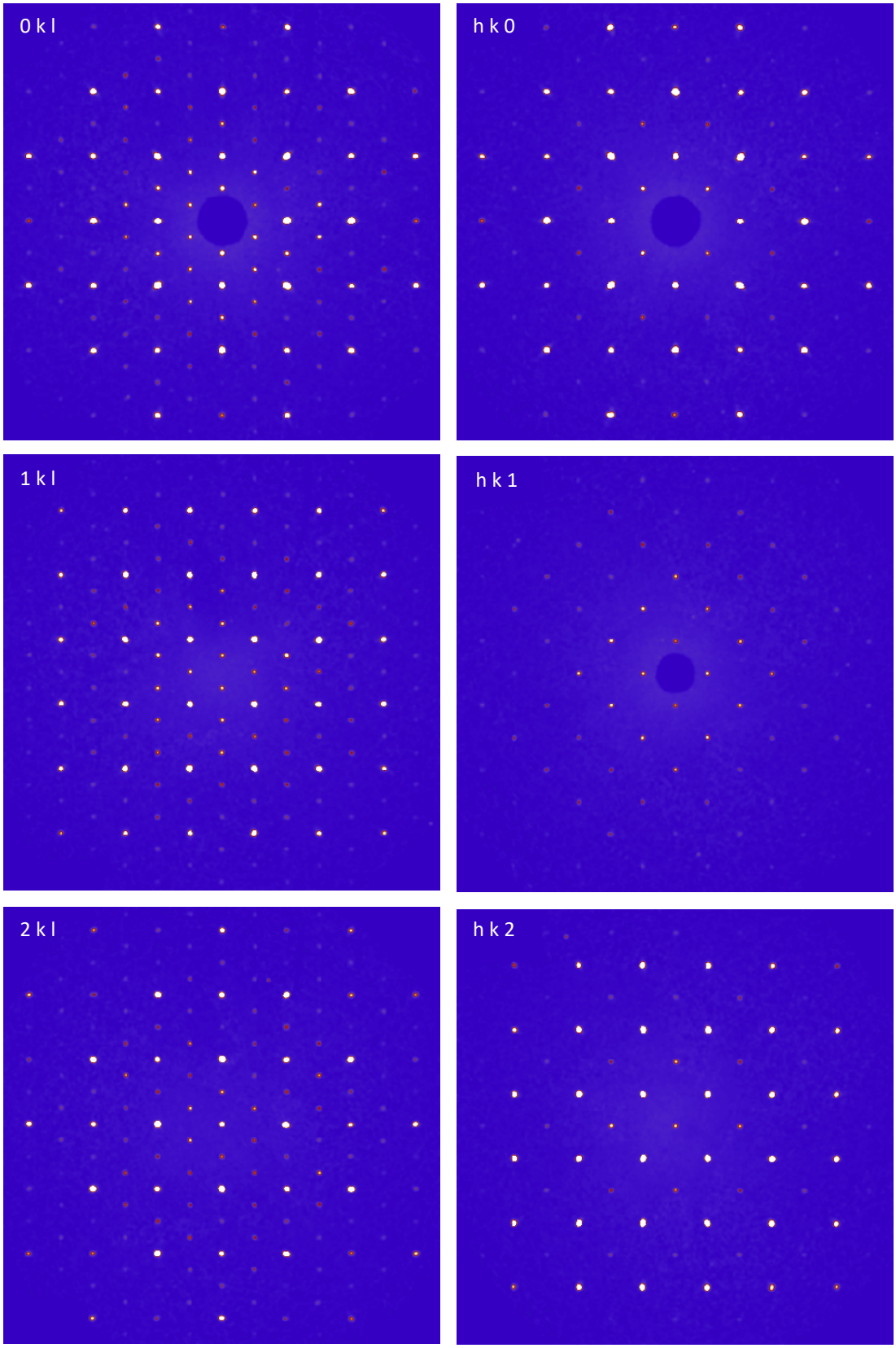

Figure 5.2 Precession diagrams showing 0kl, 1kl, 2kl, hk0, hk1 and hk2 reflections of a platelet crystal.

Table 5.1 Data collection conditions and refinement results for the SCXRD study of needle CZTS using the kesterite model and stannite model detailed in Table 1.1.

Needle	**Kesterite model**	**Stannite model**
Crystallographic composition	Cu_2ZnSnS_4	Cu_2ZnSnS_4
Space group	Tetragonal I-4	Tetragonal I-42m
a / Å	5.4282(1)	5.4282(1)
c / Å	10.8198(5)	10.8198(5)
Unit cell volume / Å^3	318.809(19)	318.809(19)
No. of formula unit per unit cell, Z	2	2
Temperature / K	298	298
No. of reflections measured	3067	3067
No. of independent reflections	519	300
R_{int}	6.68%	6.86%
No. of parameters refined	9	8
Final R_1/wR values [I > 3σ(I)]	3.78% / 4.28%	3.97% / 4.87%
Final R_1/wR values (all data)	3.83% / 4.29%	4.06% / 4.89%
GOF	1.63	2.26

Table 5.2 Data collection conditions and refinement results for the SCXRD study of platelet CZTS using the kesterite model and stannite model detailed in Table 1.1.

Platelet	**Kesterite model**	**Stannite model**
Crystallographic composition	Cu_2ZnSnS_4	Cu_2ZnSnS_4
Space group	Tetragonal I-4	Tetragonal I-42m
a / Å	5.4289(1)	5.4289(1)
c / Å	10.8256(5)	10.8256(5)
Unit cell volume / Å^3	319.062(19)	319.062(19)
No. of formula unit per unit cell, Z	2	2
Temperature / K	298	298
No. of reflections measured	2876	2876
No. of independent reflections	519	299
R_{int}	6.98%	7.25%
No. of parameters refined	9	8
Final R_1/wR values [I > 3σ(I)]	3.92% / 4.61%	4.00% / 4.76%
Final R_1/wR values (all data)	4.02% / 4.62%	4.13% / 4.77%
GOF	1.58	2.01

SCXRD was carried out on four crystals from the two synthesis batches. The precession diagrams of a needle and a platelet are shown in Figure 5.1 and Figure 5.2.

Since Cu and Zn have similar atomic scattering form factors, it is not possible to distinguish between the kesterite and stannite structure using single wavelength XRD systems, or to determine the occupancy of Cu and Zn at their nominal positions. The SCXRD data from both crystals were refined with kesterite and stannite models and are shown in Table 5.1 for the needle crystal and Table 5.2 for the platelet. The results are not significant enough to conclude which structure the crystals adopted, as expected. Note that there is a different in the R-factor and GooF value between Table 5.1, Table 5.2 and the published article because the refinements in Table 5.1 and Table 5.2 were carried out by the author using JANA2006,[1] while the refinements in the published article were carried out by co-author Prof. Weller using WinGX suite.[2] Chapter 6 describes experiments using neutron diffraction and anomalous X-ray diffraction in an attempt to resolve the copper and zinc distribution in the CZTS structures.

5.3 Raman spectroscopy: phase identification and disorder

Due to overlapping of peaks from secondary phases in XRD, Raman spectroscopy is a useful technique to analyse the structure and phase purity in CZTS. Table 1.4 (page 31) lists the Raman peaks for a number of secondary phases.

The calculated results from Khare *et al.*[3] and Gurel *et al.*[4], together with the experimental results obtained from this work, are summarised in the ESI of the paper (page 129). The deconvolution of Raman spectra in this work were fitted using Lorentzian curves following Valakh *et al.*[5] and Dimitrievska *et al.*[6] No peaks from secondary phases were observed, and all observable peaks can be assigned to one of the calculated Raman modes.

Cu/Zn disorder is a key issue in kesterite. A systematic study measuring CZTS crystals annealed at different temperatures is presented in Chapter 6. The journal article in this chapter included the preliminary results of the study by showing and comparing the resonance Raman spectra for the as-grown platelet, and platelets annealed at 150 and 300 °C (reproduced in Figure 5.3). It is very obvious that the intensity of some

peaks, *i.e.* around 303, 366 and 374 cm^{-1}, is much higher after annealing at 300 °C (*cf.* the critical temperature of CZTS is 260 °C).[7] Paris *et al.*[8] introduced two empirical parameters, Q and Q', to quantify the degree of Cu/Zn disorder in terms of the intensity ratios of the Raman peaks at 287 and 303 cm^{-1} (Q), and 338, 366 and 374 cm^{-1} (Q'):

Equation 5.1

$$Q = {I_{287}}/{I_{303}} \qquad Q' = {I_{338}}/{(I_{366} + I_{374})}$$

In contrast, the as-grown sample and the sample annealed at 150 °C have much higher Q and Q' values, indicating less disorder formed in the lattice sites. The Q and Q' values of the platelet are also higher than those reported. Even so, total ordering can only be achieved at 0 K. Using the Vineyard model calculations discussed in the introduction chapter (1.4.2.1) and the ESI of the paper (page 130) would suggest there is roughly 20 – 30% of disorder in the lattice sites, with significant consequences for bandgap fluctuations and bandgap tailing.

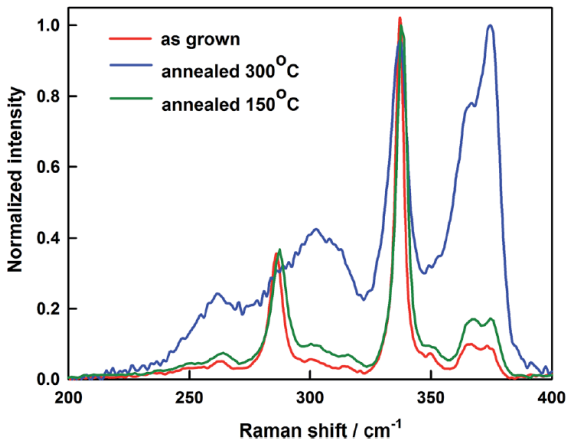

Figure 5.3 Near-resonance Raman spectrum of as-grown CZTS platelet crystal compared with the spectrum of platelets annealed at 150 and 300 °C. Reproduced from Ng *et al.*[9]

5.4 Photoluminescence (PL)

The PL results in this work agree well with reported values in terms of peak position, the blue shift observed with increased laser power, and the power law relationship.[10-12] The substantial red shift of the PL peak (1.35 eV) with respect to the bandgap of CZTS (reported: 1.5 eV, this work: 1.68 – 1.71 eV) is consistent with

emission taking place from tail states associated with disorder in the crystal.[12] The blue shift with increased laser power can be interpreted as indication of potential fluctuations in the material.[13] The data follow the power law relationship PL $\propto I^m$, with *m* values ranging from 1.3 – 1.6 (reproduced in Figure 5.4a), and is comparable to those reported in the literature with room temperature PL (1.33 – 1.54).[12] Scragg *et al.*[12] suggested such *m* values correspond to band-to-band transition or band-to-tail transition. We have also observed a second peak at 1.58 eV when a higher intensity laser (50 mW) was used (reproduced in Figure 5.4b).

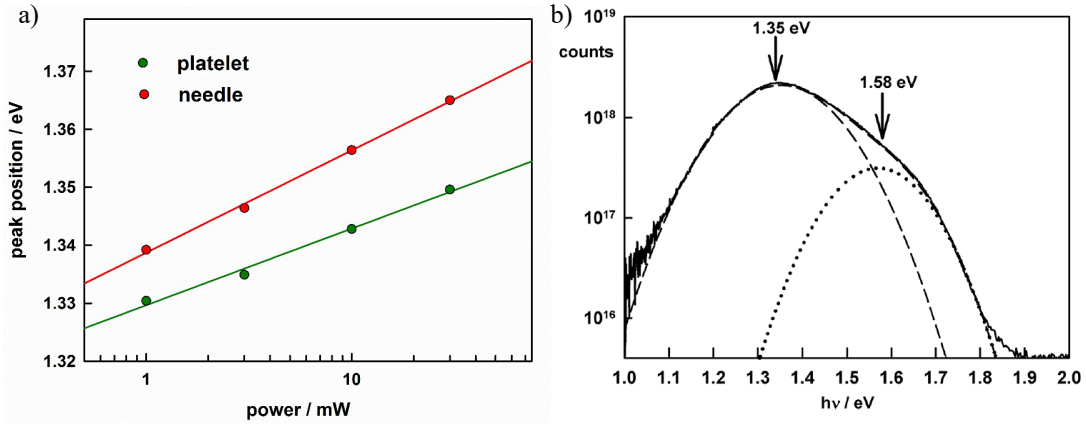

Figure 5.4 (a) Intensity dependence of PL peak energy for platelet and needles crystals. (b) PL spectrum of CZTS platelet showing shoulder at higher energy attributed to radiative band to band recombination (laser power 50 mW). Reproduced from Ng *et al.*[9]

The interpretation of the peaks were further carried out using time-resolved photoluminescence (TRPL), which has been used to characterise and understand recombination in numerous photovoltaic materials. The lifetimes obtained were 3.5 ns (1.65 eV) and 6.8 ns (1.30 eV) for the platelet. The results were compared with Gershon *et al.*[14], where their low temperature (4 K) TRPL of a CZTS device also showed two peaks, with lifetimes of 12 µs (1.2 eV), indicating carrier trapping, and 1.7 ns (1.43 eV), which is attributed to free carrier recombination. Although there are problems in comparing low temperature measurements with our results, it seems reasonable to assume that the high-energy peak in our room temperature PL is due to band-to-band transition, whereas the low energy peak corresponds to band-to-tail transition.

5.5 Spectroscopic ellipsometry (SE)

In this work, the complex dielectric functions ($\varepsilon = \varepsilon' + i\varepsilon''$) and the absorption coefficient (α) of the CZTS crystals were derived by fitting the SE data. The details of the experiment and data fitting were given in the experimental chapter (3.2.7) and in the ESI of the paper (page 125). A comparison of absorption coefficient values from this work with other reported values is reproduced in Figure 5.5. The bandgap and Urbach energy were also derived using Tauc plots and Urbach plots (reproduced in Figure 5.6). They were 1.60 eV and 6.7 $k_B T$ respectively for the platelet crystal. These values were compared to the values derived from the EQE measurements, which is discussed in the next section.

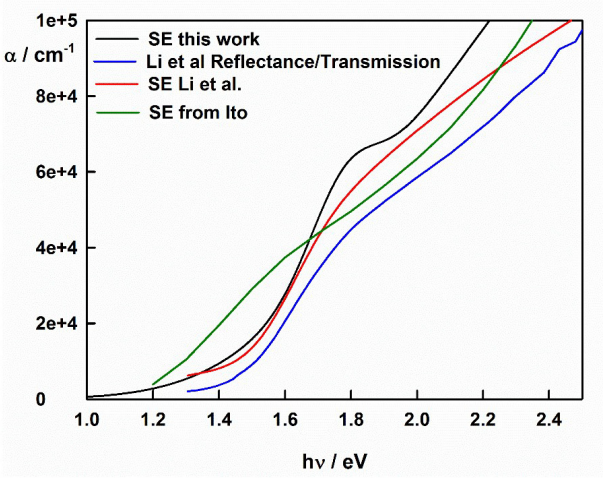

Figure 5.5 Comparison of absorption coefficient values of CZTS between this work and other reported values.[15-17] Reproduced from Ng *et al*.[9]

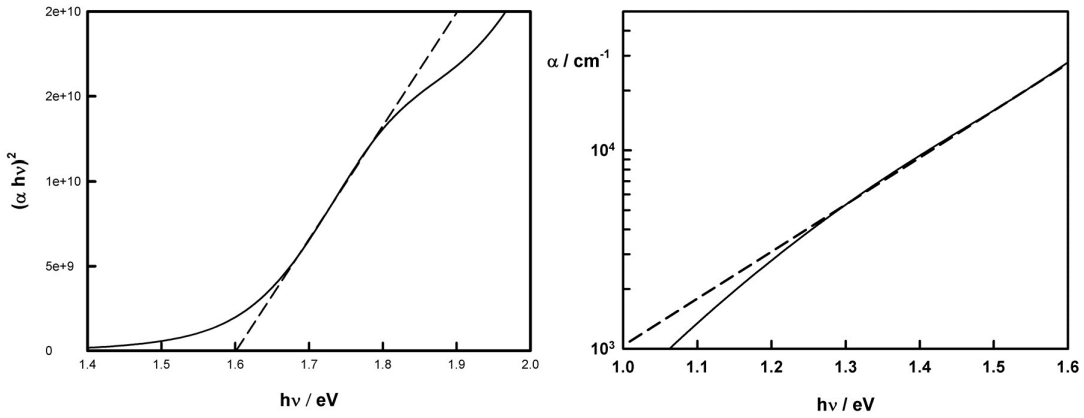

Figure 5.6 Tauc plot (left) and Urbach plot (right) of CZTS platelet crystal using data obtained from spectroscopic ellipsometry. Reproduced from Ng *et al*.[9]

5.6 External quantum efficiency (EQE) measurements

In order to measure the electrical properties of the single crystals, the crystals were contacted and embedded as shown in Figure 3.3. The crystal was etched in saturated Na_2S solution for 30 seconds followed by 30% H_2O_2/1 M H_2SO_4 for 300 seconds. After rinsing, the samples were treated with 1 M HCl, to remove metal (hydr)oxides. The EQE spectrum indicates that all photogenerated electrons are collected in the junction for photon energies above 1.7 eV (reproduced in Figure 5.7).

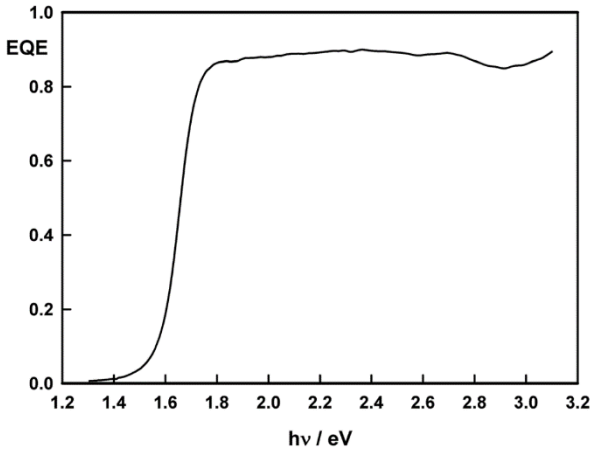

Figure 5.7 EQE spectrum of CZTS platelet (uncorrected for reflection losses). Reproduced from Ng *et al*.[9]

The bandgap and Urbach energy were found to be 1.68 eV and 2.4 k_BT respectively (reproduced in Figure 5.8), which are different to the values derived using SE data (*cf.* 1.60 eV and 6.7 k_BT). While the bandgap values derived from the Tauc plot should be considered approximate due to tail states,[18] the difference in Urbach energies suggests that lower energy optical transitions in the tail region lead to bound electron-hole states that require thermal activation to produce current in the external circuit and therefore have a lower chance of separation before recombination occurs. This can also explain why the experimental EQE spectrum shows a much steeper onset than the spectra calculated using the α value obtained by SE.

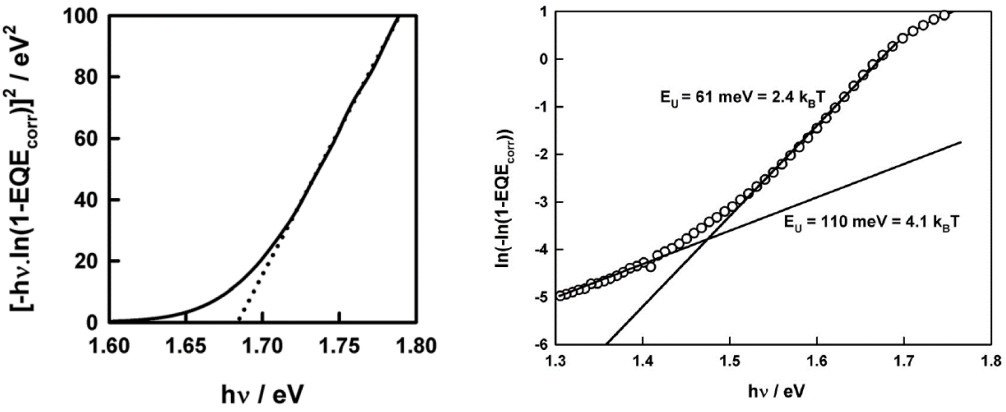

Figure 5.8 Tauc plot (left) and Urbach plot (right) of CZTS platelet crystal using data obtained from EQE measurement. Reproduced from Ng *et al*.[9]

An attempt was made to calculate the electron diffusion length using the Gärtner analysis.[19] However, it was not possible due to the presence of a high surface state capacitance (detailed in ESI of the paper, page 134). This was not surprising since the presence of surface states can be related to surface preparation, and even carefully prepared single crystal semiconductor surfaces exhibit surface recombination.[20] Nevertheless, the very steep onset near the band edge in the EQE spectrum shows that the collection of minority carriers is very efficient.

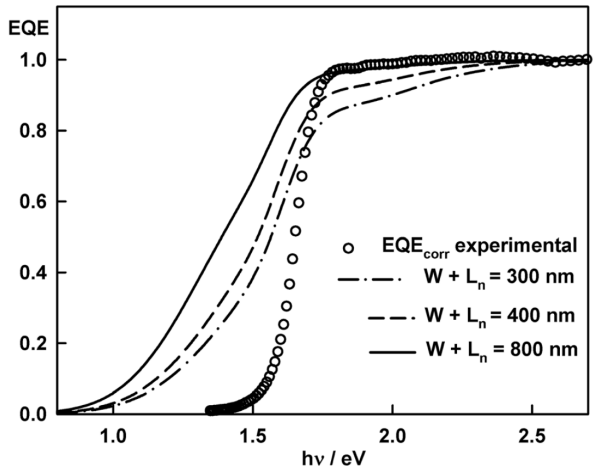

Figure 5.9 Comparison of experimental EQE with EQE calculated using Gärtner equation for the collection depth values shown. W was taken as 300 nm for the calculations, and L_n was varied. The α values were derived from spectroscopic ellipsometry. Reproduced from Ng *et al*.[9]

The EQE spectrum was also plotted against different values of collection depth *W* + L_n calculated using the Gärtner equation (reproduced in Figure 5.9):

Equation 5.2

$$\mathrm{EQE} = 1 - \frac{\exp(-\alpha W)}{1 + \alpha L_n}$$

where α is the absorption coefficient, W is the depletion width, and L_n is the diffusion length of electrons. The fitting above 1.75 eV indicated a collection depth of roughly 1 µm. In order to fit the whole EQE spectrum with a collection depth of 1 µm, the doping density would have to be 10^{15} cm^{-3}, which is at least an order of magnitude less than the reported doping density of CZTS.[21-25]

5.7 Electrolyte electroreflectance (EER)

Electroreflectance is another powerful technique for obtaining the bandgap of semiconductors. Two transitions were obtained from the EER fits, with energies of 1.71 and 1.81 eV, both being higher than the 1.68 eV derived from the Tauc plot using EQE data. Since EER should correspond to the third derivative of the imaginary part of the dielectric functions (ε''),[26] the SE data of the same sample was differentiated and is similar to the EER spectra (reproduced in Figure 5.10). A high broadening parameter of 192 meV provided further evidence of disorder leading to band energy fluctuations.

The EER spectrum was also compared with those reported in literature detailed in the main text, and also reproduced in Figure 5.10. The line shapes of our data resemble more the EER spectra reported for CZTSe solar cells,[27, 28] while it is different to the one reported for CZTS single crystal grown using a similar technique as ours.[29]

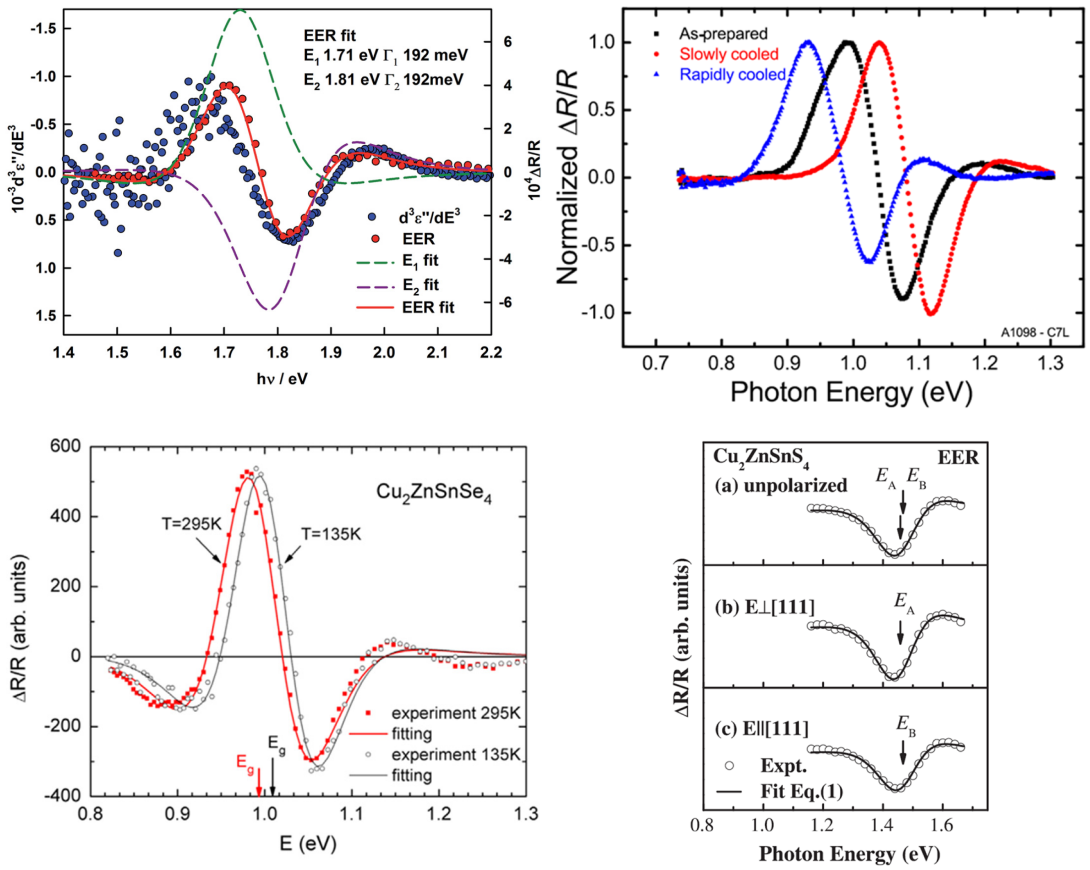

Figure 5.10 EER spectra of (Top left) CZTS platelet crystal in this work. Navy blue dots shows the third derivative of ε'' obtained from SE. Reproduced from Ng *et al.*[9] (Top right) CZTSe solar cell with different cooling profile. Reproduced from Krämmer *et al.*[27] (Bottom left) CZTSe solar cell. Reproduced from Krustok *et al.*[28] (Bottom right) CZTS single crystal. Reproduced from Levcenco *et al.*[29]

5.8 Conclusion

A series of characterisations were carried out on well-formed CZTS single crystals grown by chemical vapour transport. The results from the different techniques mostly agree with each other, for instance, the observation of a band tail using resonance Raman spectroscopy, PL, SE and EQE measurements, which is attributed to residual disorder in CZTS. However, the bandgap derived from Tauc plots using SE and EQE data are in the range of 1.60 – 1.68 eV, the band-to-band transition observed in steady state PL and TRPL are 1.58 and 1.65 eV, whereas the fitting of EER spectra indicates two distinct transitions at 1.71 and 1.81 eV. This discrepancy in bandgap values highlights the difficulty of using Tauc plots and PL to determine the bandgap in materials that have a high density of tail states.

The near unity EQE in the plateau region indicates very effective collection of photogenerated electron-hole pairs despite the fact that 20 – 30% Cu/Zn disorder is estimated in the sample, while the shape of the spectrum is consistent with a carrier collection depth approaching 1 μm. This suggested Cu/Zn disorder has minimal effect to current collection.

Finally, the effect on the optoelectronic properties of including a sodium source in the starting materials for CZTS crystal growth appears to be minor. This may indicate that the beneficial influence of sodium on the performance of CZTS solar cells is more likely to be associated with grain boundary effects.

Reference

1. Petříček, V., Dušek, M., and Palatinus, L., *Crystallographic Computing System JANA2006: General features*, in *Zeitschrift für Kristallographie - Crystalline Materials*. 2014. p. 345.
2. Farrugia, L., *WinGX suite for small-molecule single-crystal crystallography.* Journal of Applied Crystallography, 1999. **32**(4): p. 837-838.
3. Khare, A., Himmetoglu, B., Johnson, M., Norris, D.J., Cococcioni, M., and Aydil, E.S., *Calculation of the lattice dynamics and Raman spectra of copper zinc tin chalcogenides and comparison to experiments.* J. Appl. Phys., 2012. **111**(8): p. 083707.
4. Gurel, T., Sevik, C., and Cagin, T., *Characterization of vibrational and mechanical properties of quaternary compounds Cu_2ZnSnS_4 and $Cu_2ZnSnSe_4$ in kesterite and stannite structures.* Physical Review B, 2011. **84**(20).
5. Valakh, M.Y., Kolomys, O.F., Ponomaryov, S.S., Yukhymchuk, V.O., Babichuk, I.S., Izquierdo-Roca, V., Saucedo, E., Perez-Rodriguez, A., Morante, J.R., Schorr, S., and Bodnar, I.V., *Raman scattering and disorder effect in Cu_2ZnSnS_4.* physica status solidi (RRL) – Rapid Research Letters, 2013. **7**(4): p. 258-261.
6. Dimitrievska, M., Fairbrother, A., Pérez-Rodríguez, A., Saucedo, E., and Izquierdo-Roca, V., *Raman scattering crystalline assessment of polycrystalline Cu_2ZnSnS_4 thin films for sustainable photovoltaic technologies: Phonon confinement model.* Acta Materialia, 2014. **70**(0): p. 272-280.
7. Scragg, J.J.S., Choubrac, L., Lafond, A., Ericson, T., and Platzer-Björkman, C., *A low-temperature order-disorder transition in Cu_2ZnSnS_4 thin films.* Applied Physics Letters, 2014. **104**(4): p. 041911.
8. Paris, M., Choubrac, L., Lafond, A., Guillot-Deudon, C., and Jobic, S., *Solid-State NMR and Raman Spectroscopy To Address the Local Structure of Defects and the Tricky Issue of the Cu/Zn Disorder in Cu-Poor, Zn-Rich CZTS Materials.* Inorganic Chemistry, 2014. **53**(16): p. 8646-8653.
9. Ng, T.M., Weller, M.T., Kissling, G.P., Peter, L.M., Dale, P., Babbe, F., de Wild, J., Wenger, B., Snaith, H.J., and Lane, D., *Optoelectronic and spectroscopic characterization of vapour-transport grown Cu_2ZnSnS_4 single crystals.* Journal of Materials Chemistry A, 2017. **5**(3): p. 1192-1200.
10. Van Puyvelde, L., Lauwaert, J., Smet, P.F., Khelifi, S., Ericson, T., Scragg, J.J., Poelman, D., Van Deun, R., Platzer-Björkman, C., and Vrielinck, H., *Photoluminescence investigation of Cu_2ZnSnS_4 thin film solar cells.* Thin Solid Films, 2015. **582**(0): p. 146-150.
11. Quang Phuong, L., Okano, M., Yamada, Y., Nagaoka, A., Yoshino, K., and Kanemitsu, Y., *Photocarrier localization and recombination dynamics in Cu_2ZnSnS_4 single crystals.* Applied Physics Letters, 2013. **103**(19): p. 191902.
12. Scragg, J.J.S., Larsen, J.K., Kumar, M., Persson, C., Sendler, J., Siebentritt, S., and Bjorkman, C.P., *Cu-Zn disorder and band gap fluctuations in $Cu_2ZnSn(S,Se)_4$: Theoretical and experimental investigations.* Physica Status Solidi B-Basic Solid State Physics, 2016. **253**(2): p. 247-254.
13. Leitao, J.P., Santos, N.M., Fernandes, P.A., Salome, P.M.P., da Cunha, A.F., Gonzalez, J.C., Ribeiro, G.M., and Matinaga, F.M., *Photoluminescence and electrical study of fluctuating potentials in Cu_2ZnSnS_4-based thin films.* Physical Review B, 2011. **84**(2): p. 024120.

14. Gershon, T., Shin, B., Bojarczuk, N., Gokmen, T., Lu, S., and Guha, S., *Photoluminescence characterization of a high-efficiency Cu_2ZnSnS_4 device.* Journal of Applied Physics, 2013. **114**(15): p. 154905.
15. Li, S.-Y., Hägglund, C., Ren, Y., Scragg, J.J.S., Larsen, J.K., Frisk, C., Rudisch, K., Englund, S., and Platzer-Björkman, C., *Optical properties of reactively sputtered Cu_2ZnSnS_4 solar absorbers determined by spectroscopic ellipsometry and spectrophotometry.* Solar Energy Materials and Solar Cells, 2016. **149**: p. 170-178.
16. Ito, K., *Copper Zin Tin Sulfide-based Thin Film Solar Cells*. 2015, Chichester, United Kingdom: Wiley. 421.
17. Li, J., Du, H., Yarbrough, J., Norman, A., Jones, K., Teeter, G., Terry, F.L., and Levi, D., *Spectral optical properties of Cu_2ZnSnS_4 thin film between 0.73 and 6.5 eV.* Optics Express, 2012. **20**(S2): p. A327-A332.
18. Siebentritt, S., Rey, G., Finger, A., Regesch, D., Sendler, J., Weiss, T.P., and Bertram, T., *What is the bandgap of kesterite?* Solar Energy Materials and Solar Cells, 2016. **158, Part 2**: p. 126-129.
19. Gärtner, W.W., *Depletion-Layer Photoeffects in Semiconductors.* Physical Review, 1959. **116**(1): p. 84-87.
20. Peter, L.M., *CHAPTER 1 Photoelectrochemistry: From Basic Principles to Photocatalysis*, in *Photocatalysis: Fundamentals and Perspectives*. 2016, The Royal Society of Chemistry. p. 1-28.
21. Ito, K. and Nakazawa, T., *Electrical and Optical Properties of Stannite-Type Quaternary Semiconductor Thin Films.* Japanese Journal of Applied Physics, 1988. **27**(Part 1, No. 11): p. 2094-2097.
22. Fernandes, P.A., Salome, P.M.P., and da Cunha, A.F., *Precursors' order effect on the properties of sulfurized Cu_2ZnSnS_4 thin films.* Semiconductor Science and Technology, 2009. **24**(10).
23. Chan, C.P., Lam, H., and Surya, C., *Preparation of Cu_2ZnSnS_4 films by electrodeposition using ionic liquids.* Solar Energy Materials and Solar Cells, 2010. **94**(2): p. 207-211.
24. Huang, S., Luo, W., and Zou, Z., *Band positions and photoelectrochemical properties of Cu_2ZnSnS_4 thin films by the ultrasonic spray pyrolysis method.* Journal of Physics D-Applied Physics, 2013. **46**(23).
25. Cui, H., Lee, C.-Y., Li, W., Liu, X., Wen, X., and Hao, X., *Improving Efficiency of Evaporated Cu_2ZnSnS_4 Thin Film Solar Cells by a Thin Ag Intermediate Layer between Absorber and Back Contact.* International Journal of Photoenergy, 2015. **2015**: p. 9.
26. Aspnes, D.E., *Third-derivative modulation spectroscopy with low-field electroreflectance.* Surface Science, 1973. **37**: p. 418-442.
27. Krämmer, C., Huber, C., Zimmermann, C., Lang, M., Schnabel, T., Abzieher, T., Ahlswede, E., Kalt, H., and Hetterich, M., *Reversible order-disorder related band gap changes in $Cu_2ZnSn(S,Se)_4$ via post-annealing of solar cells measured by electroreflectance.* Applied Physics Letters, 2014. **105**(26): p. 262104.
28. Krustok, J., Raadik, T., Grossberg, M., Giraldo, S., Neuschitzer, M., López-Marino, S., and Saucedo, E., *Temperature dependent electroreflectance study of $Cu_2ZnSnSe_4$ solar cells.* Materials Science in Semiconductor Processing, 2015. **39**: p. 251-254.

29. Levcenco, S., Dumcenco, D., Wang, Y.P., Huang, Y.S., Ho, C.H., Arushanov, E., Tezlevan, V., and Tiong, K.K., *Influence of anionic substitution on the electrolyte electroreflectance study of band edge transitions in single crystal $Cu_2ZnSn(S_xSe_{1-x})_4$ solid solutions.* Optical Materials, 2012. **34**(8): p. 1362-1365.

UNIVERSITY OF BATH

Statement of Authorship (to preface each co-authored paper)

This declaration concerns the article entitled:									
Optoelectronic and Spectroscopic Characterization of Vapour-Transport Grown Cu_2ZnSnS_4 Single Crystals									
Publication status (tick one)									
Draft manuscript		**Submitted**		**In review**		**Accepted**		**Published**	✓
Publication details (reference)	Journal of Materials Chemistry A, 2017, **5**, 1192-1200 DOI: 10.1039/C6TA09817G								
Candidate's contribution to the paper (detailed, and also given as a percentage).	The candidate contributed to/ considerably contributed to/predominantly executed the… Formulation of ideas: (50%) It was the author's idea to grow large single crystals of CZTS so that they can be investigated and characterised. EQE measurements and EER were suggested by LMP because similar measurements with other semiconductors were carried out / supervised by LMP in the past. Spectroscopic ellipsometry and PL decay were also suggested by LMP because he knows the contact. LMP also established the relationship between the results gathered from different techniques. Design of methodology: (60%) Same as experiment work below, with the exception of EQE measurements and EER, where LMP is an expert in the setup and demonstrated the techniques to the author. Experimental work: (75%) Synthesis, elemental analysis, Raman spectroscopy, EQE measurements, EER measurements and spectroscopic ellipsometry were fully carried out by the author. MTW carried out SCXRD experiment and data analysis. MTW also supervised the author. GPK carried out impedance measurements. GPK also helped setting up the equipment for EER measurement and trained the author to carry out EQE and EER measurements. LMP helped setting up the equipment for EER measurement, and carried out the EER data analysis. LMP also facilitated all collaborations outside the author's university. PD hosted the author at the University of Luxembourg. PD was also the supervisor for FB and JdW.								

	FB carried out the analysis of steady sate PL data. JdW measured the steady state PL with the author observing next to JdW. BW measured and analysed the TRPL data. HJS provided the equipment for TRPL measurements. DL trained the author and provided the equipment for spectroscopy ellipsometry. DL also hosted the author at the University of Cranfield. Presentation of data in journal format: (15%) The majority of the manuscript was prepared by LMP.		
Statement from Candidate	This paper reports on original research I conducted during the period of my Higher Degree by Research candidature.		
Signed		**Date**	

The following journal article is reproduced by permission of The Royal Society of Chemistry

Journal of Materials Chemistry A

PAPER

View Article Online
View Journal | View Issue

Cite this: J. Mater. Chem. A, 2017, 5, 1192

Optoelectronic and spectroscopic characterization of vapour-transport grown Cu_2ZnSnS_4 single crystals†

Tat Ming Ng,[ab] Mark T. Weller,[b] Gabriela P. Kissling,‡[b] Laurence M. Peter,*[b] Phillip Dale,[c] Finn Babbe,[c] Jessica de Wild,[c] Bernard Wenger,[d] Henry J. Snaith[d] and David Lane[e]

Single crystals of Cu_2ZnSnS_4 (CZTS) have been grown by iodine vapor transport with and without addition of NaI. Crystals with tin-rich copper-poor and with zinc-rich copper-poor stoichiometries were obtained. The crystals were characterized by single crystal X-ray diffraction, energy-dispersive X-ray spectroscopy, photocurrent spectroscopy and electroreflectance spectroscopy using electrolyte contacts as well as by spectroscopic ellipsometry, Raman spectroscopy and photoluminescence spectroscopy (PL)/decay. Near-resonance Raman spectra indicate that the CZTS crystals adopt the kesterite structure with near-equilibrium residual disorder. The corrected external quantum efficiency of the p-type crystals measured by photocurrent spectroscopy approaches 100% close to the bandgap energy, indicating efficient carrier collection. The bandgap of the CZTS crystals estimated from the external quantum efficiency spectrum measured using an electrolyte contact was found to be 1.64–1.68 eV. An additional sub-bandgap photocurrent response (Urbach tail) was attributed to sub bandgap defect states. The room temperature PL of the crystals was attributed to radiative recombination *via* tail states, with lifetimes in the nanosecond range. At high excitation intensities, the PL spectrum also showed evidence of direct band to band transitions at ~1.6 eV with a shorter decay time. Electrolyte electroreflectance spectra and spectra of the third derivative of the optical dielectric constant in the bandgap region were fitted to two optical transitions at 1.71 and 1.81 eV suggesting a larger valence band splitting than predicted theoretically. The high values of the EER broadening parameters (192 meV) indicate residual disorder consistent with the existence of tail states.

Received 13th November 2016
Accepted 12th December 2016

DOI: 10.1039/c6ta09817g

www.rsc.org/MaterialsA

Introduction

The kesterites Cu_2ZnSnS_4 (CZTS) and $Cu_2ZnSnSe_4$ (CZTSe) continue to excite interest as potential earth-abundant alternatives to $CuIn_xGa_{(1-x)}Se_2$ (CIGSe) for application as absorber materials in thin film solar cells.[2–6] By 2014, the efficiency of kesterite solar cells had reached 12.6%,[7] but progress since then has focused mainly on developing safer non-toxic routes to fabrication of CZTS(Se) absorber layers. The main limiting factor for device performance is the open circuit voltage, which is ~200 mV lower than that of CIGSe cells with comparable bandgaps. The reasons for the voltage losses in kesterite cells are still not clear.[6] One possible cause is enhanced recombination due to tail states arising from Cu/Zn disorder,[8,9] but a recent review of the evidence for this explanation failed to reach a firm conclusion.[10] Alternative explanations include enhanced surface recombination at grain boundaries[11] and the influence of secondary phases.[6] In order to discover more about the bulk properties of CZTS, we have grown single crystals with different stoichiometric compositions by iodine vapor transport[12] (with and without the addition of NaI as a sodium source) and have characterized their optoelectronic properties using photocurrent spectroscopy with electrolyte contacts (PS) as well as electrolyte electroreflectance spectroscopy (EER), spectroscopic ellipsometry (SE), Raman spectroscopy and photoluminescence (PL).

[a]Centre for Sustainable Chemical Technologies, University of Bath, Bath BA2 7AY, UK
[b]Department of Chemistry, University of Bath, Bath BA2 7AY, UK. E-mail: l.m.peter@bath.ac.uk
[c]Physics and Materials Science Research Unit, University of Luxembourg, 41, rue du Brill, L-4422 Belvaux, Luxembourg
[d]University of Oxford, Clarendon Laboratory, Parks Road, Oxford, OX13PU, UK
[e]Cranfield Forensic Institute, Cranfield University, Defence Academy of the United Kingdom, Shrivenham, SN6 8LA, UK

† Electronic supplementary information (ESI) available: Oven cooling curve. Raman spectra/fitting. Comparison of SE data with ref. 1 Vineyard model and calculations. PL spectra/decay for needle. Tauc and Urbach plots. Gärtner analysis. Impedance data. EER results and validation of low field approximation. See DOI: 10.1039/c6ta09817g

‡ Present address: Department of Chemistry, University of Southampton, Southampton SO17 1BJ, UK.

It is possible to grow single phase kesterite materials with significant deviations from stoichiometry.[13] In this work, we have focused on zinc-rich/copper poor and tin-rich/copper poor materials because copper-poor stoichiometries give the best efficiencies in solar cells.[14] Our primary objectives included determination of the stoichiometry and bandgap of the single crystals and assessment of the optical properties. In addition, we have examined the dependence of the degree of substitutional disorder on composition and annealing conditions.

Analysis of the single crystal X-ray diffraction data from the Cu_2ZnSnS_4 crystals is unable to demonstrate unequivocally that they have the kesterite structure. Dumcenco *et al.*[15] have used Raman scattering to establish that CZTS crystals grown by chemical vapor transport adopt the kesterite phase. For our crystals, the presence of the kesterite phase is supported by the peak assignments in the near-resonance Raman spectra, which also showed that the as-grown crystals have a low level of disorder comparable with that achieved by low temperature (150 °C) annealing of fully disordered crystals for 24 hours.

The results obtained by PS for etched single crystals indicate that carrier collection is highly efficient in the voltage-biased single crystal/electrolyte junction, with external quantum efficiencies (EQE) corrected for reflection approaching 100%. The experimental EQE spectrum was compared with spectra calculated for different carrier collection depths using the absorption coefficient data obtained by spectroscopic ellipsometry (SE). The onset seen in the photocurrent excitation spectrum is much sharper than in the absorption spectrum derived from SE, allowing more reliable determination of the bandgap from Tauc plots. The bandgap values obtained by the Tauc/EQE analysis (1.64–1.68 eV) are close to the 1.64 eV reported by Fernandes *et al.*[16] for CZTS layers prepared from sulfurized metallic precursors, although they are considerably higher than values reported, for example, by Li *et al.*[1] for polycrystalline thin films prepared by reactive sputtering (1.55–1.59 eV). Line shape fitting of the EER spectra and the third derivative of the optical dielectric constant obtained by SE reveals two optical transitions at 1.71 eV and 1.81 eV with substantial spectral broadening (Γ = 192 meV) attributed to the presence of residual disorder, even in as-grown slow-cooled samples with near equilibrium disorder. The observed separation between the two transitions (100 meV) is larger than the crystal field splitting calculated for kesterite CZTS (40 meV) by Persson *et al.*[17]

Experimental details

The synthesis of CZTS single crystals using iodine vapor transport in a two zone furnace has been described elsewhere.[12] The CZTS starting materials were synthesized in evacuated sealed quartz ampules using the metals (Cu 99.7%, Zn 99.9%, Sn 99.85%) and elementary sulfur (99.999%). Vapor transport growth was carried out using 99.999% iodine. The effect of adding sodium was investigated in one of the growth runs by adding 1% (w/w) sodium iodide (99+%) to the CZTS starting material. The crystals were cooled naturally to room temperature over 24 hours after the oven was switched off. Further details, including the stoichiometric composition of the synthesis mixtures as well as the oven cooling curve are given in the ESI.† The as-grown crystals were rinsed in chloroform and isopropanol to remove traces of iodine.

Single-crystal X-ray diffraction (SXD) data were collected at room temperature operating with Mo-K_α radiation (λ = 0.71073 Å) (Agilent Xcalibur). Structures were solved using the WinGX suite of programmes,[18] utilizing XPREP[19] and SHELX-97,[20] by direct methods.[21] For the two crystal types obtained (needles and platelets), analysis was undertaken using the models reported in the literature for kesterite (in space group $I\bar{4}$) and stannite (space group $I\bar{4}2m$) descriptions of Cu_2ZnSnS_4.[22]

Elemental analysis of the materials was carried out using energy-dispersive X-ray spectroscopy (EDS) (10 and 20 kV, Oxford Instruments).

Near-resonance Raman measurements were performed at room temperature under ambient atmosphere (Renishaw inVia). A linearly polarized laser beam (785 nm) was focused into a spot size ~5 μm in diameter. Prior to the measurements, the system was calibrated with polycrystalline Si at 520 cm^{-1}.

The crystals were etched in saturated Na_2S solution followed by 30% H_2O_2/1 M H_2SO_4. After rinsing, the samples were treated with 1 M HCl, to remove metal (hydr)oxides. Crystals treated in this way are referred to in the text as 'etched'.

Further details of the PC, PL, EER, SE and Raman measurements and fitting procedures are given in the ESI†. For the PC and EER measurements, the mounted and etched kesterite crystals were contacted on the abraded rear side with an evaporated gold contact. Measurements were made using an air-saturated 0.1 M acetate buffer electrolyte (pH 4.5) in a 3-electrode cell with platinum counter and Ag|AgCl reference electrodes controlled by a battery-operated low-noise potentiostat.

Results and discussion

Composition and degree of disorder of the kesterite phase

Two main crystal shapes were obtained from the iodine vapor transport growth: needles (no sodium present in starting material) and platelets (1% w/w NaI present in starting material). Fig. 1 shows examples of the two types. Both crystals exhibited one smooth reflective surface suitable for SE and EER measurements.

The averaged elemental compositions of the crystals determined by EDS at 6 different points on each crystal are summarized in Table 1. The standard deviations are shown in brackets. The level of sodium (if present) in the platelet was below the limit of detection by EDS (the sensitivity is limited by

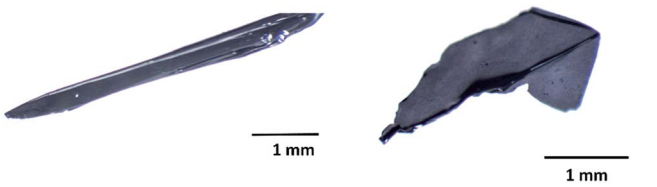

Fig. 1 Typical shapes of the Cu_2ZnSnS_4 crystals grown by iodine vapor transport. The platelet on the right was grown from CZTS starting material containing 1% (w/w) NaI.

Table 1 Elemental composition of Cu_2ZnSnS_4 crystals as determined by energy dispersive X-ray spectroscopy

Type	Cu	Zn	Sn	S	Cu/(Zn + Sn)
Needle	22.6 (±0.4)	14.2 (±0.9)	12.5 (±0.4)	50.7 (±0.4)	0.85 (±0.5)
Platelet	22.8 (±0.6)	12.1 (±0.6)	13.3 (±0.7)	51.9 (±1.0)	0.90 (±0.5)

the overlap of the Na and Zn peaks). The sodium concentration determined by atomic absorption spectroscopy corresponded to 0.13 mol% in the platelet sample. No iodine was detected in either crystal after rinsing in chloroform and isopropanol.

The compositions of the two types of crystal are illustrated in the pseudo ternary phase diagram shown in Fig. 2. The classification into type A, B, C, D and E follows the notation used by Choubrac *et al.*[23–25]

The needle composition is close to the A type line, which corresponds to the substitution

$$2Cu \rightarrow V_{Cu} + Zn_{Cu}$$

whereas the platelet stoichiometry is closer to the E type[26] line, which corresponds to the substitution

$$2Cu + Zn \rightarrow 2V_{Cu} + Sn_{Zn}$$

XRD structure analysis

Distinguishing between the kesterite and stannite structures of CZTS, which differ only in the ordering of the near isoelectronic copper and zinc atoms is not generally possible using laboratory X-ray data. Only anomalous-scattering X-ray single crystal diffraction[27] and neutron single crystal diffraction can fully distinguish the two copper and zinc distributions. Powder neutron diffraction has been proposed as a way of distinguishing the two structure descriptions,[28] but this approach is not reliable as a consequence of peak multiplicities in powder methods. In addition to the copper and zinc ordering, the sulfur position in the kesterite $I\bar{4}$ space group can be displaced on to a general (x, y, z) position (from x, x, z), potentially modifying reflection intensities.

For both needle and platelet crystals, the structure was solved and refined using the kesterite model in the space group $I\bar{4}$.

For the platelet, a final R_1 of 2.68% and wR_2 = 7.04% was obtained, and corresponding values for the needle were R_1 = 2.13% and wR_2 = 6.24%. Refinements using the disordered stannite description showed marginally worse R-factors but not significant enough to completely discount the stannite structure. No evidence of lowering of the lattice type to primitive, as in the $P\bar{4}2c$ description of Cu/Zn ordered CZTS, was observed in the single crystal XRD data. The results are summarized in Table 2.

Small but significant differences in the unit cell volume were found for the two crystal types, with the platelets giving a 0.08% higher value than the needle.

In view of the problems with the XRD interpretation, identification of the crystal structure as that of the kesterite was based on the Raman analysis described in the next section.

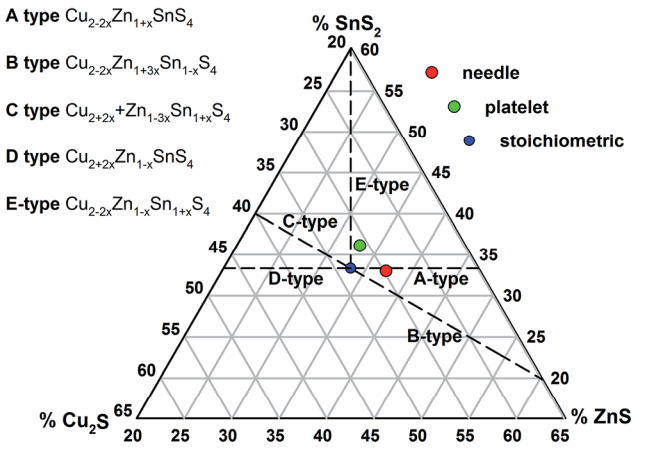

Fig. 2 Pseudo-ternary phase diagram for Cu_2ZnSnS_4 showing composition of the two sample types used in the study.

Raman spectroscopy: phase identification and disorder

Dumcenco *et al.*[15] used Raman spectroscopy to identify the kesterite crystal structure of CZTS single crystals grown by chemical vapor transport. These authors compared the observed Raman spectra with the results of theoretical calculations[29,30] for the kesterite and stannite crystal structures. A similar analysis for both types of our as-grown crystals confirms that they too have the kesterite structure (see the peak assignments and comparison with the results of the theoretical calculations given in the ESI†).

Disorder is a key issue in kesterites.[8,10,28,31,32] Studies of the order/disorder transition in CZTS[26,33,34] have shown that the degree of Cu/Zn antisite disorder exhibits second-order phase transition behaviour, with the complete disorder occurring at temperatures above *ca.* 280 °C. Paris *et al.*[35] have shown how

Table 2 Summary of single crystal XRD analysis

	Needle	Platelet
a/Å	5.4282(1)	5.4289(1)
c/Å	10.8198(5)	10.8256(5)
Unit cell volume/Å^3	318.809(19)	319.062(19)
Temperature/K	298	298
R indices observed data	R_1 = 0.0213	R_1 = 0.0268
	wR_2 = 0.0624	wR_2 = 0.0704
GooF	1.038	0.846

solid state NMR and Raman spectroscopy can be used to assess disorder in CZTS, and Rudisch *et al.*[33] have correlated Raman spectra with the degree of Cu/Zn disorder defined by the order parameter S, which is given by

$$S = \frac{P(\mathrm{Cu_{2c}}) - a_{2c}}{1 - a_{2c}} = 2P(\mathrm{Cu_{2c}}) - 1 = 2P(\mathrm{Zn_{2d}}) - 1 \quad (1)$$

here $P(\mathrm{Cu_{2c}})$ and $P(\mathrm{Zn_{2d}})$ are the probabilities that Cu and Zn atoms occupy the 2c and 2d sites in the kesterite structure respectively, and a_{2c} (=0.5) is the fraction of 2c sites in the $z = 1/4$, 3/4 lattice planes as discussed by Scragg *et al.*[8]

Rey *et al.*[36] have discussed the dynamics of the order/disorder transition for $Cu_2ZnSnSe_4$ (CZTSe) using the Vineyard model,[37] which predicts the temperature and time dependence of S for vacancy and direct interchange mechanisms (see ESI†). Since we are dealing with a second order phase transformation, perfect ordering can only exist at 0 K. In practice, the highest achievable value of S is determined by the temperature dependence of the kinetics of atom interchange: at low temperatures (below *ca.* 150 °C), the disorder becomes 'frozen in' on a realistic time scale. The calculations based on the Vineyard model that are shown in the ESI† suggest that the highest values of S achievable by prolonged low temperature annealing will be in the range 0.7–0.8.

The degree of ordering of the as-grown crystals was assessed from near-resonance Raman spectra (excitation 785 nm). Fig. 3 contrasts the Raman spectrum of an as-grown platelet with the spectrum obtained after annealing at 300 °C and quenching to freeze in complete disorder. The fully disordered crystal was then annealed at 150 °C for 24 hours to induce equilibrium ordering (*cf.* Fig. 3). The Raman spectrum of this sample resembles that of the as-grown crystal, indicating that near-equilibrium ordering occurs during the slow cooling of the crystals in the furnace. Similar trends in S as a function of annealing temperature have been reported by Rudisch *et al.*[33] for polycrystalline CZTS films prepared by reactive sputtering.

Paris *et al.*[35] have suggested that a measure of the degree of Cu/Zn disorder is provided by the use of two empirical parameters, Q and Q', defined in terms of the intensity ratios of the main near-resonance Raman peaks as follows.

$$Q = I_{287}/I_{303},\ Q' = I_{338}/(I_{366} + I_{374}) \quad (2)$$

Fig. 4 illustrates the deconvolution of the Raman spectra used to obtain the relative peak intensities for the case of the disordered platelet sample. The deconvolution of the Raman spectrum of the ordered platelet as well as the spectrum for the as-grown needle sample are given in the ESI.† Table 3 lists the Q and Q' values obtained using spectra measured on the platelet sample at two different spots and averaged before and after disordering.

For of the as-grown platelet, Q is higher than values reported for low temperature annealed CZTS films prepared by Scragg *et al.*[9] (stoichiometric CZTS, $Q < 2.5$) and by Rudisch *et al.*[33] (type B CZTS, $Q < 3.3$) using reactive sputtering. It is also higher than the value of 8.2 reported by Paris *et al.*[35] for slow-cooled (10 °C per h) – and hence relatively highly ordered – bulk polycrystalline type A CZTS. Similarly, Q' is higher than the value of 3.6 reported by the same authors for slow-cooled type A material.

We conclude that the as-grown platelet used in our study has ordering close to the equilibrium value for ~100–150 °C. The corresponding S value is unknown, but if the Vineyard model calculation in the ESI† is used as a guide, it would be in the range 0.7–0.8. Even if this level of ordering were achieved, it would still leave around 20–30% of the sites disordered, with significant consequences for band gap fluctuations and band gap tailing.

The Q and Q' values for the as-grown needle sample are both lower at around 5 and 3.5 respectively, suggesting that it may be less ordered than the platelet.

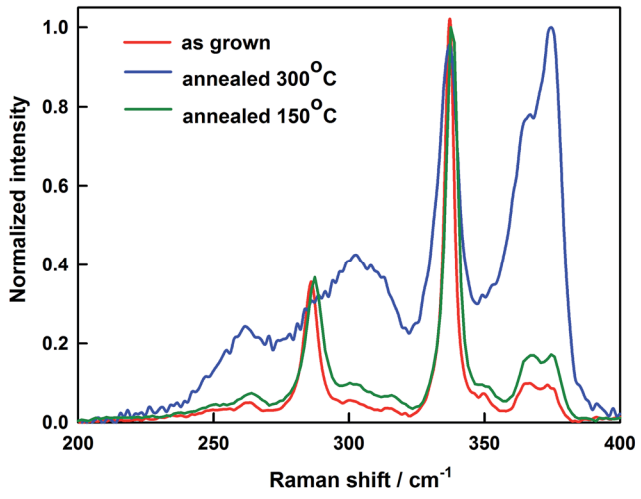

Fig. 3 Near-resonance Raman spectrum of as-grown CZTS platelet crystal compared with the spectrum of the fully disordered crystal (annealed at 300 °C). The spectrum obtained after annealing the disordered crystal for 24 h at 150 °C shows that near-equilibrium ordering is re-established.

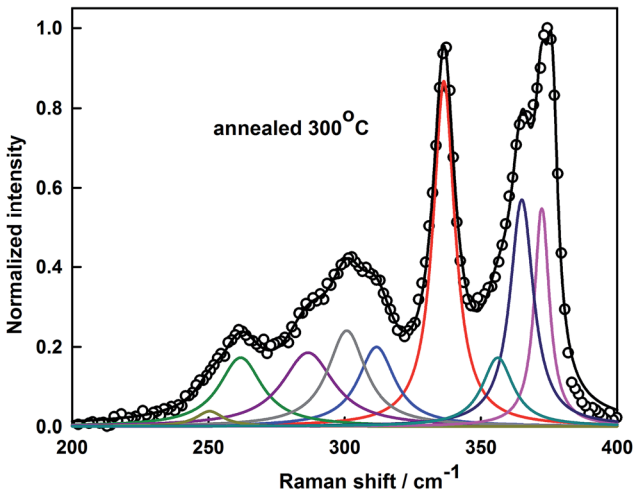

Fig. 4 Illustration of the fitting of the near-resonance Raman spectrum of the fully disordered CZTS platelet used to obtain the parameters Q and Q'.

Table 3 Q and Q' values of copper-poor platelet sample as a function of annealing conditions

Annealing	Q	Q'
As-Grown	9.1 ± 1.1	5.7 ± 0.3
Annealed 300 °C	0.75 ± 0.40	0.8 ± 0.1

Photoluminescence

Fig. 5 shows the room temperature PL spectrum of the platelet crystal. The peak of the spectrum at 1.35 eV is substantially red shifted with respect to the bandgap of the material (1.68–1.71 eV – see below), which is consistent with emission taking place from tail states associated with disorder in the crystal. The intensity dependence of the peak position shown in the inset to Fig. 5 corresponds to a blue shift of 13 meV per decade, which agrees well with reported values.[38,39]

The PL spectrum for the needle exhibits a similar blue shift with a higher slope of 18 meV per decade (see ESI†). The blue shift seen for both CZTS crystals can be interpreted as an indication of potential fluctuations in the material.[40]

The dependence of the PL emission intensity on laser power for different samples (shown in the ESI†) corresponds to a power law PL $\propto I^m$, with m values ranging from 1.3–1.6. Levcenko *et al.* have reported a similar m value (1.3) for solution-processed CZTS layers. In the case of low temperature PL, m values greater than unity are usually attributed to band to band transitions,[41] but the value has more limited significance in the case of room temperature PL. Nevertheless, we conclude that the main PL peak is associated with near band edge (tail) states.

At higher intensities, a second peak becomes evident as a shoulder in the room temperature PL spectrum as illustrated by the semi-logarithmic plot in Fig. 6. Gershon *et al.*[42] have reported the emergence of a higher energy PL peak for high efficiency CZTS devices measured at 4 K, and have attributed it to free carrier recombination. These authors compared the PL lifetimes at 4 K for the low energy (1.16 eV) and high energy (1.43 eV) peaks. The low energy emission decayed on a time scale of microseconds (lifetime *ca.* 12 μs), indicating carrier trapping, whereas the high-energy component gave a much shorter lifetime of 1.7 ns, which is attributed to free carrier recombination not requiring activation by thermal excitation from tail states. Although there are problems in comparing low temperature measurements with our results, it seems reasonable to assume that the high-energy peak in the room temperature PL spectrum shown in Fig. 6 is due to band to band recombination, whereas the low energy peak corresponds to emission from tail states.

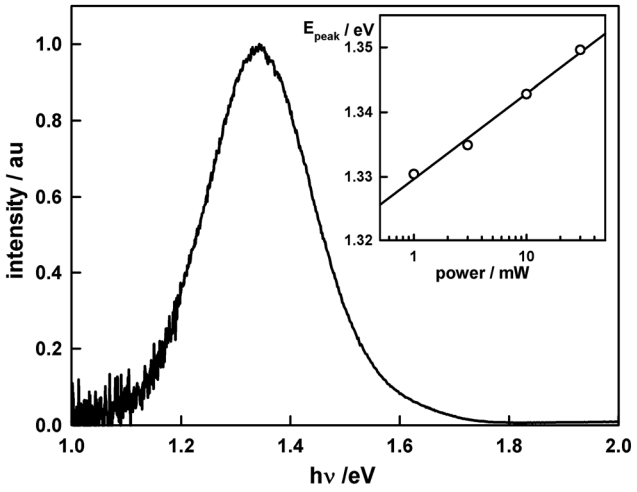

Fig. 5 Room temperature PL spectrum of CZTS platelet (laser intensity 10 mW). The inset shows the blue shift of the PL emission peak with increasing intensity.

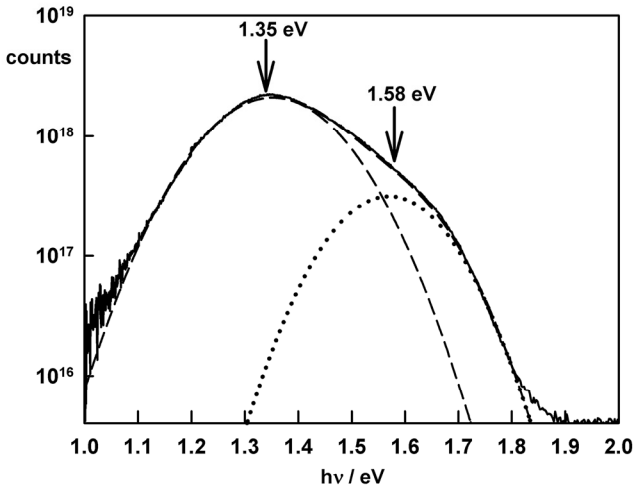

Fig. 6 PL spectrum of CZTS platelet showing shoulder at higher energy attributed to radiative band to band recombination (laser power 50 mW).

PL transients measured at room temperature for the platelet are illustrated in Fig. 7. The decay is slower when measured at 1.30 eV compared with 1.65 eV. The lifetimes obtained from the exponential fits shown in Fig. 7 are 3.5 ns (1.65 eV) and 6.8 ns (1.30 eV), similar to the 7.8 ns reported by Shin *et al.*[43] for an 8.4% efficient CZTS solar cell. However, the decay rates at the two photon energies are almost identical in the case of the needle (τ = 3.6 ns: see ESI†).

The lifetimes derived here may not correspond to the lifetime of free electrons moving in CZTS since multiple trapping processes may be involved.[39,44–46] This makes it difficult to calculate electron diffusion lengths, since the electron mobility will be reduced from the free electron value by multiple trapping. Phoung *et al.*[45] have used time-resolved femtosecond transient reflectance and optical pump-probe terahertz spectroscopy to study free carrier dynamics in CZTS single crystals, and they attribute the relatively long (ns) electron lifetimes to thermal release of carriers from tail states.

Spectroscopic ellipsometry

Spectra of the real and imaginary components of the optical dielectric constant and the absorption coefficient obtained by fitting the ellipsometric data for the platelet sample are shown

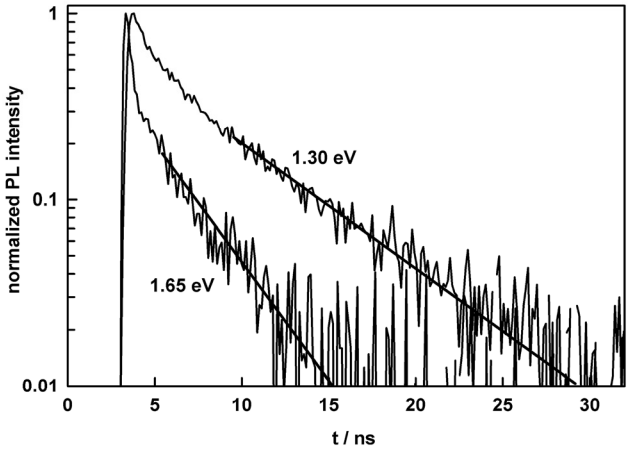

Fig. 7 Transient PL response of the CZTS platelet. Excitation energy 1.96 eV. Detection energies as shown.

in Fig. 8. Details of the fitting, as well as results for the needle sample, are given in the ESI,† which also includes a comparison with published optical data. The fitting used oscillators centred at 1.81, 2.60 and 4.27 eV. The absorption coefficient shows an exponential Urbach tail extending into the near infrared that is discussed below.

EQE measurements

Durant *et al.*[47] have reported electrolyte EQE measurements of natural kesterite crystals, but as far as we are aware, no detailed study of the photoresponse of synthetic CZTS crystals in contact with an electrolyte have been published previously. The EQE response of the single crystals was found to be strongly influenced by surface preparation. High EQE values could be obtained immediately after etching, but the photoresponse decayed slowly with time. The external quantum efficiency (EQE) for the semiconductor/electrolyte junction in the absence of surface recombination is given by the expression originally derived by Gärtner.[48]

$$\mathrm{EQE} = 1 - \frac{\exp(-\alpha W)}{1 + \alpha L_n} \quad (3)$$

Here W is the width of the space charge region, α is the wavelength dependent absorption coefficient and L_n is the diffusion length of electrons.

The EQE response of a freshly etched platelet crystal is shown in Fig. 9. Since the reflection loss is estimated to be of the order of 10% in the region where the EQE reaches a plateau, the spectrum indicates that essentially all photogenerated electrons are collected in the junction for photon energies above 1.7 eV. It follows that the second term on the right-hand side of the Gärtner equation must become negligible under these conditions. Near the band edge, we can assume that $\alpha L_n < 1$. In this case $-\ln(1 - \mathrm{EQE}_{corr}) = \alpha W$ (here EQE_{corr} is the EQE corrected for reflection losses).

Plots of $(\alpha h\nu)^2$ *vs.* $h\nu$ are commonly used to estimate the direct allowed bandgap (Tauc plots). The inset in Fig. 9 shows a plot of $[-h\nu \times \ln(1 - \mathrm{EQE}_{corr})]^2$ *vs.* photon energy, which is equivalent to the Tauc plot for a direct allowed transition. The intercept at 1.68 eV should therefore correspond to the optical bandgap, E_g, of the CZTS. A similar plot for the needle crystal gave a slightly lower bandgap of 1.64 eV (see ESI†). Tauc plots of the optical SE data for the platelet gave a slightly lower bandgap of 1.61 eV (see ESI†).

The exponential tail evident in the SE, EQE and Tauc plots is consistent with the existence of an Urbach tail associated with disorder in the CZTS crystal. The difficulties encountered when using Tauc plots for systems with sub-bandgap absorption (tail states) have been highlighted for the case of kesterites by Siebentritt *et al.*,[49] and these bandgap values should be considered approximate. As shown in the ESI,† the EQE response in the sub-bandgap energy range 1.4–1.7 eV can be fitted to an exponential Urbach distribution with $E_U = 2.2k_BT$, which is

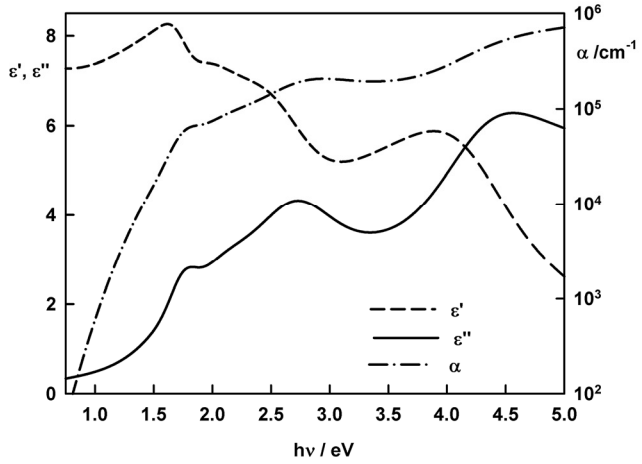

Fig. 8 Real and imaginary components of the optical dielectric constant for the CZTS platelet measured by spectroscopic ellipsometry. The figure also shows the absorption coefficient derived from the measurement.

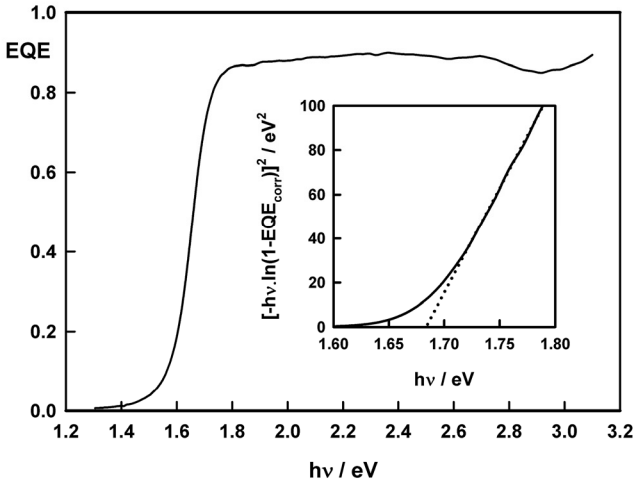

Fig. 9 EQE spectrum of CZTS platelet (uncorrected for reflection losses). Electrolyte; 0.1 M acetate buffer pH 4.5. Potential −1.0 V *vs.* Ag/AgCl. The insert shows a Tauc plot for a direct allowed transition ($E_g = 1.68$ eV).

considerably lower than the E_U value ($6.7k_BT$) derived from the SE data for the same energy range (see ESI†). The difference in Urbach energies suggests that lower energy optical transitions in the tail region lead to bound electron–hole states that require thermal activation to produce current in the external circuit and therefore have a lower chance of separation before recombination occurs.

If the semiconductor/electrolyte junction behaved ideally, the width of the space charge region should be controlled by the applied electrode potential, U, obeying the relationship $W \propto (U_{fb} - U)^{1/2}$, where U_{fb} is the flat band potential. Unfortunately, in the present case, attempts to measure the space charge capacitance as a function of applied potential by impedance spectroscopy revealed that the junction is not ideal due to the presence of a high surface state capacitance (see ESI†). This precluded full analysis of the potential dependence of the EQE spectra based on eqn (3), which can in principle give the absorption coefficient and the electron diffusion length, as demonstrated for p-GaP for example.[50] Nevertheless, the 'square' shape of the EQE spectrum in Fig. 9 shows that collection of minority carriers is very efficient even when the penetration depth of the light is large near the band edge. By contrast, the EQE spectra reported for high-performance CZTS solar cells generally show a slower rise from 1.4 eV to a peak at around 2.3 eV – see, for example, the EQE spectrum for a 2 μm CZTS absorber layer in a recent paper by Ren *et al.*[51]

Fig. 10 compares the measured EQE corrected for reflection losses with EQE plots calculated from the Gärtner equation (eqn (3)) for different values of the collection depth $W + L_n$ using values of the absorption coefficient derived from the SE measurements (*cf.* Fig. 8). Since reported doping densities for CZTS are of the order of 10^{16} cm^{-3}, the width of the space charge region under the conditions employed for EQE measurements has been taken as 300 nm (see ESI†). Using this value, the effect on the EQE spectrum of increasing the electron diffusion length was explored, and representative results are shown in Fig. 10. The fitting above *ca.* 1.75 eV indicates that the collection depth for minority carriers approaches 1 μm. This rather high value could indicate that the doping density is lower than assumed in the calculation. In the limit that $L_n \ll W$, W would be 1 μm, and the doping density would have to be *ca.* 10^{15} cm^{-3} to fit the spectrum.

It is apparent that the experimental EQE spectrum shows a much steeper onset than the spectra calculated using the α values obtained by SE. This can be explained if it is assumed that absorption of light in tails states below the band edge leads to bound states for which thermal excitation to create free charge carriers must compete with recombination.

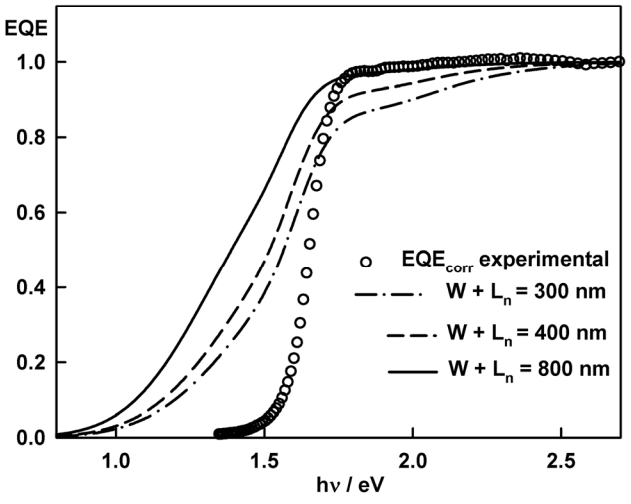

Fig. 10 Comparison of experimental EQE (Fig. 9, corrected for reflection losses) with EQE calculated using eqn (3) for the collection depth values shown. W was taken as 300 nm for the calculations, and L_n was varied. The α values were derived by spectroscopic ellipsometry.

Electrolyte electroreflectance

Electrolyte electroreflectance (EER) is a powerful technique for obtaining the bandgap of semiconductors. The method involves perturbing the electrical field in the space charge region by ac voltage modulation and detecting the synchronous changes in reflectance. Under low field conditions, the EER spectrum corresponds to the third derivative of the imaginary component of the optical dielectric constant,[52] and the results can be compared with those obtained by spectroscopic ellipsometry.[53] EER spectra can be modelled using a broadening parameter Γ that can be related to disorder and non-stoichiometry.[54,55] EER should therefore be a useful technique for characterizing cation disorder in CZTS. Fig. 11 shows the EER spectrum of the platelet crystal. A very similar EER spectrum was obtained for the needle (see ESI†).

Successful fitting of the EER spectrum required the use of two generalized line shape functions of the form proposed by Aspnes.[52,56]

$$\frac{\Delta R}{R} = \mathrm{Re}\left[Ce^{i\theta}(E - E_g - i\Gamma)^n\right] \quad (4)$$

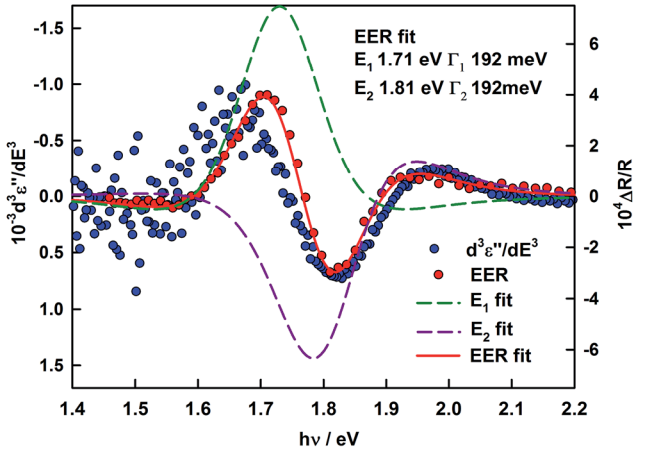

Fig. 11 EER spectrum of CZTS platelet showing fit to two transitions. The plot also shows the third derivative of the ε'' spectrum obtain by spectroscopic ellipsometry.

with $n = 5/2$ (3D critical point). Here $\Delta R/R$ is the normalized modulated reflectance, C is a scaling factor, θ is the phase projection factor, E is the photon energy, E_g is the bandgap energy and Γ is the broadening parameter. The EER response was found to depend linearly on the modulation amplitude, indicating that the low field expression is applicable[52] (see ESI†).

The fit shown in Fig. 11 corresponds to a superposition of two transitions at 1.71 eV and 1.81 eV, both values being higher than the bandgap, of *ca.* 1.68 eV derived from the Tauc plot in Fig. 9. The high Γ values obtained by the fitting of the EER spectra for CZTS provide further evidence of disorder leading to band energy fluctuations that effectively broaden the optical transitions (typical Γ values for single crystal binary semiconductors are considerably smaller, for example 53 meV for CdTe[57]). To check whether the EER spectrum does indeed correspond to the third derivative of ε'' as predicted by the Aspnes analysis, the SE data for the platelet crystal were differentiated, giving the result included in Fig. 11. The agreement confirms that the low field approximation is indeed valid.

The well-resolved EER spectrum shown in Fig. 11 differs significantly from spectra in the literature. Levcenco *et al.*[58] have reported room temperature EER spectra for CZTS single crystals grown by ICl_3 vapor transport, and their spectra (only shown over the range 1.2 to 1.6 eV) show a single peak at around 1.45 eV with very little response at higher energies. These authors also used the generalized line shape to analyse their EER spectra and reported A and B transitions at 1.457 eV and 1.464 eV. However, the line shapes of our EER spectra resemble more the EER spectra reported for CZTSe solar cells by Krämmer *et al.*[59] and by Krustok *et al.*[60] Clearly more work is needed to understand why our EER spectra differ so much from those reported in ref. 58.

Conclusions

Single crystals of CZTS have been grown with near-equilibrium disorder, as shown by near-resonance Raman spectroscopy. The band tail seen in the optical properties is attributed to residual disorder, which is also responsible for the red shift of the room temperature photoluminescence peak relative to the bandgap. The EQE spectra show much less evidence of the band tail, and this is attributed to a lower electron–hole separation efficiency for bound states created by sub-bandgap absorption. The bandgaps derived from Tauc plots of the optical and EQE data are in the range 1.60–1.64 eV, whereas the fitting of EER spectra indicates two adjacent transitions at higher energies (1.71 and 1.81 eV). This highlights the difficulty of using Tauc plots to determine the band gap in materials that have a high density of tail states.

The 100 meV separation of the transitions seen in the EER spectra could arise from crystal field splitting of the valence band, although it is higher than the 40 meV calculated by Persson *et al.*[17] for 0 K. The high value of the EQE in the plateau region of the EQE spectrum indicates 100% collection efficiency of photogenerated electron–hole pairs, while the shape of the spectrum is consistent with a collection depth approaching 1 μm. The electron lifetimes measured by PL decay are in the range 3.5–6.8 ns.

The effect on the optoelectronic properties of including a sodium source in the starting materials for CZTS crystal growth appears to be minor. This may indicate that the beneficial influence of sodium on the performance of CZTS solar cells is more likely to be associated with grain boundary effects.

Acknowledgements

This work was supported by the EPSRC PVTeam project (Grant No. EP/L017792/1). BW and HJS acknowledge EPSRC grant EP/L024667/1. TMN is funded by EPSRC Doctoral Training Centre in Sustainable Chemical Technologies at the University of Bath (Grant No. EP/G03768X/1). JdW thanks FNR for funding from the EATSS project and FB thanks FNR for funding from the CURI-K project. The authors acknowledge useful discussions with Jonathan Scragg and Shuyi Li (Angstrom Institute Uppsala) as well as Leo Choubrac and Michaël Paris (Nantes). The authors thank Shuyu Li for providing CZTS thin film optical data for comparison.

References

1 S.-Y. Li, C. Hägglund, Y. Ren, J. J. S. Scragg, J. K. Larsen, C. Frisk, K. Rudisch, S. Englund and C. Platzer-Björkman, *Sol. Energy Mater. Sol. Cells*, 2016, **149**, 170–178.
2 K. Ito, *Copper Zinc Tin Sulfide-Based Thin Film Solar Cells*, Wiley, Chichester, United Kingdom, 2015.
3 S. Adachi, *Earth-Abundant Materials for Solar Cells. Cu_2-II-IV-VI_4 Semiconductors*, Wiley, Chichester, United Kingdom, 2015.
4 T. Todorov, O. Gunawan, S. J. Chey, T. G. de Monsabert, A. Prabhakar and D. B. Mitzi, *Thin Solid Films*, 2011, **519**, 7378–7381.
5 A. Walsh, S. Chen, S.-H. Wei and X.-G. Gong, *Adv. Energy Mater.*, 2012, **2**, 400–409.
6 S. Siebentritt, *Thin Solid Films*, 2013, **535**, 1–4.
7 W. Wang, M. T. Winkler, O. Gunawan, T. Gokmen, T. K. Todorov, Y. Zhu and D. B. Mitzi, *Adv. Energy Mater.*, 2014, **4**, 1301465.
8 J. J. S. Scragg, J. K. Larsen, M. Kumar, C. Persson, J. Sendler, S. Siebentritt and C. P. Bjorkman, *Phys. Status Solidi B*, 2016, **253**, 247–254.
9 J. J. S. Scragg, L. Choubrac, A. Lafond, T. Ericson and C. Platzer-Björkman, *Appl. Phys. Lett.*, 2014, **104**, 041911.
10 S. Bourdais, C. Choné, B. Delatouche, A. Jacob, G. Larramona, C. Moisan, A. Lafond, F. Donatini, G. Rey, S. Siebentritt, A. Walsh and G. Dennler, *Adv. Energy Mater.*, 2016, **6**, 1502276.
11 D. B. Mitzi, O. Gunawan, T. K. Todorov, K. Wang and S. Guha, *Sol. Energy Mater. Sol. Cells*, 2011, **95**, 1421–1436.
12 D. Colombara, S. Delsante, G. Borzone, J. M. Mitchels, K. C. Molloy, L. H. Thomas, B. G. Mendis, C. Y. Cummings, F. Marken and L. M. Peter, *J. Cryst. Growth*, 2013, **364**, 101–110.

13 L. E. Valle Rios, K. Neldner, G. Gurieva and S. Schorr, *J. Alloys Compd.*, 2016, **657**, 408–413.
14 T. K. Todorov, K. B. Reuter and D. B. Mitzi, *Adv. Mater.*, 2010, **22**, E156–E159.
15 D. Dumcenco and Y.-S. Huang, *Opt. Mater.*, 2013, **35**, 419–425.
16 P. A. Fernandes, P. M. P. Salome, A. F. da Cunha and B.-A. Schubert, *Thin Solid Films*, 2011, **519**, 7382–7385.
17 C. Persson, R. Chen, H. Zhao, M. Kumar and D. Huang, in *Copper Zinc Tin Sulfide-Based Thin Film Solar Cells*, ed. K. Ito, Wiley, Chichester, United Kingdom, 2015, ch. 4, p. 421.
18 L. J. Farrugia, *J. Appl. Crystallogr.*, 1999, **32**, 837–838.
19 G. Sheldrick, *XPREP. Space Group Determination and Reciprocal Space Plots*, 1991.
20 G. M. Sheldrick, *Release 97-2*, University of Göttingen, Germany, 1997.
21 G. M. Sheldrick, *Acta Crystallogr., Sect. A: Found. Crystallogr.*, 2008, **64**, 112–122.
22 A. Lafond, L. Choubrac, C. Guillot-Deudon, P. Fertey, M. Evain and S. Jobic, *Acta Crystallogr., Sect. B: Struct. Sci., Cryst. Eng. Mater.*, 2014, **70**, 390–394.
23 L. Choubrac, A. Lafond, C. Guillot-Deudon, Y. Moëlo and S. Jobic, *Inorg. Chem.*, 2012, **51**, 3346–3348.
24 A. Lafond, L. Choubrac, C. Guillot-Deudon, P. Deniard and S. Jobic, *Z. Anorg. Allg. Chem.*, 2012, **638**, 2571–2577.
25 L. Choubrac, M. Paris, A. Lafond, C. Guillot-Deudon, X. Rocquefelte and S. Jobic, *Phys. Chem. Chem. Phys.*, 2013, **15**, 10722–10725.
26 L. Choubrac, A. Lafond, M. Paris, C. Guillot-Deudon and S. Jobic, *Phys. Chem. Chem. Phys.*, 2015, **17**, 15088–15092.
27 H. Nozaki, T. Fukano, S. Ohta, Y. Seno, H. Katagiri and K. Jimbo, *J. Alloys Compd.*, 2012, **524**, 22–25.
28 S. Schorr, *Sol. Energy Mater. Sol. Cells*, 2011, **95**, 1482–1488.
29 T. Gurel, C. Sevik and T. Cagin, *Phys. Rev. B: Condens. Matter Mater. Phys.*, 2011, **84**, 205201.
30 A. Khare, B. Himmetoglu, M. Johnson, D. J. Norris, M. Cococcioni and E. S. Aydil, *J. Appl. Phys.*, 2012, **111**, 083707.
31 S. Chen, X. G. Gong, A. Walsh and S.-H. Wei, *Appl. Phys. Lett.*, 2009, **94**, 041903.
32 G. Rey, T. P. Weiss, J. Sendler, A. Finger, C. Spindler, F. Werner, M. Melchiorre, M. Hála, M. Guennou and S. Siebentritt, *Sol. Energy Mater. Sol. Cells*, 2016, **151**, 131–138.
33 K. Rudisch, Y. Ren, C. Platzer-Björkman and J. Scragg, *Appl. Phys. Lett.*, 2016, **108**, 231902.
34 A. Ritscher, M. Hoelzel and M. Lerch, *J. Solid State Chem.*, 2016, **238**, 68–73.
35 M. Paris, L. Choubrac, A. Lafond, C. Guillot-Deudon and S. Jobic, *Inorg. Chem.*, 2014, **53**, 8646–8653.
36 G. Rey, A. Redinger, J. Sendler, T. P. Weiss, M. Thevenin, M. Guennou, B. E. Adib and S. Siebentritt, *Appl. Phys. Lett.*, 2014, **105**, 112106.
37 G. H. Vineyard, *Phys. Rev.*, 1956, **102**, 981–992.
38 L. Van Puyvelde, J. Lauwaert, P. F. Smet, S. Khelifi, T. Ericson, J. J. Scragg, D. Poelman, R. Van Deun, C. Platzer-Björkman and H. Vrielinck, *Thin Solid Films*, 2015, **582**, 146–150.
39 L. Quang Phuong, M. Okano, Y. Yamada, A. Nagaoka, K. Yoshino and Y. Kanemitsu, *Appl. Phys. Lett.*, 2013, **103**, 191902.
40 J. P. Leitao, N. M. Santos, P. A. Fernandes, P. M. P. Salome, A. F. da Cunha, J. C. Gonzalez, G. M. Ribeiro and F. M. Matinaga, *Phys. Rev. B: Condens. Matter Mater. Phys.*, 2011, **84**, 024120.
41 T. Schmidt, K. Lischka and W. Zulehner, *Phys. Rev. B: Condens. Matter Mater. Phys.*, 1992, **45**, 8989–8994.
42 T. Gershon, B. Shin, N. Bojarczuk, T. Gokmen, S. Lu and S. Guha, *J. Appl. Phys.*, 2013, **114**, 154905.
43 B. Shin, O. Gunawan, Y. Zhu, N. A. Bojarczuk, S. J. Chey and S. Guha, *Progress in Photovoltaics: Research and Applications*, 2013, **21**, 72–76.
44 M. Okano, L. Q. Phuong and Y. Kanemitsu, *Phys. Status Solidi B*, 2015, **252**, 1219–1224.
45 L. Q. Phuong, M. Okano, Y. Yamada, G. Yamashita, T. Morimoto, M. Nagai, M. Ashida, A. Nagaoka, K. Yoshino and Y. Kanemitsu, *Appl. Phys. Lett.*, 2014, **105**, 231902.
46 M. Maiberg, T. Hölscher, S. Zahedi-Azad, W. Fränzel and R. Scheer, *Appl. Phys. Lett.*, 2015, **107**, 122104.
47 B. K. Durant and B. A. Parkinson, *Sol. Energy Mater. Sol. Cells*, 2016, **144**, 586–591.
48 W. W. Gärtner, *Phys. Rev.*, 1959, **116**, 84–87.
49 S. Siebentritt, G. Rey, A. Finger, D. Regesch, J. Sendler, T. P. Weiss and T. Bertram, *Sol. Energy Mater. Sol. Cells*, 2016, **158**(2), 126–129.
50 R. Peat and L. M. Peter, *Appl. Phys. Lett.*, 1987, **51**, 328–330.
51 Y. Ren, J. J. S. Scragg, C. Frisk, J. K. Larsen, S.-Y. Li and C. Platzer-Björkman, *Phys. Status Solidi A*, 2015, **212**, 2889–2896.
52 D. E. Aspnes, *Surf. Sci.*, 1973, **37**, 418–442.
53 P. M. Raccah, J. W. Garland, Z. Zhang, U. Lee, D. Z. Xue, L. L. Abels, S. Ugur and W. Wilinsky, *Phys. Rev. Lett.*, 1984, **53**, 1958–1961.
54 L. E. A. Berlouis, L. M. Peter, M. G. Astles, J. Gough, R. G. Humphreys, S. J. C. Irvine and V. Steward, *J. Appl. Phys.*, 1987, **62**, 4518–4522.
55 P. M. Raccah, U. Lee, S. Ugur, D. Z. Xue, L. L. Abels and J. W. Garland, *J. Vac. Sci. Technol., A*, 1985, **3**, 138–142.
56 D. E. Aspnes, in *Handbook on Semiconductors. Vol. 2. Optical Properties Solids*, ed. T. S. Moss and M. Balkanski, North-Holland, 1972, vol. 2, pp. 109–154.
57 W. S. Enloe, J. C. Parker, J. Vespoli, T. H. Myers, R. L. Harper and J. F. Schetzina, *J. Appl. Phys.*, 1987, **61**, 2005–2010.
58 S. Levcenco, D. Dumcenco, Y. P. Wang, Y. S. Huang, C. H. Ho, E. Arushanov, V. Tezlevan and K. K. Tiong, *Opt. Mater.*, 2012, **34**, 1362–1365.
59 C. Krämmer, C. Huber, C. Zimmermann, M. Lang, T. Schnabel, T. Abzieher, E. Ahlswede, H. Kalt and M. Hetterich, *Appl. Phys. Lett.*, 2014, **105**, 262104.
60 J. Krustok, T. Raadik, M. Grossberg, S. Giraldo, M. Neuschitzer, S. López-Marino and E. Saucedo, *Mater. Sci. Semicond. Process.*, 2015, **39**, 251–254.

Supporting Information

Optoelectronic and Spectroscopic Characterization of Vapor-Transport Grown Cu_2ZnSnS_4 Single Crystals

Tat Ming Ng[a,b], Mark T. Weller[b], Gabriela P. Kissling[b], Laurence M. Peter[b,*], Phillip Dale[c], Finn Babbe[c], Jessica de Wild[c], Bernard Wenger[d], Henry J. Snaith[d], David Lane[e]

a. Centre for Sustainable Chemical Technologies, University of Bath, Bath BA2 7AY, UK

b. Department of Chemistry, University of Bath, Bath BA2 7AY, UK

c. Physics and Materials Science Research Unit, University of Luxembourg, 41, rue du Brill, L-4422 Belvaux, Luxembourg

d. University of Oxford, Clarendon Laboratory, Parks Road, Oxford, OX13PU, UK

e. Cranfield Forensic Institute, Cranfield University, Defence Academy of the United Kingdom, Shrivenham, SN6 8LA, UK

*. l.m.peter@bath.ac.uk

Growth of CZTS crystals and Cooling Curve

CZTS was synthesized in evacuated quartz ampules using copper (Sigma Aldrich 99.7%), zinc (Alfa Aeser, 99.9%), tin (Alfa Aeser 99.85%) and sulfur (Alfa Aeser 99.999%). The amounts of material and conditions used in the synthesis of the CZTS precursors for crystal growth were as follows. Needle precursor: Cu 2.3807 g, Zn 1.8368 g, Sn 2.7786 g, S 4.2093 g, 900° C for 2 days. Platelet precursor: Cu 6.2424 g, Zn 4.2829 g, Sn 6.4782 g, S 7.0112g, 750° C for 43 days. The needles were grown using ~10 g CZTS and ~0.2 g I_2 (Sigma Aldrich 99.999%), 8 days. The platelets were grown using 6.033 g CZTS, 0.749 g I_2 and 0.06 g NaI (99+%, Sigma Aldrich), 9 days. The crystals were cooled in situ after switching off the furnace. The cooling curve is shown in Fig. 1.

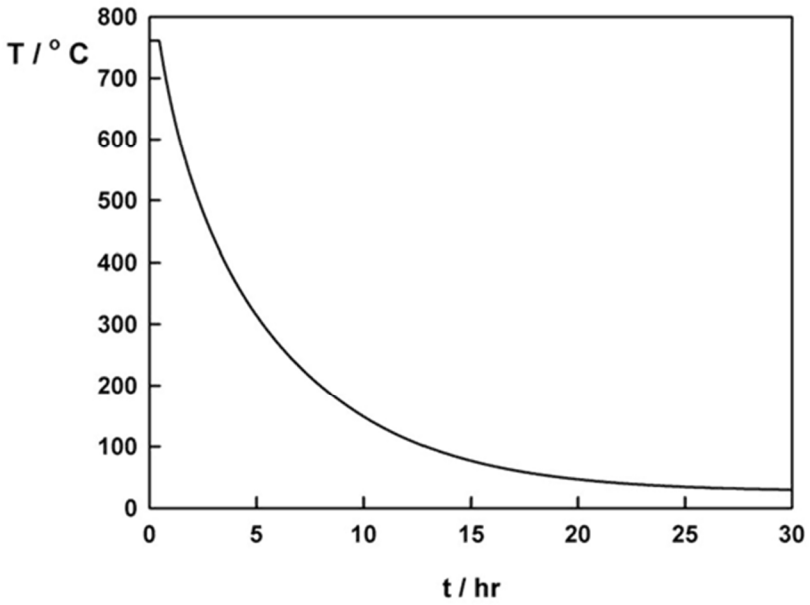

Fig. 1. Measured Cooling curve for Growth Zone of the 4-zone furnace.

Spectroscopic Ellipsometry

The crystals' complex dielectric functions ($\varepsilon = \varepsilon^{'} + i\varepsilon^{''}$) were determined using spectroscopic ellipsometry. The crystals were mounted in epoxy resin and Teflon and polished to 1µm using alumina paste, and optical microscopy was used to select areas for examination. This was done using a J.A. Woollam M20000U-Xe rotating compensator ellipsometer with focusing optics that gave a 150 µm wide spot. Measurements were carried out over a spectral range of 245 to 1690 nm

(0.734 to 5.044 eV) at three angles of incidences (45, 55 and 65°). The resulting data were analysed using the computer program CompleteEASE.[1]. This was done in two stages. First the ellipsometric parameters (Ψ and Δ) were fitted by approximating ε by a B-spline. This allowed arbitrary flexibility whilst enforcing Kramers-Kronig consistency and a positive ε_2 to ensure a physically meaningful solution. ε was then refined by converting the B-spline into a general oscillator model where its main features were represented by PSEMI-M0 oscillators[2,3], and Gaussian peaks were used to improve the overall fit. The absorption coefficient values derived by fitting the spectroscopic ellipsometry data for the platelet sample are compared with published data in Fig. 2.

Fig. 2. Comparison of α values derived by SE for platelet sample with data from Li et al.[4] for reactively sputtered thin films and tabulated by Ito[5] based on SE data from ref [6].

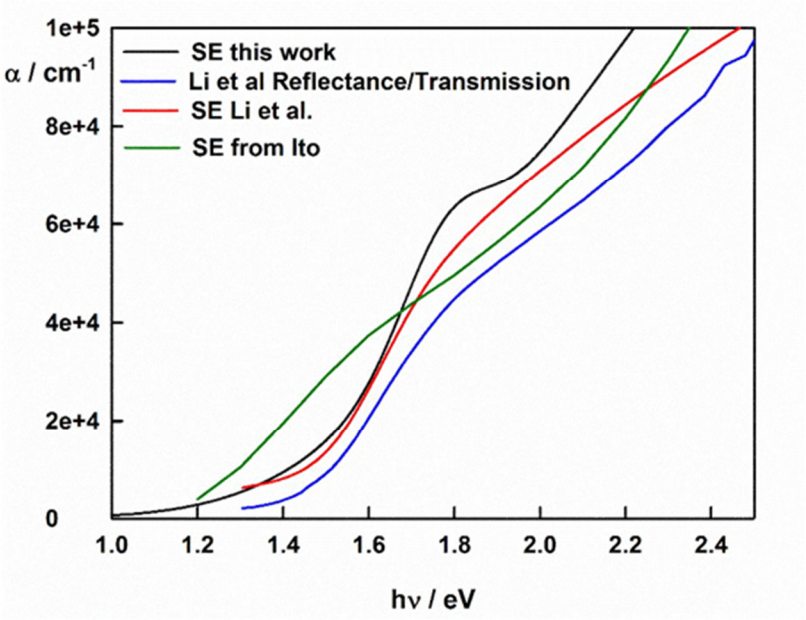

Fig. 3 shows the Tauc plot obtained using the absorption coefficient determined by SE.

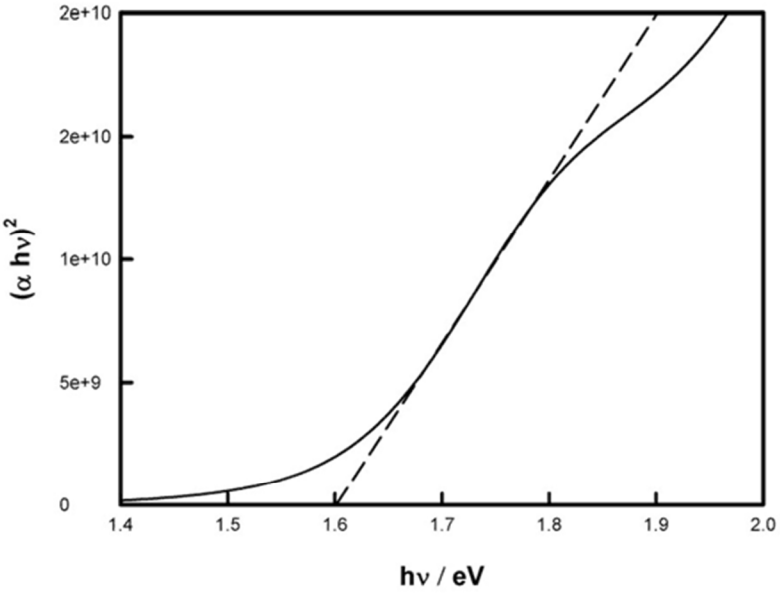

Fig. 3. Tauc plot of absorption coefficient data obtained by spectroscopic ellipsometry (platelet crystal)

Fig. 4 shows the Urbach plot for the SE data.

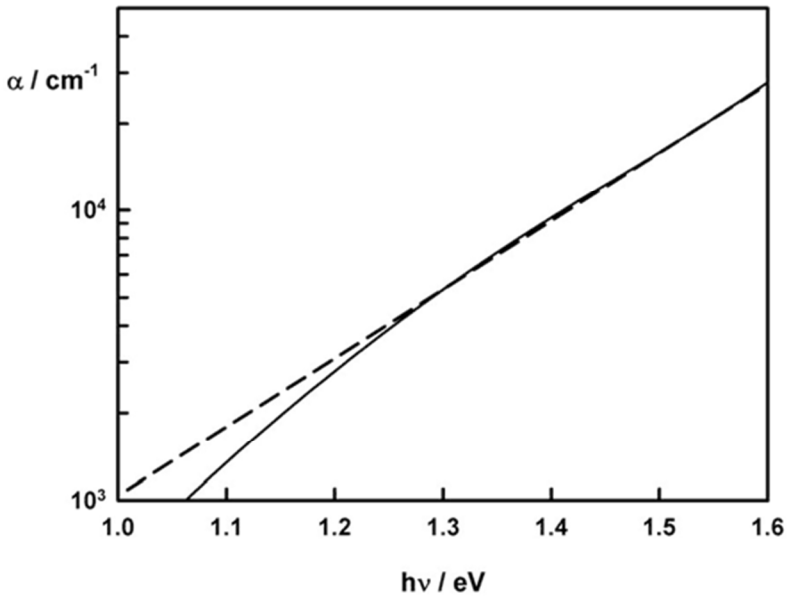

Fig. 4. Urbach plot of absorption coefficient obtained by SE for the platelet crystal.

Photocurrent Spectroscopy

Chopped collimated illumination was provided by a tungsten lamp and grating monochromator (Bentham Instruments) with a variable frequency mechanical chopper operating at 27 Hz, and the photocurrent was detected by a lock-in amplifier (Stanford Research). The spot size of the illumination was controlled by image slits and was chosen to be smaller than the smallest dimension of the crystals to ensure that all the light fell on the crystal surface. The illumination intensity was measured using a calibrated silicon photodiode traceable ±5% to NBS standards. The external quantum efficiency spectra were corrected for reflection losses due to the glass window of the cell and reflection from the crystal surface.

The Tauc plot derived from the EQE data for needle is shown in Fig. 5. The intercept gives a band gap of 1.64 eV, slightly lower than that obtained for the Tauc plot for the platelet (1.68 eV).

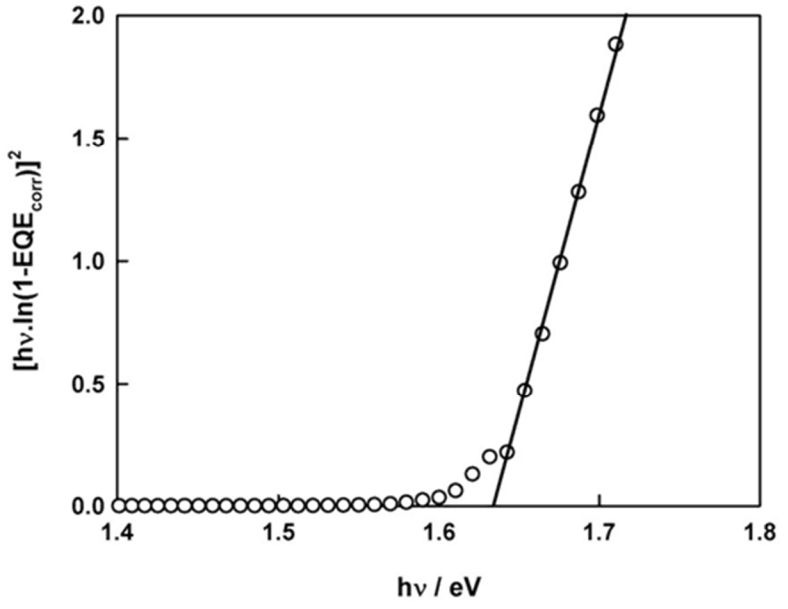

Fig. 5. Tauc plot of the EQE data for the needle sample (E_g = 1.64 eV).

The Urbach plot of the EQE data for the platelet is shown in Fig. 6.

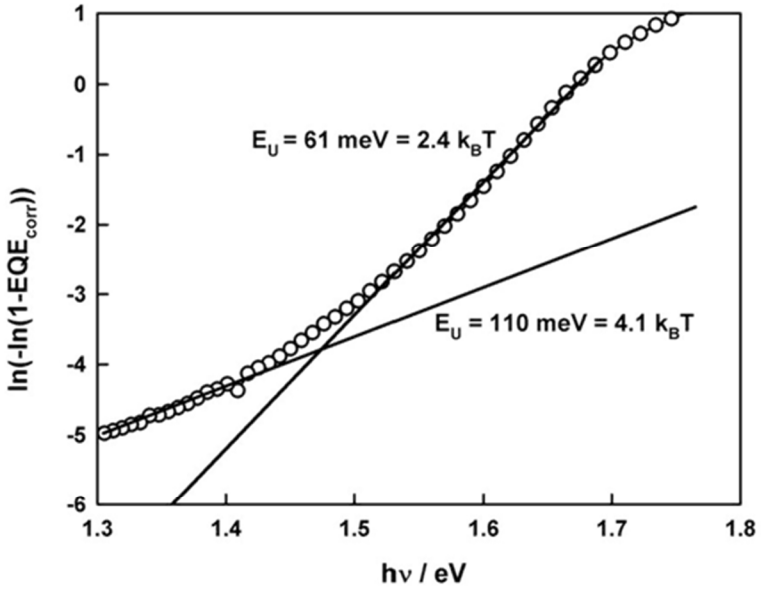

Fig. 6. Urbach plot of EQE data for the platelet.

Electrolyte Electroreflectance

For electrolyte electroreflectance measurements, unchopped illumination was incident on the crystal surface at 45°, and the reflected beam was detected by silicon photodiode. The electrode potential was modulated by an ac voltage of variable frequency and amplitude provided by the lock-in amplifier, which also detected the modulated reflectance signal from the photodiode. EER spectra reported here were recorded using 13 Hz modulation. The validity of the low field approximation was checked by varying the amplitude of the ac modulation. The results shown in Fig. 7 show that the EER signal depends linearly on the amplitude of the ac modulation as expected.

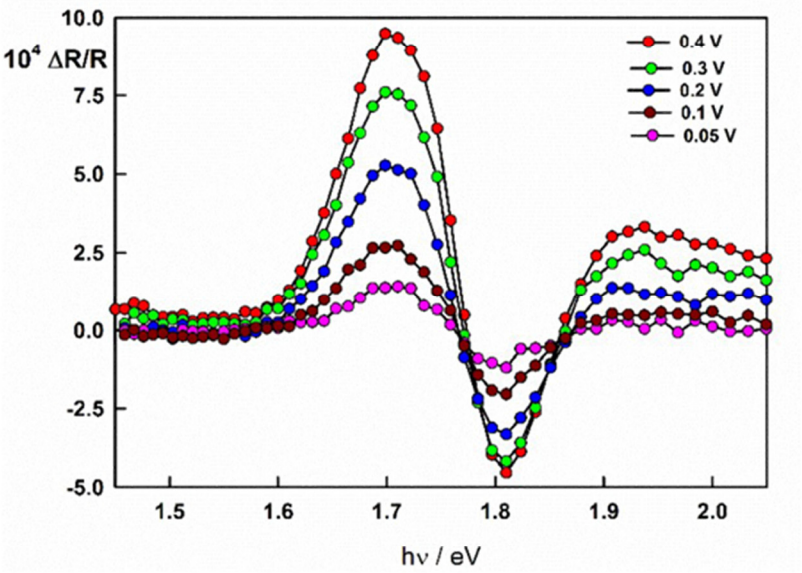

Fig.7. Dependence of the EER signal on modulation amplitude measured for the CZTS platelet sample at -0.6 V vs Ag/AgCl.

Raman Spectroscopy

Fig. 8 shows the fitting of the resonant Raman spectra of the as-grown platelet and needle.

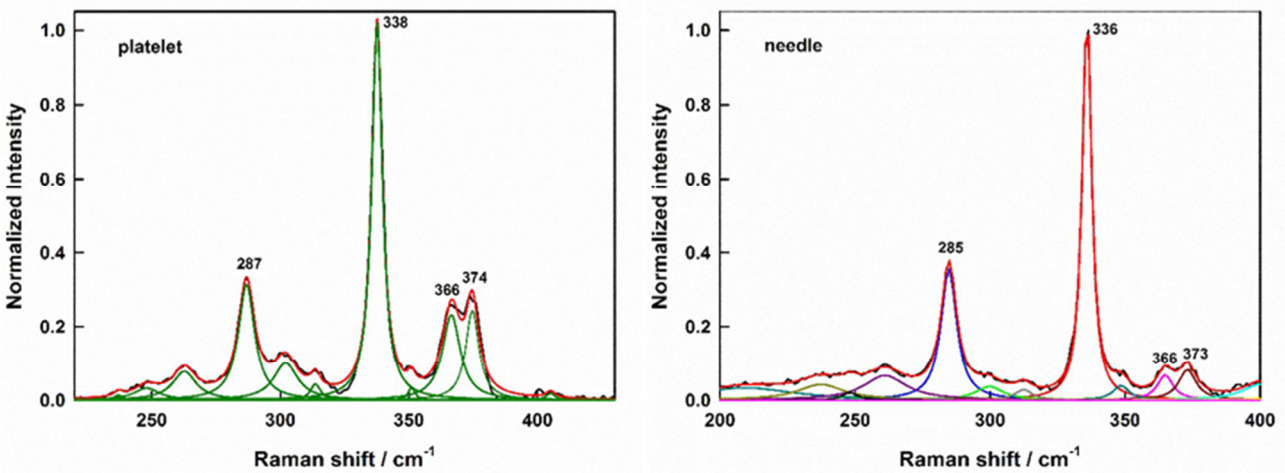

Fig. 8. Deconvolution of near-resonant Raman spectra of the as-grown platelet and needle (red lines total fit).

Assignment of the Raman peaks used to identify the kesterite phase

Platelet			**Needle**			**Theoretical kesterite** [7,8]			**Theoretical stannite** [7,8]		
Modes	Wavenumber (cm^{-1})		Modes	Wavenumber (cm^{-1})		Modes	Wavenumber (cm^{-1})		Modes	Wavenumber (cm^{-1})	
A	338		A	336		A	340.04/335.2		A_1	334.08/332.7	
	302			300			284.30/309.0			277.12/309.1	
	287			285			272.72/302.1		A_2	263.11/304.3	
B (TO LO)	351	375	B (TO LO)	349	373	B (TO LO)	355.80/354.8	374.05/366.4	B_1	291.12/324.1	
							309.56/332.7	313.19/336.1		74.17/88.1	
	236	249		237	250		238.48/269.1	254.73/285.1	B_2 (TO LO)	360.12/358.5	370.63/364.2
							166.65/179.6	168.21/179.9		277.08/306.2	291.82/320.6
							98.82/104.2	98.83/104.3		149.69/171.0	150.91/171.1
							86.70/92.3	87.51/93.1		95.85/96.4	95.86/96.4
E (TO LO)		366	E (TO LO)		365	E (TO LO)	351.55/341.4	366.35/353.2	E (TO LO)	346.01/341.3	364.87/353.7
		314			313		281.07/309.7	293.44/314.1		264.34/305.3	275.52/311.9
	245	263			261		250.26/278.2	257.85/289.8		235.41/268.7	246.58/283.3
							150.53/166.1	151.05/166.2		161.68/170.9	162.63/171.0
							105.93/101.4	106.00/101.4		97.34/106.9	97.38/106.9
							83.64/79.2	83.65/79.2		78.39/74.9	78.73/75.5

Vineyard model

The Vineyard model[9] of order-disorder transformations gives the rate constants .

$$k_{order} = 4f\exp\left(\frac{-U}{k_BT}\right)\exp\left(\frac{3\nu S}{k_BT}\right) \quad k_{disorder} = 4f\exp\left(\frac{-U}{k_BT}\right)\exp\left(\frac{-3\nu S}{k_BT}\right)$$

and the rate of change of order as

$$\frac{dS}{dt} = \frac{1}{2}\left[k_{order}(1-S)^2 - k_{disorder}(1+S)^2\right]$$

Here f is the frequency of the vibrational mode involved in the exchange of neighbouring atoms (taken as ~10^{12} Hz), U is the activation energy for place exchange (taken as 14900/k_B) and ν (taken as 358/k_B) is related to the interaction energies of the three possible nearest neighbour pairs (Cu-Cu, Zn-Zn and Cu-Zn). The values of U and ν used in the calculations shown here were taken from the fit obtained by Scragg et al.[10] Equilibrium is established at a given temperature when $dS/dt = 0$, as illustrated in Fig. 9 for a temperature of 150°C

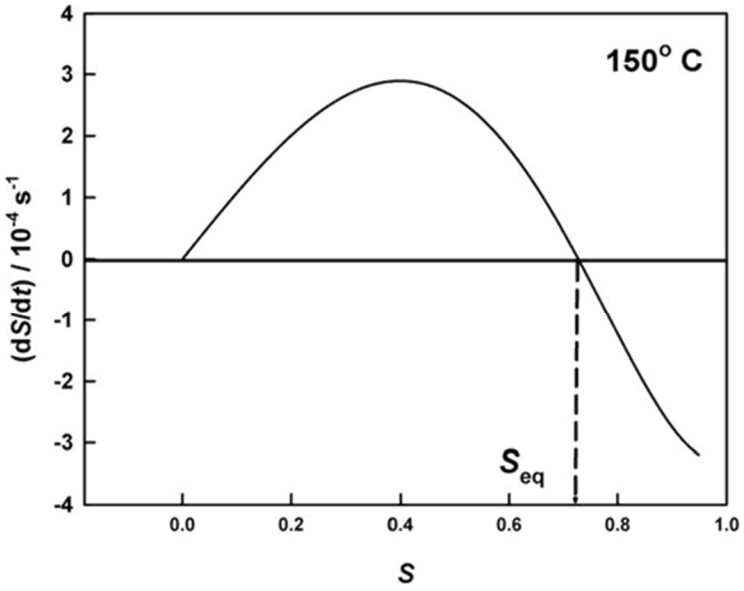

Fig. 9. Plot showing definition of equilibrium order when $dS/dt = 0$ for $T = 150$°C.

The predicted time dependence of the order parameter S for a temperature of 100°C is illustrated in Fig. 10.

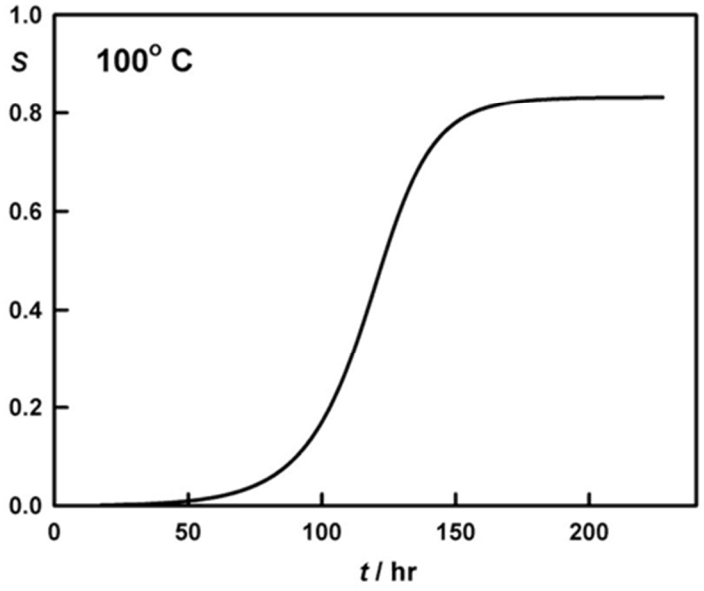

Fig. 10. Time-dependence of the order parameter S predicted for the annealing of a fully disordered crystal at 100°C.

The predicted equilibrium order parameter as a function of annealing temperature is illustrated in Fig. 11.

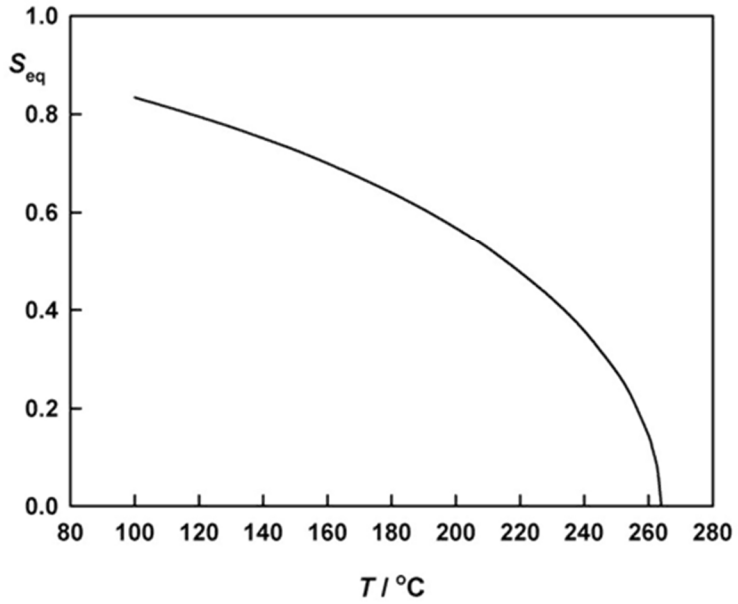

Fig. 11. Equilibrium Order Parameter *S* as a function of annealing temperature calculated from the Vineyard model for values given in text.

Photoluminescence

Photoluminescence spectra were recorded in a homebuilt set up. A green (514 nm) CW argon laser was used with a power of 1 mW and diameter of 100 µm and integrated over several minutes to obtain an optimized signal. The spectra were measured between 550 and 1050 nm with a Si camera and between 900 and 1250 nm with an InGaAs camera. High pass filters of 550 nm for the Si to exclude laser light and 850 nm for the InGaAs to exclude second order light (from laser and the sample) were used.

Time-resolved photoluminescence measurements where performed in air with a photon counting system (Fluotime 300, PicoQuant GmbH). The samples were excited with a 634 nm laser diode (LDH-P-C-635, PicoQuant GmbH, pulse duration 40 ps). Decay traces were acquired at an excitation fluence of 2.3 µJ/cm². We used an IR-PMT detector (Hamamatsu, H12694) to measure decays at 1.30 eV and a PicoQuant PMA-Hybrid detector for decays at 1.65 eV.

Fig. 12 compares the blue shift measured for the platelet and needle samples

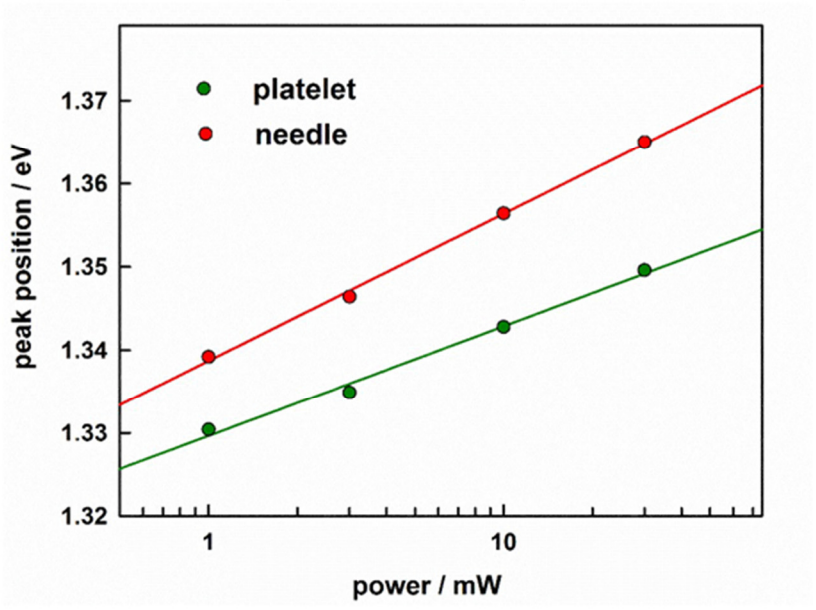

Fig. 12. Intensity dependence of PL peak energy for platelet and needles crystals

Fig. 13 shows the dependence of PL intensity on laser power for the platelet and needle samples.

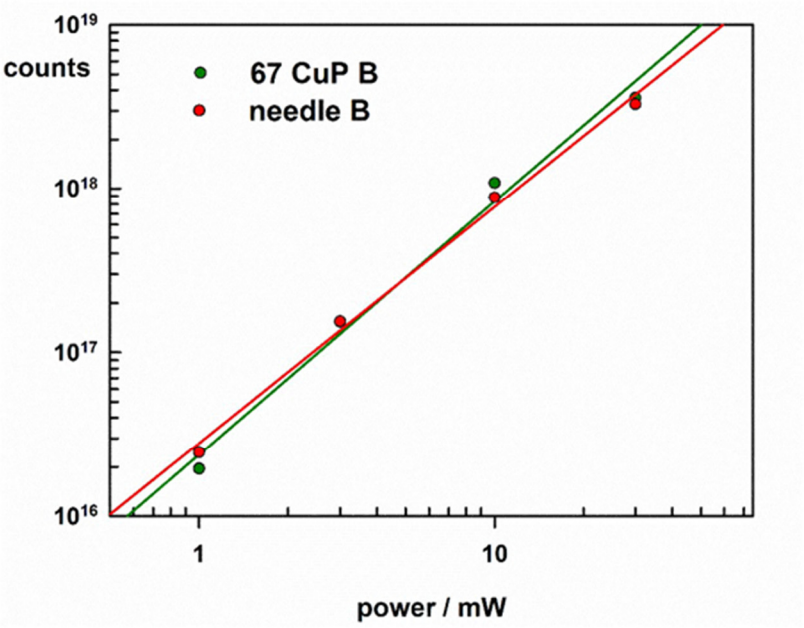

Fig. 13. Dependence of PL intensity on laser power for platelet and needle crystals.

Fig. 14 shows the PL decays measured at two different photon energies in the case of the CZTS needle. The decay times are almost identical. This contrasts with the energy dependence of the lifetime the platelet sample shown in the main text.

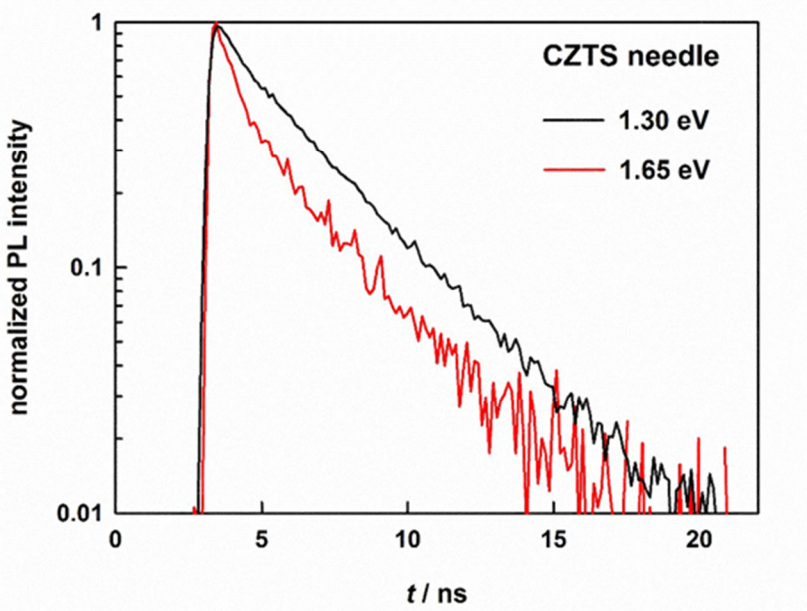

Fig. 14. PL decay plots for the CZTS needle at two different emission energies. Excitation energy 1.96 eV

Attempt to obtain the electron diffusion length using Gärtner analysis

Close to the bandgap, where $\alpha L_n << 1$, the Gärtner equation

$$EQE = 1 - \frac{\exp -\alpha W}{1 + \alpha L_n}$$

reduces to the simpler form

$$-\ln(1 - EQE) = \alpha W$$

If the semiconductor/electrolyte interface behaves ideally (no surface states), the width of the space charge region should vary with the square root of $U_{fb} - U$, where U_{fb} is the flat band potential.

$$W_{sc} = \left(\frac{2\Delta(U_{fb} - U)\varepsilon\varepsilon_0}{qN} \right)^{1/2}$$

It follows that a plot of $[\ln(1 - EQE)]^2$ vs. electrode potential U should have an intercept at U_{fb}. Fig. 15 shows plots for two wavelengths close to the band edge, from which the flat bad potential is estimated to be -0.5 V vs Ag/AgCl.

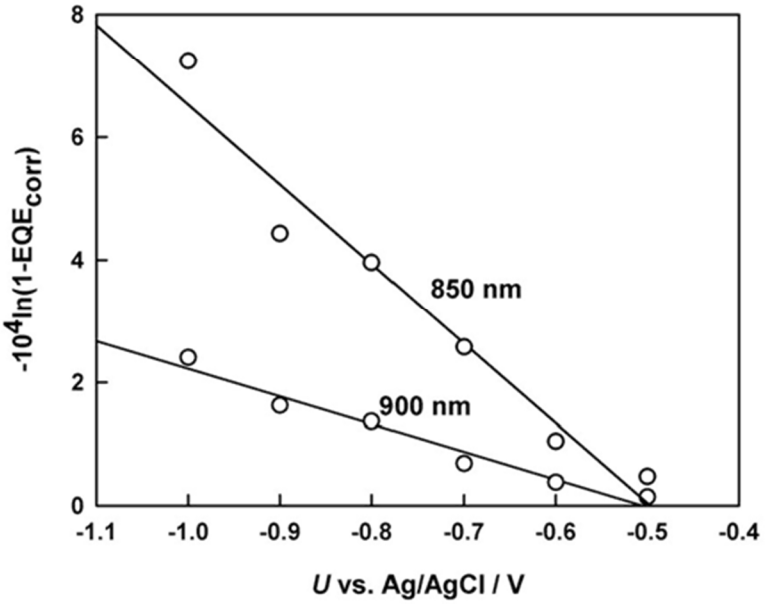

Fig. 15. Plots used to estimate the flat band potential of CZTS

The Gärtner equation can also be written in the form

$$-\left[\ln(1 - EQE) + \ln(1 + \alpha L_n)\right] = \alpha W = \alpha \left(\frac{2\Delta(U_{fb} - U)\varepsilon\varepsilon_0}{qN} \right)^{1/2}$$

so that a plot of -ln(1-EQE) vs. $(U_{fb} - U)^{1/2}$ should have an intercept on y axis equal to $\ln(1 + \alpha L_n)$. Fig. 16 shows plots of this function for three different wavelengths. The plots are clearly non-linear and so it is not possible to obtain a reliable value of the intercept on the y axis. We attribute this to non-ideal behaviour of the CZTS/electrolyte junction due to the presence of a high density of surface states. The charging of these surface states leads to a change in the potential drop across the Helmholtz layer when the electrode potential is altered, so that the simple square root relationship between the width of the space charge region and $(U_{fb}-U)$ no longer holds.

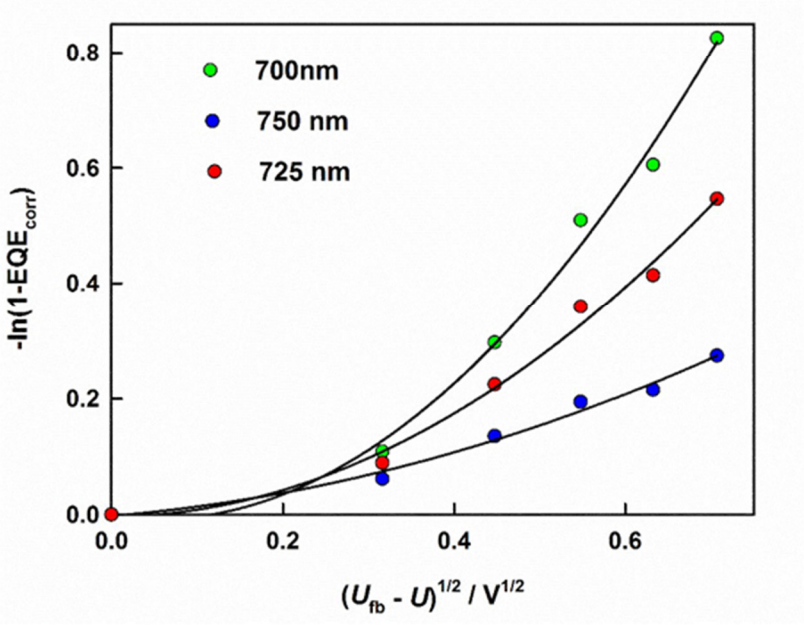

Fig. 16. Plots of -ln(1-EQE) vs .(U_{fb}-U) according to the Gärtner equation showing non-ideal junction behaviour

Impedance Measurements

Impedance measurements were carried out using a Solartron Modulab system and fitted using ZView software (Scribner). The impedance behaviour of the platelet crystal shows that the evaporated Au contact is non-ohmic with a series resistance greater than 1 kΩ and a stray capitance of around 800 pF. The series resistance is not a problem for the very low currents and low chopping frequencies in the EQE measurements.

An example of the impedance fitting to the equivalent circuit on the next page is shown below for data measured at -1.0 V vs. Ag/AgCl. The low frequency behaviour is consistent with the presence of a high surface state capacitance, modelled here by the constant phase shift element CPE1. Reliable fitting and extraction of the space charge capacitance proved difficult due to the overlap in time constants for the surface state and space charge capacitances, and consequently construction of Mott-Schottky plots to determine the doping density of the crystal was not possible.

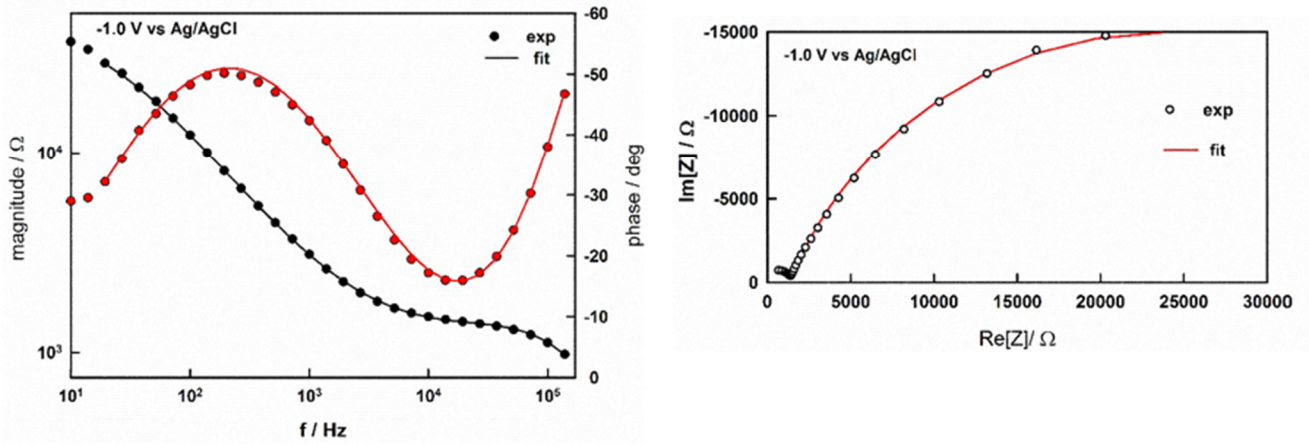

Fig. 17. Bode and Nyquist plots of impedance of etched CZTS platelet crystal. The fitting data are given below.

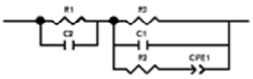

Element	Freedom	Value	Error	Error %
R1	Free(+)	1376	6.4689	0.47158
C2	Free(+)	8.6322E-10	7.3385E-12	0.85013
R3	Free(+)	46185	1034.5	2.2399
C1	Free(+)	4.1256E-08	1.2771E-09	3.0955
R2	Free(+)	1537	201.27	13.095
CPE1-T	Free(+)	7.2261E-07	4.1279E-08	5.7125
CPE1-P	Free(+)	0.67597	0.0078146	1.1561

Chi-Squared:	0.00021708
Weighted Sum of Squares:	0.010637
Data File:	C:\Users\chslmp\LMP Files\Papers 2016\CZTS single crystal\SI Figures\impedance at -1 V.txt
Circuit Model File:	
Mode:	Run Fitting / Selected Points (0 - 27)
Maximum Iterations:	100
Optimization Iterations:	0
Type of Fitting:	Complex
Type of Weighting:	Calc-Modulus

R_1 contact resistance

R_2 surface state resistance

R_3 Faradaic resistance

C_1 space charge capacitance

C_2 contact capacitance

CPE1 surface state CPE

References

1. J. A. Woollam Co. Inc., Lincoln, NE, US

2. US Patent 5,796,983, "Dielectric function parametric model, and method of use", 18 August 1998, C. M. Herzinger, B. D. Johs, J. A. Woollam Co. Inc., Lincoln, NE, US

3. B. Johs, C.M. Herzinger, J.H. Dinan, A. Cornfeld, J.D. Benson, *Thin Solid Films*, 1998 1**37-142**, 313-314

4. S-Y Li, C. Hägglund, Y Ren, J.J.S. Scragg, J.LK. Larsen,C. Frisk,K. Rudisch,S. Englund, C. Platzer-Björkman, *Solar Energy Materials and Solar Cells* 2016**, 149**, 170-178.

5. K. Ito, *Copper Zin Tin Sulfide-based Thin Film Solar Cells*. Wiley: Chichester, United Kingdom, 2015; p 421.

6. J. Li, H.Du, J. Yarbrough, A. Norman, K. Jones, G. Teeter, F.L. Terry, D. Levi, *Optics Express* 2012**, 20**, (S2), A327-A332.

7. T. Gurel, C. Sevik and T. Cagin, *Physical Review B*, 2011, **84**. 205201.

8. A. Khare, B. Himmetoglu, M. Johnson, D. J. Norris, M. Cococcioni and E. S. Aydil, *J. Appl. Phys.*, 2012, **111**, 083707.

9. G. Vineyard, Phys. Rev. 1956, **102**, 981.

10. J.J.S. Scragg, J. K. Larsen, M. Kumar, C. Persson, J. Sendler,S. Siebentritt, C.P. Bjorkman, *Physica Status Solidi B-Basic Solid State Physics* 2016**, 253**, (2), 247-254.

6 Determination of Cu/Zn disorder in CZTS

In section 1.4.2 (page 25), the author gave a brief introduction on Cu/Zn disorder in CZTS and referenced a few techniques that can demonstrate the degree of disorder experimentally using powder neutron diffraction,[1] solid state NMR[2] and near-resonant Raman scattering[3] qualitatively. This chapter details the attempts to qualify and quantify the degree of disorder in CZTS single crystals and powders using near-resonant Raman spectroscopy, neutron diffraction and anomalous X-ray diffraction.

6.1 Results and Discussion

6.1.1 Resonance Raman spectroscopy

Figure 6.1 shows the resonance Raman spectra of a selection of CZTS single crystals that underwent ordering procedures at different annealing temperatures in the range of 110 °C to 275 °C. All observed Raman modes have been reported before for kesterite CZTS in experimental[4] and theoretical[5] studies. When comparing the Raman spectra, the relative peak intensities exhibit clear trends when changing the annealing temperature. The intensities of the two Raman peaks at 366 and 374 cm^{-1} decrease for samples annealing at lower temperatures, causing an increasing ratio Q'. Similarly, the peak at 287 cm^{-1} increases in intensity while the peak at 303 cm^{-1} decreases when the annealing temperature decreases, causing an increasing ratio Q.

Peak broadening is also observed in samples annealed at high temperature, particularly above the critical temperature. The full width half maximum (FWHM) of the main Raman A mode at 338 cm^{-1}, as well as the parameters Q and Q' are listed in Table 6.1.

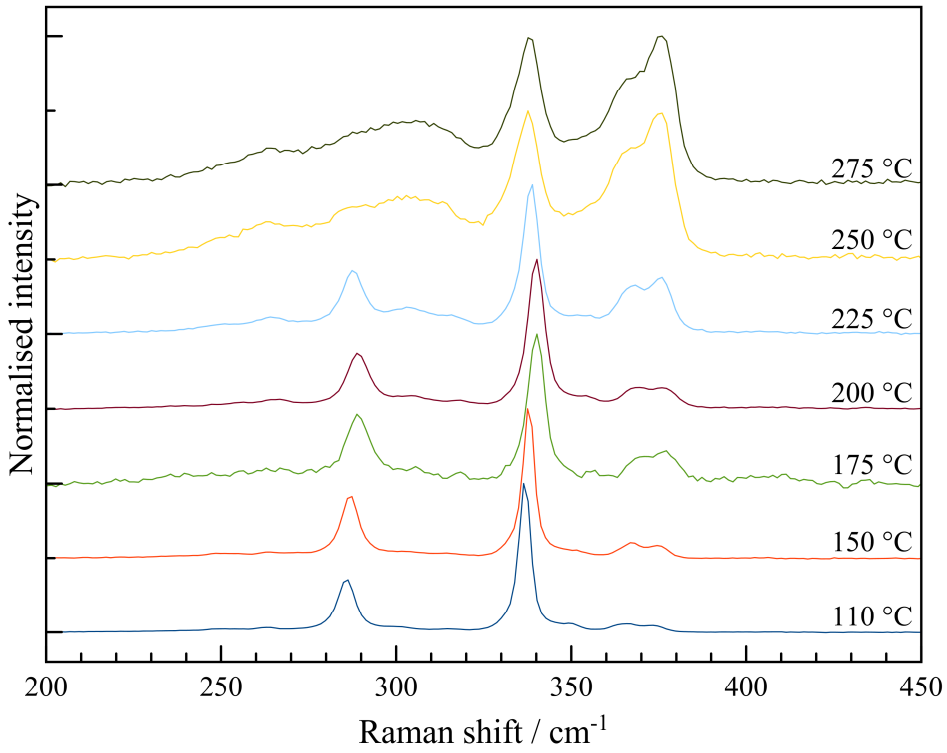

Figure 6.1 Resonance Raman spectra of CZTS single crystals annealed at different temperatures.

Table 6.1 List of samples which were investigated in this study including the annealing temperature, duration, the full width half maximum and the parameters Q and Q' obtained from the resonance Raman spectra.

Temp. / °C	**Duration / h**	**FWHM at main A mode / cm^{-1}**	**Q**	**Q'**
110	1000	4.36 ± 0.61	17.2 ± 2.0	9.2 ± 3.0
150	312	3.75 ± 0.08	12.0 ± 4.7	5.4 ± 0.8
175	432	5.75 ± 0.20	6.5 ± 0.9	3.4 ± 0.3
200	192	5.74 ± 0.38	4.0 ± 1.9	3.0 ± 1.4
225	24	5.10 ± 0.49	2.3 ± 0.7	1.4 ± 0.3
250	24	9.82 ± 0.24	0.8 ± 0.2	0.6 ± 0.1
275	1	8.82 ± 0.57	0.9 ± 0.1	0.6 ± 0.1
300	1	9.12 ± 0.55	0.7 ± 0.1	0.8 ± 0.1

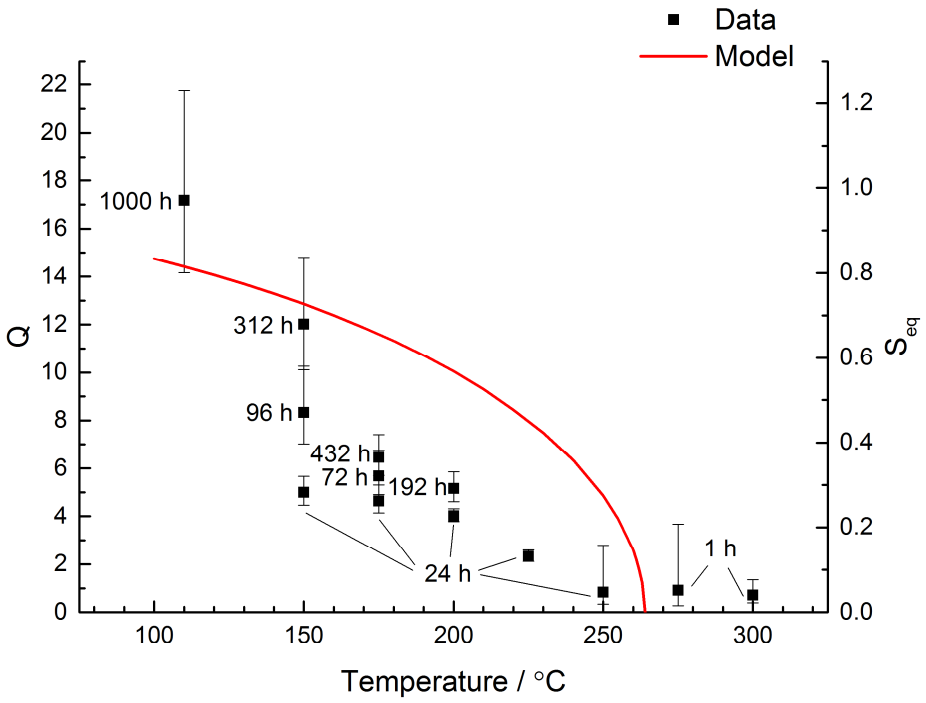

Figure 6.2 Variation in resonance Raman order parameter Q with respect to annealing temperature. Labels indicate the anneal times for the samples. The temperature dependence of S (Vineyard model) is plotted as the red curve.

An attempt to fit the data to the Vineyard model is shown in Figure 6.2. The values used for the fitting were the ones shown in the ESI in Chapter 3 (page 130) and also in Scragg *et al.*'s[6] work: f = 1 Thz, U/k_B = 14900 K, v/k_B = 358 K. It is clearly that the model does not fit the data and the possible causes are:

(i) the Q value at 110 °C (17.2 ± 2.0) is at least six times higher than Scragg *et al.* (2.5 ± 0.1). This is mainly due to the fact that the intensity of the peak at 303 cm^{-1} is so weak that it is barely integratable (Figure 6.1). On the other hand, since the raw resonance Raman spectra suffered from strong fluorescence, as shown in Figure 4.5, different background subtraction treatment will affect the relative intensities. Scragg *et al.* also noted that the Q value can deviate substantially in composition and preparation method of the sample.

(ii) the samples haven't reached equilibrium after the first 24 hours. An annealing time of 24 hours was chosen initially because the same duration was used in Scragg *et al.*'s work. The Vineyard model also suggested an annealing time of 24

hours should be sufficient for CZTS samples to reach equilibrium for temperatures above 125 °C (Figure 6.3). Samples at 150, 175 and 200 °C were reannealed for longer durations, and there is a clear increase in the Q values, as shown in Figure 6.2. However, even with extended annealing time, the data still does not fit in the Vineyard model.

Judging from the Q value and the FWHM of the Raman spectra at 338 cm^{-1}, the critical temperature of this particular batch of CZTS is around 250 °C, which is just within the error range of Scragg *et al.*'s result (260 ± 10 °C).[3]

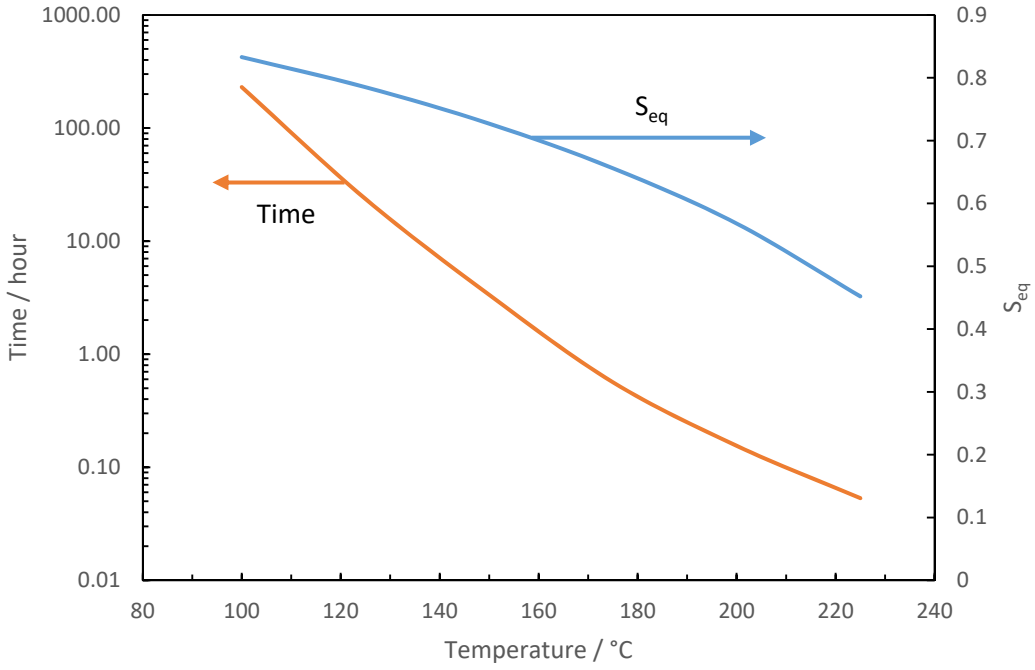

Figure 6.3 The calculated time needed to reach equilibrium and the corresponding S value for a given annealing temperature using the Vineyard model.

6.1.2 Neutron diffraction

Although Schorr *et al.* and her co-workers undertook a lot of powder neutron diffraction studies on CZTS(e), experiments using single crystal neutron diffraction have not been previously reported. One of the reasons is that, even for powder neutron diffraction, a large amount of sample is needed to obtain a good signal to noise ratio. In the case of single crystal neutron diffraction, a large single crystal with dimensions of a few millimetre is required, and this PhD project has successfully synthesised CZTS single crystals of that dimension. The disadvantage of using powder

diffraction in CZTS(e) samples is because in the tetragonal structure, the Bragg reflections hkl and khl always superimpose. This degrades the ability to distinguish between the x and y coordinates leading to high errors on these figures. Single crystal neutron diffraction separates hkl and khl reflections potentially leading to much higher accuracy in extracting the fractional coordinates of the atoms.

Table 6.2 Powder neutron diffraction simulation (λ = 0.8386 Å) for CZTS in the range of fully disordered (S = 0) to fully ordered (S = 1) using FullProf suite and CrystalDiffraction software.

Order parameter S	**Normalised intensity relative to 1 1 2**					
	0 1 1		1 3 2		0 0 8	
	FullProf	CrystalDiff	FullProf	CrystalDiff	FullProf	CrystalDiff
1	0.008	0.014	0.859	0.279	1.352	0.080
0.8	0.006	0.010	0.859	0.279	1.352	0.080
0.6	0.004	0.008	0.859	0.279	1.352	0.080
0.4	0.003	0.007	0.859	0.279	1.352	0.080
0.2	0.003	0.006	0.859	0.279	1.352	0.080
0	0.003	0.006	0.859	0.279	1.352	0.080

Powder neutron diffraction simulation in the range of fully disordered CZTS (S = 0) to fully ordered CZTS (S = 1) was carried out using FullProf suite[7] and CrystalDiffract software.[8] The wavelength was chosen to be the same as the experiment (λ = 0.8386 Å). Some examples are shown in Table 6.2. In the simulation, it is clearly seen the relative intensities of reflection 0 1 1 decrease as the order parameter S decreases. In contrast, the relative intensities for all allowed reflections with l equal even numbers do not change with the S values. This was also observed in Ritscher *et al.*'s[9] work. Note that Ritscher *et al.* only expressed their result in 2θ = 18.3° (λ = 154.818 pm). This reflection corresponds to the 0 1 1 reflection.

However, no intensity was observed for 0 1 1 reflection in all samples during the initial measurements. It was only realised later a critical mistake was made during the initial indexing of all the samples. Since the lattice parameter a in CZTS is roughly equal to c/2, the hkl reflection was mistakenly indexed as h$\frac{l}{2}$k or $\frac{l}{2}$kh. This explains why no allowed odd l reflections were observed. For the 300 °C sample it was possible to partially re-measure the diffraction data, using the correct crystal

orientation. Hence the quality of this data (Table 6.4) is not as good as the data for the sample annealed at 150 °C (Table 6.3), but still yield R-factor and standard errors similar to those reported in literatures using powder diffraction techniques.[10, 11] The single crystal neutron diffraction data and single crystal X-ray diffraction (SCXRD) data from the same sample were refined simultaneously using JANA2006[12]. The refinement was carried out using four models: (i) an ordered kesterite model with S = 1; (ii) a disordered kesterite model with S = 0; (iii) the occupancy factors in 2c and 2d sites were refined; and (iv) the occupancy factors in 2a, 2c and 2d sites were refined. Since Bosson *et al.*[13] highlighted the observation of a substantial amount of sulphur vacancy in their work, the sulphur occupancy factors were refined in models (v) and (iv) to compare with the results in models (iii) and (iv). Constraints were applied for models (iii), (iv), (v) and (iv) so that the occupancy factor per site is equal to one (except for sulphur in models (v) and (iv), and the occupancy factor of Cu in 2c site equals to that of Zn in 2d site. If these constraints were not applied, the occupancy factors of these sites yielded unreasonable numbers, and a warning about strong correlations between the occupancy factors of 2c and 2d sites was notified. Többens *et al.*[10] also highlighted the same problem with regards to the strong correlations. It is thought that the strong correlations between the occupancy factors in the different sites is due to the pseudosymmetry of the kesterite structure.

The *R*-factors from neutron data without odd l reflections and SCXRD data for all the models are similar, with difference < 0.5 %, while the *R*-factors from the neutron data with odd l reflections clearly confirms the crystals are disordered, with difference > 2%. This is expected as the information about the Cu/Zn disorder is contained in the odd l reflections as demonstrated in the simulation (Table 6.2).

When the sulphur occupancy is refined, the Cu occupancy factor at 2c site was increased from 0.599(4) to 0.629(4) in the sample annealed at 150 °C with almost the same R-factors (Table 6.3 and Table 6.6). We can also concluded that the sample annealed at 150 °C is more ordered than the sample annealed at 300 °C (*cf.* Cu occupancy at 2c site = 0.56(3). A small amount of sulphur vacancy is observed in this work, with occupancy factor of 0.95(1), as opposed to ≤0.83 (standard error not given) in Bosson *et al*'s work.[13] We can confirm there is no Cu/Zn disorder occurred at 2a

site for the sample annealed at 150 °C, with Cu occupancy of 1.049(20), as opposed to 0.67(8) measured at 300 K in Bosson *et al*'s work.[11] Nevertheless, we have demonstrated using single crystal neutron diffraction to quantify the occupancy factors of Cu and Zn in CZTS.

Table 6.3 Fitting of CZTS single crystal annealed at 150 °C using ordered and disordered kesterite models and refinement of lattice site occupancy factors using single crystal neutron and X-ray diffraction data simultaneously.

Sample annealed at 150 °C	**Ordered kesterite**	**Disordered kesterite**	**Occupancy factors refined with constraint**	
Space group	Tetragonal I -4	Tetragonal I -4	Tetragonal I -4	Tetragonal I -4
a / Å	5.4308(3)	5.4308(3)	5.4308(3)	5.4308(3)
c / Å	10.8328(6)	10.8328(6)	10.8328(6)	10.8328(6)
Unit cell volume / Å^3	319.48(3)	319.48(3)	319.48(3)	319.48(3)
No. of formula unit per unit cell, Z	2	2	2	2
Temperature / K	298	298	298	298
Occupancy				
Cu 2a	1	1	1	1.049(20)
Zn 2a				-0.049(20)
Cu 2c	1	0.5	0.599(4)	0.599(4)
Zn 2c		0.5	0.401(4)	0.401(4)
Cu 2d		0.5	0.401(4)	0.401(4)
Zn 2d	1	0.5	0.599(4)	0.599(4)
No. of parameters refined	11	11	12	13
Neutron diffraction data with odd l reflections				
No. of reflections measured	623	623	623	623
No. of ind. reflections	580	580	580	580
R_{int}	4.05%	4.05%	4.05%	4.05%
wR values (obs/all)	6.39% / 7.07%	3.92% / 4.27%	4.03% / 4.42%	4.00% / 4.41%
X-ray diffraction data				
No. of reflections measured	2959	2959	2959	2959
No. of ind. reflections	516	516	516	516
R_{int}	8.58%	8.58%	8.58%	8.58%
wR values (obs/all)	5.26% / 5.26%	4.92% / 4.92%	4.92% / 4.92%	4.91% / 4.91%
Overall wR values (obs/all)	5.76% / 6.09%	4.53% / 4.66%	4.56% / 4.72%	4.55% / 4.70%

Table 6.4 Fitting of CZTS single crystal deliberately disordered by annealing at 300 °C using ordered and disordered kesterite models and refinement of lattice site occupancy factors using single crystal neutron and X-ray diffraction data simultaneously.

Sample annealed at 300 °C	**Ordered kesterite**	**Disordered kesterite**	**Occupancy factors refined with constraint**	
Space group	Tetragonal I -4	Tetragonal I -4	Tetragonal I -4	Tetragonal I -4
a / Å	5.4332(4)	5.4332(4)	5.4332(4)	5.4332(4)
c / Å	10.8432(7)	10.8432(7)	10.8432(7)	10.8432(7)
Unit cell volume / Å^3	320.10(4)	320.10(4)	320.10(4)	320.10(4)
No. of formula unit per unit cell, Z	2	2	2	2
Temperature / K	298	298	298	298
Occupancy				
Cu 2a	1	1	1	0.94(3)
Zn 2a				0.06(3)
Cu 2c	1	0.5	0.55(3)	0.56(3)
Zn 2c		0.5	0.45(3)	0.44(3)
Cu 2d		0.5	0.45(3)	0.44(3)
Zn 2d	1	0.5	0.55(3)	0.56(3)
No. of parameters refined	13	13	14	15
Neutron diffraction data without odd l reflections				
No. of reflections measured	216	216	216	216
No. of ind. reflections	216	216	216	216
R_{int}	N/A	N/A	N/A	N/A
wR values (obs/all)	2.72% / 3.42%	2.80% / 3.50%	2.80% / 3.50%	2.82% / 3.47%
Neutron diffraction data with odd l reflections				
No. of reflections measured	142	142	142	142
No. of ind. reflections	138	138	138	138
R_{int}	16.75%	16.75%	16.75%	16.75%
wR values (obs/all)	6.83% / 7.76%	4.24% / 4.48%	4.21% / 4.44%	4.21% / 4.43%
X-ray diffraction data				
No. of reflections measured	2947	2947	2947	2947
No. of ind. reflections	520	520	520	520
R_{int}	6.39%	6.39%	6.39%	6.39%
wR values (obs/all)	5.69% / 5.69%	5.59% / 5.60%	5.59% / 5.60%	5.59% / 5.59%
Overall wR values (obs/all)	5.26% / 5.56%	4.77% / 4.93%	4.77% / 4.93%	4.77% / 4.92%

Table 6.5 Fitting of CZTS single crystal annealed at 150 °C and 300 °C with sulphur occupancy factor refined using single crystal neutron and X-ray diffraction data simultaneously.

	Sample annealed at 150 °C		**Sample annealed at 300 °C**	
Occupancy				
Cu 2a	1	1.048(20)	1	0.94(3)
Zn 2a		-0.048(20)		0.06(3)
Cu 2c	0.629(4)	0.630(4)	0.56(3)	0.56(3)
Zn 2c	0.371(4)	0.370(4)	0.44(3)	0.44(3)
Cu 2d	0.371(4)	0.370(4)	0.44(3)	0.44(3)
Zn 2d	0.629(4)	0.630(4)	0.56(3)	0.56(3)
S	0.966(9)	0.964(9)	0.95(1)	0.95(1)
No. of parameters refined	13	14	15	16
Neutron diffraction data without odd l reflections				
wR values (obs/all)	-	-	2.58% / 3.37%	2.59% / 3.33%
Neutron diffraction data with odd l reflections				
wR values (obs/all)	4.03% / 4.45%	4.02% / 4.45%	4.11% / 4.34%	4.11% / 4.33%
X-ray diffraction data				
wR values (obs/all)	4.91% / 4.91%	4.90% / 4.90%	5.59% / 5.60%	5.59% / 5.59%
Overall wR values (obs/all)	4.56% / 4.72%	4.54% / 4.71%	4.72% / 4.89%	4.72% / 4.88%

6.1.3 Anomalous X-ray scattering

Anomalous diffraction data from Cu-edge, Zn-edge and far from the edges were refined simultaneously using TOPAS academic version.[14] The powder patterns are shown in Figure 6.4 for data acquired at Cu-edge (8972 eV), Figure 6.5 at Zn-edge (9647 eV), and Figure 6.6 at far from the edges (15 keV).

There is no correlation between the lattice parameter a and temperature, while the lattice parameter c increases with annealing temperature (Figure 6.7). A similar trend was also observed in Többens *et al.*'s[10] work.

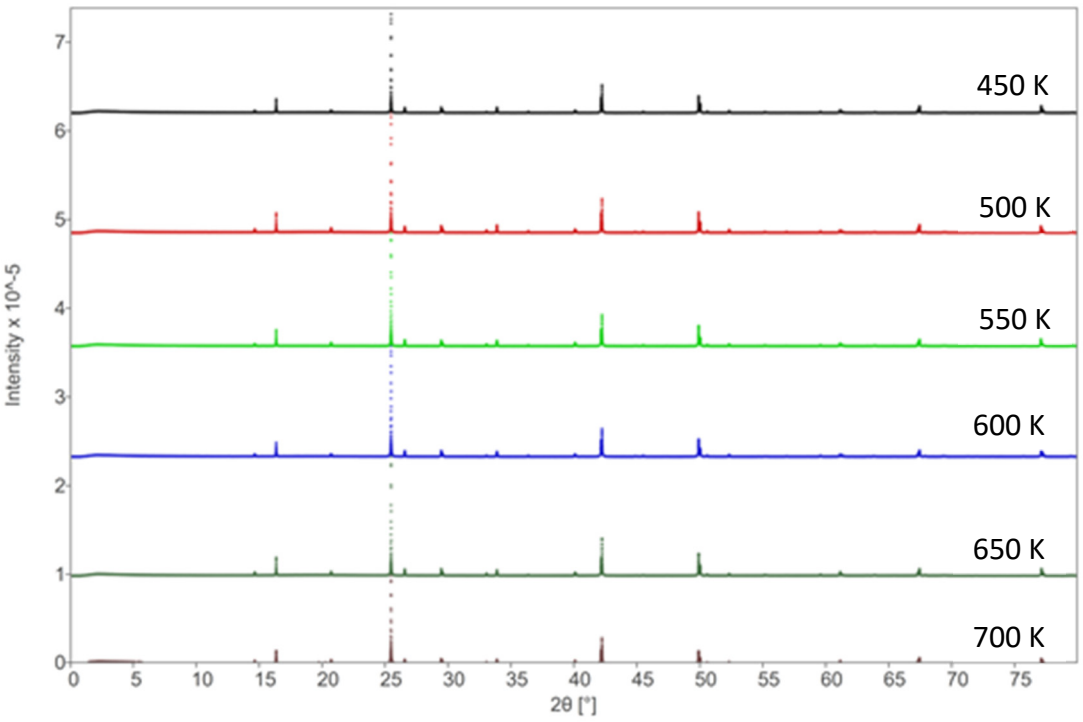

Figure 6.4 X-ray diffraction pattern for CZTS samples annealed in the range of 450 K and 700 K. Measurements taken at room temperature using 8972 eV X-rays (near Cu-edge) at Diamond I11.

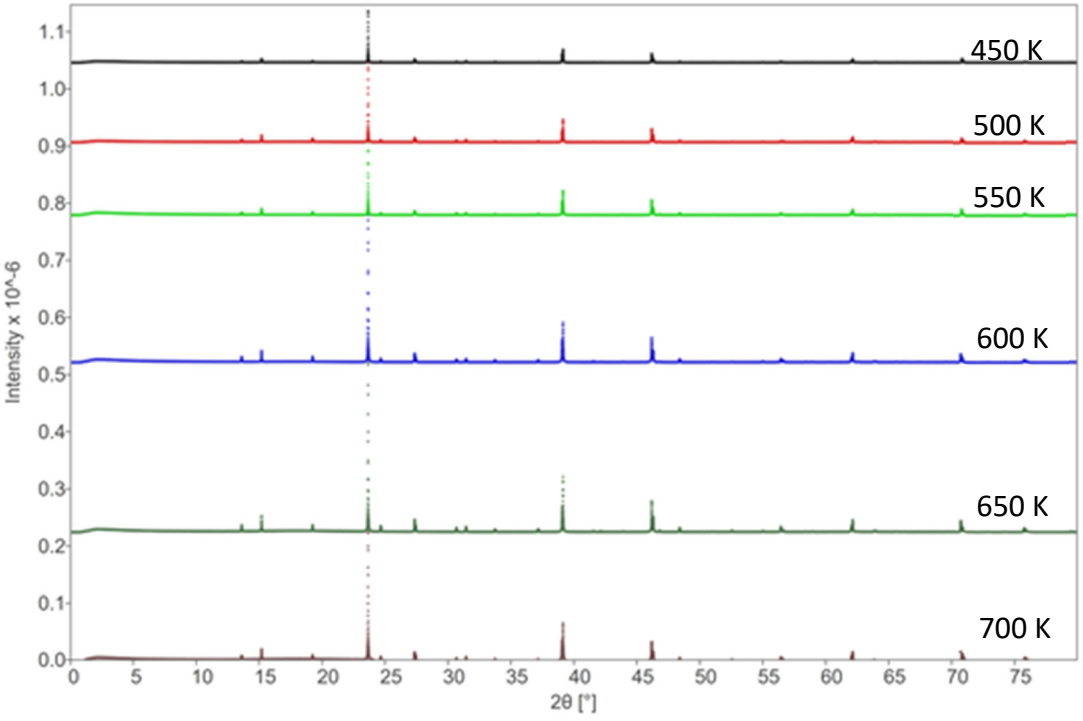

Figure 6.5 X-ray diffraction pattern for CZTS samples annealed in the range of 450 K and 700 K. Measurements taken at room temperature using 9647 eV X-rays (near Zn-edge) at Diamond I11.

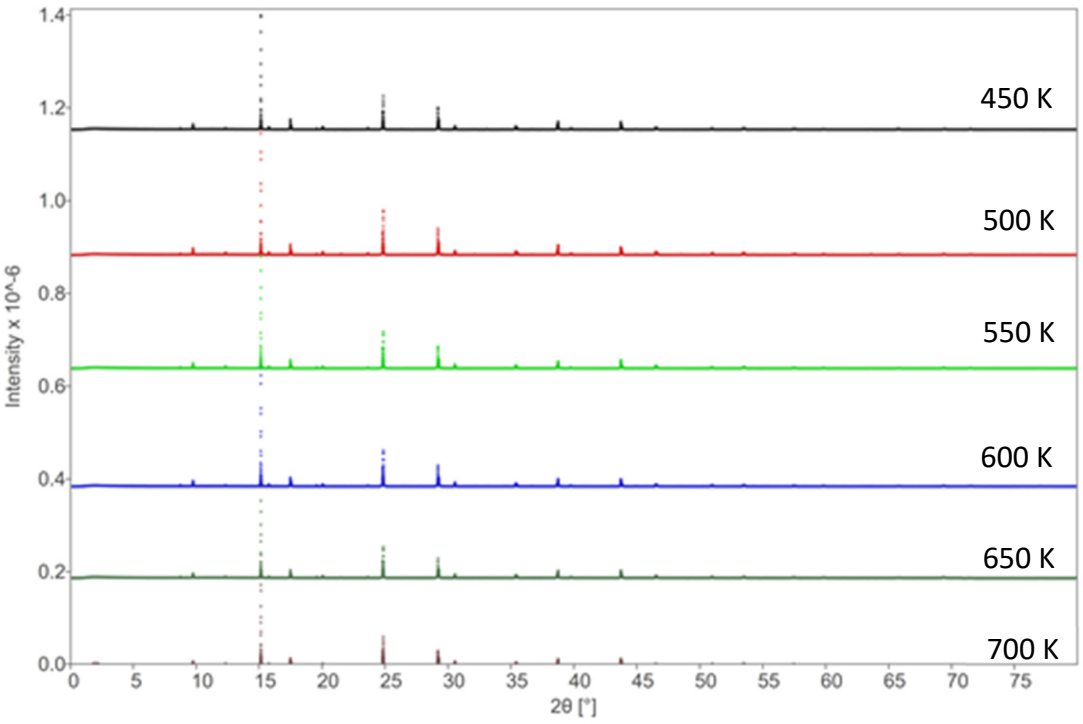

Figure 6.6 X-ray diffraction pattern for CZTS samples annealed in the range of 450 K and 700 K. Measurements taken at room temperature using 15 keV X-rays at Diamond I11.

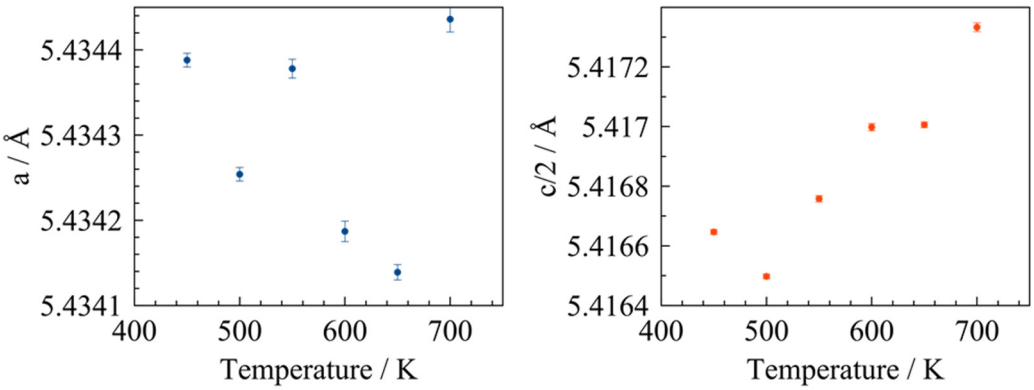

Figure 6.7 Lattice parameter of annealed CZTS samples obtained from anomalous diffraction data.

The anomalous scattering factors of Cu and Zn were refined and the result is presented in Figure 6.8. While the anomalous scattering factor was expected to be constant regardless of annealing temperature, there was an increase in f'_{Cu} with increasing annealing temperature, while f'_{Zn} was totally random. This suggested the anomalous scattering factor should not be refined. f'_{Cu} and f'_{Zn} were then fixed using

estimated values from the calculations in Figure 2.5 ($f'_{Cu,\ Zn}$ = -7 or -7.5) for subsequent Rietveld refinements.

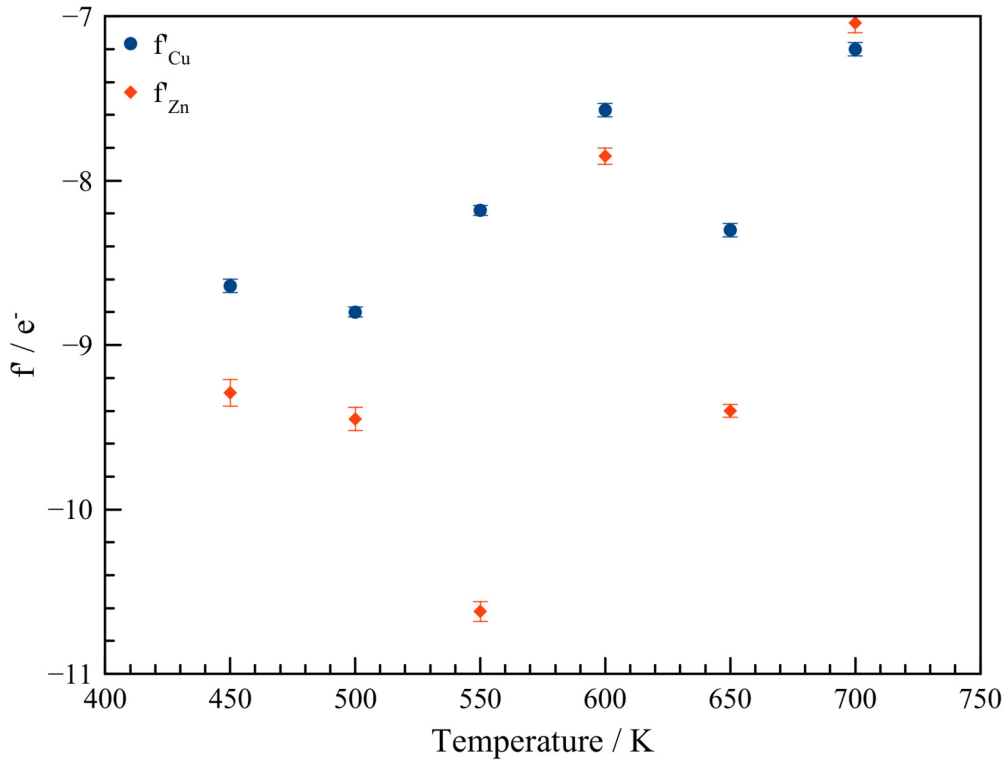

Figure 6.8 Anomalous scattering factors of Cu and Zn obtained from the refinement of anomalous diffraction data.

Rietveld refinements were attempted in more than 10 models and all models yield similar results. Examples of site occupancy factors for Cu at 2c site and Zn at 2d site is presented in Figure 6.9. In these refinements, the anomalous scattering factors were fixed at -7 or -7.5. Constraints were also applied so that (i) the site occupancy factor per site is equal to one; and (ii) the thermal parameters for all atoms in 2c and 2d sites are the same. The result shows the occupancy factors decreased when the anomalous scattering factors of Cu and Zn were decreased from -7 to -7.5. The result also shows the sample annealed at 650 K is not disordered, however, resonance Raman spectra confirmed that all samples annealed above 600 K were disordered. The resonance Raman order parameter Q for these samples are presented in Figure 6.10. The refinement result for samples annealed at 450 K and 650 K is presented in Table 6.6 and Table 6.7. To prove whether the anomalous scattering effect near the absorption edges can distinguish between ordered and disordered kesterite, refinement were carried out using the ordered kesterite and disordered kesterite

models similar to the ones carried out for the neutron diffraction data in section 6.1.2. The R_{wp} factors for both models at all annealed temperatures are very similar (Table 6.8), which concluded that the anomalous diffraction data we acquired cannot distinguish between ordered and disordered kesterite.

Table 6.6 Refinement of CZTS annealed at 450 K using ordered and disordered kesterite models using synchrotron diffraction data taken at Cu-edge, Zn-edge and 15 keV simultaneously.

Sample annealed at 450 K	**Ordered kesterite**	**Disordered kesterite**	**Occupancy factors refined with constraint**	
Space group	Tetragonal I -4	Tetragonal I -4	Tetragonal I -4	Tetragonal I -4
a / Å	5.434293(8)	5.434293(8)	5.434290(8)	5.434292(8)
c / Å	10.833059(17)	10.833059(17)	10.833052(17)	10.833057(17)
Unit cell volume / Å^3	319.917(1)	319.917(1)	319.916(1)	319.917(1)
No. of formula unit per unit cell, Z	2	2	2	2
Temperature / K	298	298	298	298
f'$_{Cu}$	-7.5	-7.5	-7.0	-7.5
f'$_{Zn}$	-7.5	-7.5	-7.0	-7.5
Occupancy				
Cu 2c	1	0.5	1.000(12)	0.949(11)
Zn 2c		0.5	0.000(12)	0.050(11)
Cu 2d		0.5	0.000(12)	0.047(11)
Zn 2d	1	0.5	1.000(12)	0.953(11)
No. of parameters refined	127	127	134	134
R_{exp}	3.90%	3.90%	3.90%	3.90%
R_{wp}	8.68%	8.69%	8.53%	8.54%
R Bragg	4.86%	4.31%	4.74%	4.80%

Table 6.7 Refinement of CZTS annealed at 650 K using ordered and disordered kesterite models using synchrotron diffraction data taken at Cu-edge, Zn-edge and 15 keV simultaneously.

Sample annealed at 650 K	**Ordered kesterite**	**Disordered kesterite**	**Occupancy factors refined with constraint**	
Space group	Tetragonal I -4	Tetragonal I -4	Tetragonal I -4	Tetragonal I -4
a / Å	5.434044(9)	5.434044(9)	5.434041(9)	5.434043(9)
c / Å	10.833791(19)	10.833791(19)	10.833787(19)	10.833790(19)
Unit cell volume / Å^3	319.909(1)	319.909(1)	319.909(1)	319.909(1)
No. of formula unit per unit cell, Z	2	2	2	2
Temperature / K	298	298	298	298
f'$_{Cu}$	-7.5	-7.5	-7.0	-7.5
f'$_{Zn}$	-7.5	-7.5	-7.0	-7.5
Occupancy				
Cu 2c	1	0.5	1.000(10)	0.992(9)
Zn 2c		0.5	0.000(10)	0.008(9)
Cu 2d		0.5	0.000(9)	0.032(8)
Zn 2d	1	0.5	1.000(9)	0.968(8)
No. of parameters refined	127	127	134	134
R_{exp}	2.84%	2.84%	2.84%	2.84%
R_{wp}	7.01%	7.06%	6.59%	6.60%
R Bragg	2.67%	2.57%	2.57%	2.67%

Table 6.8 R_{wp} factor from the refinement using ordered and disordered kesterite models in the anomalous diffraction experiment.

Temperature / K	**Ordered kesterite**	**Disordered kesterite**
450	8.68%	8.69%
500	7.34%	7.35%
550	9.54%	9.54%
600	7.87%	7.82%
650	7.01%	7.06%
700	6.67%	6.63%

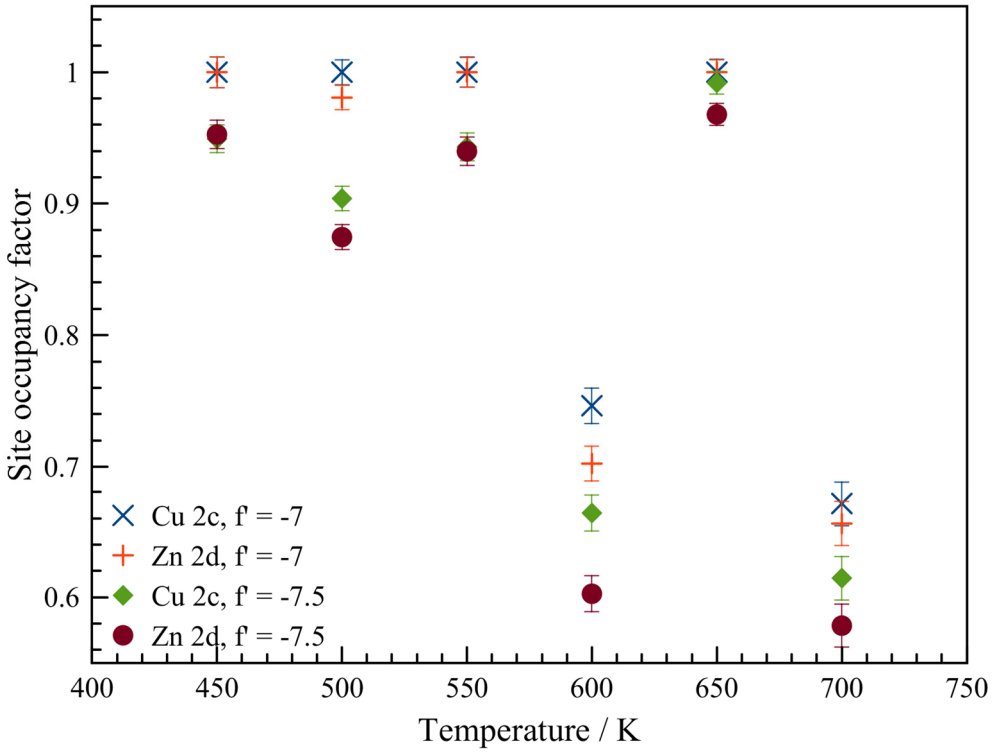

Figure 6.9 Site occupancy factors of Cu at 2c site and Zn at 2d site refined using fixed anomalous scattering factors.

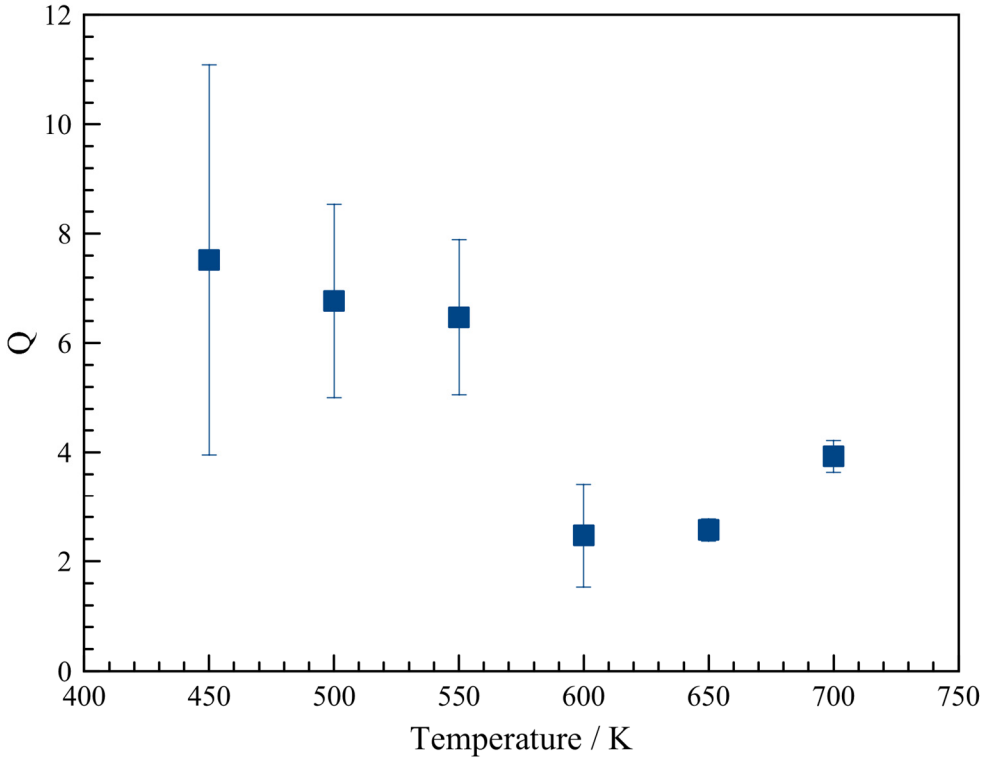

Figure 6.10 Resonance Raman order parameter Q for the annealed CZTS samples used in the synchrotron diffraction experiment.

Többens *et al.*[10] later reported successful attempt to determine the occupancy factors of Cu and Zn in kesterite using anomalous diffraction at ten different wavelength energies. Többens *et al.*[10] highlighted the problem about the strong correlation between the occupancy factors due to the pseudosymmetry of kesterite structure, and developed a two-stage process detailed in a different report[15] to derive reliable site occupancy factors. In the report, Többens *et al.* refined the occupancy factors from the different wavelengths independently, and linearised the occupancy factors using the following equations:

Equation 6.1

$$\mathrm{occ}^{\mathrm{calc}}(\mathrm{Cu}) = \mathrm{occ}(\mathrm{Zn})\frac{f(\mathrm{Zn})}{f(\mathrm{Cu})} + \mathrm{occ}(\mathrm{Cu})$$

$$\mathrm{occ}^{\mathrm{calc}}(\mathrm{Zn}) = \mathrm{occ}(\mathrm{Cu})\frac{f(\mathrm{Cu})}{f(\mathrm{Zn})} + \mathrm{occ}(\mathrm{Zn})$$

where $\mathrm{occ}^{\mathrm{calc}}$(X) is the occupancy factor of atom X in the refinement, *f*(X) is the atomic form factor for atom X (Equation 2.4), and occ(X) is the actual site occupancy factor.

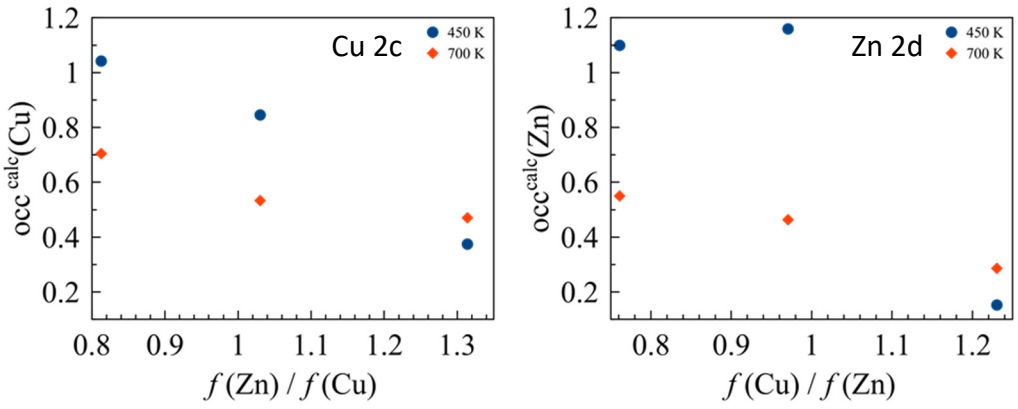

Figure 6.11 Linearisation plot of refined occupancy factors to scattering power ratio.

Attempts were carried out to linearise the anomalous diffraction data in this work, and negative slopes were observed (Figure 6.11). The observation of negative slope was mentioned in Többens *et al.*'s report,[15] and Többens *et al.* attributed it to problems in either experiment or analysis procedure, however, there was no detail on how to troubleshoot the problem.

Bosson *et al.*[13] also reported successful attempt to determine the occupancy factors of Cu and Zn in kesterite using anomalous diffraction at seven wavelength energies. Bosson *et al.* observed polymorphic splitting in some of their CZTS samples (Figure 6.12). However, it was not observed in this work (Figure 6.13).

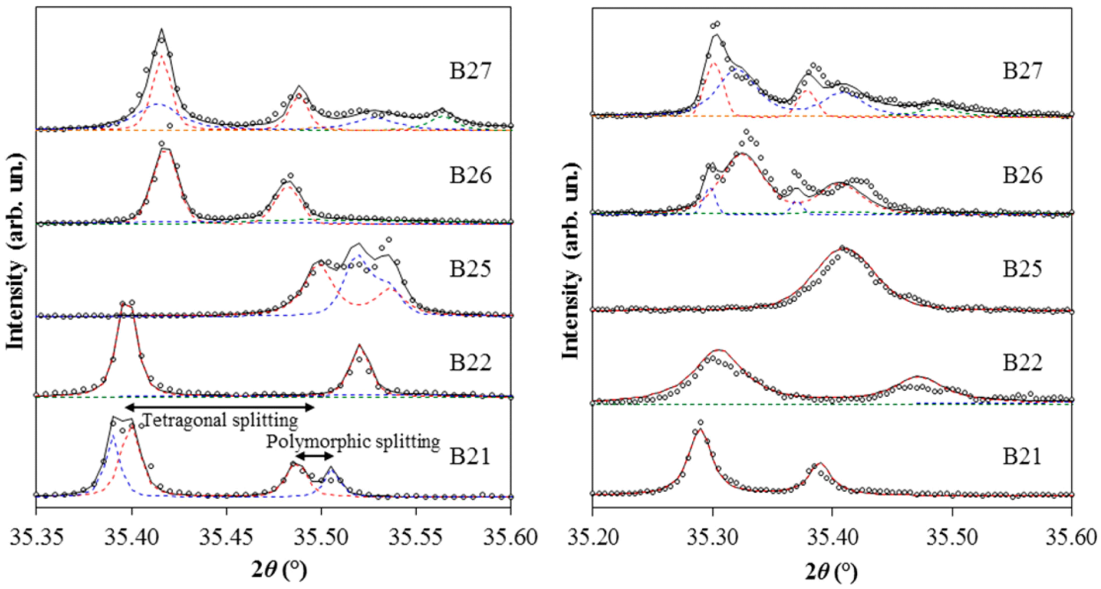

Figure 6.12 Peak splitting due to multiple CZTS phases in 15 keV patterns: (left) 300 K; (right) 600 K. Reproduced from Bosson *et al.*[13]

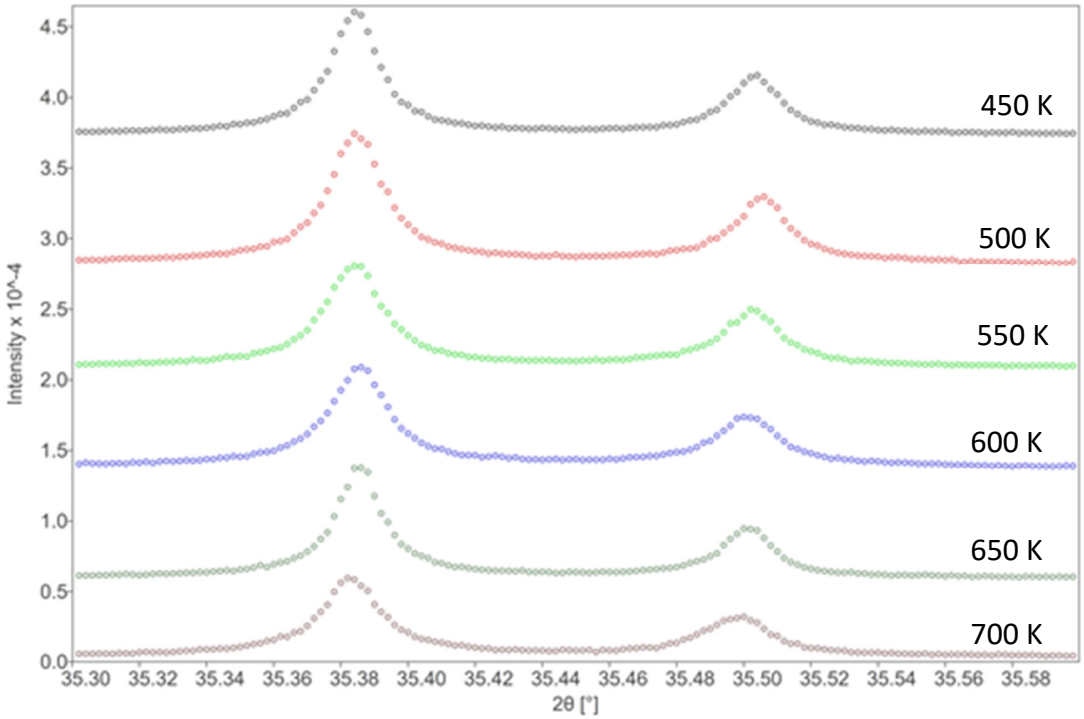

Figure 6.13 PXRD pattern collected at 15 keV between 2θ 35.3° and 35.6°.

6.2 Conclusion

Although Cu/Zn disorder is presented in all synthetic CZTS(e) materials, it is not possible to quantify the site occupancy factors using single wavelength X-ray diffraction (XRD) methods due to the similarity in the atomic form factors of isoelectronic Cu^{+} and Zn^{2+}. This thesis attempted to qualify and quantify the degree of disorder in CZTS single crystals and powders using near-resonant Raman spectroscopy, neutron diffraction and anomalous diffraction. These techniques also have different penetration depths, i.e. few tens to a hundred nm in Raman spectroscopy;[16] few hundred nm in a laboratory X-ray diffractometer; and the bulk in neutron diffraction. While this thesis is focused on characterising bulk single crystals, the thickness of CZTS(e) film in actual CZTS(e) devices is in the sub-micron region.

Resonance Raman spectroscopy provides a quick way to qualitatively distinguish between partially ordered and disordered CZTS(e) by comparing the intensity ratio between the peaks at 287 and 303 cm^{-1} (the Q parameter), and the peaks at 338, 366 and 374 cm^{-1} (the Q' parameter). It was observed that the peak intensity at 303 cm^{-1} became very weak in samples that were annealed at lower temperatures (*i.e.* less disordered), which increased the uncertainty in determining the Q parameter. It was also observed that the annealing time needed for the samples to reach equilibrium ordering were longer than the ones calculated using the Vineyard model. This may be due to the different composition and the preparation method to the literature.[6] The critical temperature of CZTS analysed in this thesis is around 250 °C using the data from resonance Raman spectroscopy.

The initial neutron diffraction experiment was unsuccessful due to the mis-indexing of the tetragonal unit cell. Only the sample annealed at 150 °C was measured successfully, and the disordered sample (300 °C) was partially measured. Both sets of data clearly showed a significant lower *R*-factor when refined using a partially disordered kesterite model compared to a fully disordered kesterite or other other structural model. The refinements also proved the sample annealed at 150 °C is also more ordered than the sample annealed at 300 °C. We can conclude that single crystal neutron diffraction can quantify accurately the occupancy factors of Cu and

Zn in CZTS(e) materials. This is also the first reported single crystal neutron diffraction experiment for CZTS.

Although in theory the anomalous scattering effect should enhance the scattering of Cu and Zn near their absorption edges, it was not as straightforward in practice. The initial refinements appeared to show that the sample annealed at 650 K was ordered kesterite, but analysis of the resonance Raman spectra led to the opposite conclusion. There was also no significant difference in the *R*-factors between fits to the ordered and disordered kesterite models. A second attempt to analyse the data with a two-stage process proposed by Többens *et al.*[15] was also unsuccessful. Since the powder patterns in this work were only collected at three different wavelength energies, in contrast, Többens *et al.*[10] and Bosson *et al.*[13] performed data collection at ten and seven different wavelength energies respectively. We attributed the cause for the unsuccessful refinement to the inadequate of datasets collected.

Reference

1. Schorr, S., *The crystal structure of kesterite type compounds: A neutron and X-ray diffraction study.* Solar Energy Materials and Solar Cells, 2011. **95**(6): p. 1482-1488.
2. Choubrac, L., Paris, M., Lafond, A., Guillot-Deudon, C., Rocquefelte, X., and Jobic, S., *Multinuclear (^{67}Zn, ^{119}Sn and ^{65}Cu) NMR spectroscopy - an ideal technique to probe the cationic ordering in Cu_2ZnSnS_4 photovoltaic materials.* Physical Chemistry Chemical Physics, 2013. **15**(26): p. 10722-10725.
3. Scragg, J.J.S., Choubrac, L., Lafond, A., Ericson, T., and Platzer-Björkman, C., *A low-temperature order-disorder transition in Cu_2ZnSnS_4 thin films.* Applied Physics Letters, 2014. **104**(4): p. 041911.
4. Dimitrievska, M., Fairbrother, A., Fontané, X., Jawhari, T., Izquierdo-Roca, V., Saucedo, E., and Pérez-Rodríguez, A., *Multiwavelength excitation Raman scattering study of polycrystalline kesterite Cu_2ZnSnS_4 thin films.* Applied Physics Letters, 2014. **104**(2): p. 021901.
5. Gurel, T., Sevik, C., and Cagin, T., *Characterization of vibrational and mechanical properties of quaternary compounds Cu_2ZnSnS_4 and $Cu_2ZnSnSe_4$ in kesterite and stannite structures.* Physical Review B, 2011. **84**(20).
6. Scragg, J.J.S., Larsen, J.K., Kumar, M., Persson, C., Sendler, J., Siebentritt, S., and Bjorkman, C.P., *Cu-Zn disorder and band gap fluctuations in $Cu_2ZnSn(S,Se)_4$: Theoretical and experimental investigations.* Physica Status Solidi B-Basic Solid State Physics, 2016. **253**(2): p. 247-254.
7. Rodríguez-Carvajal, J., *Recent advances in magnetic structure determination by neutron powder diffraction.* Physica B: Condensed Matter, 1993. **192**(1): p. 55-69.
8. *CrystalDiffract*, CrystalMaker Software Limited, Begbroke Science Park, Oxfordshire, UK.
9. Ritscher, A., Hoelzel, M., and Lerch, M., *The order-disorder transition in Cu_2ZnSnS_4 – A neutron scattering investigation.* Journal of Solid State Chemistry, 2016. **238**: p. 68-73.
10. Többens, D.M., Gurieva, G., Levcenko, S., Unold, T., and Schorr, S., *Temperature dependency of Cu/Zn ordering in CZTSe kesterites determined by anomalous diffraction.* physica status solidi (b), 2016. **253**(10): p. 1890-1897.
11. Bosson, C.J., Birch, M.T., Halliday, D.P., Knight, K.S., Gibbs, A.S., and Hatton, P.D., *Cation disorder and phase transitions in the structurally complex solar cell material Cu_2ZnSnS_4.* Journal of Materials Chemistry A, 2017. **5**(32): p. 16672-16680.
12. Petříček, V., Dušek, M., and Palatinus, L., *Crystallographic Computing System JANA2006: General features*, in *Zeitschrift für Kristallographie - Crystalline Materials*. 2014. p. 345.
13. Bosson, C.J., Birch, M.T., Halliday, D.P., Tang, C.C., Kleppe, A.K., and Hatton, P.D., *Polymorphism in Cu_2ZnSnS_4 and New Off-Stoichiometric Crystal Structure Types.* Chemistry of Materials, 2017. **29**(22): p. 9829-9839.
14. Coelho, A.A., Evans, J., Evans, I., Kern, A., and Parsons, S., *The TOPAS symbolic computation system.* Powder Diffraction, 2012. **26**(S1): p. S22-S25.
15. Többens, D.M., Gunder, R., Gurieva, G., Marquardt, J., Neldner, K., Valle-Rios, L.E., Zander, S., and Schorr, S., *Quantitative anomalous powder diffraction*

analysis of cation disorder in kesterite semiconductors. Powder Diffraction, 2016. **31**(3): p. 168-175.

16. Dimitrievska, M., Xie, H., Fairbrother, A., Fontané, X., Gurieva, G., Saucedo, E., Pérez-Rodríguez, A., Schorr, S., and Izquierdo-Roca, V., *Multiwavelength excitation Raman scattering of $Cu_2ZnSn(S_xSe_{1-x})_4$ ($0 \leq x \leq 1$) polycrystalline thin films: Vibrational properties of sulfoselenide solid solutions.* Applied Physics Letters, 2014. **105**(3): p. 031913.

7 The fabrication and characterisation of CZTS single crystal device

CZTS single crystals were fabricated into solar cells using the configuration normally reported in CZTS(e) cells, *i.e.* Mo/CZTS/CdS/Al:ZnO/i-Zn:O/Ni. By characterising a single crystal device, we hope to obtain CZTS properties without grain boundary effects, and hence allowing us to find out what other factors cause the low performance in CZTS.

7.1 Results and Discussion

Photographic images of the completed CZTS single crystal device are shown in Figure 7.1.

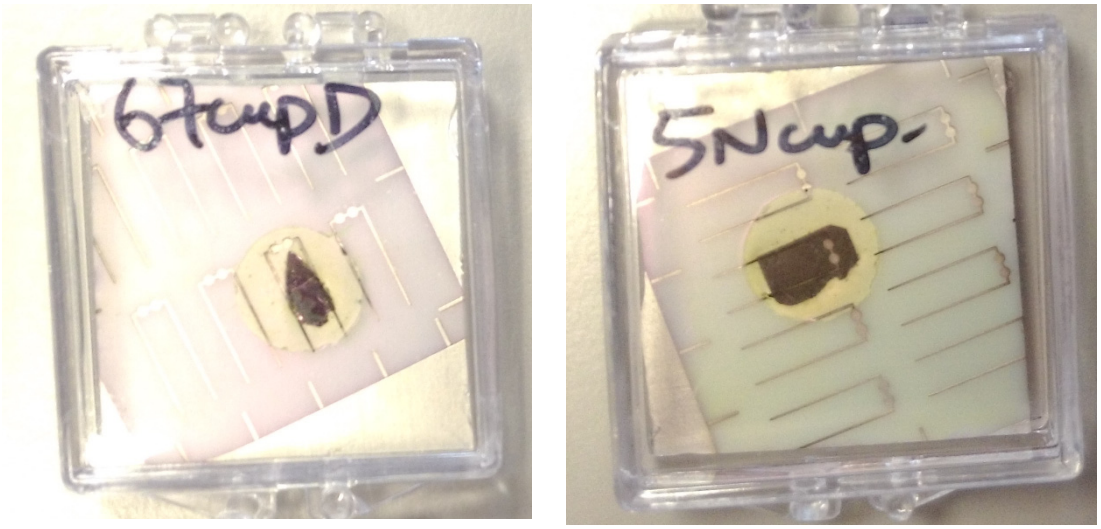

Figure 7.1 Photographic images showing CZTS single crystals device (left) 67D and (right) 85.

The JV performance of the devices are presented in Figure 7.2. For device 67D, a V_{OC} of 588 mV is in the same range with most reported CZTS devices. However, a linear current-voltage relationship indicates a high series resistance, and deteriorates the J_{SC}. The series resistance calculated using Ohm's law is 420 Ω cm^{-2}, which is a few orders of magnitude higher than a usual working solar cell. I attribute this high series resistance to the non-ohmic back contact between the Mo and CZTS. Note that in a polycrystalline CZTS(e) thin film device, the Mo reacts with sulphur or selenium during annealing to form a $MoS(e)_2$ layer, which is beneficial to the ohmicity of the

Mo back contact.[1] For device 85, a very low V_{OC} suggests the device is severely shunted during device fabrication.

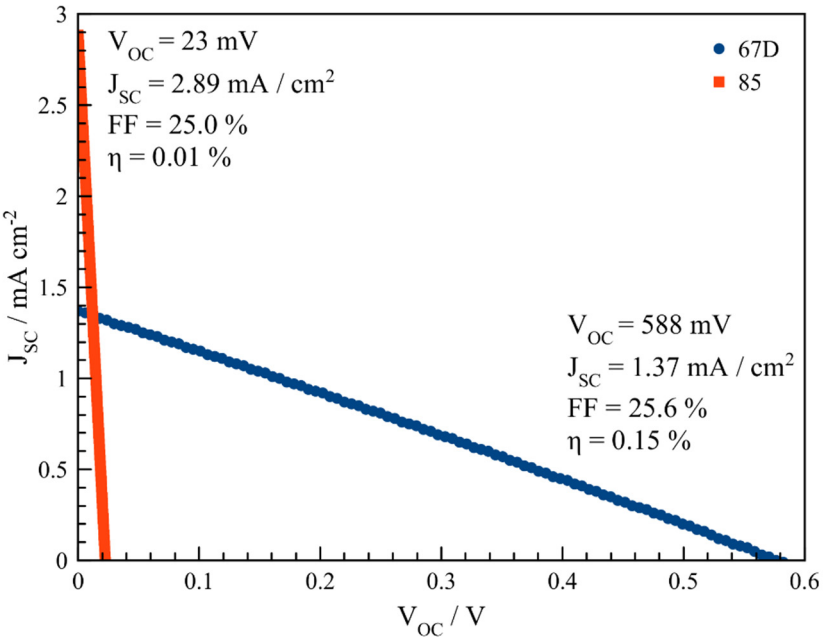

Figure 7.2 Solar device performance for single crystal CZTS device.

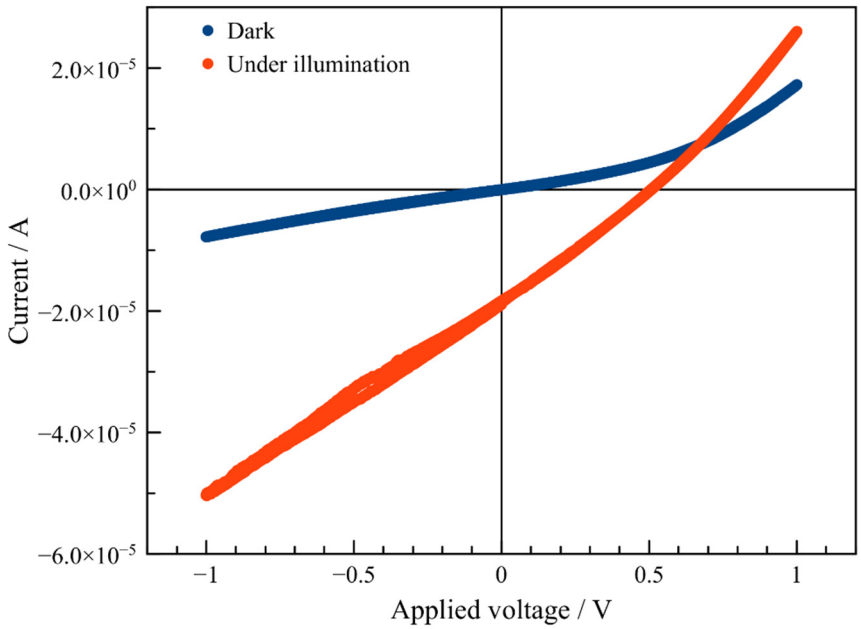

Figure 7.3 The current-voltage characteristic for device 67D in the dark and under illumination at a scan rate of 0.1 V s^{-1}.

The current-voltage characteristic for device 67D is shown in Figure 7.3. The plot also agrees the series resistance in the device is huge, especially when the current did not reach a plateau even a large reverse potential was applied. Hysteresis was observed in the dark and under illumination after a large reverse potential was applied.

The EQE response of device 67D at short circuit is shown in Figure 7.4. The steep onset and a bandgap of 1.64 eV is similar to the CZTS platelet studied in my published work.[2] (*cf.* E_g = 1.68 eV, page 121) It is assumed that the steep onset is due to the competition between thermal detrapping and recombination in tail states.

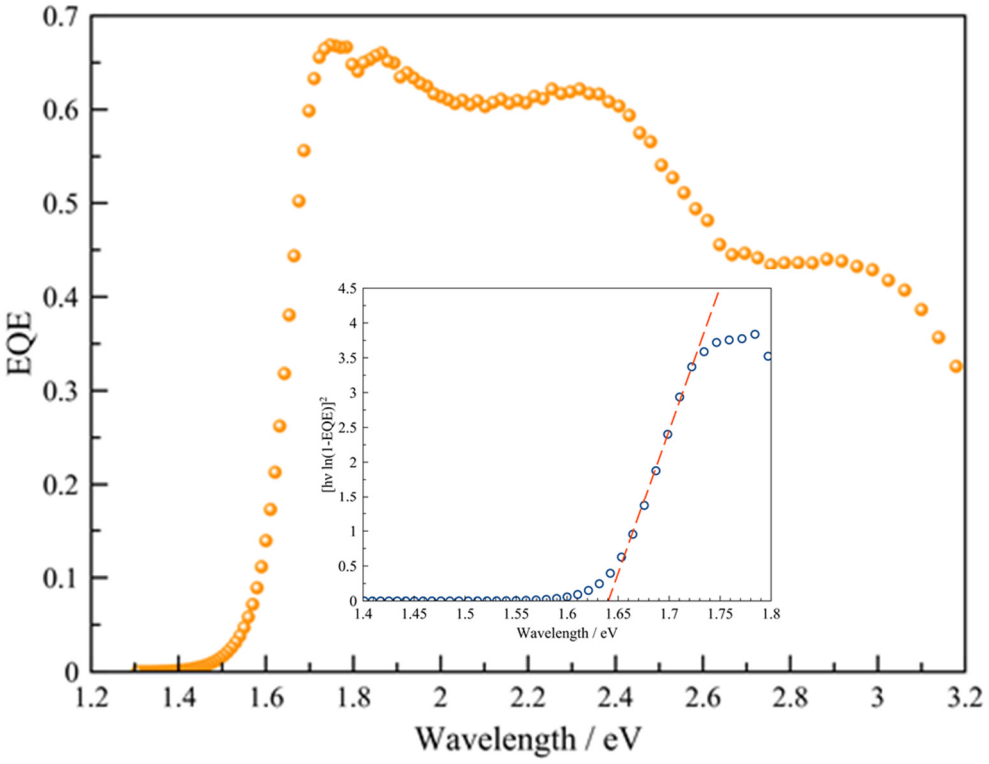

Figure 7.4 EQE spectrum for CZTS single crystal device 67D at -0.5 V applied potential. The insert shows a Tauc plot for a direct transition (E_g = 1.64 eV).

Gärtner analysis was carried out to estimate the built-in potential. Examples of Gärtner plots are shown in Figure 7.5. At all wavelengths where Gärtner analysis was carried out, three lines can be extrapolated in different regions of the plot: under reverse potential, between 0 – 0.3 V, and > 0.3 V. I attribute the intercept for the slope under reverse potential to the true built-in potential of CZTS (1.04 ± 0.01 V), because under reverse potential, the band bending at the junction increases, and

results in surface states located near the valence band being occupied, and hence the Fermi level is 'unpinned'. The intercepts at 0.66 ± 0.02 and 0.48 ± 0.01 V can be attributed to surface states. Surface states are states caused by the incomplete covalent bonds at the surface of a semiconductor. They result in electron energy levels within the energy bandgap. Electrons from the valence band fall into these surface states and cause the Fermi energy 'pinning' to the level of which these surface states are filled.[3]

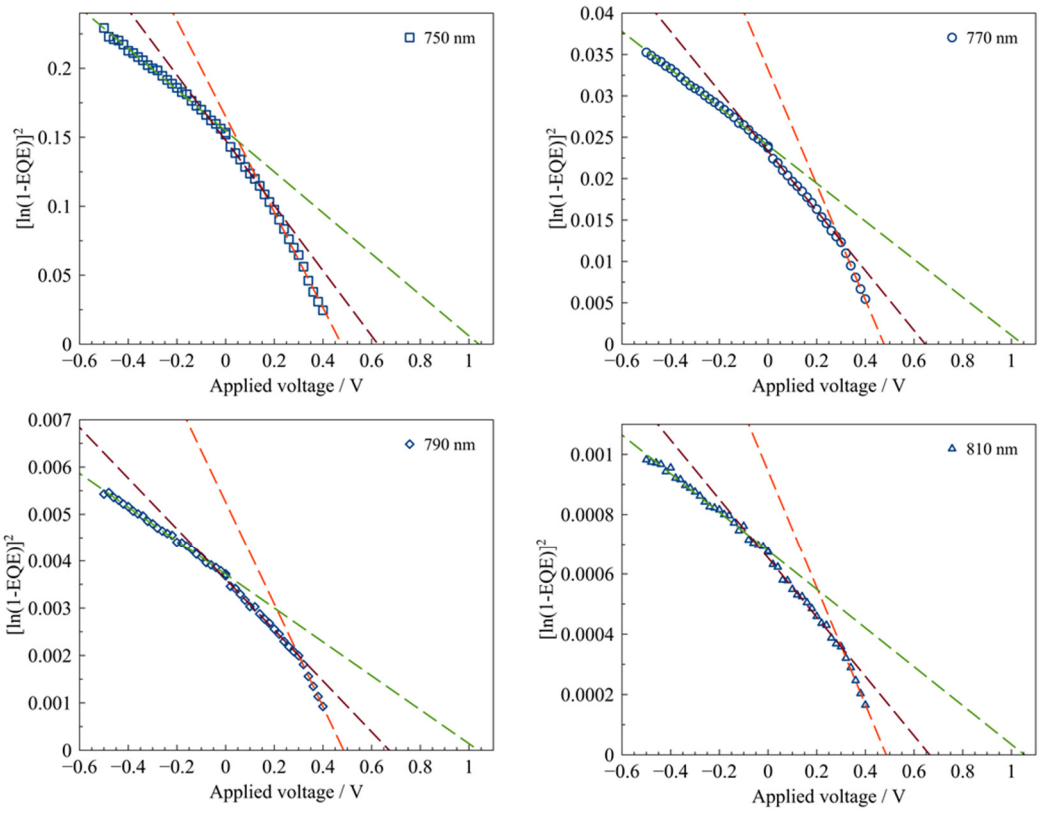

Figure 7.5 Examples of Gärtner plots taken at 750, 770, 790 and 810 nm to estimate the built-in potential of CZTS.

The impedance result for device 67D is presented in the Nyquist plots and Bode plots shown in Figure 7.6 and Figure 7.7. Near-semicircle shapes were observed in the Nyquist plots, which is the characteristic in photovoltaic devices.[4-6] The impedance data were then fitted using the equivalent circuits used by Fernandes *et al.*[5] (Figure 2.12). The fitting results is shown in Figure 7.8. None of the models (M1, M2 and M3) fitted the experimental data nicely, so model M2 was modified as shown in Figure 7.9.

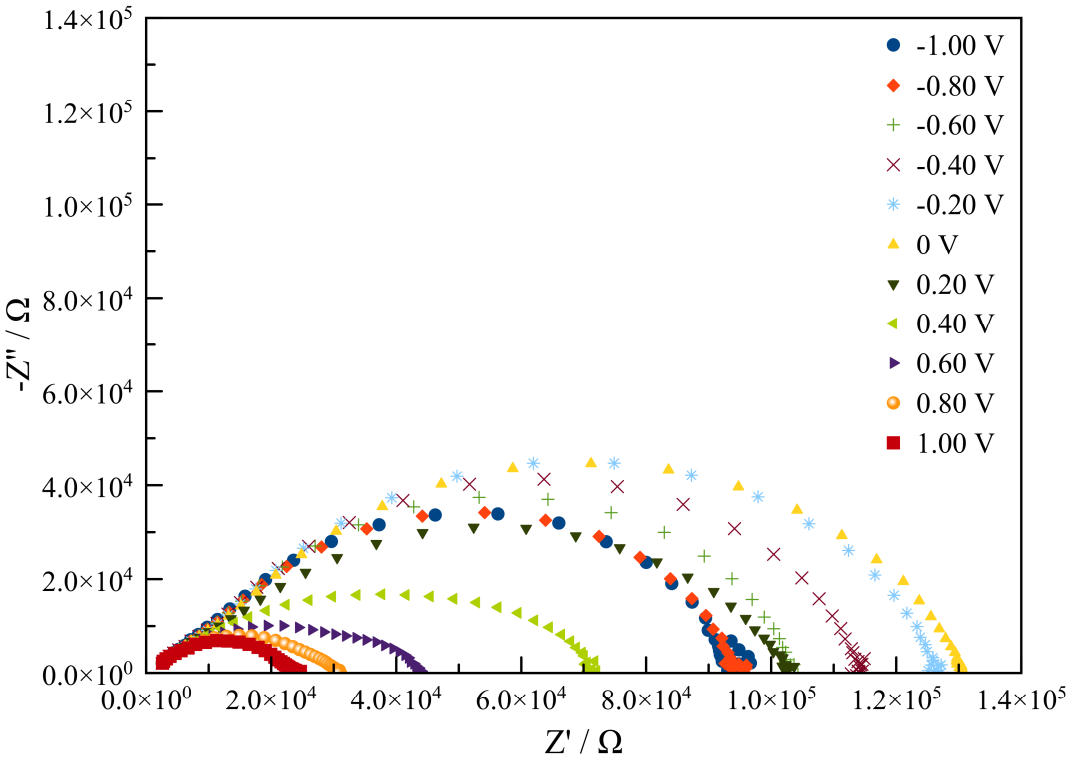

Figure 7.6 Nyquist plot showing the impedance data for CZTS single crystal device 67D at applied potential between -1.0 and 1.0 V.

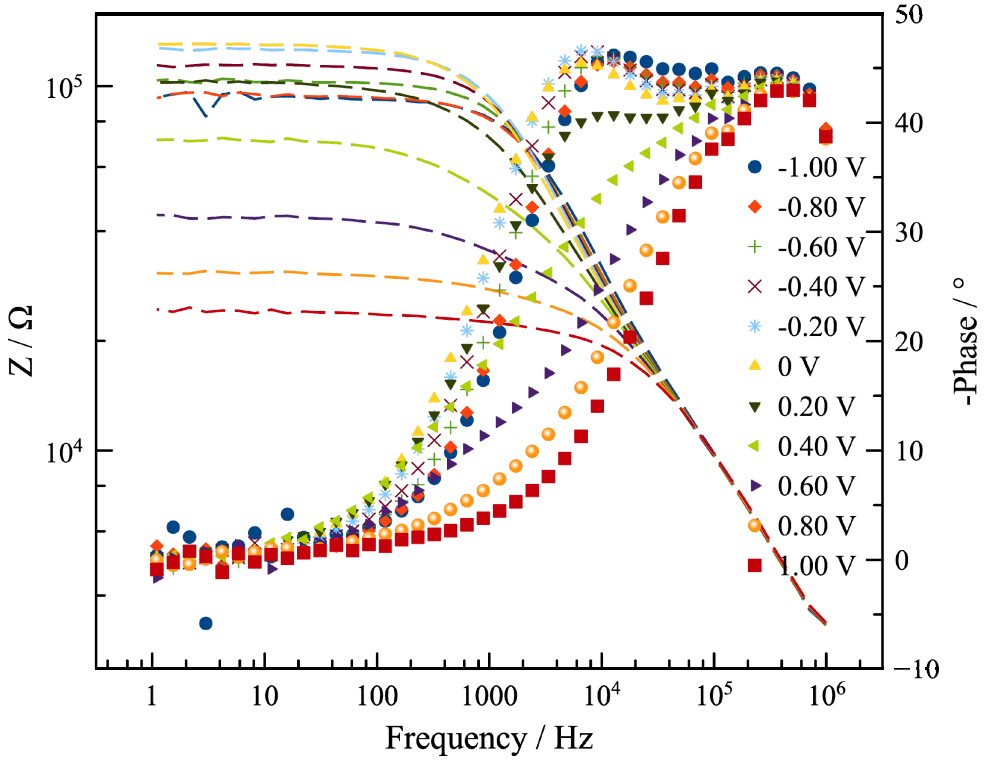

Figure 7.7 Bode plot showing the impedance data for CZTS single crystal device 67D at applied potential between -1.0 and 1.0 V. Primary axis: Z, dashed lines. Secondary axis: phase, data points.

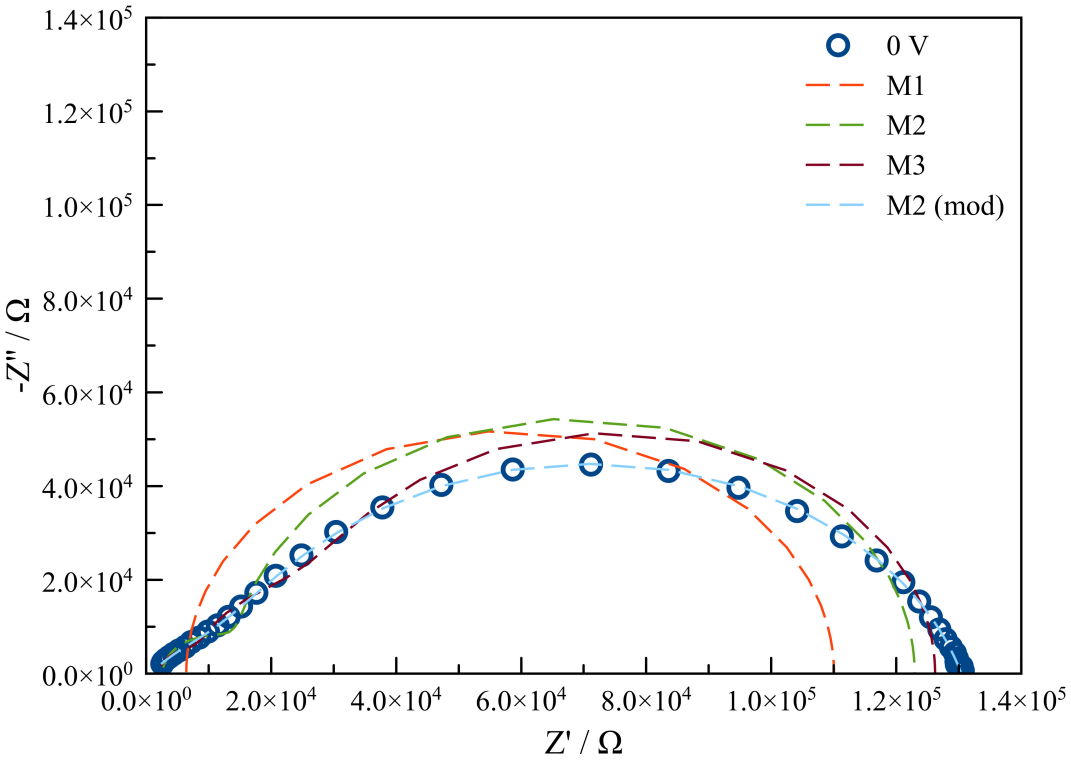

Figure 7.8 The results of the fittings at 0 V for the equivalent circuits.

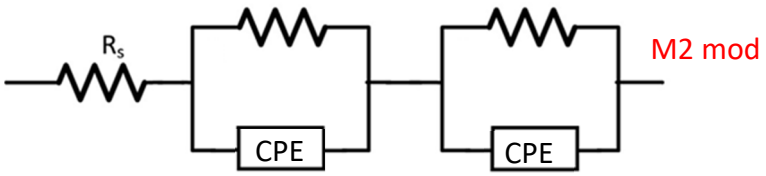

Figure 7.9 Modified equivalent circuits used in the fitting of impedance data in this work. CPE: constant phase element.

In the modified M2 model, the capacitors were replaced by a constant phase element (CPE) to reflect the 'depressed' semicircle in the Nyquist plots. The use of CPE to fit the data indicates presence of inhomogeneities in the system.[7] Fernandes *et al.*[5] also noted that a depressed semicircle in the Nyquist plot can be related to absorber layer inhomogeneity and low quality heterointerface.

Since the impedance of a constant phase element is:

Equation 7.1

$$Z_{CPE} = \frac{1}{Q_0(j\varpi)^{\psi}}$$

where Q_0 and ψ are frequency-independent parameters which usually depend on temperature, and $0 \leq \psi \leq 1$. $\Psi = 1$ in an ideal capacitor, and $\Psi = 0$ in an ideal resistor.[7] The equivalent capacitance, C of the CPE in the parallel circuit containing a resistor with *R* resistance can be calculated using the following equation:[8]

Equation 7.2

$$\mathrm{C} = \frac{(Q_0 R)^{-\psi}}{R}$$

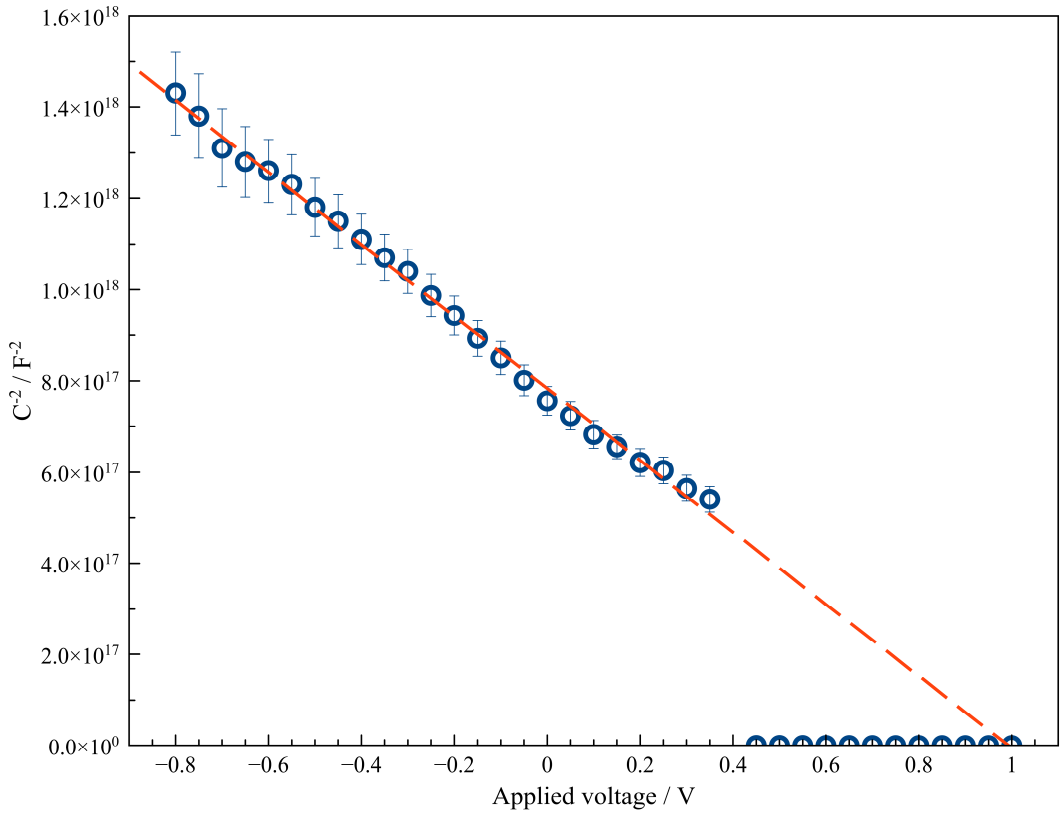

Figure 7.10 Mott-Schottky plots for CZTS single crystal device 67D.

Table 7.1 Estimated values for the doping density (N_A), built-in potential and depletion width for CZTS single crystal device 67D calculated from Mott-Schottky equations. $\varepsilon_{CdS} = 5.4$;[9] $\varepsilon_{CZTS} = 6.7$;[10] $N_D = 10^{17}$ cm^{-1}.[11]

	N_A / cm^{-3}	V_{bi} / V	W_p / nm	
			Eqn. 1.16	Eqn. 1.17
Eqn. 1.14	2.26×10^{15}	1.01	574	566
Eqn. 1.15	2.33×10^{15}	1.01	566	558

Mott-Schottky analysis was then carried out by plotting $1/C^2$ vs. the applied potential as shown in Figure 7.10. There is a sudden change in the Mott-Schottky behaviour at forward bias above 0.4 V. Similar change was also observed in the Nyquist plot and Bode plot in Figure 7.6 and Figure 7.7. The doping density, built-in potential and depletion width were calculated using Mott-Schottky equations and presented in Table 7.1. The difference in doping density and depletion width between using the metal-semiconductor junction and p-n hetrojunction expressions are not significant, suggesting using the simpler equations (Equation 1.14 and 1.16) is adequate to estimate the doping density and depletion width in CZTS. A doping density in the order of 10^{15} cm^{-3} agrees with the conclusion made in my published work (*cf.* 10^{15} cm^{-3}).[2] A depletion width of 570 nm is doubled to what has been reported (*cf.* 200 – 230 nm),[5, 12] but is again leaning towards the conclusion made in my published work (*cf.* 1 µm). The wider depletion width is due the lower doping density. A built-in potential of 1.01 V was obtained from the Mott-Schottky analysis, which also agrees with the value obtained from the Gärtner analysis.

Since the depletion width is now known, the absorption coefficient in the onset region can be calculated using the Gärtner equation (Equation 5.2) and is shown in the insert in Figure 7.11. Figure 7.11 compares the measured EQE with EQE plots calculated from the Gärtner equation using the depletion width calculated from the Mott-Schottky analysis (*cf.* 570 nm), and absorption coefficient derived from the SE measurements (Figure 5.5) and Gärtner plots (Figure 7.5). The estimation of α value using Gärtner plots did not carry on until the plateau because an assumption on $L_n << W$ was made and is only valid for low EQE.[13]

Mott-Schottky analysis for the single crystal device under illumination was not possible, with possibility due to a non-ideal back contact and / or non-ideal junction.

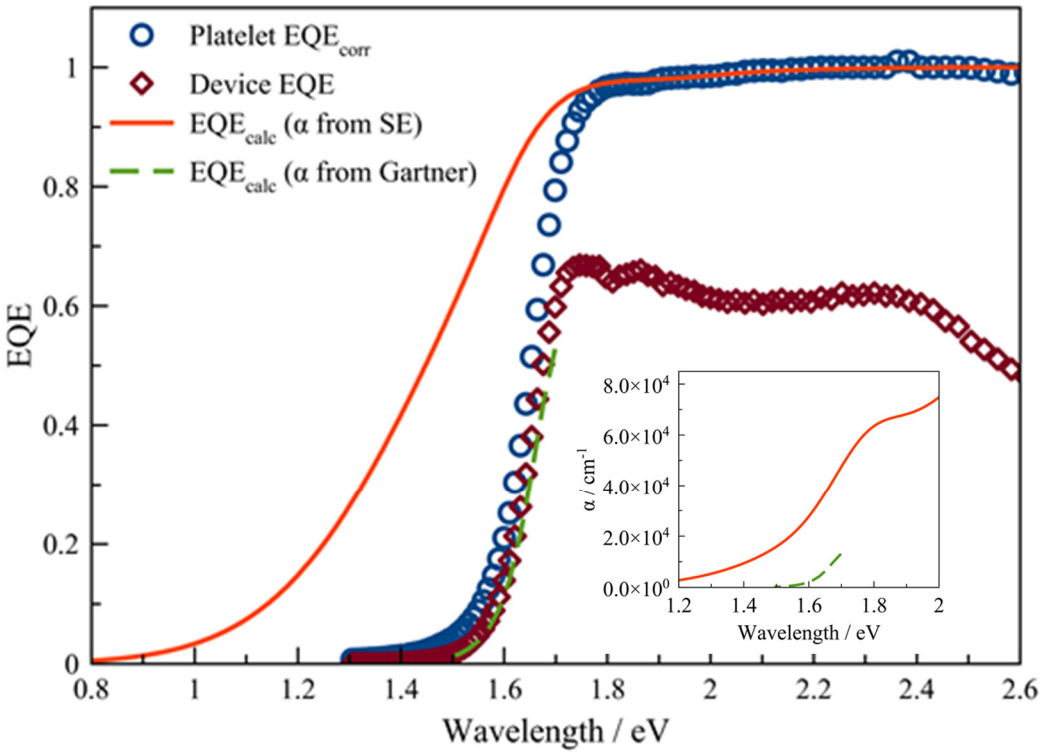

Figure 7.11 Comparison of experimental EQE with EQE calculated using the Gärtner equation using depletion width calculated in Mott-Schottky analysis. The α values were derived by spectroscopic ellipsometry and Gärtner plots as annotated and is shown in the insert.

7.2 Conclusion

This chapter has presented the fabrication of the first CZTS single crystal device. It obtained a V_{OC} in the same range with most other reported CZTS devices, however the cell suffered from very high series resistance due to the non-ideal back contact. The single crystal device behaved similarly to the platelet crystal in my published work: a steep EQE onset, and a bandgap of 1.64 eV. The results obtained from both Gärtner analysis and Mott-Schottky analysis further established the assumption made in my published work: a doping density in the order of 10^{15} cm^{-1}, and a wider depletion width than literature values. Both Gärtner analysis and Mott-Schottky analysis estimated a built-in potential of *ca.* 1 V for the single crystal CZTS cell.

Deviations from ideal Mott Schottky behaviour were attributed to Fermi level pinning caused by surface states at the junction.

Reference

1. Liu, X., Feng, Y., Cui, H., Liu, F., Hao, X., Conibeer, G., Mitzi, D.B., and Green, M., *The current status and future prospects of kesterite solar cells: a brief review.* Progress in Photovoltaics: Research and Applications, 2016. **24**(6): p. 879-898.
2. Ng, T.M., Weller, M.T., Kissling, G.P., Peter, L.M., Dale, P., Babbe, F., de Wild, J., Wenger, B., Snaith, H.J., and Lane, D., *Optoelectronic and spectroscopic characterization of vapour-transport grown Cu_2ZnSnS_4 single crystals.* Journal of Materials Chemistry A, 2017. **5**(3): p. 1192-1200.
3. Van Zeghbroeck, B. *Principles of semiconductor devices*. 2004.
4. Suresh, M.S., *Measurement of solar cell parameters using impedance spectroscopy.* Solar Energy Materials and Solar Cells, 1996. **43**(1): p. 21-28.
5. Fernandes, P.A., Salomé, P.M.P., Sartori, A.F., Malaquias, J., da Cunha, A.F., Schubert, B.-A., González, J.C., and Ribeiro, G.M., *Effects of sulphurization time on Cu_2ZnSnS_4 absorbers and thin films solar cells obtained from metallic precursors.* Solar Energy Materials and Solar Cells, 2013. **115**: p. 157-165.
6. Hwang, Y., Park, B.-I., Lee, B.-S., Kim, J.Y., Jeong, J.-H., Kim, H., Ko, M.J., Kim, B., Son, H.J., Lee, S.Y., Lee, J.-S., Park, J.-K., Cho, S.-H., and Lee, D.-K., *Influences of Extended Selenization on $Cu_2ZnSnSe_4$ Solar Cells Prepared from Quaternary Nanocrystal Ink.* The Journal of Physical Chemistry C, 2014. **118**(48): p. 27657-27663.
7. Raistrick, I.D., Franceschetti, D.R., and Macdonald, J.R., *Theory*, in *Impedance Spectroscopy*. 2005, John Wiley & Sons, Inc. p. 27-128.
8. Orazem, M.E., Shukla, P., and Membrino, M.A., *Extension of the measurement model approach for deconvolution of underlying distributions for impedance measurements.* Electrochimica Acta, 2002. **47**(13): p. 2027-2034.
9. Sze, S.M. and Ng, K.K., *p-n Junctions*, in *Physics of Semiconductor Devices*. 2006, John Wiley & Sons, Inc. p. 77-133.
10. Persson, C., *Electronic and optical properties of Cu_2ZnSnS_4 and $Cu_2ZnSnSe_4$.* Journal of Applied Physics, 2010. **107**(5).
11. Gloeckler, M., *Numerical Modeling of CIGS Solar Cells: Definition of the Baseline and Explanation of Superposition Failure*. 2003.
12. Ananthoju, B., Sonia, F.J., Kushwaha, A., Bahadur, D., Medhekar, N.V., and Aslam, M., *Improved structural and optical properties of Cu_2ZnSnS_4 thin films via optimized potential in single bath electrodeposition.* Electrochimica Acta, 2014. **137**(0): p. 154-163.
13. Gokmen, T., Gunawan, O., Todorov, T.K., and Mitzi, D.B., *Band tailing and efficiency limitation in kesterite solar cells.* Applied Physics Letters, 2013. **103**(10): p. 103506.

8 Synthesis and characterisation of other earth abundant photovoltaic materials

During the preliminary stage of the study, secondary phase compounds, specifically Cu_xS, SnS_x, and Cu_2SnS_3, were synthesised and used as the precursor in CZTS synthesis. A brief investigation on Bi_2S_3 was also carried out because it was found to be easier to synthesise and has a less complex structure, in terms of potential for disorder, than CZTS. Synthesis of Ag_2ZnSnS_4 was also attempted, with the aim of replacing copper with an alternative isoelectronic cation (but with an ionic radius significantly different to that of divalent zinc) in order to attempt to eliminate the problems that arise from Cu/Zn disorder in CZTS.

8.1 Cu_xS

Cu_xS can exist in a large number of phases, with x = 1 (CuS, covellite), x = 1.8 ($Cu_{1.8}S$, digenite), x = 1.94 ($Cu_{1.94}S$, djurleite) and x = 2 (Cu_2S, chalcocite).[1] However, a useful photovoltaic effect has only been observed for Cu_2S, which has a bandgap of about 1.2 eV.[2] Thin film Cu_2S device with a CdS buffer layer already achieved an efficiency of 9.15% in the early 80's,[3] however, it suffered from instability due to the formation of Cu vacancies.[4] The aim of this section is mainly to synthesise CuS phases to understand the synthetic conditions and used as the precursor in CZTS synthesis.

8.1.1 Characterisation of Cu_xS

Polycrystalline CuS ingots with a distinctive dark blue colour were obtained from solid state synthesis (Figure 8.1). All peaks in the PXRD pattern of the product can be assigned to a hexagonal CuS (PDF 78-0877) as shown in Figure 8.1. EDS analysis also shows a uniform composition of Cu/S = 1.04 ± 0.05 across different sites on the bulk material. Raman spectrum (Figure 8.3) also showed the CuS peak at 475 cm^{-1} with no other peaks observed.

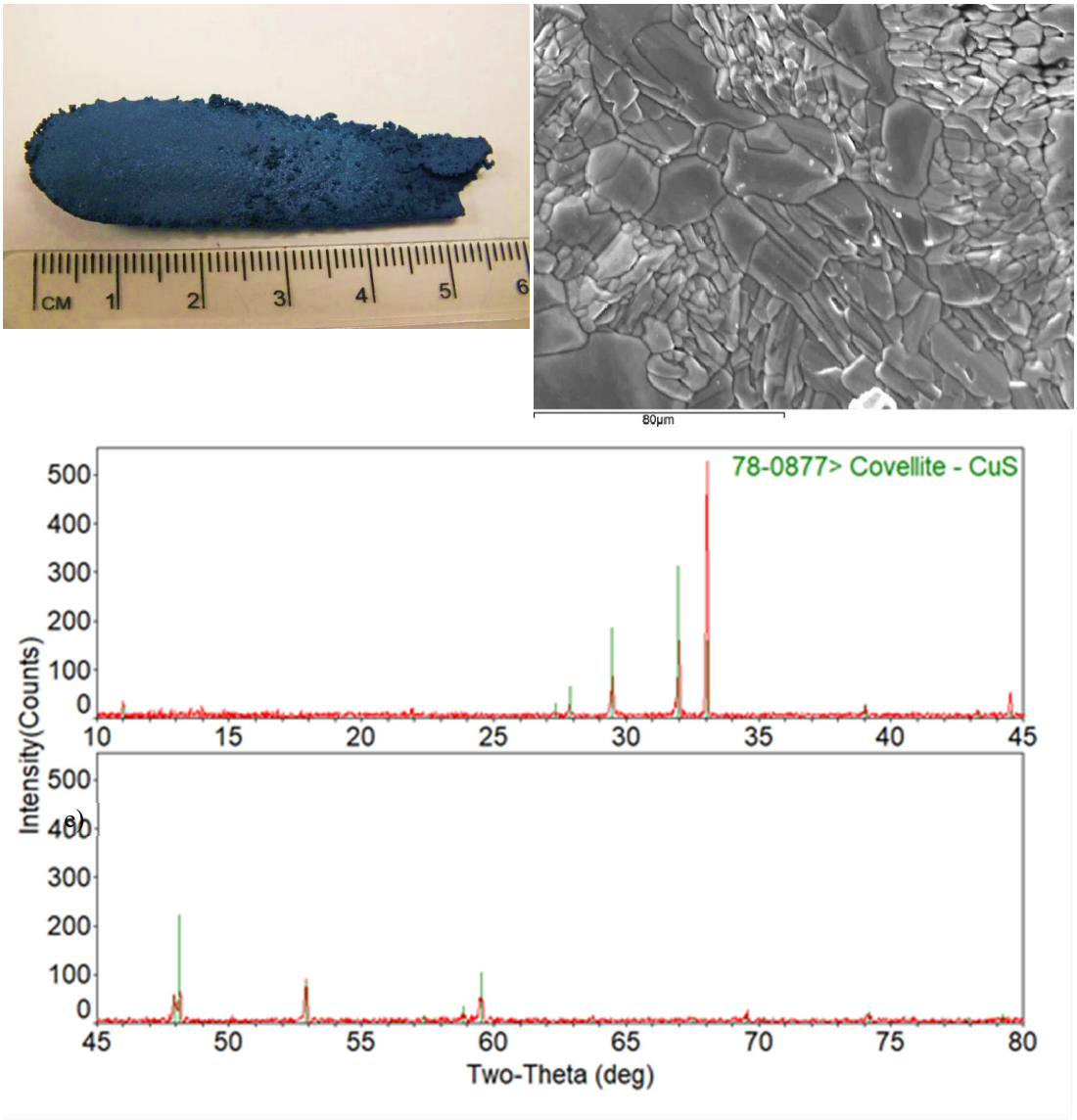

Figure 8.1 Photographic and SEM images, and PXRD pattern with reference PDF overlaid of CuS synthesised from solid state method.

Attempts to synthesise CuS using low temperature techniques were carried out with hydrothermal reactions, and a dark blue powder was obtained. All peaks in the PXRD pattern of the CuS synthesised at 180 ° can be assigned to a hexagonal CuS (PDF 78-0877) as shown in Figure 8.2. EDS analysis shows a composition of Cu/S = 1.02 ± 0.02. Lowering the reaction temperature to 175 °C resulted in extra peaks in the PXRD pattern at 2θ = 32.5, 46.5 and 55.1, which can be assigned to cubic $Cu_{1.95}S$ (PDF 89-2072)(Figure 8.2).

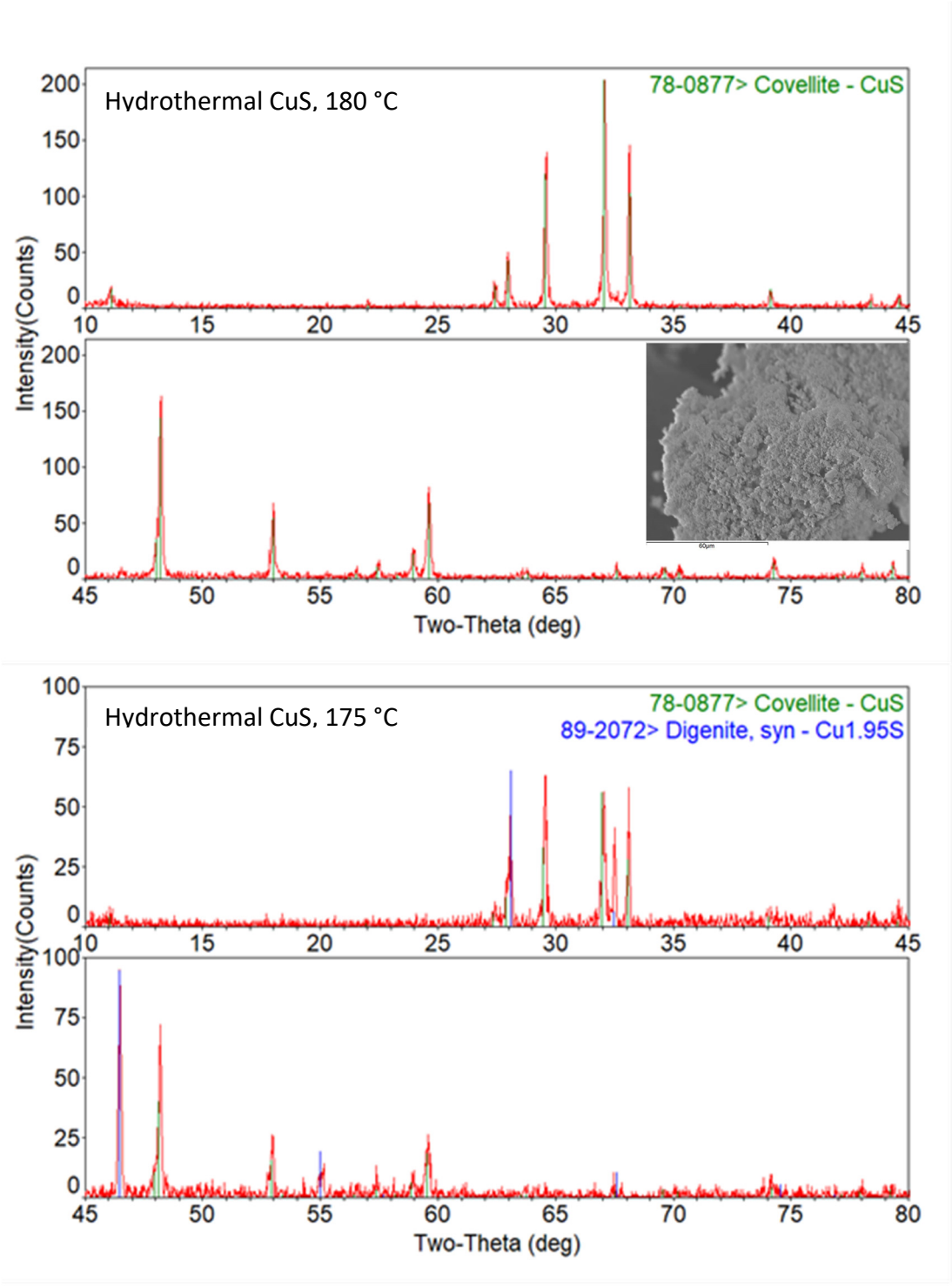

Figure 8.2 PXRD pattern with reference PDF overlaid of CuS synthesised from hydrothermal reactions at (Top) 180 °C for 3 days, and (Bottom) 175 °C for 3 days. (Inset) SEM image.

Raman analyses, using 532 and 785 nm excitation, for homemade CuS and commercial Cu_2S (Alfa Aesar) are shown in Figure 8.3. CuS obtained from both solid state and hydrothermal reactions have the signature peak at 475 cm^{-1}. It is expected that peak intensity of the hydrothermal CuS is much weaker because of the poorer

crystallinity, as seen in the SEM images (Figure 8.1and Figure 8.2).[5] No Raman peaks can be observed in commercial Cu_2S, which could be due to strong reflectivity or absorption in the visible range. This suggests that if Cu_2S is present in CZTS, as might be expected from Equation 1.13:

$$Cu_2ZnSnS(e)_{4(s)} \rightleftharpoons Cu_2S(e)_{(s)} + ZnS(e)_{(s)} + SnS(e)_{(s)} + 0.5S(e)_{2(g)}$$

$$SnS(e)_{(s)} \rightleftharpoons SnS(e)_{(g)}$$

it will not be possible to identify its presence using Raman spectroscopy using 532 and 785 nm excitation wavelengths.

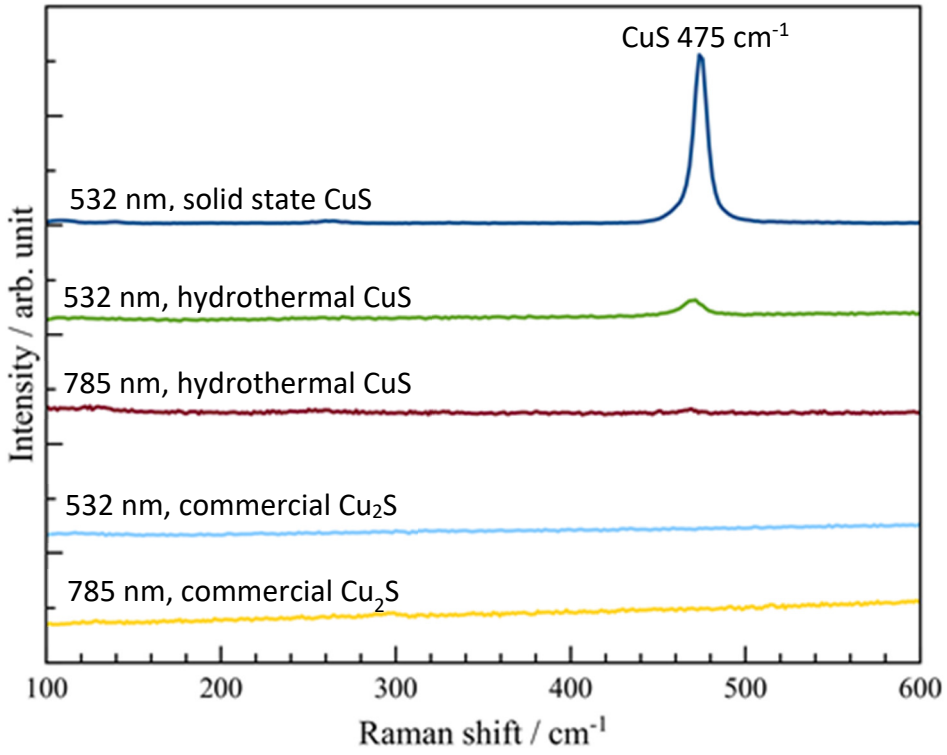

Figure 8.3 Raman spectra of CuS synthesised from solid state reaction and hydrothermal reaction, and Cu_2S bought commercially.

8.2 Sn_xS_y

There are also a number of Sn_xS_y compounds, but only three of them are discrete phases: SnS, SnS_2, and Sn_2S_3. The bandgap of these phases are 1.3,[6] 2.12 – 2.44,[7] and 2.0[8] respectively, which makes SnS a potential absorber material and SnS_2 a potential buffer layer material. The current record efficiency for SnS solar cell is

4.36% achieved in 2014,[9] and more work is needed to improve the efficiency. Again, the aim of this section is mainly to synthesise SnS_x phases to understand the synthetic conditions and used as the precursor in CZTS synthesis.

8.2.1 Characterisation of SnS_x

The Raman spectra of SnS synthesised from solid state and hydrothermal reaction is shown in Figure 8.4. All spectra show the presence of a SnS_2 band at 314 cm^{-1} with similar intensity to SnS bands at 219, 190 and 160 cm^{-1}. A co-existence of both SnS and SnS_2 phases is also observed in both SnS and SnS_2 films in the Raman spectra in the work of Barone *et al.*[10] A visual inspection of the PXRD pattern (Figure 8.5) also confirm the presence of both SnS (PDF 75-1803) and SnS_2 (PDF 75-0367).

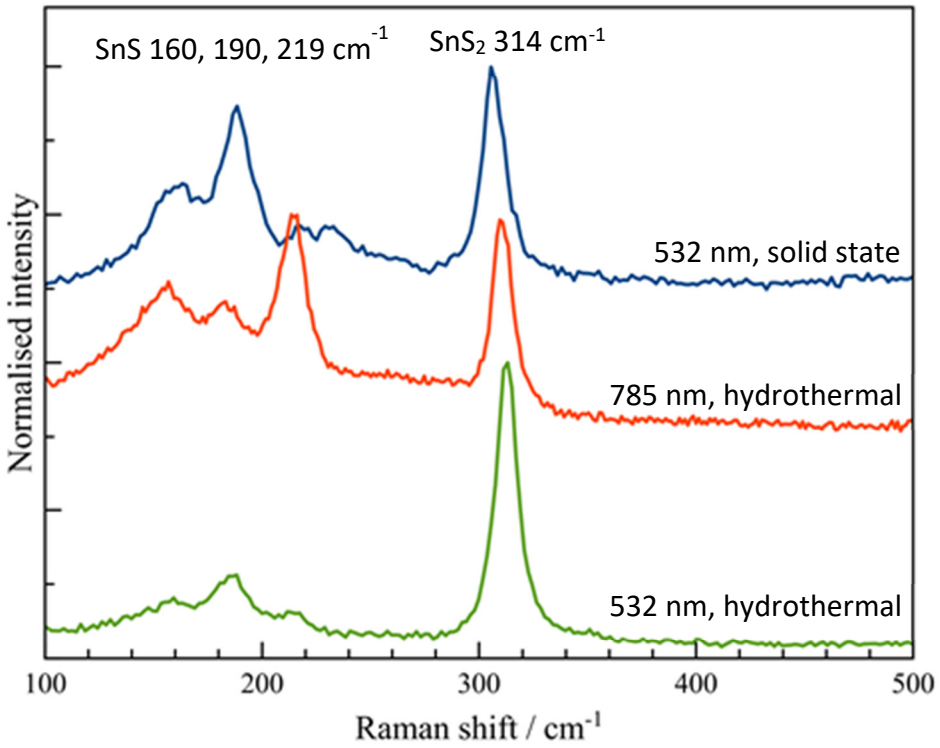

Figure 8.4 Raman spectra of SnS synthesised from solid state and hydrothermal reaction

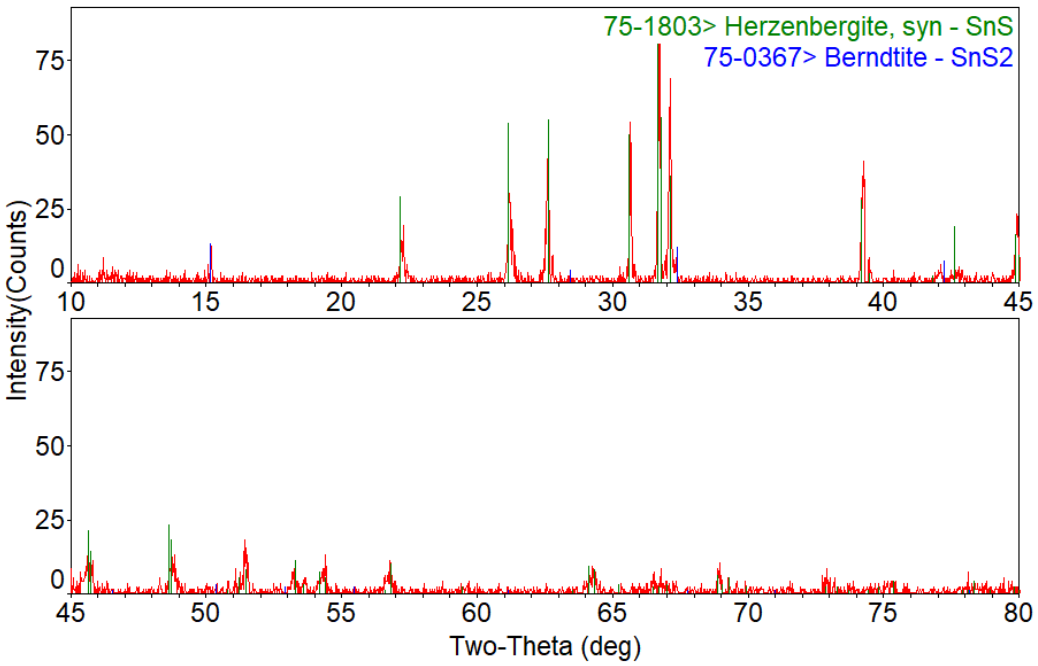

Figure 8.5 PXRD pattern with reference PDF overlaid of SnS synthesised from hydrothermal reaction.

Solid state synthesis of SnS_2 yield a bulk material with a distinctive orange colour (Figure 8.6 inset). A visual inspection of the PXRD pattern (Figure 8.6) shows the majority of peaks can be assigned to SnS_2 (PDF 23-0677). However, three peaks at 2θ = 28.8, 47.8 and 56.6 cannot be assigned to any other Sn_xS_y phases.

The hydrothermal synthesis of SnS_2 yielded a grey powder very similar to the one obtained from the hydrothermal synthesis of SnS. The PXRD pattern of hydrothermal SnS_2 (Figure 8.7) is also very similar to hydrothermal SnS (Figure 8.5), with presence of SnS (PDF 75-1803) and trace of SnS_2 (PDF 75-0367).

Attempts to synthesise phase pure SnS and SnS_2 via hydrothermal and solid state route were not carried out further because the main focus of this thesis is to synthesis and characterise CZTS material.

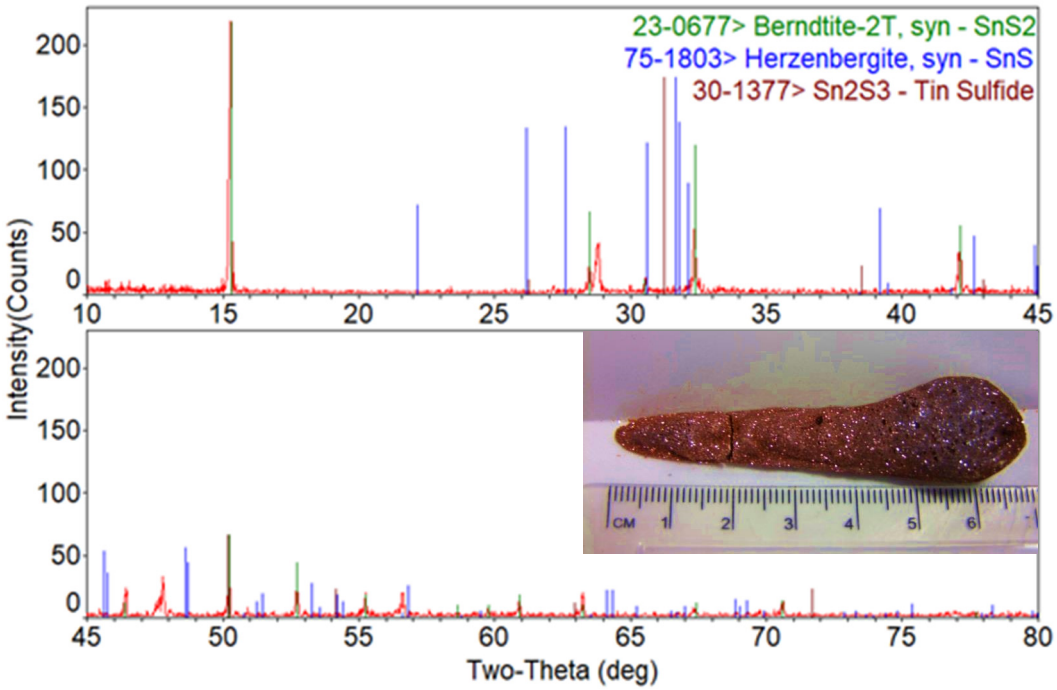

Figure 8.6 PXRD pattern with reference PDF overlaid of SnS_2 synthesised from solid state reaction. Inset: photographic image of as-synthesised SnS_2 ingot.

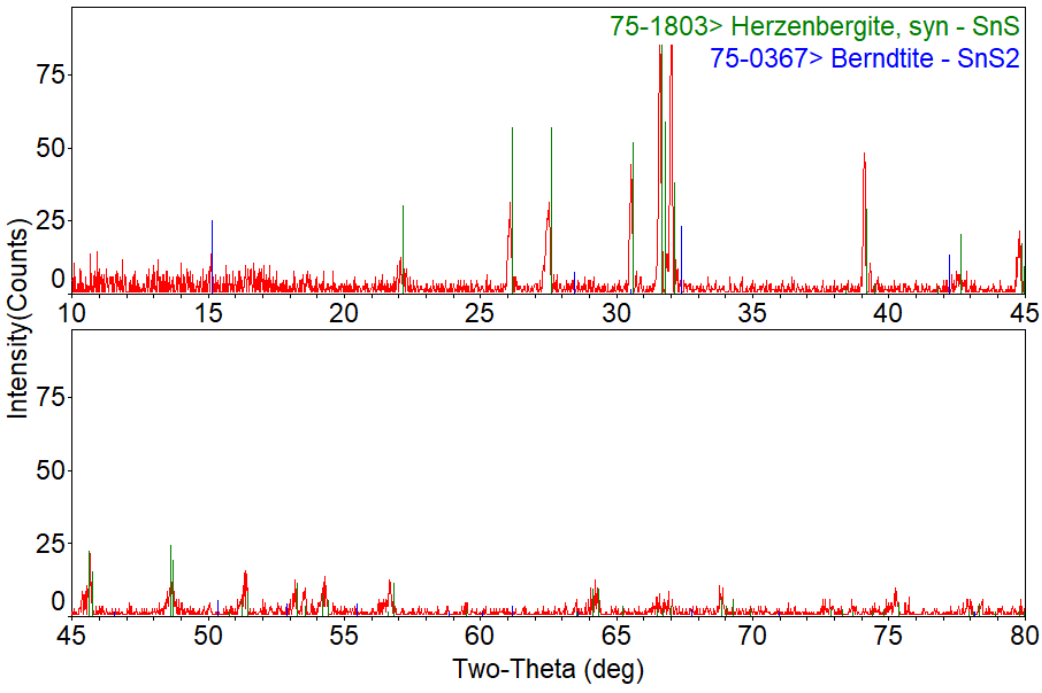

Figure 8.7 PXRD pattern with reference PDF overlaid of SnS_2 synthesised from hydrothermal reaction.

8.3 Cu_2SnS_3 (CTS)

Cu_2SnS_3 is another chalcogenide that exhibit photovoltaic behaviour and has a bandgap of 1.35, 0.96 and 0.93 eV for tetragonal, cubic and monoclinic Cu_2SnS_3 respectively.[11, 12] The current record Cu_2SnS_3 cell achieved an efficiency of 4.63% in 2015 and has a monoclinic structure.[13]

8.3.1 Characterisation of Cu_2SnS_3

The solid state synthesis of Cu_2SnS_3 with stoichiometric amount of precursor yields a non-uniform bulk material, which can be easily distinguished visibly by the blue colour of CuS (Figure 8.8). The presence of CuS is also confirmed by EDS and Raman analysis (Figure 8.9). Excess sulphur and a lower reaction temperature (900 °C instead of 1050 °C) were used in an attempt to prevent the decomposition of Cu_2SnS_3. However, decomposition still occurred.

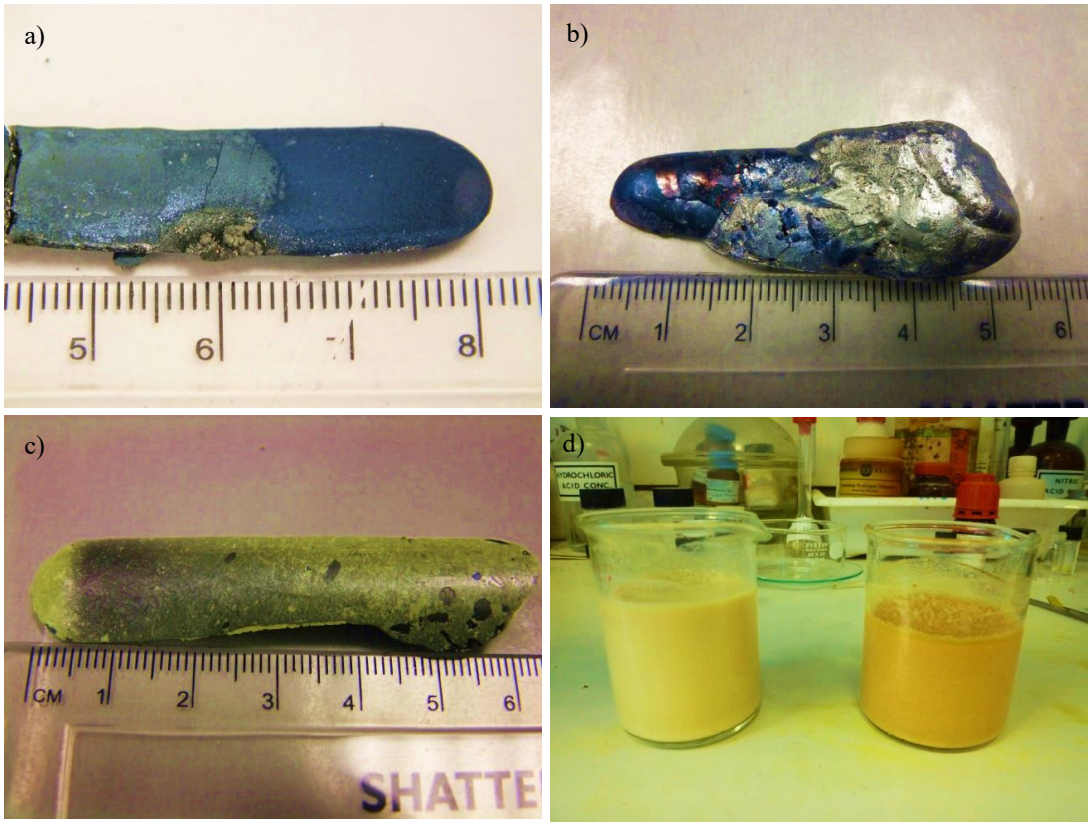

Figure 8.8 Images of Cu_2SnS_3 synthesised by solid state reaction at the following condition: (a) 1050 °C with no excess sulphur; (b) 1050 °C with 50% excess sulphur, (c) 900 °C with 20% excess sulphur. (d) Cu_2SnS_3 hydrothermal precursor solution (left) with aging and (right) without aging.

In order to isolate the desired Cu_2SnS_3, the bulk materials were ball milled, followed by etching in 10% KCN solution. The removal of CuS using KCN etching is a very commonly used process in the CIGS community.[14-16] The elemental composition of the post-etched materials have a Cu/Sn ratio of 1.94 – 2.01 and S/metal ratio of 0.98 – 1.02 for three different batches. Raman spectra (Figure 8.9) also show only bands due to monoclinic CTS at 290, and 351 cm^{-1}[17] (*cf.* 303 and 356 cm^{-1} for cubic CTS).[18] However, PXRD pattern (Figure 8.10) matches that of a cubic CTS (PDF 89-2877), and did not show any monoclinic CTS peaks (PDF 27-0198). Oliva *et al.*[19] concluded that "it is quite difficult to differentiate monoclinic CTS from cubic CTS with standard characterisation techniques." UV/Vis spectra (Figure 8.11) from all three batches of KCN-etched materials show strong absorption between 600 and 1310 nm.

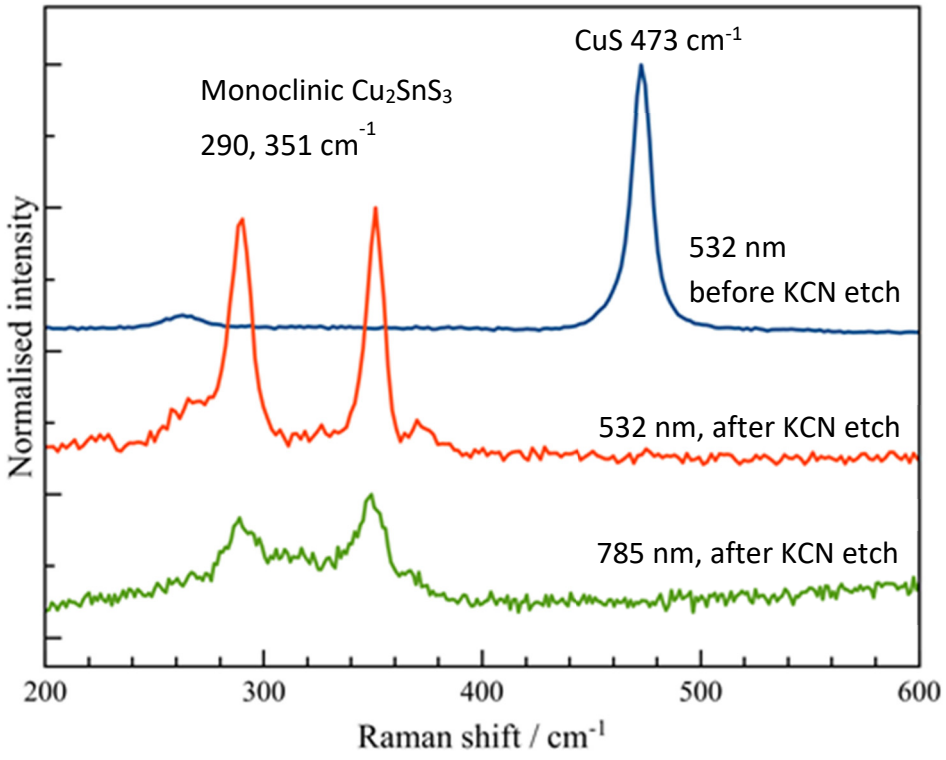

Figure 8.9 Raman spectra of Cu_2SnS_3 synthesised from solid state reaction pre- and post- KCN etch.

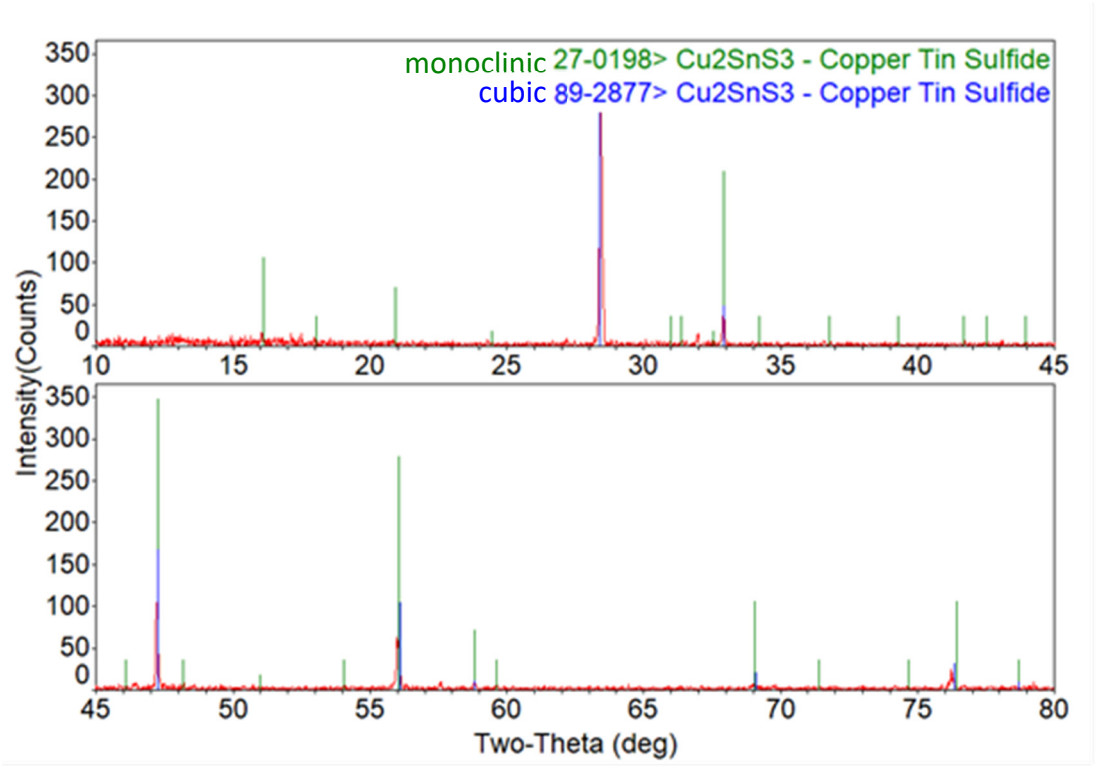

Figure 8.10 PXRD pattern with reference PDF overlaid of Cu_2SnS_3 synthesised from solid state reaction after KCN etch.

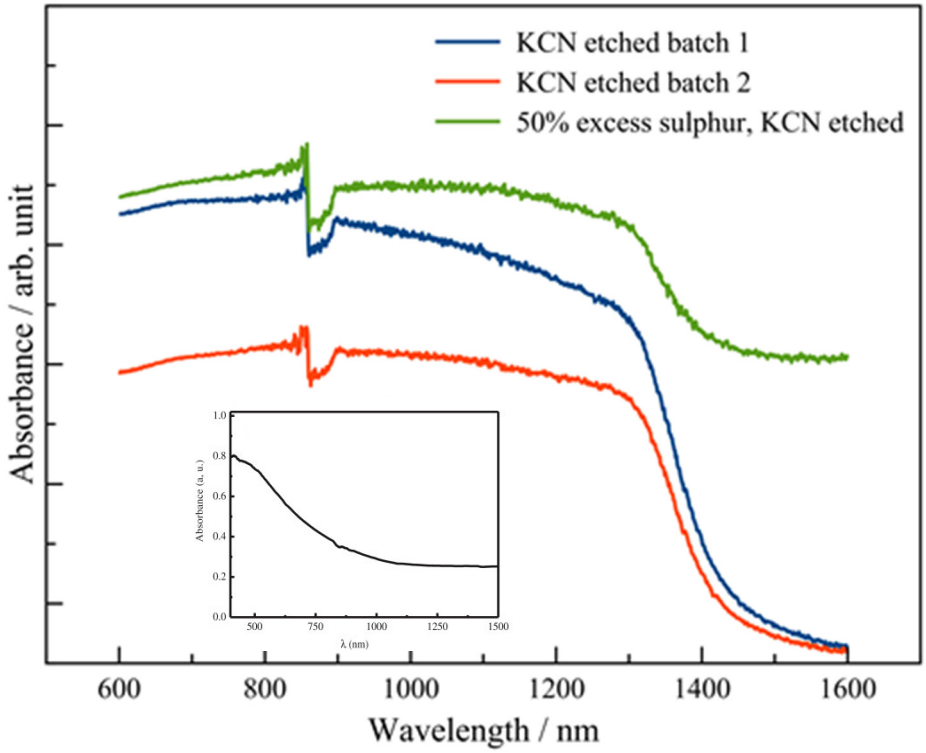

Figure 8.11 UV/Vis spectra of Cu_2SnS_3 synthesised from solid state reaction after KCN etch. The spike around 860 nm is due to instrument artefact. Insert: UV/Vis spectra of Cu_2SnS_3 adapted from Dahman *et al.*[20]

Low temperature syntheses of Cu_2SnS_3 were attempted using dry powder, solution and hydrothermal reactions. The dry powder reaction was comparable to the one described by Tiwari *et al.*[21]. The reaction was very vigorous and resulted in a fine black powder. The quality of PXRD pattern (Figure 8.12) is very poor, and is probably due to poor crystallinity of the product. Hence the powder was further annealed in a sealed ampoule at 750 °C for 1 day in attempt to improve the crystallinity of the product. However, an explosion occurred during the recovery of the product by breaking the ampoule after it was cooled. It was not known what caused the explosion since the ampoule did not explode during annealing. The sample was lost and could not be characterised.

The same precursors as the dry powder reaction were dissolved and refluxed in 2MOE in another attempt to synthesise Cu_2SnS_3. A black precipitate was obtained. The powder was then annealed at 280 °C under ambient atmosphere and a green powder was formed. No characterisation was performed on the green powder.

In the hydrothermal synthesis of Cu_2SnS_3, the Cu and Sn precursors were dissolved in water and aged overnight before the addition of thiourea to the reaction mixture in one of the experiments. The idea was borrowed from Xin *et al.*[22] as they suggested the redox reaction of Cu^{2+} and Sn^{2+} to Cu^{+} and Sn^{4+} will compete with the complexation reactions between the metal cations with thiourea if all precursors were added simultaneously, resulting an unstable solution. Figure 8.8d shows the precursor solution had a paler colour if the metal precursors were aged. PXRD pattern (Figure 8.12) showed peaks with stronger intensity for the batch with aged metal precursor, indicating larger particle size and better crystallinity.

All attempts to grow larger Cu_2SnS_3 crystals using chemical vapour transport methods were unsuccessful despite using a higher iodine load as in the CZTS synthesis. Further attempts were not carried out.

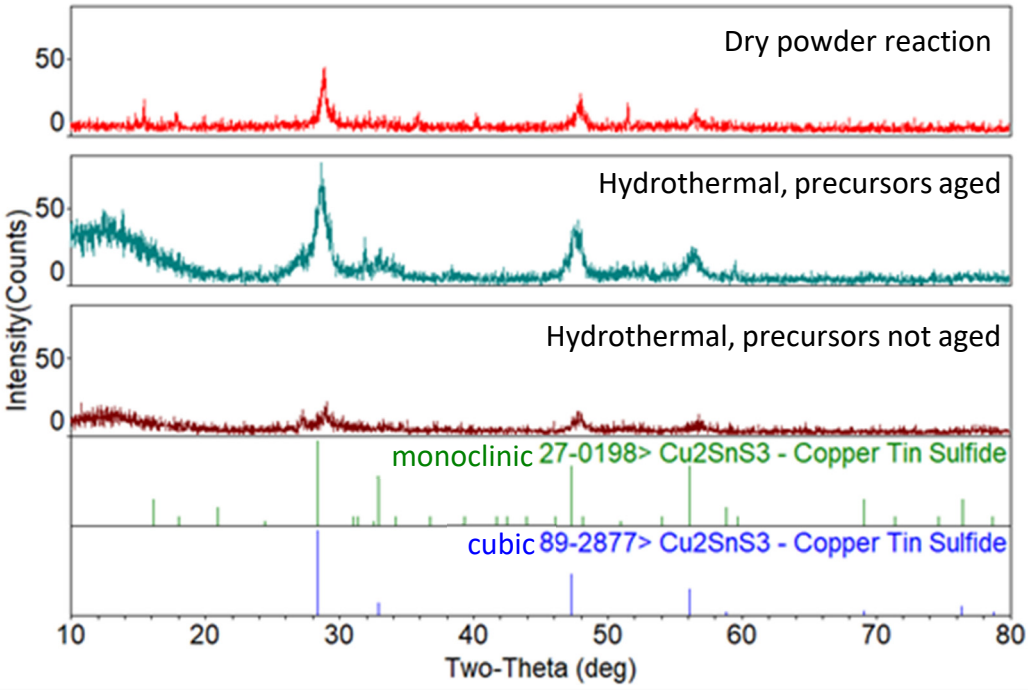

Figure 8.12 PXRD patterns with reference pattern of Cu_2SnS_3 synthesised from: (red) dry powder reaction; (turquoise) hydrothermal reaction with aged metal salt solution; (brown) hydrothermal reaction without precursor solution aging.

8.4 Bi_2S_3

The bandgap of Bi_2S_3 is reported in the range of 1.2 to 1.7 eV,[23-28] which is within the optimal range for a photovoltaic material. Despite the optical and electrical properties of Bi_2S_3 films were well studied,[23-30] no Bi_2S_3 devices have been reported yet.

8.4.1 Characterisation of Bi_2S_3

Bi_2S_3 was chosen to investigate the potential of being a sustainable photovoltaic material, because it is easier to synthesise and has a less complex structure than CZTS. In the preliminary experiment, Bi_2S_3 was synthesised via the hydrothermal route using $Bi_2(NO_3)_3{\cdot}5H_2O$ and 25% excess of thiourea. A grey powder was obtained. A visual inspection of the PXRD pattern (Figure 8.13) matches the reference pattern of Bi_2S_3 (PDF 17-0320). UV-Vis spectra (Figure 8.14) shows strong absorption between 830 and 600 nm, which is comparable to CZTS.

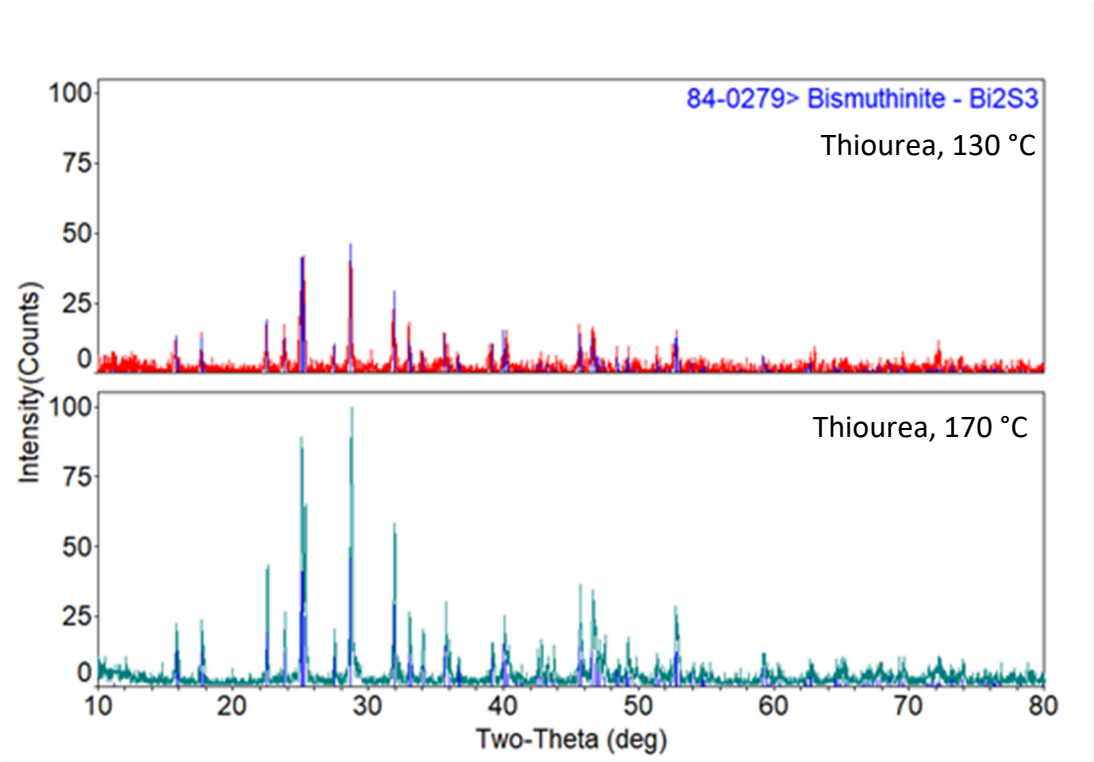

Figure 8.13 PXRD pattern with reference PDF overlaid of Bi_2S_3 synthesised from hydrothermal reactions using thiourea at (Top) 130 °C and (Bottom) 170 °C.

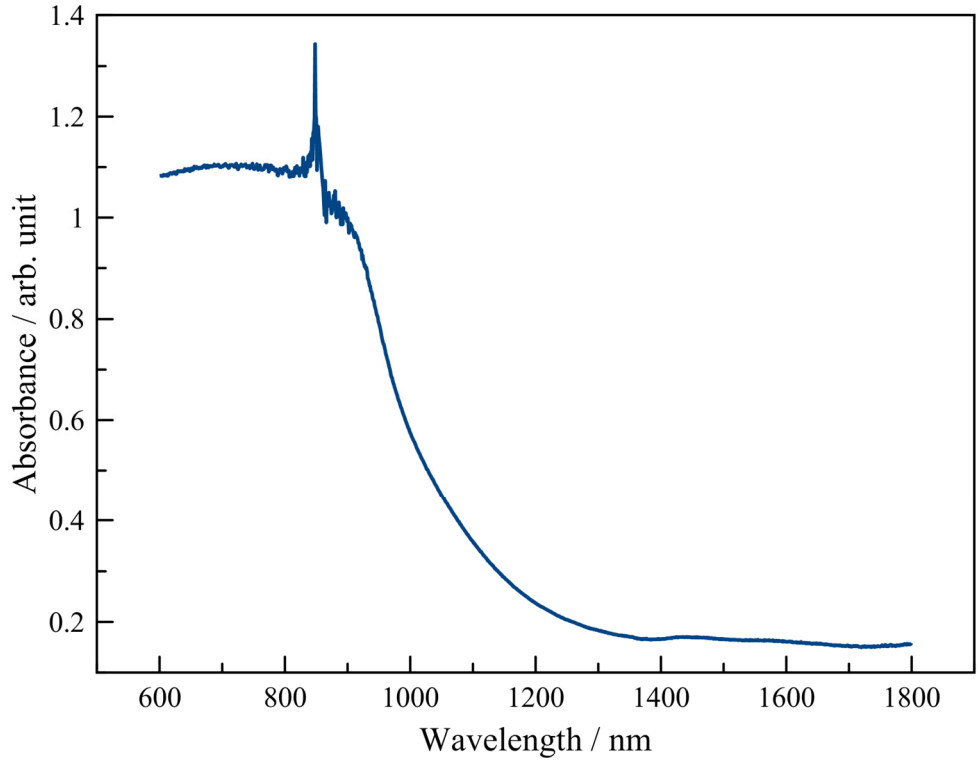

Figure 8.14 UV/Vis spectra of Bi_2S_3 synthesised from hydrothermal reaction. The spike around 860 nm is due to instrument artefact.

Since the precursor solution containing $Bi_2(NO_3)_3 \cdot 5H_2O$ and thiourea is insoluble in water, and solvents that are known to dissolve $Bi_2(NO_3)_3 \cdot 5H_2O$ are volatile. The reaction temperature was lowered from 170 °C to 130 °C. The PXRD pattern (Figure 8.13) is similar to the higher temperature product, with full width half maximum (FWHM) values at 2-Theta angle 28.7° being 0.139(10) and 0.188(14) for 170 °C and 130 °C respectively. Further synthesis were carried out at 130 °C.

Ethanol, propan-2-ol, acetone and dilute nitric acid were used as the solvent in an investigation to obtain a soluble precursor solution. However, none of the solvents can dissolve the precursor mixture and hydrothermal reactions were carried out in a suspension. A translucent yellow solution with no precipitate was obtained with dilute nitric acid so no further characterisation was carried out. For reactions using ethanol, propan-2-ol and acetone, a brown powder was obtained. PXRD patterns (Figure 8.15) of all three batches have very broad peaks and very weak intensities compared with reactions using water (Figure 8.13). It can be concluded that water gives the best result.

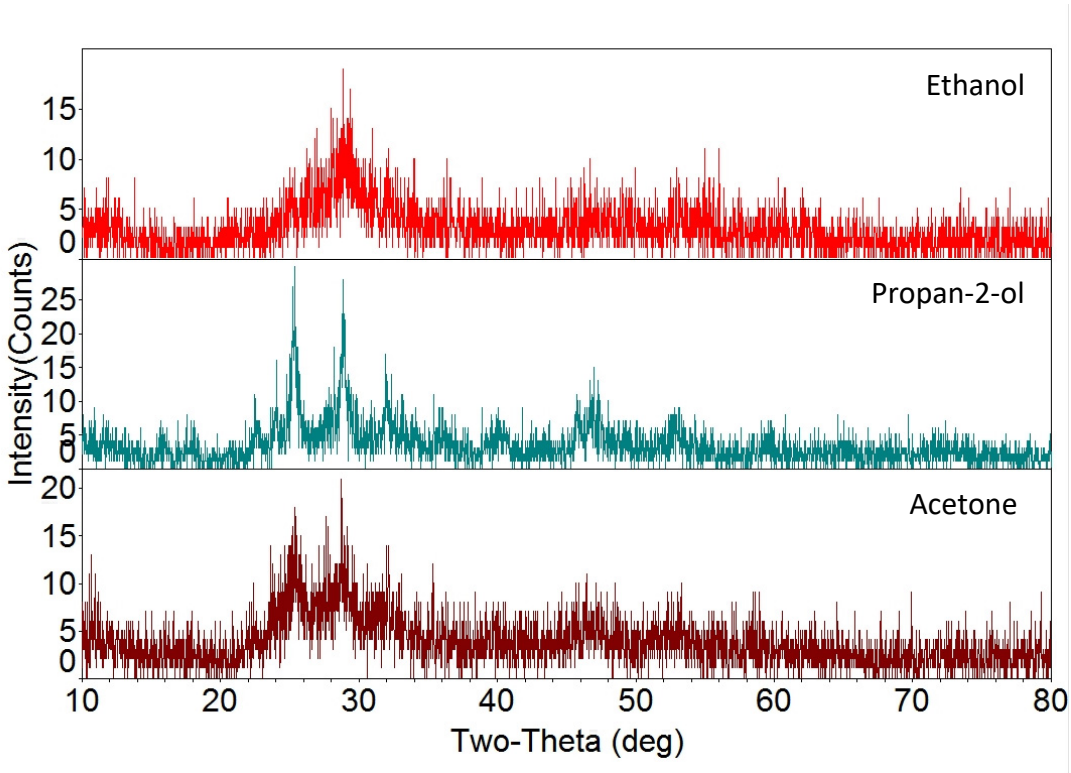

Figure 8.15 PXRD patterns of Bi_2S_3 synthesised from hydrothermal reaction using different solvents: (red) ethanol; (turquoise) propan-2-ol; (brown) acetone

Hydrothermal synthesis of Bi_2S_3 was further studied by changing the sulphur precursor. Thioacetamide, thioglycolic acid and sodium sulphide nonahydrate were used during the study, and different compounds were obtained. A grey powder, which has the same appearance to the one synthesised with thiourea, was obtained with $Na_2S{\cdot}9H_2O$. The PXRD pattern of Bi_2S_3 synthesised with $Na_2S{\cdot}9H_2O$ (Figure 8.16) is also similar to the one synthesised with thiourea (Figure 8.13). A visual inspection of the PXRD pattern matches the reference pattern of Bi_2S_3 (PDF 65-2435). A pale yellow powder was obtained with thioacetamide, and the PXRD pattern (Figure 8.17) matches that of $Bi_2O(OH)_2SO_4$ (PDF 45-1439). Grey grains were obtained with thioglycolic acid, and both Bi_2S_3 (PDF 75-1306) and $Bi_2O(OH)_2SO_4$ (PDF 76-1102) phases were found with visual inspection of the PXRD pattern (Figure 8.18). This concludes thiourea and $Na_2S{\cdot}9H_2O$ can be used as a sulphur precursor in the hydrothermal synthesis of Bi_2S_3.

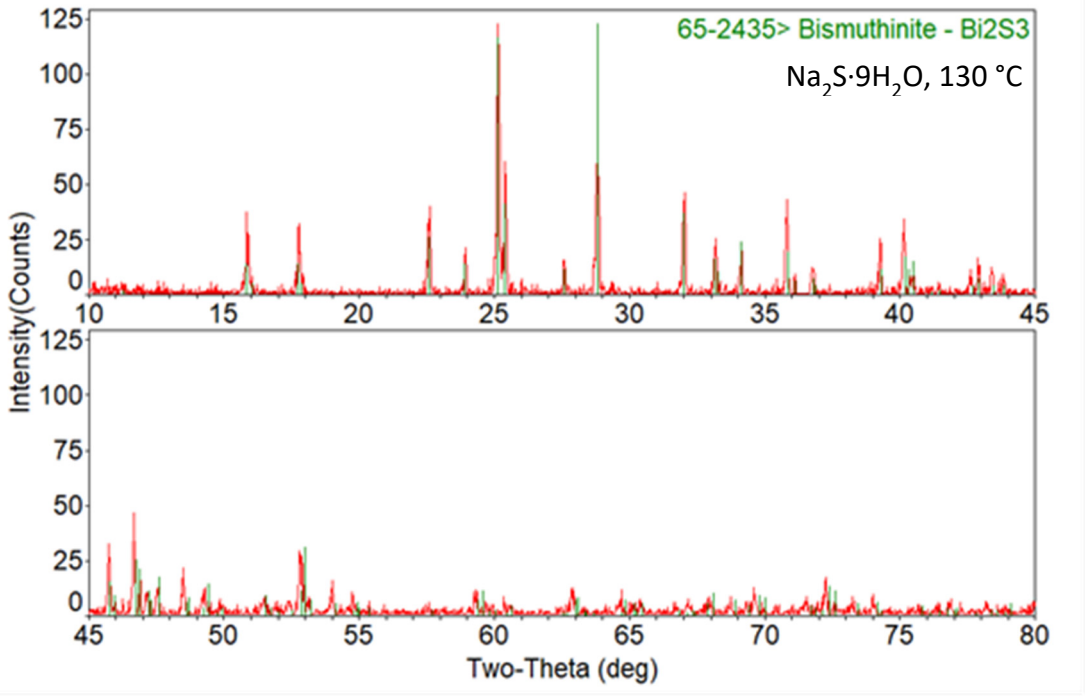

Figure 8.16 PXRD patterns with reference PDF overlaid of Bi_2S_3 synthesised from hydrothermal reaction using $Na_2S{\cdot}9H_2O$

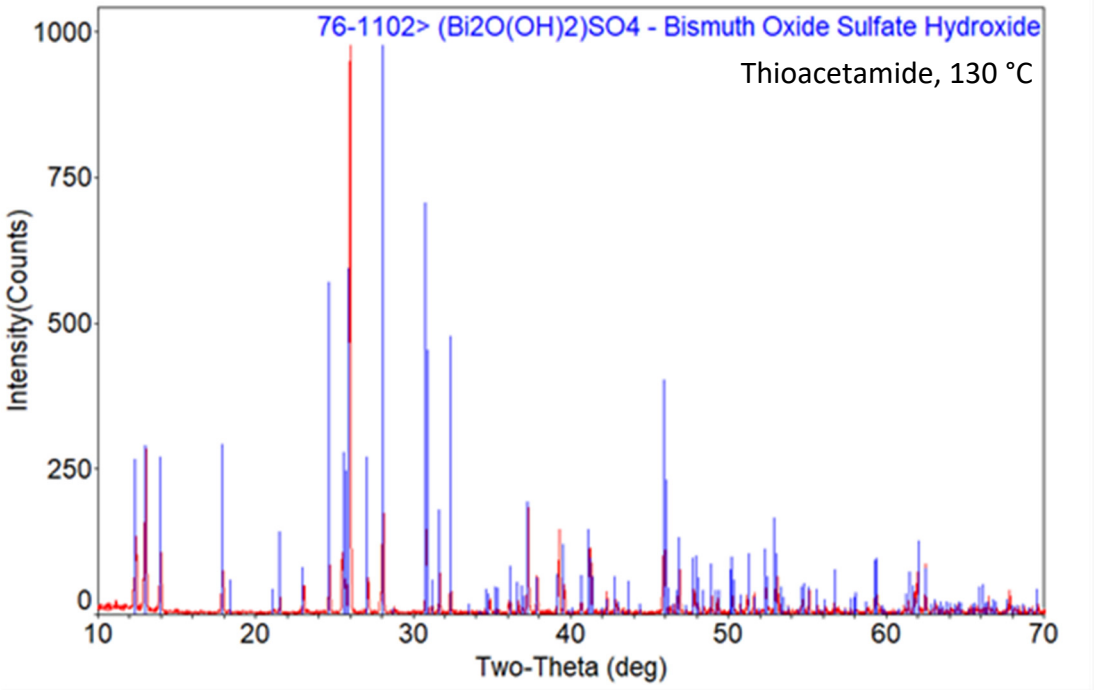

Figure 8.17 PXRD patterns with reference PDF overlaid of $Bi_2O(OH)_2SO_4$ synthesised from hydrothermal reaction using thioacetamide.

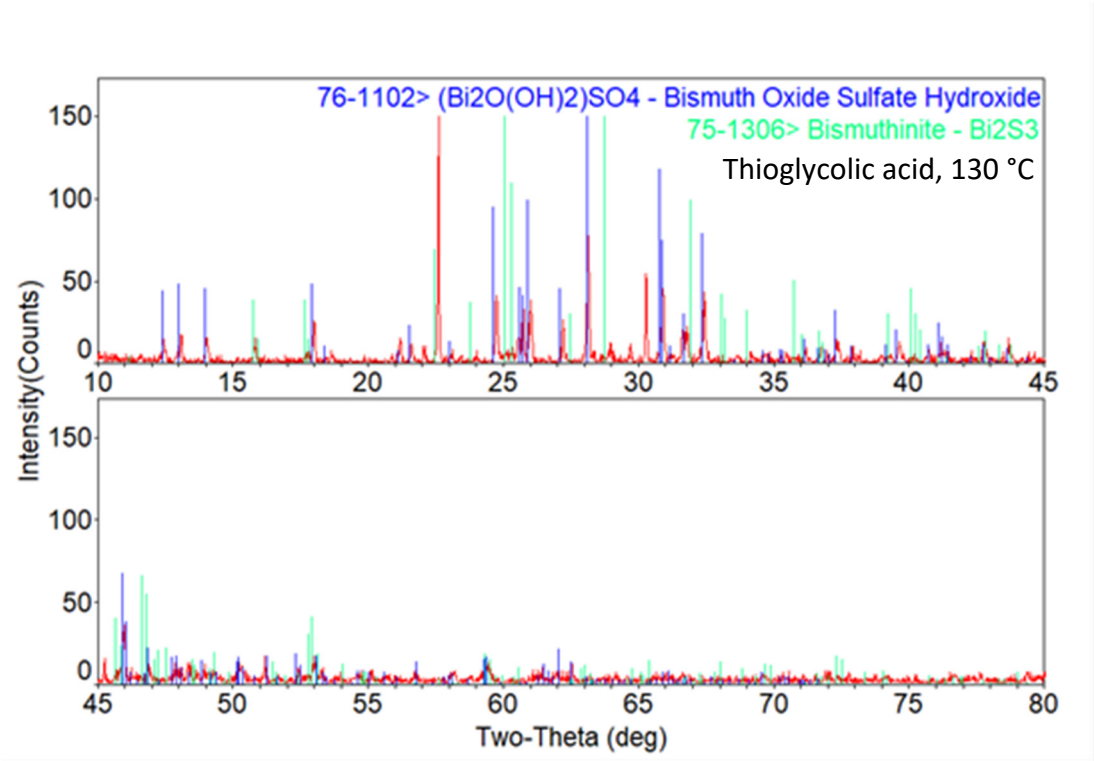

Figure 8.18 PXRD patterns with reference PDF overlaid of product synthesised from hydrothermal reaction using bismuth nitrate and thioglycolic acid.

Raman spectra (Figure 8.19) of Bi_2S_3 have stronger intensities when a 785nm laser was used instead of 532nm. This suggested Bi_2S_3 has a resonance frequency at high wavelength and/or strong absorption at low wavelength. Three bands were observed at 180, 232 and 256 cm^{-1}, which agrees with both theoretical[31] and experimental[32] values reported.

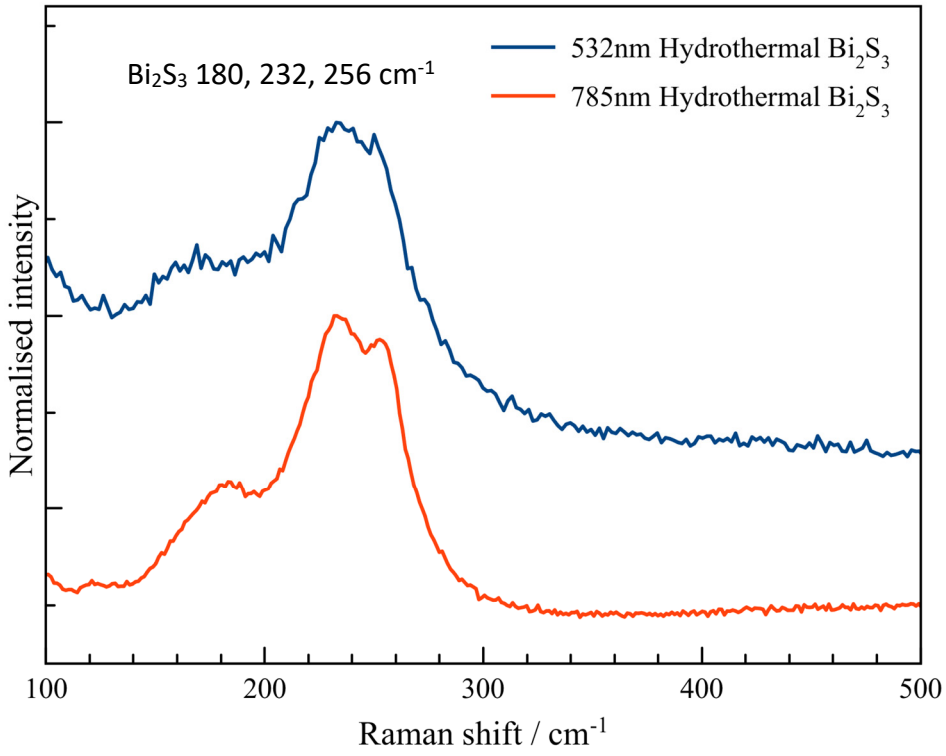

Figure 8.19 Raman spectra of Bi_2S_3 synthesised from hydrothermal reaction.

TGA and DSC (Figure 8.20) was carried out under ambient atmosphere using a heating rate of 5 °C/min. There is a sudden exothermic change observed just after 400 °C followed by a 3 – 5% weight gain. A white powder was obtained after the characterisation. The TGA and DSC conclude Bi_2S_3 is stable under ambient atmosphere up to 400 °C.

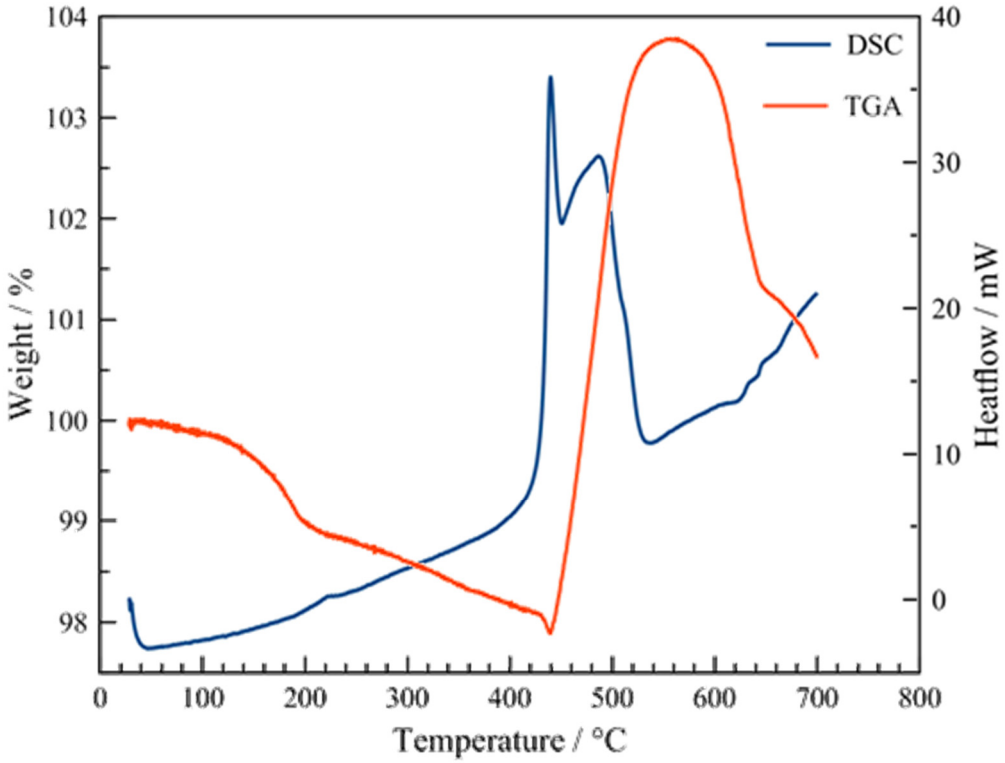

Figure 8.20 TGA plot (primary axis) and DSC plot (secondary axis) for Bi_2S_3 from hydrothermal reaction. Heating rate: 5 °C/min, ambient atmosphere

8.5 Ag_2ZnSnS_4 (AZTS)

AZTS was studied with the aim of replacing copper with an alternative isoelectronic cation (but with an ionic radius significantly different to that of divalent zinc) in order to attempt to eliminate the problems that arise from Cu/Zn disorder in CZTS. The reported bandgap for AZTS is 2.0 eV.[33-35] The current record efficiencies for AZTS, $Ag_2ZnSnSe_4$ (AZTSe) and $(Cu_{1-x}Ag_x)_2ZnSn(S,Se)_4$ (CAZTSSe) devices are 1.38%,[36] 5.2%[37] and 10.36%[38] respectively.

8.5.1 Synthesis of Ag_2ZnSnS_4

The initial solid state reaction carried out at 750 °C yielded an ingot, suggesting the melting point of AZTS is much lower than CZTS (*cf.* 990 °C).[39] The solid state reaction carried out at 600 °C yielded a shiny, dark orange powder.

The initial chemical vapour transport reaction carried out at the gradient of 650 – 580 °C did not see any crystal growth. A grey / silver ingot was obtained in the reaction carried out at the gradient of 750 – 650 °C.

8.5.2 Characterisation of Ag_2ZnSnS_4

PXRD was carried out on AZTS synthesised with solid state and chemical vapour transport reactions. PXRD patterns (Figure 8.21) for both samples show matching peaks from AZTS (PDF 35-0544) and by-products SnS_2 (PDF 23-0677) and $Ag_4Sn_3S_8$ (PDF 38-0245) from visual inspection. There were no sign of other silver tin sulphide phases such as Ag_2SnS_3 (PDF 39-0140) nor Ag_8SnS_6 (PDF 38-0245). Silver iodide (PDF 09-0399) was also observed in the sample synthesised from chemical vapour transport reaction. The result suggests it is not straightforward to synthesise phase pure AZTS due to the possibility of a complex phase diagram of the material similar to the one of CZTS(e) compounds.

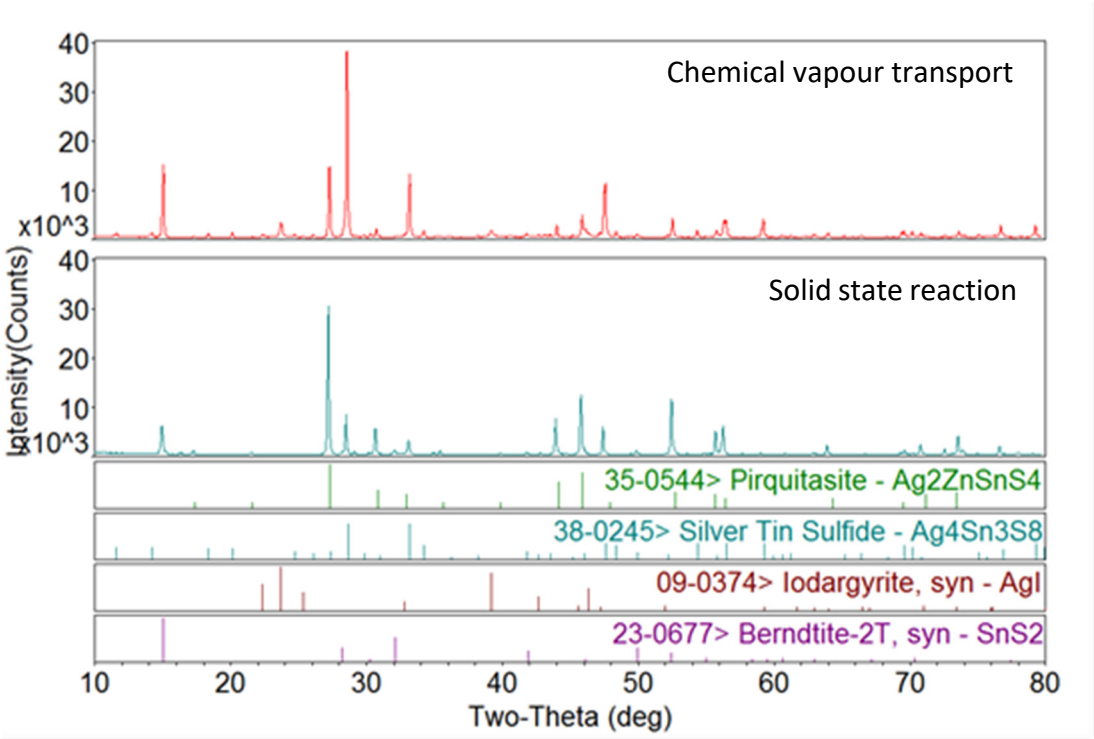

Figure 8.21 PXRD patterns with reference spectra of Ag_2ZnSnS_4 synthesised from solid state reaction and chemical vapour transport reaction.

Raman analysis were also carried out for both AZTS samples (Figure 8.22). The Raman analysis carried out using 532 nm excitation produced spectra with backgrounds that were not straight forward to process, in contrast, Raman analysis using 785 nm excitation produced spectra with a good signal to noise ratio and a number of weaker peaks were observed. The peak at 310 cm^{-1} can be attributed to either SnS_2 and/or $Ag_4Sn_3S_8$.[18, 40] Note that both SnS_2 and $Ag_4Sn_3S_8$ only have one signature peak at 310 cm^{-1} so that it was not possible to distinguish between these two compounds using Raman analysis alone. In this work, both SnS_2 and $Ag_4Sn_3S_8$ were also observed in the PXRD patterns. The peaks observed for AZTS are (in descending order of intensity) 341, 266, 365, 211, 125 and 80 cm^{-1}. Assuming the two most intense peaks (341 and 266 cm^{-1}) correspond to the A mode and compare with the peak position of those in CZTS, there is a small red shift for the peak at 341 cm^{-1} (*cf.* 338 cm^{-1} in CZTS), and a large blue shift for the peak at 266 cm^{-1} (*cf.* 287 cm^{-1} in CZTS). It can also be assumed large blue shift for the peaks at 211 and 125 cm^{-1} (*cf.* 236 and 151 cm^{-1} in CZTS).

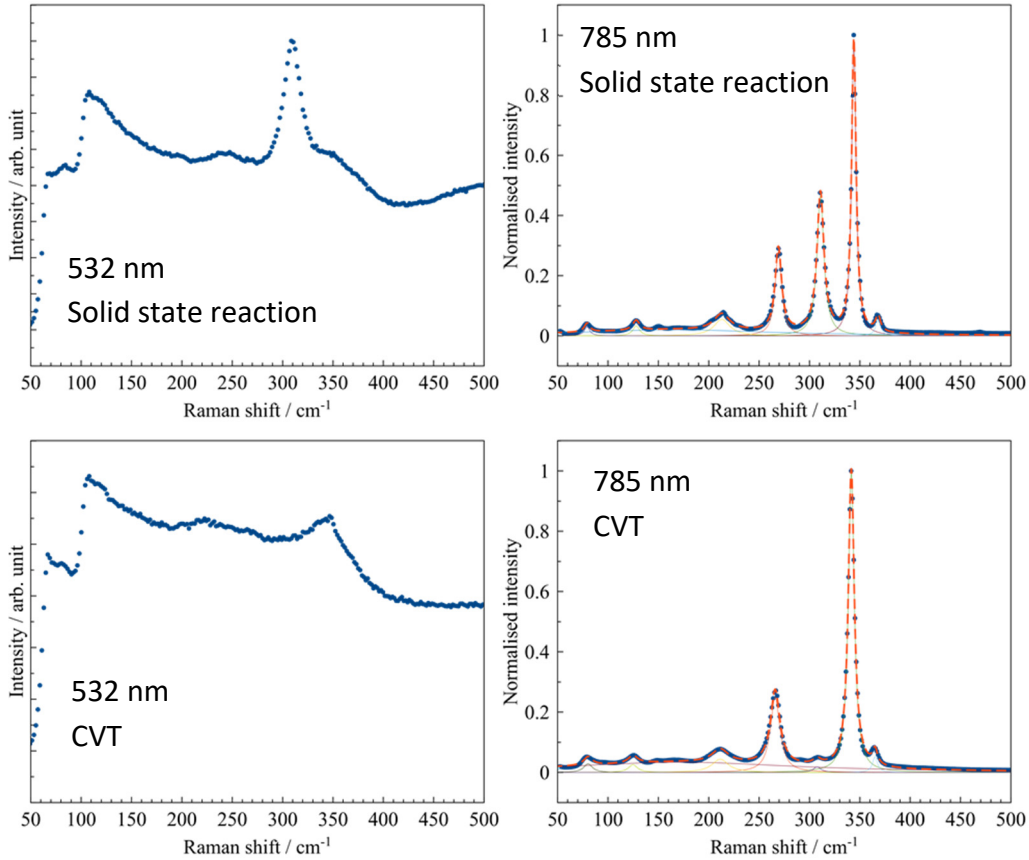

Figure 8.22 Raman spectra of Ag_2ZnSnS_4 synthesised from solid state reaction and chemical vapour transport.

Unfortunately resonance Raman spectroscopy of AZTS could not be carried out because laser with excitation wavelength close to the band gap of AZTS was not available, otherwise it is predicted that more peaks would be observable, and hence the assignment of Raman peaks and comparison with CZTS would be easier.

UV-Vis spectra of both solid state and CVT AZTS show more than one transitions. Some of these transitions can be attributed to the by-products SnS_2 and $Ag_4Sn_3S_8$ detected in PXRD patterns and Raman spectra. The onset around 650 nm for both samples can be attributed to AZTS. This transition translated to a band gap of 1.95 eV in the Tauc plot, which agrees with the value of 2.0 eV reported in literature.[33] The onset around 550 nm can be attributed to SnS_2 which has a band gap between 2.12 – 2.44 eV.[7] It was assumed that the few transitions between 1000 and 650 nm can be attributed to silver tin sulphide. The band gap of various silver tin sulphide phases are as follow: Ag_2SnS_3 (1.26 eV);[41, 42] Ag_8SnS_6 (1.30 – 1.50 eV);[43, 44] and $Ag_8SnS_6/Ag_4Sn_3S_8$ mixture (1.27 – 1.36 eV).[45] There was no report on the band gap of phase pure $Ag_4Sn_3S_8$.

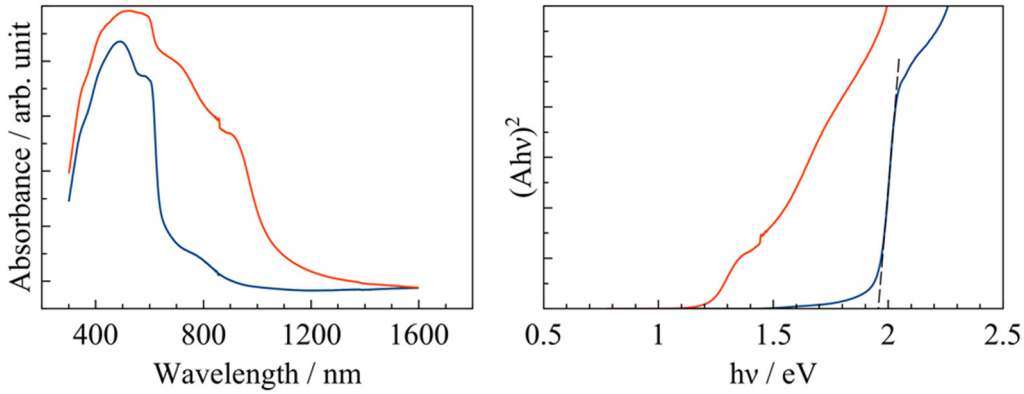

Figure 8.23 UV-Vis spectra and Tauc plot of AZTS synthesised from solid state reaction (blue line) and chemical vapour transport (red line). The step around 860 nm was due to an artefact in the equipment.

8.6 Conclusion

The solid state synthesis of CuS from the elements in sealed reaction conditions were successfully undertaken, while hydrothermal synthesis of CuS required reaction temperature above 180 °C.

The Raman spectra and PXRD patterns for SnS synthesised from both solid state and hydrothermal reactions indicate the presence of SnS_2. Fortunately, it has been

suggested that secondary phases (*i.e.* SnS_2) could have a low impact on SnS solar cell performance.[46]

The solid state synthesis of Cu_2SnS_3 yielded a mixture of CuS and Cu_2SnS_3. A KCN etch was carried out and successfully removed the CuS phase. Although Raman spectra suggested the Cu_2SnS_3 synthesised is monoclinic, monoclinic CTS peaks were not observed in the PXRD pattern. UV-Vis spectra of Cu_2SnS_3 showed promising absorption characteristics for photovoltaic applications between 600 and 1310 nm. Hydrothermal synthesis of Cu_2SnS_3 yielded products with poor crystallinity. All attempts to grow bigger Cu_2SnS_3 crystals using chemical vapour transport methods were unsuccessful.

The synthetic conditions for Cu_XS, SnS_x and Cu_2SnS_3 are very similar to that of CZTS, so the formation of these secondary phases during CZTS synthesis is unavoidable. One of the ways to drive the reaction towards the formation of CZTS is to supply excess sulphur because CZTS $\rightleftharpoons Cu_2S + ZnS + SnS + 0.5\ S_2$.

Bi_2S_3 was successfully synthesised via hydrothermal methods. Initial investigations into the synthesis of Bi_2S_3 were carried out using different sulphur precursor and solvent, with thiourea and $Na_2S{\cdot}9H_2O$ being the best sulphur precursor and water being the best solvent. UV-Vis spectra of Bi_2S_3 shows promising absorption characteristics for photovoltaic applications between 600 and 830 nm.

Initial attempts to synthesise Ag_2ZnSnS_4 using solid state and chemical vapour transport reactions yielded a mixture of SnS_2, $Ag_4Sn_3S_8$ and Ag_2ZnSnS_4, suggesting the synthesis of phase-pure AZTS is as complicated as CZTS.

Reference

1. Wells, A.F., *Structural Inorganic Chemistry 4th Edition*. 1975: Oxford University Press.
2. Martinuzzi, S., *Trends and problems in CdS/Cu_xS thin film solar cells: A review.* Solar Cells, 1982. **5**(3): p. 243-268.
3. Bragagnolo, J.A., Barnett, A.M., Phillips, J.E., Hall, R.B., Rothwarf, A., and Meakin, J.D., *The design and fabrication of thin-film CdS/Cu_2S cells of 9.15-percent conversion efficiency.* IEEE Transactions on Electron Devices, 1980. **27**(4): p. 645-651.
4. Xu, Q., Huang, B., Zhao, Y., Yan, Y., Noufi, R., and Wei, S.-H., *Crystal and electronic structures of CuxS solar cell absorbers.* Applied Physics Letters, 2012. **100**(6): p. 061906.
5. Shirai, K., Moriguchi, Y., Ichimura, M., Usami, A., and Saji, M., *Relationship between Raman Spectra and Crystallinity of CdS Films Grown by Cathodic Electrodeposition.* Japanese Journal of Applied Physics, 1996. **35**(4R): p. 2057.
6. Raadik, T., Grossberg, M., Raudoja, J., Traksmaa, R., and Krustok, J., *Temperature-dependent photoreflectance of SnS crystals.* Journal of Physics and Chemistry of Solids, 2013. **74**(12): p. 1683-1685.
7. Said, G. and Lee, P.A., *Electrical conduction mechanisms in tin disulphide.* physica status solidi (a), 1973. **15**(1): p. 99-103.
8. Khadraoui, M., Benramdane, N., Mathieu, C., Bouzidi, A., Miloua, R., Kebbab, Z., Sahraoui, K., and Desfeux, R., *Optical and electrical properties of Sn_2S_3 thin films grown by spray pyrolysis.* Solid State Communications, 2010. **150**(5): p. 297-300.
9. Sinsermsuksakul, P., Sun, L., Lee, S.W., Park, H.H., Kim, S.B., Yang, C., and Gordon, R.G., *Overcoming Efficiency Limitations of SnS-Based Solar Cells.* Advanced Energy Materials, 2014. **4**(15): p. 1400496.
10. Barone, G., Hibbert, T.G., Mahon, M.F., Molloy, K.C., Price, L.S., Parkin, I.P., Hardy, A.M.E., and Field, M.N., *Deposition of tin sulfide thin films from tin(iv) thiolate precursors.* Journal of Materials Chemistry, 2001. **11**(2): p. 464-468.
11. Fernandes, P.A., Salome, P.M.P., and da Cunha, A.F., *A study of ternary Cu_2SnS_3 and Cu_3SnS_4 thin films prepared by sulfurizing stacked metal precursors.* Journal of Physics D-Applied Physics, 2010. **43**(21): p. 215403.
12. Berg, D.M., Djemour, R., Guetay, L., Zoppi, G., Siebentritt, S., and Dale, P.J., *Thin film solar cells based on the ternary compound Cu_2SnS_3.* Thin Solid Films, 2012. **520**(19): p. 6291-6294.
13. Nakashima, M., Fujimoto, J., Yamaguchi, T., and Izaki, M., *Cu_2SnS_3 thin-film solar cells fabricated by sulfurization from NaF/Cu/Sn stacked precursor.* Applied Physics Express, 2015. **8**(4): p. 042303.
14. Hashimoto, Y., Kohara, N., Negami, T., Nishitani, M., and Wada, T., *Surface Characterization of Chemically Treated Cu(In,Ga)Se_2 Thin Films.* Japanese Journal of Applied Physics, 1996. **35**(9R): p. 4760-4764.
15. Weinhardt, L., Fuchs, O., Groß, D., Umbach, E., Heske, C., Dhere, N.G., Kadam, A.A., and Kulkarni, S.S., *Surface modifications of Cu(In,Ga)S_2 thin film solar cell absorbers by KCN and H_2O_2/H_2SO_4 treatments.* Journal of Applied Physics, 2006. **100**(2): p. 024907.

16. Buffière, M., Mel, A.-A.E., Lenaers, N., Brammertz, G., Zaghi, A.E., Meuris, M., and Poortmans, J., *Surface Cleaning and Passivation Using $(NH_4)_2S$ Treatment for Cu(In,Ga)Se_2 Solar Cells: A Safe Alternative to KCN.* Advanced Energy Materials, 2015. **5**(6): p. 1401689.
17. Berg, D.M., Djemour, R., Gütay, L., Siebentritt, S., Dale, P.J., Fontane, X., Izquierdo-Roca, V., and Pérez-Rodriguez, A., *Raman analysis of monoclinic Cu_2SnS_3 thin films.* Applied Physics Letters, 2012. **100**(19): p. 192103.
18. Fernandes, P.A., Salome, P.M.P., and da Cunha, A.F., *Study of polycrystalline Cu_2ZnSnS_4 films by Raman scattering.* Journal of Alloys and Compounds, 2011. **509**(28): p. 7600-7606.
19. Oliva, F., Arques, L., Acebo, L., Guc, M., Sanchez, Y., Alcobe, X., Perez-Rodriguez, A., Saucedo, E., and Izquierdo-Roca, V., *Characterization of Cu_2SnS_3 polymorphism and its impact on optoelectronic properties.* Journal of Materials Chemistry A, 2017. **5**(45): p. 23863-23871.
20. Dahman, H., Rabaoui, S., Alyamani, A., and El Mir, L., *Structural, morphological and optical properties of Cu_2SnS_3 thin film synthesized by spin coating technique.* Vacuum, 2014. **101**: p. 208-211.
21. Tiwari, D., Chaudhuri, T.K., Shripathi, T., and Deshpande, U., *Synthesis of earth-abundant Cu_2SnS_3 powder using solid state reaction.* Journal of Physics and Chemistry of Solids, 2014. **75**(3): p. 410-415.
22. Xin, H., Katahara, J.K., Braly, I.L., and Hillhouse, H.W., *8% Efficient $Cu_2ZnSn(S,Se)_4$ Solar Cells from Redox Equilibrated Simple Precursors in DMSO.* Advanced Energy Materials, 2014. **4**(11): p. 1301823.
23. Lukose, J. and Pradeep, B., *Electrical and optical properties of bismuth sulphide [Bi_2S_3] thin films prepared by reactive evaporation.* Solid State Communications, 1991. **78**(6): p. 535-538.
24. Mahmoud, S., *Studies on chemically deposited films of Bismuth-sulfide (Bi_2S_3).* FIZIKA, 1996. **A 5**: p. 153-162.
25. Mahmoud, S., Eid, A.H., and Omar, H., *Optical characteristics of Bismuth sulfide (Bi_2S_3) thin films.* FIZIKA, 1997. **A 6**: p. 111-120.
26. Mahmoud, S. and Sharaf, F., *Optical and electrical properties of Bismuth-sulfide (Bi_2S_3) thin films prepared by thermal evaportaion.* FIZIKA, 1997. **A 5**: p. 205-213.
27. Rincón, M.E., Sánchez, M., George, P.J., Sánchez, A., and Nair, P.K., *Comparison of the Properties of Bismuth Sulfide Thin Films Prepared by Thermal Evaporation and Chemical Bath Deposition.* Journal of Solid State Chemistry, 1998. **136**(2): p. 167-174.
28. Kachari, T. and Rahman, A., *Optical properties of bismuth sulfide thin film prepared by thermal evaporation method.* Indian Journal of Physics, 2015. **89**(4): p. 405-410.
29. Nair, M.T.S. and Nair, P.K., *Photoconductive bismuth sulphide thin films by chemical deposition.* Semiconductor Science and Technology, 1990. **5**(12): p. 1225.
30. Liufu, S.-C., Chen, L.-D., Yao, Q., and Wang, C.-F., *Bismuth Sulfide Thin Films with Low Resistivity on Self-Assembled Monolayers.* The Journal of Physical Chemistry B, 2006. **110**(47): p. 24054-24061.

31. Zhao, Y., Chua, K.T.E., Gan, C.K., Zhang, J., Peng, B., Peng, Z., and Xiong, Q., *Phonons in Bi_2S_3 nanostructures: Raman scattering and first-principles studies.* Physical Review B, 2011. **84**(20): p. 205330.
32. Zumeta-Dubé, I., Ortiz-Quiñonez, J.-L., Díaz, D., Trallero-Giner, C., and Ruiz-Ruiz, V.-F., *First Order Raman Scattering in Bulk Bi_2S_3 and Quantum Dots: Reconsidering Controversial Interpretations.* The Journal of Physical Chemistry C, 2014. **118**(51): p. 30244-30252.
33. Tsuji, I., Shimodaira, Y., Kato, H., Kobayashi, H., and Kudo, A., *Novel Stannite-type Complex Sulfide Photocatalysts A^{I2}-Zn-A^{IV}-S_4 (A^I = Cu and Ag; A^{IV} = Sn and Ge) for Hydrogen Evolution under Visible-Light Irradiation.* Chemistry of Materials, 2010. **22**(4): p. 1402-1409.
34. Gong, W., Tabata, T., Takei, K., Morihama, M., Maeda, T., and Wada, T., *Crystallographic and optical properties of $(Cu,Ag)_2ZnSnS_4$ and $(Cu,Ag)_2ZnSnSe_4$ solid solutions.* physica status solidi (c), 2015. **12**(6): p. 700-703.
35. Li, K., Chai, B., Peng, T., Mao, J., and Zan, L., *Synthesis of multicomponent sulfide Ag_2ZnSnS_4 as an efficient photocatalyst for H_2 production under visible light irradiation.* Rsc Advances, 2013. **3**(1): p. 253-258.
36. Ma, C., Guo, H., Zhang, K., Yuan, N., and Ding, J., *Fabrication of p-type kesterite Ag_2ZnSnS_4 thin films with a high hole mobility.* Materials Letters, 2017. **186**(Supplement C): p. 390-393.
37. Gershon, T., Sardashti, K., Gunawan, O., Mankad, R., Singh, S., Lee, Y.S., Ott, J.A., Kummel, A., and Haight, R., *Photovoltaic Device with over 5% Efficiency Based on an n-Type $Ag_2ZnSnSe_4$ Absorber.* Advanced Energy Materials, 2016. **6**(22): p. 1601182.
38. Qi, Y., Tian, Q., Meng, Y., Kou, D., Zhou, Z., Zhou, W., and Wu, S., *Elemental Precursor Solution Processed $(Cu_{1-x}Ag_x)_2ZnSn(S,Se)_4$ Photovoltaic Devices with over 10% Efficiency.* Acs Applied Materials & Interfaces, 2017. **9**(25): p. 21243-21250.
39. Matsushita, H., Ichikawa, T., and Katsui, A., *Structural, thermodynamical and optical properties of Cu_2-II-IV-VI_4 quaternary compounds.* Journal of Materials Science, 2005. **40**(8): p. 2003-2005.
40. Lai, W.-H., Haynes, A.S., Frazer, L., Chang, Y.-M., Liu, T.-K., Lin, J.-F., Liang, I.C., Sheu, H.-S., Ketterson, J.B., Kanatzidis, M.G., and Hsu, K.-F., *Second Harmonic Generation Response Optimized at Various Optical Wavelength Ranges through a Series of Cubic Chalcogenides $Ba_6Ag_{2.67+4\delta}Sn_{4.33-\delta}S_{16-x}Se_x$.* Chemistry of Materials, 2015. **27**(4): p. 1316-1326.
41. Edgar, B. and Braulio, J.F., *Temperature Dependence of the Optical Absorption of the Ternary Compound Ag_2SnS_3.* Japanese Journal of Applied Physics, 2000. **39**(S1): p. 293.
42. Fedorchuk, A.O., Zhbankov, O.Y., Lakshminarayana, G., Kityk, I.V., Tokaichuk, Y., Myronchuk, G.L., Davydyuk, G.Y., Yakymchuk, O.V., and Parasyuk, O.V., *Synthesis and spectral features of Ag_2SnS_3 crystals.* Materials Chemistry and Physics, 2012. **135**(2): p. 249-253.
43. Hu, W.-Q., Shi, Y.-F., and Wu, L.-M., *Synthesis and Shape Control of Ag_8SnS_6 Submicropyramids with High Surface Energy.* Crystal Growth & Design, 2012. **12**(7): p. 3458-3464.

44. Kameyama, T., Fujita, S., Furusawa, H., and Torimoto, T., *Size-Controlled Synthesis of Ag_8SnS_6 Nanocrystals for Efficient Photoenergy Conversion Systems Driven by Visible and Near-IR Lights.* Particle & Particle Systems Characterization, 2014. **31**(11): p. 1122-1126.
45. Yeh, L.-Y. and Cheng, K.-W., *Preparation of chemical bath synthesized ternary Ag–Sn–S thin films as the photoelectrodes in photoelectrochemical cell.* Journal of Power Sources, 2015. **275**: p. 750-759.
46. Andrade-Arvizu, J.A., Courel-Piedrahita, M., and Vigil-Galán, O., *SnS-based thin film solar cells: perspectives over the last 25 years.* Journal of Materials Science: Materials in Electronics, 2015. **26**(7): p. 4541-4556.

9 Conclusion

The main objective of the work described in this thesis was to synthesise high quality CZTS single crystals and to characterise them using a variety of techniques to study the structural and optoelectronic properties of CZTS to try to understand CZTS fundamentally. Most studies use thin films of CZTS that may contain secondary phases, but single crystals are better defined because of the absence of grain boundaries, the absence of secondary phases, and macroscopic in size. This thesis presents the most comprehensive study on CZTS single crystals to-date.

As discussed in Chapter 2, it is a challenge to synthesise phase pure CZTS material due to the complex phase diagram and the relatively small absolute deviation from the ideal stoichiometric composition that can be tolerated at typical reaction temperatures.[1] Initial synthesis of polycrystalline CZTS were attempted using solid state reaction, and the following conditions were varied: reaction temperature, duration, amount of excess sulphur, and precursors. However, nearly all attempts resulted in some level of secondary phase formation as revealed by EDS and/or Raman spectroscopy. Various secondary phases, namely Cu_xS, SnS_x, and Cu_2SnS_3 were also synthesised as described in Chapter 8. The synthetic conditions of these phases are very similar to that of CZTS, and so the formation of secondary phases during CZTS synthesis is unavoidable. Although CZTS $\rightleftharpoons Cu_2S + ZnS + SnS + 0.5\ S_2$, single phase polycrystalline CZTS was obtained with ball milled elemental precursors at 750 °C with a reaction time of at least 7 days regardless of using excess sulphur. The higher temperature and longer reaction time than thin film synthesis is the reason for producing pure phase CZTS.

Initial attempts to grow bigger CZTS crystals using chemical vapour transport resulted in only two successful syntheses. One batch yielded large grains of sizes around 0.5 – 1 mm, and another batch yielded a mixture of smaller crystal grains of sizes around 100 µm and needle-shaped crystals around 1 mm wide and 10 – 20 mm long. Successful growth of crystal by using chemical vapour transport was achieved by increasing the iodine concentration by up to four times the amount reported in

literatures. Large CZTS crystals with dimensions in the sub-centimetre range were obtained.

The elemental composition of the CZTS crystals proved difficult to establish precisely. Atomic absorption spectroscopy is unreliable because it was very difficult to completely dissolve CZTS. Although the standard deviation in EDS is between 1 and 5%, the accuracy of the data is often in doubt if EDS is not properly calibrated. In theory XRF should give the most reliable result, but unfortunately there was no access to an XRF facility on-site so only a few samples were measured elsewhere late in the project.

Chapter 5 describes a series of characterisations carried out on well-formed CZTS single crystals grown by chemical vapour transport. The results from the different techniques mostly agree with each other, for instance, the observation using resonance Raman spectroscopy, PL, spectroscopic ellipsometry (SE) and external quantum efficiency (EQE) measurements of a band tail which is attributed to residual disorder in CZTS. However, the bandgap derived from Tauc plots using SE and EQE data are in the range of 1.60 – 1.64 eV, whereas the fitting of electroreflectance (EER) spectra indicates two distinct transitions at 1.71 and 1.81 eV. This discrepancy in bandgap values highlights the difficulty of using Tauc plots to determine the bandgap in materials that have a high density of tail states.

The near unity EQE in the plateau region indicates very effective collection of photogenerated electron-hole pairs despite the fact that 20 – 30% Cu/Zn disorder is estimated in the sample. The steep onset in the EQE spectrum compared to literature[2] is attributed to the competition between thermal detrapping and recombination of carriers in tail states.

Chapter 7 describes the fabrication of the first CZTS single crystal device using the 'standard' CZTS cell configuration: Mo/CZTS/CdS/Al:ZnO/i-ZnO/Ni. The V_{OC} of 588 mV obtained is in the same range with other reported CZTS devices, however the cell suffered from very high series resistance due to the non-ideal back contact. The EQE result of the single crystal device shows similar features to those of the single crystal with electrolyte contact described in Chapter 5. A doping density in the order of 10^{15}

cm^{-3} and a depletion width of 570 nm at short circuit were obtained from Mott-Schottky analysis. Although the doping density is lower than values reported for thin films (which subsequently have higher depletion widths), these values are evidently valid for the single crystals studied as demonstrated in both Chapter 5 and Chapter 7. Both Gärtner analysis and Mott-Schottky analysis estimated a built-in potential of *ca.* 1 V for the single crystal CZTS cell. Deviations from ideal Mott Schottky behaviour were attributed to Fermi level pinning caused by surface states at the junction.

From the results in Chapter 5 and Chapter 7, it can be suggested that the V_{OC} deficit in CZTS is limited by surface recombination rather than by bulk recombination. The CZTS community should therefore focus on surface treatment and on alternative buffer layers for CZTS.

Chapter 6 presents attempts to quantify Cu/Zn disorder in CZTS using single crystal neutron diffraction and powder anomalous diffraction, because it is not possible to quantify the site occupancy factors using single wavelength XRD methods due to the similarity in the atomic form factors of isoelectronic Cu^{+} and Zn^{2+}. Resonance Raman spectroscopy, which detects Cu/Zn disorder qualitatively, was also used. The resonance Raman order parameter Q follows the usual trend that has been reported, *i.e.* higher Q at lower annealing temperatures. However, the Q values of the most ordered sample in this thesis is several times higher than reported values, which may due to the difference in composition and the sample preparation method. It was also observed that the annealing time needed for the samples to reach equilibrium ordering were longer than the ones calculated using the Vineyard model. The critical temperature of CZTS analysed in this thesis is around 250 °C using the data from resonance Raman spectroscopy.

The initial neutron diffraction experiment was unsuccessful due to the mis-indexing of the tetragonal unit cell. Only the sample annealed at 150 °C was measured successfully, and the disordered sample (300 °C) was partially measured. The data clearly showed a significant lower *R*-factor when refined using the disordered kesterite model. This is the first reported single crystal neutron diffraction experiment for CZTS.

Although in theory the anomalous scattering effect should enhance the scattering of Cu and Zn near their absorption edges, it was not as straightforward in practice. The initial refinements appeared to show that the sample annealed at 650 K was ordered kesterite, but analysis of the resonance Raman spectra led to the opposite conclusion. There was also no significant different between the *R*-factor between fits to the ordered and disordered kesterite models. A second attempt to analyse the data with a two-stage process proposed by Többens *et al.*[3] was also unsuccessful. It is thought that more datasets taken from different wavelength energies are needed to refine the structure successfully.

Chapter 8 describes the synthesis of several other photovoltaic materials composed of only earth-abundant and non-toxic materials: Cu_xS, SnS_x, Cu_2SnS_3, Bi_2S_3, and Ag_2ZnSnS_4. The choice of the metal and sulphur precursors, and reaction temperature were found to have a large impact on the composition of the final product. SnS, Cu_2SnS_3, and Bi_2S_3 are potential absorber materials that are easy to synthesise, but again the community should pay more attention to the semiconductor surfaces and junctions to improve the performance of solar cells fabricated using these materials.

Reference

1. Siebentritt, S. and Schorr, S., *Kesterites - a challenging material for solar cells.* Progress in Photovoltaics, 2012. **20**(5): p. 512-519.
2. Ren, Y., Scragg, J.J.S., Frisk, C., Larsen, J.K., Li, S.-Y., and Platzer-Björkman, C., *Influence of the Cu_2ZnSnS_4 absorber thickness on thin film solar cells.* physica status solidi (a), 2015. **212**(12): p. 2889-2896.
3. Többens, D.M., Gunder, R., Gurieva, G., Marquardt, J., Neldner, K., Valle-Rios, L.E., Zander, S., and Schorr, S., *Quantitative anomalous powder diffraction analysis of cation disorder in kesterite semiconductors.* Powder Diffraction, 2016. **31**(3): p. 168-175.